SELF-PRESSURIZING PROPELLANT TANK DYNAMICS

A DISSERTATION
SUBMITTED TO THE DEPARTMENT OF
AERONAUTICS AND ASTRONAUTICS
AND THE COMMITTEE ON GRADUATE STUDIES
OF STANFORD UNIVERSITY
IN PARTIAL FULFILLMENT OF THE REQUIREMENTS
FOR THE DEGREE OF
DOCTOR OF PHILOSOPHY

Jonah E. Zimmerman
December 2015

This dissertation is online at: http://purl.stanford.edu/ds271zh2987

I certify that I have read this dissertation and that, in my opinion, it is fully adequate in scope and quality as a dissertation for the degree of Doctor of Philosophy.

Brian Cantwell, Primary Adviser

I certify that I have read this dissertation and that, in my opinion, it is fully adequate in scope and quality as a dissertation for the degree of Doctor of Philosophy.

Juan Alonso

I certify that I have read this dissertation and that, in my opinion, it is fully adequate in scope and quality as a dissertation for the degree of Doctor of Philosophy.

Greg Zilliac

Approved for the Stanford University Committee on Graduate Studies.

Patricia J. Gumport, Vice Provost for Graduate Education

This signature page was generated electronically upon submission of this dissertation in electronic format. An original signed hard copy of the signature page is on file in University Archives.

Abstract

Hybrid rockets frequently use nitrous oxide (N_2O) as a self-pressurizing oxidizer, where the high vapor pressure of the oxidizer is used to force the liquid out of the propellant tank and into the combustion chamber. This allows for a simple propulsion system with no external pressurant or turbopump, however an accurate model for the internal dynamics of the propellant tank is necessary for the prediction of motor performance. Although previous researchers have developed models, they have been shown to be inaccurate in many situations.

To build a robust and accurate model, an in-depth knowledge of the heat and mass transfer mechanisms within the tank is required. To this end, a series of small-scale pressure vessels with optical access have been developed that can be filled with N_2O and then drained in a manner that replicates the conditions within a hybrid rocket. A high-speed camera has been used to visualize the N_2O within the propellant tank and identify relevant phenomena.

Experiments have identified two separate temporal regimes that are common to all blowdown tests: a transient and steady state, each described by distinct features. The transient regime is characterized by a rapid pressure drop and recovery, with homogeneous condensation of the ullage and heterogeneous nucleation and growth of bubbles in the liquid. The steady state regime begins when a large population of bubbles has been formed in the liquid and a balance is established between nucleation of new bubbles and death of bubbles as they reach the free surface and transfer their mass to the ullage. During this steady state regime the liquid and vapor are both homogeneous two-phase mixtures and the pressure drops in a linear fashion as the liquid drains from the tank.

Testing was mostly performed with carbon dioxide (CO_2) after it was identified as a possible simulant fluid for N_2O that presents lower costs and reduced fire and explosion hazards. Comparison tests between the two have also been performed to prove that CO_2 acts as an accurate analog for N_2O. This low-cost simulant enabled a large number of tests that examined the effect of parameter variations, including flow rate, fill level, temperature, and scaling effects.

Experimental data from this system have been used to develop a new model for self-pressurizing propellant tank dynamics. This was done by blending the 0-D lumped-node methods of previous researchers with a novel 1-D method that captures the dynamics of a changing bubble population. This population possesses a size distribution that varies in both space and time, and a modeling technique known as the direct quadrature method of moments was used to develop partial differential equations for parameters of this distribution.

The proposed model was compared against experimental data and shown to have good agreement. The pressure drop and recovery seen in the transient regime, which is not captured by previous models, is visible in the model predictions. Convergence studies were performed in order to determine suitable parameters of the numerical integration schemes and the discretizations used. To complete the model, numerous submodels were incorporated by using relations from various sources in the literature. The effect of variations in these submodels was studied in order to justify the selection of adjustable constants.

Acknowledgments

This work would not have been possible without the help I received from many people. My advisor, Professor Brian Cantwell, has been an invaluable resource to me, giving advice whenever I needed it and also gave me the independence to pursue my own research interests. Greg Zilliac supported my work in many ways, lending me equipment but more importantly his limitless knowledge.

I would like to thank my reading committee, Professors Juan Alonso and John Eaton for their time, insight, and helpful comments. I would also like to thank Professor Craig Criddle for chairing my defense committee.

Professor Scott Hubbard has been a great help to me in my graduate career, taking me under his wing to work on an FAA project that I was completely unqualified for and enabling me to turn it into a success.

Throughout much of my studies I was funded by a NASA Space Technology Research Grant (#NNX11AN14H) which truly made this research possible. Through this program I had two great mentors, Jeremy Corpening and Harry Ryan, both of whom have been wonderful resources. Harry was also responsible for getting me an internship at NASA Stennis Space Center, where I learned what "large scale" really means in of rocket propulsion.

Several people at NASA Ames Research Center have also made contributions: Kurt Long, Rabi Mehta, JT Heineck, and Dennis Acosta.

The current and former members of our research group (Ashley Chandler, Tim Szwarc, Ben Waxman, Beth Jens, Brian Evans, David Murakami, Pavan Narsai, Flora Mechentel, and others) have been great coworkers and friends, except when they don't put tools away.

My parents have been very understanding and gave me an unreasonably small amount of grief for visiting them so infrequently over the past 6 years (you know the planes go both ways, right Mom?).

Lastly and most importantly I would like to thank my wife Stephanie, whose enduring love and support has made the past 12 years better than I ever could have imagined.

Nomenclature

α	Thermal diffusivity or coefficient of thermal expansion
$\bar{S}$	Moment transform of S
β	Volumetric thermal expansion coefficient or bubble growth constant
Δh_{LV}	Enthalpy of vaporization
ΔT_s	Superheat or subcooling temperature
δ	Dirac delta function
$\dot{m}$	Mass flow rate
$\dot{Q}$	Rate of heat transfer
$\dot{R}$	Particle velocity in external space
$\dot{W}$	Rate of work transfer
$\dot{X}$	Particle velocity in internal space
ϵ	Strain
γ	Ratio of specific heats or cell fill level
$\hat{n}$	Unit normal vector
κ	Parameter from Dyer flow model

λ	Eigenvalue
$\mathbf{A}$	Matrix used in direct quadrature method of moments
$\mathcal{O}$	Order of magnitude
Eo	Eotvos number
Mo	Morton number
Nu	Nusselt number
μ	Dynamic viscosity or mean
μ_k	k^{th} statistical moment
ν	Kinematic viscosity or Poisson's ratio
ω	Acentric factor
$\overline{T}_i$	Mean initial temperature (area averaged)
ϕ	Probability of failure per unit volume or void fraction
ρ	Density or non-dimensional radius
σ	Surface tension or mechanical stress
σ_o	Weibull scaling factor, also known as the characteristic or nominal strength
τ	Nondimensional time
Ja	Jakob number
CP	Casalino & Pastrone model
EQ	Phase equilibrium model
L/D	Length-to-diameter ratio
O/F	Oxidizer-to-fuel ratio

ZK	Zilliac & Karabeyoglu model
Θ	Nondimensional temperature
A	Area or eigenfunction expansion coefficient
a	Flaw or crack size or source term in weight transport equation
b	Source term in source term in weighted abscissa transport equation
Bi	Biot number
C	Coefficient
c	Specific heat capacity or convection constant
$c*$	Characteristic exhaust velocity
C_d	Orifice discharge coefficient
c_P	Isobaric specific heat capacity
C_v	Metering valve flow coefficient
c_V	Isochoric specific heat capacity
c_w	Tank wall specific heat capacity
c_{liq}	Liquid specific heat capacity (assuming ideal liquid, $c_P = c_V = c$)
D	Diameter
d_{32}	Sauter mean diameter
E	Young's modulus
E_{ZK}	Empirical heat transfer factor in the ZK model
F	Heterogeneous nucleation geometric factor or force
f_1	Particle distribution function

f_{dep}	Departure frequency
Fo	Fourier number
G	Flux
g	Acceleration due to gravity
G_g	Gas specific gravity
h	Specific enthalpy or heat transfer coefficient or birth/death term
k	Thermal conductivity or effective volume/area coefficient
k_B	Boltzmann constant
K_I	Stress intensity used in crack growth rate
k_s	Bubble growth rate shape factor
K_{IC}	Critical stress intensity used in crack growth rate
L	Length
M	Molecular weight
m	Mass or Weibull modulus, also known as the shape factor or shape parameter
N	Number density
n	Number of nodes or number density of bubbles or droplets
N_{MV}	Metering valve setting
N_{ns}	Nucleation site surface density
P	Pressure or probability
P_f	Probability of failure

P_s	Probability of success
Pr	Prandtl number
q	Mass flow rate in C_v calculation or heat transfer rate
R	Specific gas constant
r	Radius
r^*	Critical radius
Ra	Rayleigh number
S	Direct quadrature method of moments source term
s	Standard deviation or entropy
T	Temperature
t	Time
U	Internal energy or uncertainty
u	Specific internal energy or speed
V	Volume
v	Speed or specific volume
w	Weight used in direct quadrature method of moments
x	Horizontal coordinate or fluid quality or internal coordinate
Y	Crack growth rate shape factor or continuous phase vector
y	Vertical coordinate
Z	Compressibility fator
z	Vertical coordinate

Subscripts

1	Upstream of the injector
2	Downtream of the injector
∞	Far from the bubble
HEM	Homogeneous equilibrium model
SPI	Single phase incompressible
surf	Saturated liquid surface layer
θ	Circumferential direction
active	Active nucleation sites
ave	Average
B	Buoyancy
Ba	Basset force
bub	Bubble
c	Critical point
cond	Conduction or condensation
D	Drag
dep	Bubble departure
evap	Evaporation
exp	Value from experiment
hom	Homogeneous
i	Inner or initial

in	Into the node
l	Liquid
lim	Limit
liq	Liquid
LRO	Liquid run out point
M	Molecule
m	Scaling quantity
max	Maximum
min	Minimum
$model$	Value from model
n	Normalized
$nonsat$	Non-saturation or not saturated
o	Outer or reference
opt	Optimal
out	Out of the node
$outlet$	Flow out through the injector
r	Reduced value (eg $T_r = T/T_c$) or radial direction or external coordinate
sat	Saturation or saturated
$spin$	Spinodal
SS	Stainless steel
$tank$	Tank property

tot	Total within the tank
v	Vapor
vap	Vapor
VM	Virtual mass
w	Tank wall

Contents

Abstract v

Acknowledgments vii

1 Introduction 1

1.1 Self-Pressurizing Propellants . . . 1
1.2 Nitrous Oxide . . . 4
1.3 Equilibrium and Stability . . . 8
1.4 Literature Review . . . 9

2 Evaluation of Existing Models 18

2.1 Common Model Features . . . 18
2.1.1 Fundamental Theory . . . 19
2.1.2 Outlet Flow . . . 22
2.1.3 Heat Transfer and the Tank Walls . . . 24
2.1.4 Fluid Properties . . . 26
2.2 Equilibrium Model . . . 28
2.3 Zilliac & Karabeyoglu Model . . . 30
2.4 Casalino & Pastrone Model . . . 34
2.5 Model Evaluation . . . 38
2.5.1 Overview and Procedure . . . 39
2.5.2 Evaluation of Time Histories . . . 41
2.5.3 Evaluation of Parameter Variations . . . 47
2.6 Summary and Conclusions . . . 49

3 Experimental Systems **52**
3.1 Carbon Dioxide as a Simulant . . . 53
3.2 Polycarbonate Tube System . . . 62
3.3 Quartz Tube System . . . 68
3.3.1 End Plug Design . . . 84
3.3.2 Summary of Quartz Tube System Design . . . 87
3.4 Flat Glass Gauge . . . 90
3.5 Common System Components . . . 93
3.6 Measurements with Saturated Fluids . . . 98

4 Experimental Results **104**
4.1 Basic Behavior . . . 104
4.1.1 Results . . . 105
4.1.2 Discussion . . . 107
4.1.3 Summary and Conclusions . . . 115
4.2 Parameter Variations . . . 116
4.2.1 Flow Rate . . . 121
4.2.2 Fill Level . . . 126
4.2.3 Temperature . . . 131
4.2.4 Initial Bubble Population . . . 147
4.2.5 Feed System Length . . . 151
4.2.6 Valve Opening Time . . . 158
4.2.7 Vessel size . . . 164
4.2.8 Exotic Conditions . . . 168
4.2.9 Summary and Conclusions . . . 181
4.3 Comparison of Carbon Dioxide and Nitrous Oxide . . . 183
4.3.1 Initial Tests in Polycarbonate System . . . 183
4.3.2 Follow-up Tests . . . 195
4.3.3 Summary and Conclusions . . . 214
4.4 Multicomponent Mixtures . . . 218
4.4.1 Nitrogen Added to Ullage . . . 219

4.4.2 Nitrogen Added to Liquid and Ullage . . . 224
4.4.3 Summary and Conclusions . . . 227

5 Proposed Model 232
5.1 Conclusions from Experiments . . . 232
5.2 Overview . . . 233
5.3 Governing Conservation Equations . . . 235
5.3.1 Mass and Energy . . . 236
5.3.2 Direct Quadrature Method of Moments . . . 238
5.4 Submodels . . . 242
5.4.1 Bubble Dynamics . . . 243
5.4.2 Wall Heat Transfer . . . 274
5.4.3 Outflow . . . 277
5.4.4 Adjustable Constants . . . 279
5.5 Numerical Methods . . . 280
5.5.1 DQMOM . . . 280
5.5.2 Wall Conduction . . . 283
5.5.3 Time Integration . . . 284
5.5.4 Fluid Properties . . . 288
5.6 Model Results . . . 290
5.6.1 Results . . . 290
5.6.2 Discussion . . . 297
5.7 Effect of Model Parameter Variation . . . 301
5.7.1 Numerical Parameters . . . 301
5.7.2 Adjustable Constants . . . 306
5.8 Summary and Conclusions . . . 308

6 Conclusions and Future Work 310
6.1 Summary and Conclusions . . . 310
6.2 Recommendations . . . 313
6.2.1 Current Operations . . . 313
6.2.2 Future Experiments . . . 314

6.2.3 Future Modeling Efforts 316

A Test Parameters **318**

B dV/dt Expression **320**

C Overview of DQMOM **322**

D Model Equations **335**

Bibliography **336**

List of Tables

2.1 Heat transfer constants, from Bergman et al[38]. 25
2.2 Tank dimensions from each data set. 39
2.3 Experimental conditions from each data set. 40
2.4 Model parameters for each data set. 41
2.5 Normalized error in pressure histories. 47

3.1 Estimates of chemical atmospheric lifetimes and global warming potentials [57]. 54
3.2 Overview of thermodynamic similarity of nitrous oxide and carbon dioxide. 55
3.3 Comparison of REFPROP uncertainty and maximum differences between nitrous oxide and carbon dioxide. 61
3.4 Orifice dimensions. All dimensions in *mm*. 94

4.1 Test parameters for the nitrous oxide and carbon dioxide comparison tests in the polycarbonate system. 184

5.1 Parameters used in model results. 290

A.1 Test parameters table. 319

List of Figures

1.1 Different liquid propellant feed system configurations. 2
1.2 Vapor pressure of various fuels and oxidizers. 3
1.3 Characteristic exhaust velocity of various oxidizers with paraffin fuel. 5
1.4 Various properties of saturated nitrous oxide versus temperature. Data from REFPROP [2]. 6
1.5 Tank pressure time history, data from Van Pelt et al [3]. 7
1.6 Diagram demonstrating aspects of stability and equilibrium. 9
1.7 Results of Zilliac and Karabeyoglu [7] from the blowdown of an N_2O tank. 11
1.8 Results of Casalino and Pastrone [9]. 12
1.9 Results of Campbell [11] from a blowdown test of a N_2 tank. p_C is the tank pressure, while $p-3$ is the pressure at a point in the discharge line. 13
1.10 Results of Bentz and Wilkinson [19] showing the pressure time history from the blowdown of nitrogen vessel. Reprinted with permission. . 14
1.11 Results of Elliott et al [27] showing the blowdown of a vessel containing a mixture of nitrogen and halon. 17

2.1 Diagrams showing the nodes and the heat and mass transfer processes between them. 19
2.2 Predicted mass fluxes from the HEM, SPI, and Dyer models. 23
2.3 Pv diagram showing isotherms through the metastable and unstable regions. 27

2.4 Specific heat capacity of saturated liquid N_2O calculated from various sources. . . . 28
2.5 Pressure, temperature, and mass time histories from the equilibrium model using the conditions of Van Pelt et al[3]. . . . 30
2.6 Pressure, temperature, and mass time histories from the ZK model using the conditions of Van Pelt et al [3]. . . . 34
2.7 Pressure and temperature time histories as E_{ZK} is varied. . . . 35
2.8 Pressure, temperature, and mass time histories from the CP model using the conditions of Van Pelt et al[3]. . . . 38
2.9 Comparison of model results to the experimental data of Zilliac & Karabeyoglu [7]. . . . 42
2.10 Comparison of model results to the experimental data of Van Pelt et al [3]. . . . 42
2.11 Pressure time histories from the CP model, showing effects of varying thermodynamic properties. . . . 43
2.12 Comparison of model results to the ground and flight test data of Prince et al [49]. . . . 43
2.13 Comparison of experimental pressure to the results of models. . . . 45
2.14 Specific heat transfer rate from tank wall into liquid. . . . 46
2.15 Normalized pressure at the liquid run out point. . . . 48

3.1 Comparison of Peng-Robinson and REFPROP saturated N_2O density calculations. . . . 56
3.2 Relative difference in some properties of N_2O and CO_2 along the saturation line. . . . 57
3.3 Phase boundaries for carbon dioxide and nitrous oxide. . . . 59
3.4 Comparison of N_2O and CO_2 properties away from saturation line. . . 60
3.5 Picture of the polycarbonate tubing test vessel. The right side is the base and the left is the top. . . . 63
3.6 Plumbing and instrumentation diagram for the polycarbonate tubing system. . . . 64

3.7 Failed hydraulic hose used for helium supply. Red circles highlight regions where the hose burst. 65
3.8 Picture of the polycarbonate tube setup at NASA Ames Research Center. 66
3.9 Pictures of acrylic tube showing crazing. White arrows show some crazing lines. 70
3.10 Temperature profiles. Each curve shows the profile at a different time. 79
3.11 Thermal stresses. Each curve shows the profile at a different time. . 79
3.12 Mechanical stresses. 80
3.13 Probability of failure for quartz tube versus wall thickness. 82
3.14 Time to failure for quartz tube versus wall thickness. 85
3.15 Images of the top and bottom of the end plug. Visible are the plastic tube fittings and hose used to circulate the heat transfer fluid within the end plug. 88
3.16 CAD model of the quartz tube with end caps. 88
3.17 Drawing of longitudinal section of quartz tube apparatus. 89
3.18 Annotated still image from high speed video of quartz tube apparatus. 89
3.19 Image of the flat glass gauge. Also visible is the aluminum adapter mount and the steel strut stand. 91
3.20 Image of the two pipe plugs used to allow for instrumentation access within the flat glass gauge. 92
3.21 Drawings of longitudinal sections of flat glass gauge apparatus. . . . 92
3.22 Annotated still image from high speed video of flat glass gauge apparatus. 93
3.23 Sample of orifice dimensions. Dimensions in inches, with bracketed dimensions in mm. Flow is from left to right. 94
3.24 Picture of some of the orifices used in this work. The upstream side is facing the camera. 94
3.25 Simplified plumbing and instrumentation diagram for quartz tube and flat glass gauge systems. 96
3.26 Picture of the control box. 96

3.27 Bad pressure transducer data 98
3.28 Pressure transducer heating requirements. 99
3.29 Pressure transducer with heaters and thermocouple installed. 100
3.30 Image sequence showing presence and evaporation of film of liquid carbon dioxide on thermocouple bead. 101
3.31 Temperature time history, showing measured values from thermocouple 5 as well as the saturation temperature calculated from the pressure. 101
3.32 Still image showing boiling on thermocouple bead. 102
3.33 Temperature histories showing spurious temperature measurements from all 6 thermocouple probes during a test. 103

4.1 Image sequence from high speed video. 105
4.2 Pressure and temperature histories. Test performed with CO_2. . . . 106
4.3 Still images of the ullage for the early times. 108
4.4 Pressure time history for the first 250 ms. Test performed with CO_2. 109
4.5 Pressure-volume diagrams for the expanding ullage. Data from REFPROP [2]. 110
4.6 Droplet nucleation rate versus temperature for CO_2 for several levels of subcooling, according to classical homogeneous nucleation theory. 111
4.7 Still image sequence of liquid showing instantaneous superheat. . . . 112
4.8 Initial temperature profile. Test performed with CO_2. 118
4.9 Experimental data on the nucleation site density and departure frequency for heterogeneous nucleation of bubbles in liquid. 119
4.10 Image sequence with altered pixel intensities. Numbers below indicate the time in seconds since the start of the test. Test performed with CO_2. 120
4.11 Pressure time histories for the slow and fast tests. Tests were performed with CO_2. 121
4.12 Normalized pressure time histories from the slow and fast tests. Tests were performed with CO_2. 122

4.13 Initial temperature profiles from the slow and fast tests. Tests were performed with CO_2. 122
4.14 Image sequence comparison for early times for slow and fast tests. . 123
4.15 Image sequence comparison for later times for slow and fast tests. . 124
4.16 Pressure and normalized pressure time histories for the 91% and 72% fill level tests. Tests were performed with CO_2. 126
4.17 Initial temperature profiles from the 91% and 72% fill level tests. Tests were performed with CO_2. 127
4.18 Image sequence comparison for early times from the 91% and 72% fill level tests. 128
4.19 Image sequence comparison for later times from the 91% and 72% fill level tests. 129
4.20 Pressure and normalized pressure time histories for the ambient and hot tests. Tests were performed with CO_2. 132
4.21 Initial temperature profiles from the ambient and hot tests. Tests were performed with CO_2. 132
4.22 Image sequence comparison for early times from the ambient and hot tests. 133
4.23 Image sequence comparison for later times from the ambient and hot tests. 134
4.24 Nucleation sizes as a function of temperature for different levels of superheat/subcooling, for CO_2 and expressed in $°C$. 135
4.25 Heterogeneous bubble nucleation rate for CO_2. 137
4.26 Pressure and normalized pressure histories for the ambient and cold. Tests were performed with CO_2. 138
4.27 Initial temperature profiles from the ambient and cold tests. Tests were performed with CO_2. 138
4.28 Image sequence comparison for early times from the ambient and cold tests. 139
4.29 Image sequence comparison for later times from the ambient and cold tests. 140

4.30 Equilibrium model predictions with varying wall heat transfer into the liquid. Legend shows the factor by which wall heat transfer has been scaled by. Simulation performed for CO_2. 142
4.31 Initial temperature profiles from the uniform, top hot, and bottom cold tests. Tests were performed with CO_2. 143
4.32 Pressure and normalized pressure histories for the uniform, top hot, and bottom cold tests. Tests were performed with CO_2. 144
4.33 Image sequence comparison for early times from the uniform, top hot, and bottom cold tests 145
4.34 Image sequence comparison for later times from the uniform, top hot, and bottom cold tests 146
4.35 Pressure and normalized pressure histories for the flat and bubbly tests. Tests were performed with CO_2. 147
4.36 Initial temperature profiles from the flat and bubbly tests. Tests were performed with CO_2. 148
4.37 Image sequence comparison for early times from the flat and bubbly tests. 149
4.38 Image sequence comparison for later times from the flat and bubbly tests. 150
4.39 Pressure and normalized pressure histories for the tests with different feed line lengths. Tests were performed with CO_2. 152
4.40 Initial temperature profiles from the tests with different feed line lengths. Tests were performed with CO_2. 152
4.41 Image sequence comparison for early times from the different feed line length tests. 153
4.42 Image sequence comparison for later times from the different feed line length tests. 154
4.43 Pressure time histories for the 0 cm, 24 cm, and 52 cm tests. Tests were performed with CO_2. 155
4.44 Image sequence comparison for very early times from the different feed line length tests. 156

4.45 Valve position versus time for various driving air pressures. Legend shows the air pressure in kPa. 159
4.46 Valve rotation time versus the driving air pressure. 159
4.47 Pressure and normalized pressure histories for the fast and slow valve speed tests. Tests were performed with CO_2. 160
4.48 Initial temperature profiles from the fast and slow valve speed tests. Tests were performed with CO_2. 160
4.49 Image sequence comparison for early times from the tests with fast and slow valve speeds. 161
4.50 Image sequence comparison for later times from the tests with fast and slow valve speeds. 162
4.51 Pressure and normalized pressure time histories for quartz tube and flat glass gauge tests. Tests were performed with CO_2. 165
4.52 Initial temperature profiles for the quartz tube and flat glass gauge tests. 165
4.53 Image sequence comparison for early times from the quartz tube and flat glass gauge tests. 166
4.54 Image sequence comparison for later times from the quartz tube and flat glass gauge tests. 167
4.55 Pressure time history for the extremely high flow rate test. Test performed with CO_2. 169
4.56 Initial temperature profile from the extremely high flow rate test. Test performed with CO_2. 169
4.57 Image sequence of early times from the extremely high flow rate test. 170
4.58 Image sequence of later times from the extremely high flow rate test. 170
4.59 Image sequence highlighting bubble nucleation in the extremely high flow rate test. 171
4.60 Pressure time history for the near critical point test. Test performed with CO_2. 173
4.61 Initial temperature profile from the near critical point test. Test performed with CO_2. 173

4.62 Image sequence of early times from the near critical point test. . . . 174
4.63 Image sequence of later times from the near critical point test. . . . 174
4.64 Image sequence highlighting bubble nucleation in the near critical point test. . . . 175
4.65 Temperature-entropy diagram for CO_2 showing the saturation and spinodal lines. . . . 177
4.66 Pressure time history for the supercritical test. Test performed with CO_2. . . . 178
4.67 Initial temperature profile from the supercritical test. Test performed with CO_2. . . . 178
4.68 Image sequence of early times from the supercritical test. . . . 179
4.69 Image sequence of later times from the supercritical test. . . . 179
4.70 Image sequence highlighting bubble nucleation in the supercritical test. 180
4.71 Measured metering valve flow coefficient versus the valve handle setting, for both N_2O and CO_2. . . . 185
4.72 Pressure at the liquid runout point versus the valve flow coefficient for all CO_2 and N_2O tests. . . . 186
4.73 Time at the liquid runout point versus the valve flow coefficient for all CO_2 and N_2O tests. . . . 186
4.74 Pressure and normalized pressure histories for all CO_2 tests. . . . 187
4.75 Pressure and normalized pressure histories for all N_2O tests. . . . 187
4.76 Pressure and normalized pressure histories for the low flow rate CO_2 and N_2O tests. . . . 188
4.77 Image sequence for the low flow rate CO_2 and N_2O tests. . . . 189
4.78 Pressure and normalized pressure histories for the medium flow rate CO_2 and N_2O tests. . . . 190
4.79 Image sequence for the medium flow rate CO_2 and N_2O tests. . . . 190
4.80 Pressure and normalized pressure histories for the high flow rate CO_2 and N_2O tests. . . . 191
4.81 Image sequence for the high flow rate CO_2 and N_2O tests. . . . 191

4.82 Image sequence from the high flow rate CO_2 test showing the single large bubble. 192
4.83 Image sequence shown in figure 4.82 but with the image intensity remapped to a range of colors to increase contrast. 192
4.84 Diagram describing the geysering phenomenon, from Morgan [78]. Reprinted with permission. 193
4.85 Pressure and normalized pressure time histories for CO_2 and N_2O tests. 196
4.86 Initial temperature profiles for the CO_2 and N_2O tests. 196
4.87 Image sequence comparison for early times from the CO_2 and N_2O tests. 197
4.88 Image sequence comparison for later times from the CO_2 and N_2O tests. 198
4.89 Pressure and normalized pressure time histories for the ambient and hot tests. 200
4.90 Initial temperature profiles from the ambient and hot N_2O tests. . . 200
4.91 Image sequence comparison for early times from the ambient and hot tests. 201
4.92 Image sequence comparison for later times from the ambient and hot tests. 202
4.93 Pressure and normalized pressure time histories for CO_2 and N_2O tests. 204
4.94 Initial temperature profiles for the CO_2 and N_2O tests. 205
4.95 Image sequence comparison for early times from the CO_2 and N_2O tests. 206
4.96 Image sequence comparison for later times from the CO_2 and N_2O tests. 207
4.97 Image sequence comparison the times at which the Taylor bubble is most visible for the CO_2 and N_2O tests. 208
4.98 Image sequence showing “mild” Taylor bubble formation in N_2O. . . 209
4.99 Image sequence showing “moderate” Taylor bubble formation in N_2O. 209
4.100 Image sequence showing “strong” Taylor bubble formation in N_2O. . 210
4.101 Image sequence showing “very strong” Taylor bubble formation in N_2O. 210

4.102 Pressure and normalized pressure time histories for the flat and bubbly tests. Tests performed with CO_2. 211
4.103 Initial temperature profiles for the flat and bubbly tests. Tests performed with CO_2. 212
4.104 Image sequence comparison for early times from the flat and bubbly tests. 213
4.105 Pressure and normalized pressure time histories for CO_2 and N_2O tests. 213
4.106 Initial temperature profiles for the CO_2 and N_2O tests. 214
4.107 Image sequence comparison for early times from the CO_2 and N_2O tests. 215
4.108 Image sequence comparison for later times from the CO_2 and N_2O tests. 216
4.109 Pressure and normalized pressure time histories for the pure and dissolved tests. Tests performed with CO_2. 220
4.110 Initial temperature profiles for the pure and dissolved tests. Tests performed with CO_2. 220
4.111 Image sequence comparison for early times from the pure and dissolved tests. 221
4.112 Image sequence comparison for later times from the pure and dissolved tests. 222
4.113 Pressure time histories for the pure and dissolved tests in the very early times. Tests performed with CO_2. 224
4.114 Image sequence comparison between four different tests with different amounts of N_2 dissolved into the CO_2. 225
4.115 Pressure and normalized pressure time histories for the layered and uniform tests. Tests performed with CO_2. 226
4.116 Initial temperature profiles for the layered and uniform tests. Tests performed with CO_2. 227
4.117 Image sequence comparison for early times from the layered and uniform tests. 228

4.118 Image sequence comparison for later times from the layered and uniform tests. 229
4.119 Image sequence for the layered test highlighting the bubble nucleation process. 230
4.120 Initial temperature profiles for the layered and uniform tests. Tests performed with CO_2. 231

5.1 Diagrams showing the nodes and the heat and mass transfer processes between them for the proposed model. 234
5.2 Diagram of bubble nucleation in a conical cavity, from Cole [87]. Reprinted with permission. 244
5.3 Comparison of full and simplified growth models after Scriven . . . 252
5.4 Images showing how bubbles nucleating on the thermocouple probe sheath can be tracked in the high speed camera data. 254
5.5 Experimentally measured bubble radius versus time. 255
5.6 Experimentally measured bubble rise velocity. Both the raw data and the filtered result are shown. 255
5.7 Comparison of model predictions and experimental measurements of bubble growth rates. 255
5.8 Minimum superheat to prevent bubble from shrinking. Calculated based on the experimental data in figure 5.5. 257
5.9 Comparison of Jensen and Memmel's correlation with data. The "present correlation" line is equation (5.48). 259
5.10 Comparison of forces on bubble, using data from figures 5.5 and 5.6. 262
5.11 Comparison of forces on bubble, using data from figures 5.5 and 5.6. 262
5.12 Bubble rise velocity versus time as predicted by simulation. 266
5.13 Bubble radius versus time as predicted by simulation. 266
5.14 Normalized difference in bubble rise velocity. 267
5.15 Normalized difference in bubble radius. 267
5.16 Comparison of measured drag coefficient and that predicted by Ishii and Zuber [100]. 268

5.17 Diagram showing the steps of bubble coalescence. Diagram from Yeoh et al, [102]. Reprinted with permission. 271
5.18 Boiling heat transfer data for carbon dioxide. 275
5.19 Mass flux of carbon dioxide through an orifice as a function of pressure and quality. This is figure 18 from Hesson [35]. 278
5.20 Diagram showing the grid geometry for the DQMOM terms. 282
5.21 Initial temperature profile for experimental data used as model test case. 291
5.22 Pressure time history comparison of model results and experiment. . 292
5.23 Fill level time history comparison of model results and experiment. . 292
5.24 Temperature time history for the liquid and ullage. 293
5.25 Liquid superheat as a function of time. 293
5.26 Mass flow rate out of the tank as a function of time. 294
5.27 Time history of the ullage vapor mass fraction. 294
5.28 DQMOM weights versus height, at 8 time points. 295
5.29 DQMOM abscissas versus height, at 8 time points. 295
5.30 Void fraction within the liquid versus height, at 8 time points. . . . 296
5.31 Bubble number density within the liquid versus height, at 8 time points. 296
5.32 Bubble Sauter mean diameter versus height, at 8 time points. 296
5.33 Temperature profiles in the lower portion of the tank wall 298
5.34 Temperature profiles in the upper portion of the tank wall 298
5.35 Time step history. 298
5.36 Relative error in pressure versus time. The different curves correspond to different spatial grid resolution. 302
5.37 Integrated relative error versus the number of nodes in the spatial grid. 302
5.38 Relative error in pressure versus time for simulations with different numbers of moments. 303
5.39 Integrated relative error versus the number of moments used in the model. 303
5.40 Relative error in pressure versus time for simulations with different relative error tolerances. 304

5.41 Integrated relative error versus the time integration tolerance. . . . 304
5.42 Relative error in pressure versus time for simulations with different numbers of nodes in the wall. 305
5.43 Integrated relative error versus the number of nodes in the wall. . . 305
5.44 Variation in pressure for changes in $C_{\dot{Q}_{lw}}$. 306
5.45 Variation in pressure for changes in $C_{collision\ efficiency}$. 307
5.46 Difference in pressure history for changes in $C_{collision\ efficiency}$. 307
5.47 Variation in pressure for changes in $C_{nucleation\ rate}$. 308
5.48 Difference in pressure history for changes in $C_{nucleation\ rate}$. 308

Chapter 1

Introduction

1.1 Self-Pressurizing Propellants

Liquid propellants are commonly used in rocket propulsion systems including liquid rockets, where both the fuel and oxidizer are in liquid form and hybrid rockets, where one component, usually the fuel, is a solid and the other is a liquid. Rocket combustion chambers typically operate with pressures between 0.5 MPa and 20 MPa and so to move this liquid propellant from its tank into the chamber the tank must either be pressurized to a pressure higher than the combustion chamber or a pump must be used. These two configurations are commonly referred to as "pressure-fed" and "pump-fed" and are shown schematically in figure 1.1.

In both cases a significant amount of inert mass must be added to the rocket, either as pressurant vessels, valves, and regulators in the pressure-fed case, or as pumps, turbines, and extra propellant needed to drive the pump in the pump-fed case. In addition to the increased inert mass, these components add complexity and failure modes to the propulsion system.

A different concept involves selecting a propellant with a high vapor pressure and using this vapor as the pressurant. If this vapor pressure is higher than the chamber pressure, no additional pump or pressurization system is needed (see figure 1.1). As the liquid is drawn out of the base of the tank some liquid boils or evaporates into the ullage space to maintain the tank pressure. This configuration is known as a

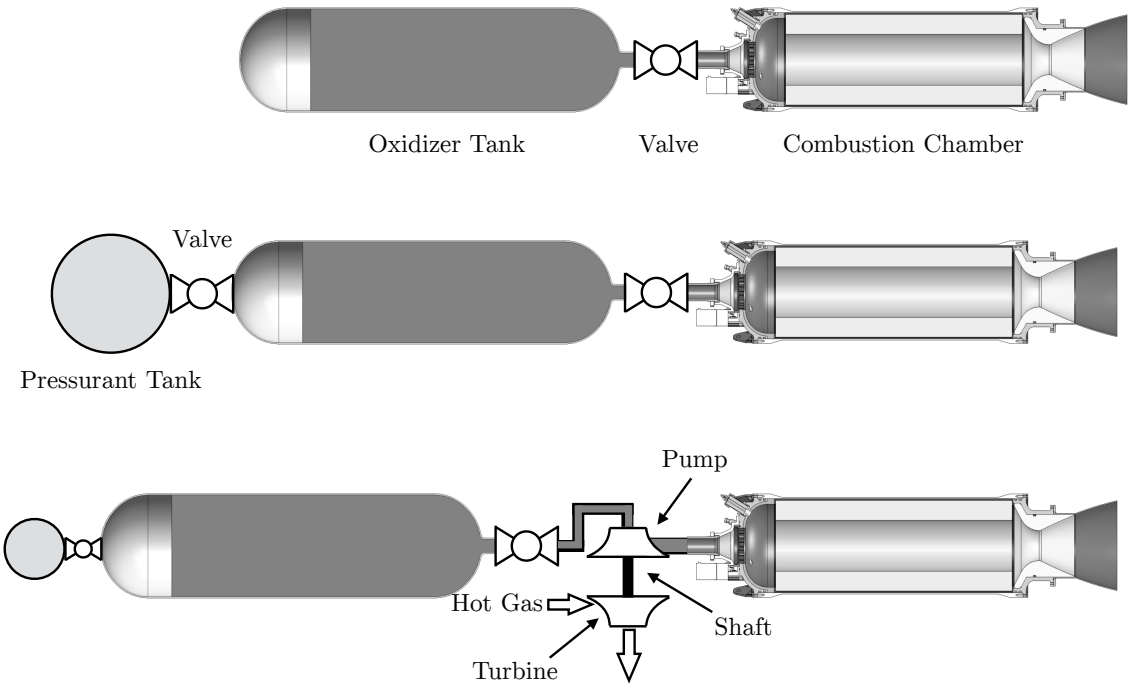

Figure 1.1: Different liquid propellant feed system configurations.

self-pressurizing propellant.

A variety of fluids may be used as self-pressurizing propellants, including both fuels and oxidizers. The only requirement is a vapor pressure high enough to overcome the chamber pressure, ideally at a temperature close to ambient and therefore requiring minimal thermal control. Figure 1.2 shows the vapor pressures of various fuels and oxidizers as a function of temperature. Note that RP-1, a common propellant, is not shown because it is a mixture of a wide variety of hydrocarbons and as a result has no single well defined vapor pressure.

Of these, only a handful have vapor pressures high enough to be practical self-pressurizing propellants: nitrous oxide, oxygen, methane, MON-10, MON-30, ethylene, ethane, and propane. MON-10 and MON-30 are both two-component mixtures and as such are possibly undesirable because any boiling or evaporation of liquid will change the composition of both the liquid and vapor. Therefore the remaining options are nitrous oxide, oxygen, and the light hydrocarbons. These have all been used, tested, or proposed as self-pressurizing propellants either in liquid or hybrid

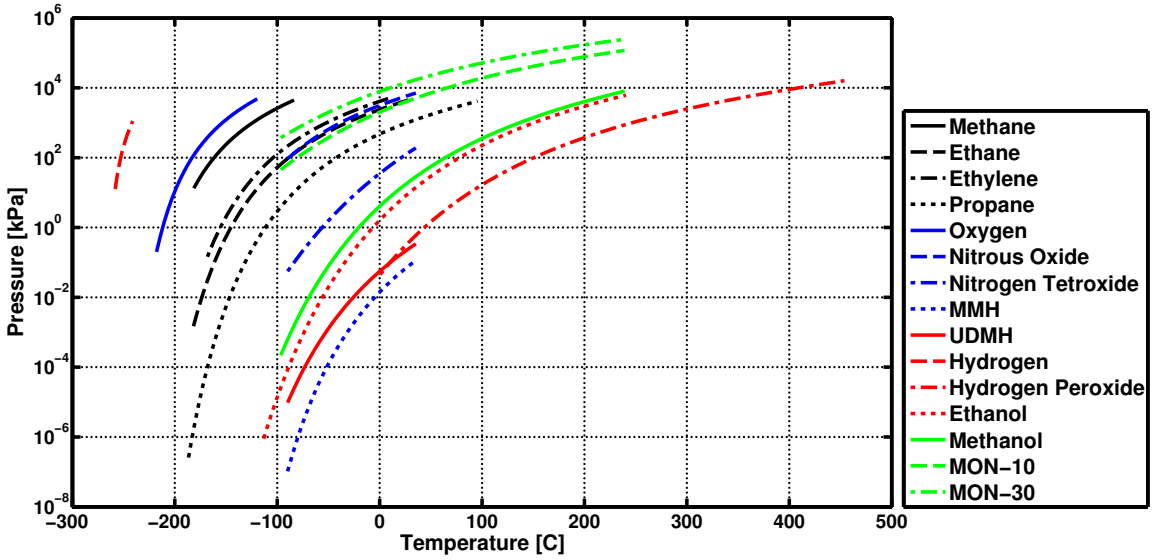

Figure 1.2: Vapor pressure of various fuels and oxidizers. Curves extend from the triple point to the critical point. MMH: monomethyl hydrazine, UDMH: unsymmetrical dimethyl hydrazine, MON-10: mixed oxides of nitrogen with 10% NO and 90% N_2O_4, MON-30: mixed oxides of nitrogen with 30% NO and 70% N_2O_4.

rockets.

The concept of a self-pressurizing propellant is not unique to rockets. Numerous everyday consumer systems use liquids stored at their vapor pressure and at equilibrium with their vapor. Propane and butane tanks used for cooking or heating are common examples. Carbon dioxide and halon fire extinguishers are another. A ubiquitous example is "canned air" gas dusters, which are in fact not air but usually contain the refrigerant R-134a (1,1,1,2-tetrafluoroethane).

However, there are important differences between these systems and rockets. While nearly all of these withdraw the vapor from the storage vessel, rockets withdraw the liquid. Secondly, the flow rates encountered in rockets are much larger and result in the vessel being drained much more rapidly. Lastly, a rocket propulsion system requires extensive knowledge about the propellant flow rate, in contrast to many of these systems.

1.2 Nitrous Oxide

Most oxidizers used in rockets are difficult fluids to handle. Liquid oxygen is cryogenic, requiring tanks and piping to be heavily insulated and rendering it challenging to store for long periods of time. Hydrogen peroxide will cause severe burns on contact with skin and decomposes over time, making long term storage difficult and possibly causing explosions. Nitric acid is compatible with few metals due to its highly corrosive nature and is also poisonous. Nitrogen tetroxide is toxic and will spontaneously combust when it contacts some organic materials.

In contrast, nitrous oxide is easily storable, is non-corrosive, and relatively non-toxic. This was recognized by the rocket pioneer Robert Goddard, who suggested N_2O and gasoline as propellants. Nitrous oxide's ease of handling and use continues to appeal to propulsion system designers who seek a rocket that is simple, easy to develop and operate, and presents a minimum of hazards to personnel. These are in turn many of the selling points of hybrid rockets and explains why nitrous oxide is commonly used in these systems. Nitrous oxide's attractiveness is compounded by its capabilities as a self-pressurizing oxidizer, with no added complexity from a pressurant system or pump.

Thermochemically, nitrous oxide's performance is similar to other storable oxidizers including nitric acid, hydrogen peroxide, or nitrogen tetroxide but is substantially lower than oxygen. This is shown in figure 1.3, where the characteristic velocity of several oxidizers with paraffin is shown as a function of the oxidizer-to-fuel ratio (O/F). Paraffin is used here because it is a common hybrid rocket fuel and also a hydrocarbon, giving similar performance to other hydrocarbon fuels such as RP-1.

The location of the peak in $c*$ for nitrous oxide is at a higher O/F than the other oxidizers. This can be an advantage in some hybrid rockets as more of the system mass is in liquid form and hence there is more flexibility in packaging. Depending on the fuel and the grain configuration there may also be volume savings, but often the solid fuel is more dense and hence a higher O/F results in a larger rocket. The peak for both nitrous oxide and hydrogen peroxide are both quite broad, allowing for a substantial shift in O/F away from the peak with only minimal performance penalty.

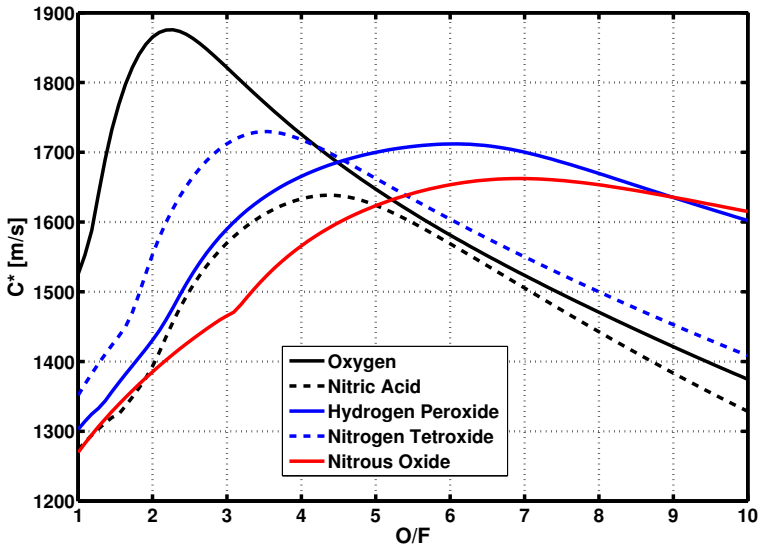

Figure 1.3: Characteristic exhaust velocity of various oxidizers with paraffin fuel, plotted as a function of oxidizer-to-fuel ratio and at a chamber pressure of 3.5 MPa.

When any of the oxidizers in figure 1.3 are burned with a fuel, the majority of the combustion energy is released by the reaction of oxygen atoms with the fuel to form products such as H_2O or CO_2. Therefore one would expect N_2O, a molecule that must carry two extraneous nitrogen atoms for every one of oxygen to have much lower thermochemical performance than the other oxidizers examined in figure 1.3. The reason for the relatively good performance of N_2O lies in the chemical energy stored in the bonds of the molecule itself.

Nitrous oxide, like hydrogen peroxide, has a positive heat of formation meaning that the reaction $N_2O \rightarrow N_2 + \frac{1}{2}O_2$ is exothermic, releasing heat (1.864 MJ/kg or 82.05 kJ/mol). This is a benefit for a chemical propulsion system as it adds energy to the combustion gases on top of that released by the oxidation reaction and even enables nitrous oxide to be used as a monopropellant [1]. However, this reaction can also take place in storage vessels, propellant tanks, and feed lines, where the heat released by one molecule can supply the activation energy required by another, leading to a chain reaction and in some situations an explosion.

These decomposition events have only been observed in nitrous oxide vapor and

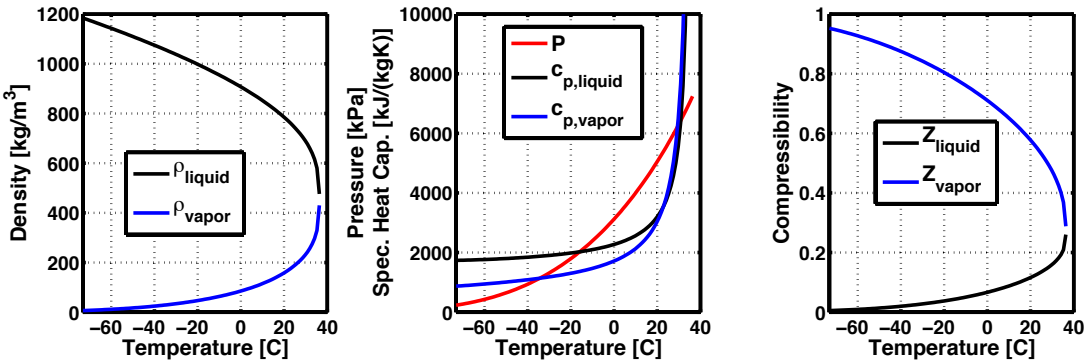

Figure 1.4: Various properties of saturated nitrous oxide versus temperature. Data from REFPROP [2].

therefore a simple method for inhibiting them is to limit the formation of vapor in the feed line and prevent nitrous oxide vapor from encountering ignition sources. Practically, this means that care should be taken in the design of a propellant feed line such that it has a minimum of features that may cause cavitation. Secondly, during a motor firing, once the tank has been drained of all liquid the main oxidizer valve should be closed and the burn stopped to prevent the flow of vapor from the tank to the combustion chamber. If left unchecked, this would create a possible path for a decomposition reaction started in the combustion chamber to get back to the tank and cause it to fail. Alternatively, motors can be specifically designed to operate with a vapor phase burn by taking care to prevent propagation of a flame upstream.

As a non-reacting fluid, nitrous oxide has several drawbacks when compared to other oxidizers including a relatively low liquid density and a critical point that is close to standard conditions ($T_c = 36.37\ ^\circ C$). The proximity of the critical point makes the various properties very sensitive to changes in temperature or pressure. To illustrate, figure 1.4 shows how several of nitrous oxide's fluid properties vary with temperature along the saturation line.

These plots show how much the various properties can change and how they vary increasingly rapidly as the critical point is approached. For example, the density of saturated liquid N_2O changes by 5.3% as the temperature changes from 20 $^\circ C$ to 25 $^\circ C$. By comparison, with nitrogen tetroxide the change is 0.7% and with hydrogen peroxide it is only 0.4%.

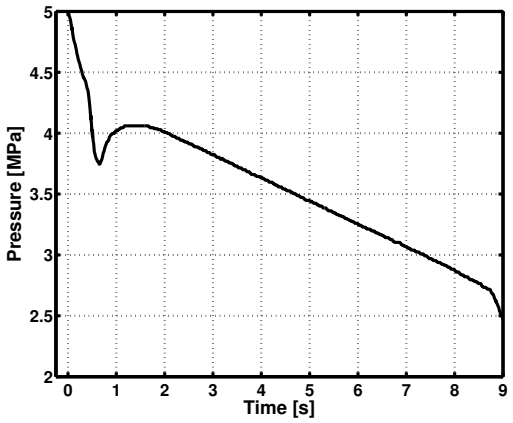

Figure 1.5: Tank pressure time history, data from Van Pelt et al [3].

Rocket propulsion systems with pumps or external pressurants can maintain a constant propellant flow rate with relative ease. With self-pressurizing propellants however the heat and mass transfer processes within the tank dictate how rapidly liquid will transform to vapor. This generally causes the tank pressure to decay with time, but in a non-monotonic manner. This is exemplified by figure 1.5, which shows the oxidizer tank pressure time history from a small hybrid rocket using nitrous oxide as a self-pressurizing propellant.

The primary features of figure 1.5 are typical of self-pressurizing propellant tank dynamics: a steep drop followed by a short increase, then a linear drop towards a sharp cusp. The cusp (at $t = 8.7s$ here) is the point when no liquid remains in the tank and only vapor flows out. One of the primary disadvantages of using N_2O in a self-pressurizing configuration is its seemingly unpredictable nature.

This thesis is devoted solving this problem. First, the existing models in the literature are shown to be inaccurate. Then, the dynamics of self-pressurizing propellant tanks are investigated experimentally in order to identify and describe the fundamental physical phenomena. Then, this knowledge is used to develop a new model that can accurately predict the behavior of this system.

1.3 Equilibrium and Stability

The concepts of thermodynamic equilibrium and stability will be used frequently in this thesis and therefore they will be defined and discussed here. A system that is in thermodynamic equilibrium is one whose properties do not change at an observable rate after being isolated from its surroundings [4].

A system is at a stable equilibrium state if it returns to this state upon being disturbed and is usually characterized by a minimum of some potential function, such as the Gibbs free energy. Conversely if an unstable equilibrium state is attained, any perturbation will result in the system continuing to move away from equilibrium.

This definition is binary and if adhered to no metastable states can be defined as any equilibrium state must simply be stable or unstable [5]. However, metastable states are frequently discussed within thermodynamics. Such states are in fact stable equilibrium states, however the term metastable refers to the presence of a nearby stable state with a lower potential.

These concepts can be visualized with the simple example of a ball rolling down a hill, shown in figure 1.6. At point A, the ball is rolling down the side of the hill, and therefore is not in equilibrium. If the ball comes to rest at point B it has reached a stable equilibrium state because it will return to point B if perturbed to the left or right. The same is true of point D however this point is a metastable condition, because of the close presence of point B with a lower gravitational potential energy. If the ball stops at point C, it is an unstable equilibrium point and will move to point B or D if disturbed.

An example of a stable thermodynamic system could be the water in a glass at room temperature. If the water were isolated from its surroundings, the pressure, temperature, enthalpy, etc. would not change and hence it is in equilibrium. It is also a stable equilibrium, which can be demonstrated by dividing the water in half and removing some energy from one half (thereby decreasing the temperature) and given to the other half (increasing its temperature), the temperature difference would cause heat to continue to flow from the warmer half to the cooler, restoring the initial state.

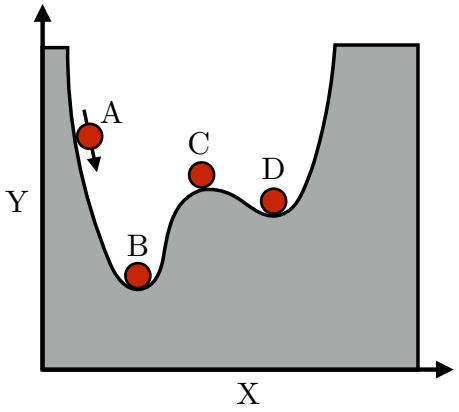

Figure 1.6: Diagram demonstrating aspects of stability and equilibrium.

An unstable thermodynamic system is not commonly found, but one can be imagined: a fluid with a negative specific heat capacity. In this fluid, if energy is added, the temperature decreases. Therefore, if the same experiment described above were performed, the portion of fluid from which heat was removed would warm while the portion with added heat would cool. This would cause a continual flow of energy from one half to the other, getting further and further from the initial state. This is a demonstration of thermal stability, but similar arguments can be made for mechanical or chemical stability as well.

Another related term that will be used is that of phase equilibrium. This refers to two fluid states, usually liquid and gas, that are in mechanical, thermal, and chemical equilibrium. This in turn means that the two phases have identical pressures, temperatures, and chemical potentials and are therefore both saturated.

1.4 Literature Review

Here a brief summary will be given of the experimental and modeling efforts made by previous researchers. This will encompass works focused specifically on nitrous oxide propellant tanks as well as other related systems, including other propellants and systems outside the field of rocket propulsion, such as petroleum refineries and nuclear reactors.

Nitrous oxide's popularity as a self-pressurizing rocket propellant has driven several members of the field to develop and test models that predict its behavior. Three different works will be discussed here, but they will also be covered in much greater detail later in chapter 2.

The first work was that of Zakirov and Li [6] in 2005, who studied a system where gaseous nitrous oxide was being removed from the top of the tank in order to feed small bipropellant or monopropellant thrusters. To model the flow rate out of the tank as a function of time, they simplified the system by assuming that the entire tank remained in phase equilibrium. Effectively, they assumed that the removal of mass from the system is a slow process compared to the heat and mass transfer between the liquid and vapor. This also implies that the tank has a uniform temperature field. Zakirov and Li also performed an experiment, using a 1 L vessel and draining it of liquid in approximately 1200 s. Their model compared well with the experimental data once a correction to the exit gas temperature to account for heat transfer that occurred between the vapor and the tubing after the N_2O left the vessel. While the equilibrium assumption may have been reasonably accurate in this system, it will be shown later that when the time scale is reduced to typical values encountered in hybrid rockets ($\sim$ 10 s), it is no longer accurate. Therefore this model cannot be directly extended.

Less than one week after the publication of Zakirov and Li, a model developed by Zilliac and Karabeyoglu was presented at a different conference [7]. This model was based on early studies of traditional liquid rocket propellant dynamics by Morey and Traxler [8] and in general is much more complex. In contrast to Zakirov and Li, these researchers were studying hybrid rockets that would drain liquid N_2O from the tank in a much shorter time scale, $\mathcal{O}(10\ s)$. While Zilliac and Karabeyoglu effectively assumed that the vapor would remain saturated, they allowed the liquid to become superheated and used traditional natural convection heat transfer relations to model the heat transfer between from the liquid to the vapor. They also performed experiments using a 35.4 L tank that was drained of liquid N_2O in approximately 5 s. After modifying the natural convection heat transfer relations based on experimental data, the model compared well with their experimental results, although the initial

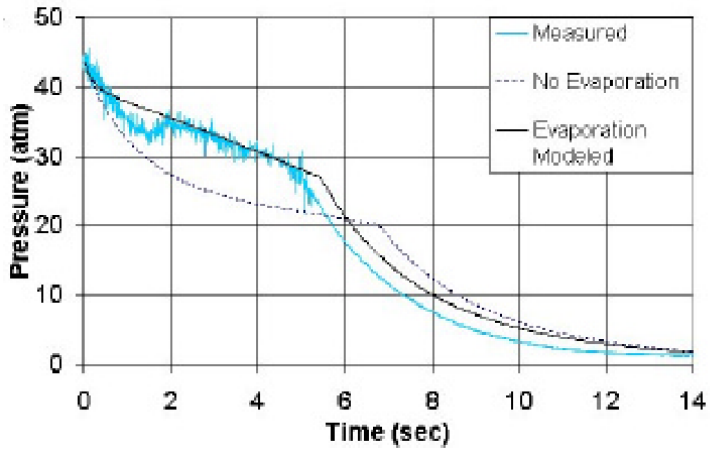

Figure 1.7: Results of Zilliac and Karabeyoglu [7] from the blowdown of an N_2O tank.

drop and recovery (similar to that shown in figure 1.5) was not fully captured. An example of their results is shown in figure 1.7.

The following year, Casalino and Pastrone [9] presented a comparison of two models and used them in a sounding rocket design study. The two models resulted in vehicle designs with substantially different performance, highlighting the need for an accurate model. One model used by Casalino and Pastrone was essentially that of Zakirov and Li, whereby the tank remained in phase equilibrium but liquid was drained from the tank instead of vapor. The second model was novel and assumed that the liquid would become superheated but would follow a path that placed it equidistant to both the saturation line and the spinodal line. The vapor remained saturated. This model compared well with the data of Van Pelt et al [3] but like the model of Zilliac and Karabeyoglu, failed to fully capture the initial pressure drop and recovery. Their results are shown in figure 1.8.

Later in 2010 Whitmore and Chandler [10] presented another equilibrium model very similar to that of Zakirov and Li and Casalino and Pastrone. They also performed an experiment with a 3.2 L tank, draining the liquid in approximately 10 s. This experiment is noteworthy in that their data shows no initial drop and recovery. The likely cause for this is that Whitmore and Chandler vented the ullage for approximately 55 s before beginning to drain liquid from the tank and continued to

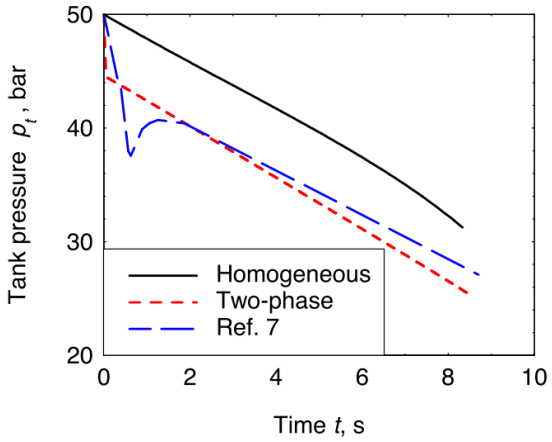

Figure 1.8: Results of Casalino and Pastrone [9]. Homogeneous refers to the equilibrium model, while two-phase is the second model. Reference 7 refers to the data of Van Pelt et al. Reprinted with permission.

do so while the liquid was draining. This venting process dropped the tank pressure by about 150 kPa and caused significant boiling within the liquid, turning it into a two-phase equilibrium mixture. This enabled a phase equilibrium model to accurately capture the system dynamics but this venting process is not a practical solution for propulsion systems, and therefore the phase equilibrium model is frequently inaccurate.

Rocket propellants other than nitrous oxide have also been studied for their self-pressurizing capabilities. Perhaps one of the earliest works is that of Campbell in 1965 [11]. Campbell studied the flow of self-pressurized liquid oxygen from a spherical tank and out through a lengthy discharge line. His experimental work was of an impressive scale: a 1.727 m internal diameter, 2,582 L spherical tank was mounted on the top of a 12.2 m tower to allow for a long discharge line, simulating practical launch vehicle conditions. Numerous pressure, temperature, flow rate, and fluid quality sensors were included and nitrogen was used to simulate oxygen while reducing costs and risks. Campbell's modeling work was focused on two-phase flow in discharge line and he presented only limited data on the conditions within the tank itself. Some of his results are shown in figure 1.9, including the tank pressure history.

A series of studies have been produced on liquid rocket engines using self-pressurizing

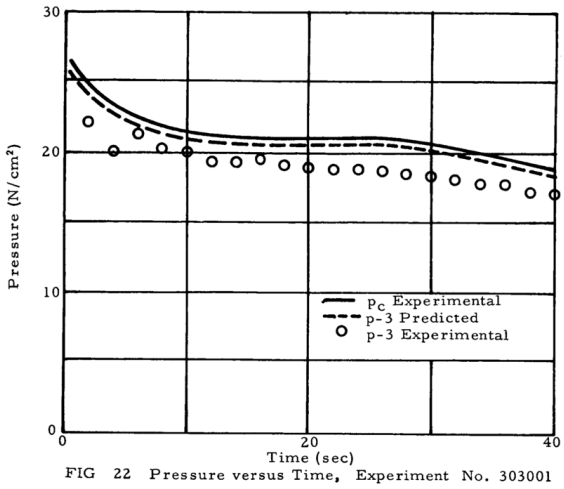

Figure 1.9: Results of Campbell [11] from a blowdown test of a N_2 tank. p_C is the tank pressure, while $p-3$ is the pressure at a point in the discharge line.

propellants for both fuel and oxidizer. Most numerous are a series of works from Ewig et al [12, 13, 14, 15, 16] that proposed liquid oxygen as an oxidizer and propane or methane as fuels. The main drawback to these propellants is that their vapor pressures are relatively low, meaning that the chamber pressure is generally limited to about 2.5 MPa which is considerably lower than typical values for liquid rocket engines. This was overcome by designing an air-launched vehicle; at higher altitudes the low atmospheric pressure reduces the performance penalty for low chamber pressures. Ewig et al developed models, performed several cold flow experiments, and also numerous engine hot fire tests. Their model is essentially a phase equilibrium model similar to those described earlier.

Another possible configuration was studied by Dunn [17]. Here, propane was used as a self-pressurized propellant but the fuel vapor was also used to pressurize the oxidizer. This was done by containing the oxidizer within a bladder inside the fuel tank to prevent the two propellants from contacting each other. Dunn performed an experiment using water as a simulant for hydrogen peroxide and keeping it in a separate tank but connecting the ullage volumes of the two tanks with tubing to allow fuel vapor to flow. He drained the tanks in 780 s and obtained accurate predictions with a phase equilibrium model.

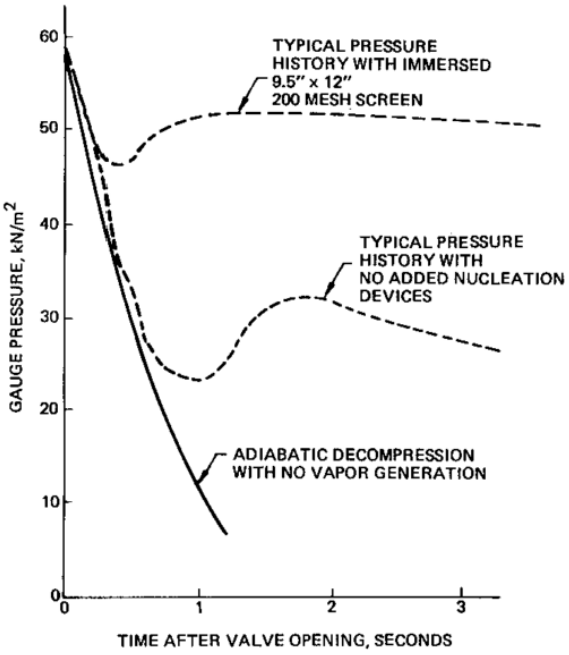

Figure 1.10: Results of Bentz and Wilkinson [19] showing the pressure time history from the blowdown of nitrogen vessel. Reprinted with permission.

In 2006 Herdy [18] presented the development and testing of a small liquid rocket engine using nitrous oxide and propane as self-pressurizing propellants. No detail was given for the evolution of the tank pressure with time or any modeling performed.

In 1983, Bentz and Wilkinson [19] performed experiments rapidly venting the ullage of a 172 L spherical tank of liquid nitrogen with the goal of understanding the behavior of cryogenic propellant tanks that are rapidly drained. Their results were very similar to those shown earlier for self-pressurized nitrous oxide tanks, including the transient drop and recovery in the pressure time history. An interesting test performed by Bentz and Wilkinson involved suspending a rolled wire mesh screen within the liquid to provide additional nucleation sites. This had an appreciable effect on the pressure time history, as shown in figure 1.10. No modeling was attempted.

Akyuzlu et al [20] and Coote [21] developed 1-D models for the blowdown of self-pressurized tanks of liquid oxygen that allowed for varying temperature across the

length of the tank (termed stratification). This is the only existing model for self-pressurized tanks that can capture effects of temperature stratification within the vessel, as all others are 0-D and assume a uniform temperature field. Evaporation and condensation were assumed to occur in the amount needed to prevent the liquid from becoming superheated or the ullage from becoming subcooled. In Coote's work a detailed study of the effect of parameter variations was performed. Unfortunately in both works there were no comparisons made to experimental data.

A large body of work studying a system similar to self-pressurized propellant tanks exists in the area of nuclear engineering, specifically in the field of pressurized water reactors. In these systems water is used as a reactor coolant and becomes heated above its normal boiling point. To prevent it from boiling and possibly losing cooling capacity, the water is pressurized. A failure scenario for these reactors is a loss of coolant accident whereby a component fails and rapidly depressurizes the water. The water then suddenly becomes superheated as the pressure drops below its saturation point and boiling occurs, increasing the system pressure back towards saturation. This produces pressure drops and recoveries very similar to those seen in nitrous oxide systems.

Numerous researchers have studied this system, performing experiments on sub-scale vessels and developing analytical and empirical models. The work most applicable to self-pressurized propellant tanks is that of Hutcherson et al [22, 23, 24]. These researchers performed experiments with a 153 L vessel filled with heated, pressurized water and drained when a rupture disk on the end of a pipe was burst. They also developed a 0-D model that directly incorporated bubble nucleation and growth dynamics. This model transitioned to a phase equilibrium model when a certain void fraction was reached. While this model showed good agreement with their experimental data, a severe disadvantage is that in the transition from the bubble growth to the equilibrium regimes, only the pressure could be matched and as a result a step change in temperature or internal energy was required.

Another related topic is that of boiling liquid expanding vapor explosions (BLEVEs). These occur when a liquid is stored at a temperature above its normal boiling point and for some reason the container fails catastrophically. As the liquid is suddenly

depressurized and hence is superheated, a significant portion of it vaporizes nearly instantaneously, rapidly increasing in volume and generating a blast wave. If the liquid is flammable, a fireball can also be generated. Many researchers have studied these systems and have developed models for the vapor generation rate (eg Pinhasi et al [25, 26]) however much of the results cannot directly be applied to self-pressurizing propellant tank dynamics due to the large levels of superheat and short time scales involved. Specifically, this causes the details of the boiling process to change, approaching homogeneous bubble nucleation.

Fire extinguishers are another system that are quite similar to self-pressurized propellants. Systems using halon or halon alternatives are often pressurized with nitrogen such that the nitrogen dissolves into the liquid. Then, when the tank is rapidly drained in a fire scenario, the nitrogen begins to bubble out of the solution and causes a pressure increase similar to the drop and recovery seen in nitrous oxide tanks. In 1984 Elliott et al [27] performed experiments with tanks of halon pressurized with nitrogen and developed a model for the tank and diffuser system dynamics. Later, Yang used a sight glass to visualize the internal flow of several halon alternatives as they were depressurized [28].

As a final example, some workers in the petroleum industry have developed models for the blowdown of large pressure vessels containing mixtures of hydrocarbons and possibly other fluids, which are common at refineries [29, 30, 31]. There are two concerns in these cases related to the low temperatures achieved within the vessel. First, one component of the mixture may freeze and could block the tank exit. Second, the fluid within the tank may become so cold that the tank wall temperature is brought below the ductile-brittle transition temperature and the vessel's structural integrity is reduced. These models are generally concerned with low flow rates out of the tank, and do not show any pressure recovery like that seen in N_2O tanks.

In this section, a variety of previous works have been presented both from the hybrid rocket propulsion literature and other fields. None of these works have resulted in a detailed model or even physical understanding of the processes that occur within a self-pressurized N_2O tank.

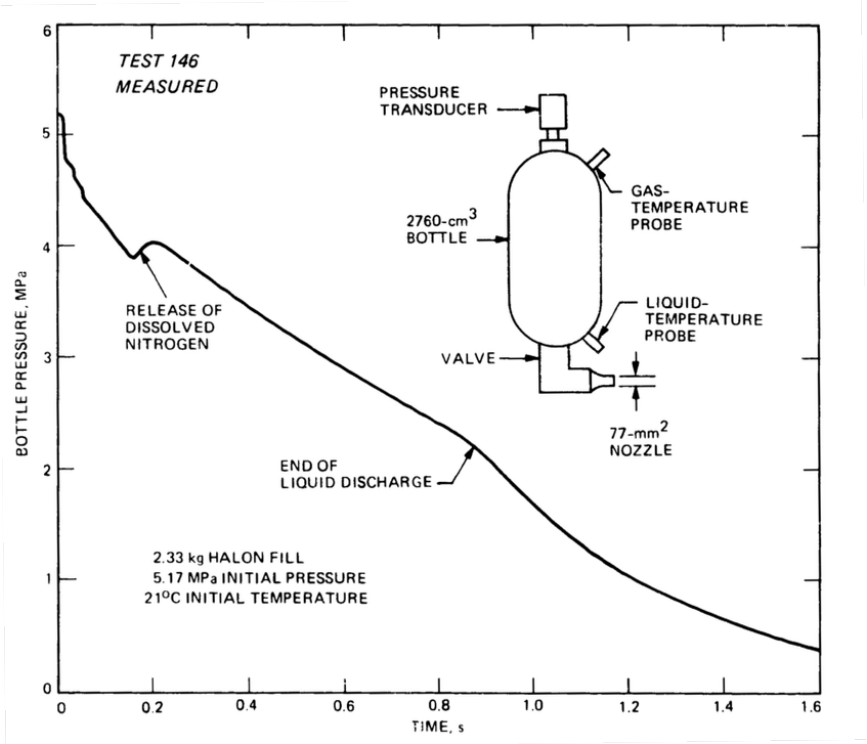

Figure 1.11: Results of Elliott et al [27] showing the blowdown of a vessel containing a mixture of nitrogen and halon.

Chapter 2

Evaluation of Existing Models

Several groups have developed models for nitrous oxide tank dynamics. This includes Whitmore & Chandler [10], Zilliac & Karabeyoglu [7], and Casalino & Pastrone [32]. However, while these models have been used by these researchers to reproduce their own experimental results they use conflicting assumptions and it is unclear which model (if any) is valid for a given system. This uncertainty stems from the fundamental lack of knowledge about what is going on inside a draining self-pressurized propellant tank.

In this chapter, the three existing models for self-pressurized N_2O tanks will be evaluated: a phase equilibrium model (hereafter referred to simply as the equilibrium model), the non-equilibrium model of Zilliac & Karabeyoglu, and the non-equilibrium model of Casalino & Pastrone. The goal is to examine the performance of each of these models by comparing them to eachother and to several sets of experimental data.

2.1 Common Model Features

These three models share many similar features. These will be discussed first, followed by a derivation of each model and a description of its main features. The common features between the models include some basic physical assumptions and mathematical forms, characterization of the flow out of the tank, heat transfer calculations, and

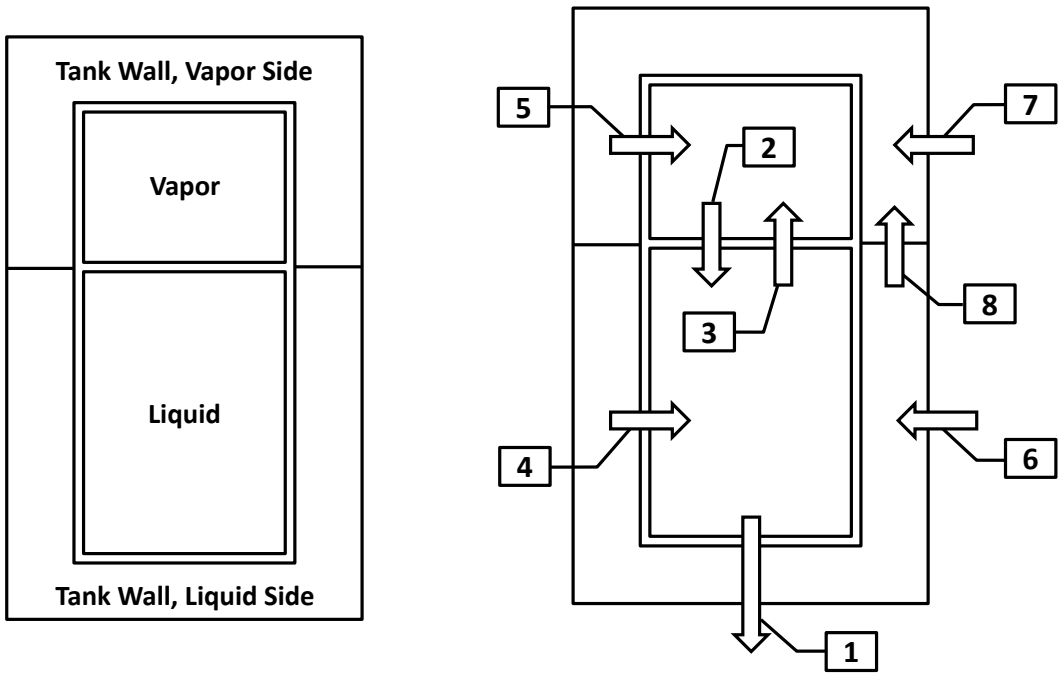

(a) Nodes (b) Heat and Mass Transfer

Figure 2.1: Diagrams showing the nodes and the heat and mass transfer processes between them.

numerical methods.

2.1.1 Fundamental Theory

The models all begin by dividing the tank into a small number of regions and representing each as a single node with averaged properties. Figure 2.1 shows the four nodes used by the models discussed in this paper: the liquid nitrous oxide, the vapor nitrous oxide, the portion of the tank wall in contact with the liquid, and the portion of the tank wall in contact with the vapor.

The heat and mass transfer processes between the nodes are numbered in figure 2.1 and described here:

1. Mass flow of liquid nitrous oxide out of the tank

2. Heat and mass transfer from the vapor to the liquid via condensation, diffusion, and convection

3. Heat and mass transfer from the liquid to the vapor via boiling, evaporation, diffusion, and convection

4. Heat transfer from the liquid side of the tank wall to the liquid

5. Heat transfer from the vapor side of the tank wall to the vapor

6. Heat transfer from the atmosphere to the liquid side of the tank wall

7. Heat transfer from the atmosphere to the vapor side of the tank wall

8. Heat and mass transfer from the liquid side of the tank wall to the vapor side via conduction and motion of the boundary

The dynamics of the wall nodes will be discussed later in section 2.1.3 and we begin here with the liquid and vapor nodes. The development presented in this section is general and is not limited to a system of two fluid nodes. To determine the number of equations needed to describe the dynamics of the liquid and vapor nodes we begin with Gibbs' Phase Rule:

$$\#\text{ degrees of freedom} = \#\text{ components} - \#\text{ phases} + 2 \tag{2.1}$$

This gives the number of intensive variables needed to fix the thermodynamic state of a node. An additional extensive variable is needed to fix the size of each node, expressed in any form such as mass, volume, entropy, etc. There are two additional constraints on the system. The first is from assuming that the pressure is uniform within the tank, yielding the intensive constraint

$$P_{node\ i} = P_{node\ j} \tag{2.2}$$

Which is actually $n - 1$ constraints, where n is the number of nodes. The second constraint is extensive in nature and arises from the fixed volume of a propellant

tank:

$$\sum_i V_{node\ i} = V_{tank} \tag{2.3}$$

Combining equations (2.1) through (2.3) we can write

$$\begin{aligned} \#\text{ equations} &= \#\text{ intensive variables} + \#\text{ extensive variables} \\ &\quad - P\text{ constraints} - V\text{ constraint} \\ &= (2n_{nonsat} + n_{sat}) + n_{tot} - (n_{tot} - 1) - 1 \\ &= n_{tot} + n_{nonsat} \end{aligned} \tag{2.4}$$

Where n_{tot} is the total number of nodes, n_{nonsat} is the number of nodes that are not maintained at a saturation state and n_{sat} is the number of nodes that are saturated. Note that here saturated nodes are assumed to be either saturated liquid or saturated vapor and not a mixture. If a mixture is assumed, then an additional variable is needed to fix the vapor mass fraction of the node and when determining the total number of equations needed, such a node can be treated as non-saturated. All the models discussed in this chapter that have saturated nodes assume pure liquid or vapor. Equation (2.4) dictates that at most two equations will be needed for each node in the system. The two equations of choice are conservation of mass and energy:

$$\frac{dm}{dt} = \sum(\dot{m})_{in} - \sum(\dot{m})_{out} \tag{2.5}$$

$$\frac{dU}{dt} = \sum\left[\dot{m}\left(h + \frac{v^2}{2} + gz\right)\right]_{in} - \sum\left[\dot{m}\left(h + \frac{v^2}{2} + gz\right)\right]_{out} + \dot{Q}_{in} + \dot{W}_{in} \tag{2.6}$$

In equation (2.6), the velocity and acceleration terms will be neglected in all the models. The pressure gradients caused by acceleration can be significant in rockets with high thrust to weight ratios, so it is possible that this assumption will create inaccuracies in flight vehicles. Equations (2.5) and (2.6) yield a system of ordinary differential equations that are integrated in time. The key features that differentiate one model from another are twofold: whether or not nodes are assumed to be saturated and the way in which the heat and mass transfer terms are modeled.

2.1.2 Outlet Flow

An important aspect of any tank model is the description of the outlet flow (arrow 1 in figure 2.1), which in a propulsion system is established by the injector configuration and chamber pressure. In nitrous oxide feed systems, especially those that are self-pressurized, the prediction and modeling of injectors is an ongoing research topic and there is no universally accepted method for predicting the flow rate. For this work, the model proposed by Dyer et al [33] will be used:

$$G = \frac{\kappa G_{SPI} + G_{HEM}}{1 + \kappa} \tag{2.7}$$

$$G_{SPI} = C_d \sqrt{2\rho_1 (P_1 - P_2)} \tag{2.8}$$

$$G_{HEM} = C_d \rho_2 \sqrt{2(h_1 - h_2)} \tag{2.9}$$

$$\kappa = \sqrt{\frac{P_1 - P_2}{P_{1,sat} - P_2}} \tag{2.10}$$

Here h_2 is found assuming that the fluid expands through the injector isentropically. Note that equation (2.7) in the original publication and in Whitmore & Chandler [10] had an error that was later identified by Solomon [34]. Solomon's corrected equation is shown above.

The Dyer model is a combination of two classic models: the single phase incompressible (SPI) model and the homogeneous equilibrium model (HEM), each of which describes one of two regimes of the flow through an orifice. In principle, the HEM is accurate when the fluid residence time in the orifice is much longer than the bubble growth time, meaning there is sufficient time for interphase heat and mass transfer to bring the fluid to equilibrium. Conversely the SPI model is accurate when the residence time is smaller than the bubble growth time, and there is insufficient time for interphase heat and mass transfer. The parameter κ is derived as a ratio of bubble growth time to residence time in the orifice and is an indication of the dominant regime. When κ is large the Dyer model approaches the SPI model, while at low κ it approaches the HEM. For saturated liquid entering the injector, the various components of G are shown in figure 2.2 as a function of the downstream pressure.

Critical flow is a well known phenomenon that occurs in multiphase flows through

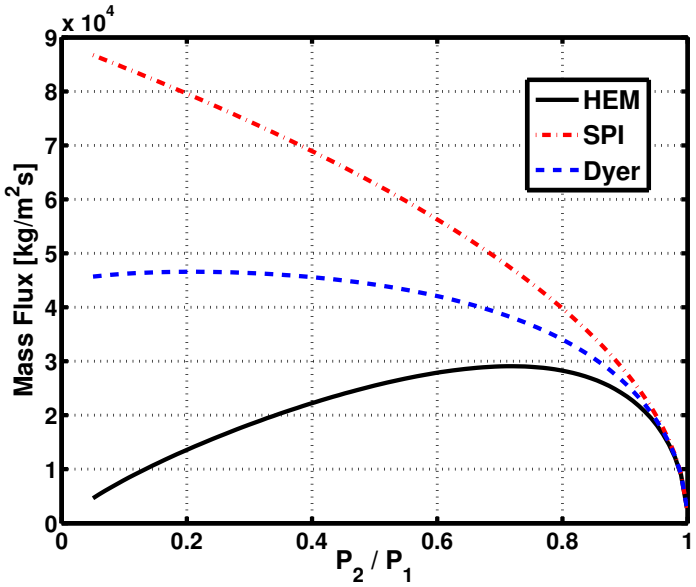

Figure 2.2: Predicted mass fluxes from the HEM, SPI, and Dyer models verses downstream pressure. Upstream, the conditions are saturated liquid at $293K$.

orifices or other restrictions. In this case, if the pressure drop across the orifice is sufficiently large, the flow rate becomes insensitive to the downstream pressure and is only controlled by the upstream conditions. Experimental work with carbon dioxide by Hesson [35, 36] and recently with both carbon dioxide and nitrous oxide by Waxman et al [37] has demonstrated that this often occurs in the conditions found in hybrid rocket motor feed systems. Note that equations (2.8) and (2.9) show a dependence on the downstream conditions and the Dyer flow model in general cannot predict the mass flux in this regime without making additional corrections. However, in the limited case of saturated liquid entering the injector ($P_1 = P_{1,sat}$) this type of behavior is predicted, as evidenced by the flat trajectory of the Dyer flow model in figure 2.2.

For this work, the importance of this phenomenon is that as long as the downstream pressure is appreciably below the saturation pressure, the flow rate is approximately independent of the downstream pressure and P_2 can be taken as 0 without losing accuracy. Therefore, experimental data taken in hot-fire tests and cold-flow tests can be easily used without requiring measurements of P_2. This is dependent on

P_2 being significantly below $P_{1,sat}$, a condition that is violated in motors that operate at high chamber pressures but should be accurate in the data sets used throughout this work.

This result also suggests that when developing a tank model it does not need to be coupled to a combustion chamber ballistics model. Alternatively, if the combustion chamber pressure is being modeled P_2 can of course be inserted.

In the work done by other researchers on modeling nitrous oxide tank dynamics, some (Zilliac & Karabeyoglu, Casalino & Pastrone) have chosen to use the SPI model, while others (Whitmore & Chandler) have used equation (2.7). In the following work only equation (2.7) will be used in order to provide consistency.

2.1.3 Heat Transfer and the Tank Walls

In two of the models used in this work, natural convection heat transfer is calculated. Standard correlations [38] for the Nusselt number as a function of the Rayleigh number will be used for calculating heat fluxes between the ambient air and the tank wall (arrows 6 and 7 in figure 2.1), between the tank wall and the propellant (arrows 4 and 5), and in the case of the Zilliac & Karabeyoglu model fluxes between the liquid free surface and both the liquid and vapor (arrows 2 and 3). The relations used are:

$$\dot{Q} = hA\Delta T \tag{2.11}$$

$$h = Nu\frac{k}{L} \tag{2.12}$$

$$Nu = cRa^n \tag{2.13}$$

$$Ra = \frac{c_P\rho^2 g\beta|\Delta T|L^3}{\mu k} \tag{2.14}$$

Fluid properties are evaluated at the film temperature, defined as the mean of the fluid and surface temperatures. Table 2.1 gives values of the constants c and n used for calculations in the present work.

If heat transfer to and from the tank wall is calculated, the wall temperature must be known. Therefore, in addition to the ordinary differential equations derived from the three models in this paper, a pair of differential equations are needed to describe

Table 2.1: Heat transfer constants, from Bergman et al[38].

Fluid	Surface	c	n
Ambient air	Tank wall	0.59	1/4
Liquid N_2O	Tank wall	0.021	2/5
Vapor N_2O	Tank wall	0.021	2/5
Liquid N_2O	Saturated liquid surface	0.15	1/3
Vapor N_2O	Saturated liquid surface	0.15	1/3

the tank wall temperature, both for the portion in contact with liquid and that in contact with vapor. We draw a control volume for each of the two portions of the tank wall, and applying conservation of energy to each yields

$$\begin{aligned} \frac{dT_{w,liq}}{dt} &= \frac{\dot{Q}_{w,liq,in} - \dot{Q}_{w,liq,out} + \dot{Q}_{w,liq,cond} + \dot{m}_{w,liq,in} c_w (T_{w,liq,in} - T_{w,liq})}{m_{w,liq} c_w} \\ \frac{dT_{w,vap}}{dt} &= \frac{\dot{Q}_{w,vap,in} - \dot{Q}_{w,vap,out} + \dot{Q}_{w,vap,cond} + \dot{m}_{w,vap,in} c_w (T_{w,vap,in} - T_{w,vap})}{m_{w,vap} c_w} \end{aligned} \tag{2.15}$$

where $\dot{m}_{w,in}$ here accounts for the changing liquid level and hence the moving boundary of the control volume. The heat transfer into the wall is natural convection from ambient air, modeling a ground testing situation and not a flight vehicle. The heat transfer out of the wall is natural convection to the fluid within the tank. Conduction between the two portions of the tank wall is modeled after Corpening [39], who approximated Fourier's heat conduction law in the following way:

$$\dot{Q}_{w,cond} = k_w A \frac{dT}{dx} \tag{2.16}$$

$$\frac{dT}{dx} \simeq \frac{(\Delta T)_w}{L_{w,cond}} \tag{2.17}$$

$$A = \pi (r_o^2 - r_i^2) \tag{2.18}$$

where $L_{w,cond}$ is the distance between the center of the liquid volume and the center of the vapor volume. $(\Delta T)_w$ is the difference in temperature of the liquid and vapor

sections of the wall. The result is

$$\dot{Q}_{w,cond} = \frac{k_w(\Delta T)_w \pi (r_o^2 - r_i^2)}{L_{w,cond}} \tag{2.19}$$

2.1.4 Fluid Properties

A difficulty in working with nitrous oxide is the calculation of thermodynamic and transport properties. Nitrous oxide's critical point (309.52 K) is near standard conditions and therefore in most systems the physical properties are sensitive to small changes in temperature or pressure. A technical equation of state has been developed for nitrous oxide by Span, Wagner, and Lemmon [40, 41, 42] and can be used to calculate any thermodynamic property at saturated and non-saturated states. Unfortunately no such single source exists for transport properties (for example viscosity or thermal conductivity) and instead a collection of theoretical forms fit to experimental results must be used, differing in structure for each property. The National Institute of Standards and Technology (NIST) has compiled a computer program, REFPROP, that contains numerous equations of state and expressions for transport properties [2] that can be used with an extensive range of fluids. For nitrous oxide thermodynamic properties it utilizes the technical equation of state mentioned above and for transport properties it uses a collection of sources. REFPROP will be used to calculate all thermodynamic and transport properties used in this work.

A limitation of this type of technical equation of state is that it is developed by fitting theoretical functional forms to numerous sets of experimental data. While they typically are highly accurate and can often calculate P, ρ, T properties with less than 0.5% error, their accuracy is unknown outside the range of experimental data used during development of the equation of state. This is problematic for modeling nitrous oxide feed systems because metastable states are often assumed to occur, requiring calculation of the properties of the fluid in these states. There is very limited data available for fluid properties in this region and hence the equation of state's accuracy is unknown. This problem was detailed in a work by Shamsundar and Lienhard [43], in which they compared the predictions of various equations of state in the metastable regions to demonstrate how they can give wildly different results, even when their

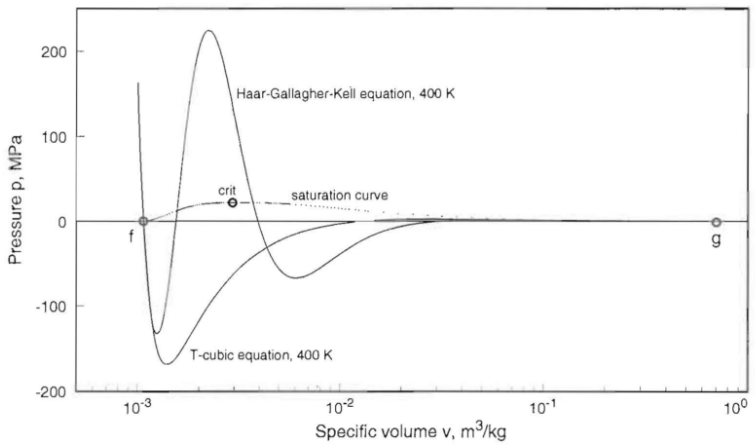

Figure 2.3: Pv diagram showing isotherms through the metastable and unstable regions from Shamsundar and Lienhard [43]. Plot compares the results of a cubic equation of state with the complex Haar-Gallagher-Kell equation of state at a temperature of 400 K for water. Reprinted with permission.

results are similar for stable states. An example of their results is shown in figure 2.3.

An alternative to technical equations of state is to use a simpler equation of state, such as Peng-Robinson [44]. These may have reduced accuracy in general when compared to technical equations of state but are much simpler to implement and may be more accurate in the metastable region [43]. When properties are only required at saturation conditions, curve fits to experimental or EOS results can be used and have been developed by multiple groups [7, 45, 46]. These are typically simple functions of temperature and are the simplest to implement and use.

As a demonstration of both the sensitivity of these properties to temperature and the variability in different methods of calculating them, figure 2.4 shows the specific heat capacity for saturated liquid as a function of temperature. Note that different sources report values that differ by more than 100%. Also noteworthy is the large difference between the isobaric and isochoric specific heat capacity of the liquid, a result of its high compressibility.

All the models here are systems of ordinary differential equations and are integrated using a 4th order adaptive Runge-Kutta-Fehlberg routine [47]. This scheme was chosen over traditional 4th order Runge-Kutta methods because of its ability

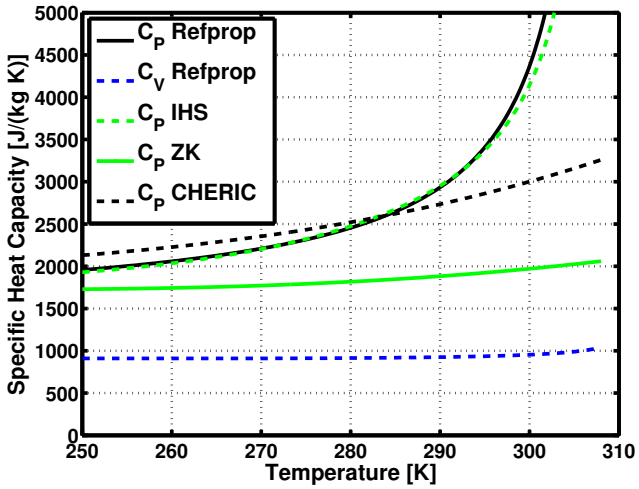

Figure 2.4: Specific heat capacity of saturated liquid N_2O calculated from various sources. The lines labeled IHS and CHERIC are correlations for the saturation state developed by the two organizations [45, 46], and ZK is the saturation correlation derived by Zilliac & Karabeyoglu [7].

to calculate and control error in the results. Additionally, it poses advantages over pre-made integration routines because of the ability to manually control the step refinement near points of interest.

2.2 Equilibrium Model

Equilibrium models for nitrous oxide tanks have been presented by Zakirov & Li [6], Whitmore & Chandler [10], and Casalino & Pastrone [32]. The model presented here includes heat transfer between the fluid and the walls, which Zakirov & Li included but Whitmore & Chandler and Casalino & Pastrone did not.

The equilibrium model assumes that all propellant in the tank remains in phase equilibrium. Physically this is equivalent to assuming that the flow out of the tank is slow compared to the heat and mass transfer between the liquid and vapor. The model then consists of two saturated nodes, which Gibbs' phase rule (equation (2.4)) says requires two equations. The governing equations chosen for this model are conservation of mass and energy (equations (2.5) and (2.6)) which are applied to the

combined liquid and vapor in the tank as a whole. This allows interphase heat and mass transfer calculations to be avoided. With no mass flow into the tank, only allowing flow out via the tank outlet, and no net work done on or by the propellant, the equations simplify to

$$\frac{dm_{tot}}{dt} = -\dot{m}_{outlet} \tag{2.20}$$

$$\frac{dU_{tot}}{dt} = -\dot{m}_{outlet} h_{outlet} + \dot{Q}_{in} \tag{2.21}$$

Where $\dot{m}_{outlet}$ is calculated from equation (2.7) and for h_{outlet} it is assumed that saturated liquid is exiting the tank. $\dot{Q}_{in}$ is calculated from equations (2.11) through (2.14). While m_{tot} and U_{tot} are convenient variables to solve for with the simple ODE's shown above, they are not useful for determining fluid properties. The entire tank remains saturated and thus a single value of temperature or pressure would be sufficient to describe both the liquid and vapor properties. Temperature is often the more convenient variable, and so to find the fluid temperature at a given time from the variables m_{tot} and U_{tot}, the volume constraint (equation (2.3)) is introduced

$$V_{tank} = m_{tot} \left[\frac{1-x}{\rho_{liq}} + \frac{x}{\rho_{vap}} \right] \tag{2.22}$$

$$x = \frac{\frac{U_{tot}}{m_{tot}} - u_{liq}}{u_{vap} - u_{liq}} \tag{2.23}$$

Where ρ and u are calculated from T using an equation of state or correlation at saturation conditions and (2.23) is given for convenience and is derived from the definition of m_{tot} and U_{tot}. A value of T must be chosen such that $\rho_{liq}(T)$, $\rho_{vap}(T)$, and $x(u_{vap}(T), u_{liq}(T))$ satisfy (2.22). Once the temperature is known, any property of either phase can be directly computed.

We now have a set of four ordinary differential equations to integrate: (2.15) for $T_{w,liq}$ and $T_{w,vap}$, (2.20) for m_{tot}, and (2.21) for U_{tot}. An important feature of equilibrium models is that they require properties only at the saturation state, meaning that complex equations of state are not strictly necessary. This is because as long

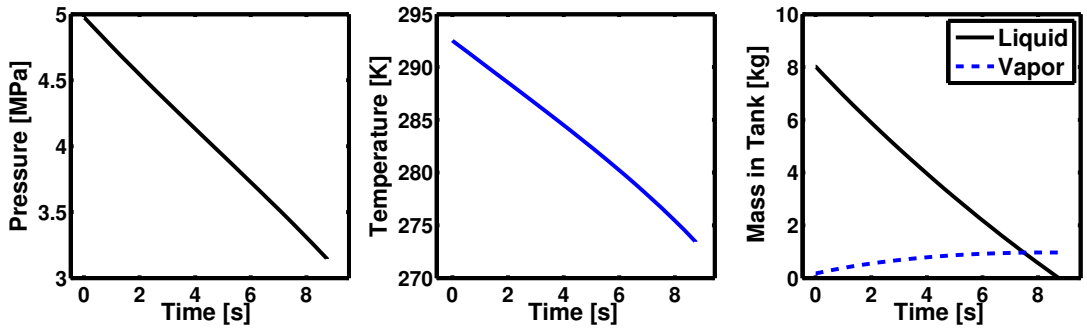

Figure 2.5: Pressure, temperature, and mass time histories from the equilibrium model using the conditions of Van Pelt et al[3]. Details of the conditions will be discussed later in section 2.5.

as the fluid is saturated, there is only one degree of freedom and hence curve fits to saturation properties such as P_{sat}, ρ_{liq}, ρ_{vap}, u_{liq}, and u_{vap} can be used. These are used in place of more complicated equations of state and simplify and accelerate both the implementation and solution times. However caution must be used when selecting these correlations because when separate relations are used for individual properties, the results may be inconsistent with each other.

Figure 2.5 shows the results when applied to a tank typical of a small sounding rocket, namely the case of Van Pelt et al [3]. The details of this experiment will be discussed in section 2.5. All curves follow approximately linear trajectories, with the exception of vapor mass. Note that when compared to figure 1.5, the initial drop and recovery are not captured with this model. The character of these curves does not change when this model is applied with a wide variety of initial conditions.

2.3 Zilliac & Karabeyoglu Model

In a paper by Zilliac & Karabeyoglu [7], a model is presented that builds a level of complexity onto the equilibrium model by allowing the liquid and vapor to be at different temperatures and directly calculating the heat and mass transfer between the phases. In a later work, Fernandez [48] evaluated this model in detail and also applied it to nitrous oxide tanks in which helium pressurant was added. This type of

model is based on the work of Morey & Traxler [8], initially developed for traditional liquid propellant pressurization systems. Some alterations from the work by Zilliac & Karabeyoglu have been made but the basic assumptions and core structure of the model is retained.

Mathematically, the model contains two non-saturated nodes, which equation (2.4) dictates requires four equations. Therefore we apply conservation of mass and energy separately to each phase:

$$\frac{dm_{vap}}{dt} = \dot{m}_{evap} - \dot{m}_{cond} \tag{2.24}$$

$$\frac{dm_{liq}}{dt} = -\dot{m}_{evap} + \dot{m}_{cond} - \dot{m}_{outlet} \tag{2.25}$$

$$\frac{dU_{vap}}{dt} = \dot{m}_{evap}h_{evap} - \dot{m}_{cond}h_{cond} - P\frac{dV_{vap}}{dt} + \dot{Q}_{in,vap} \tag{2.26}$$

$$\frac{dU_{liq}}{dt} = -\dot{m}_{outlet}h_{outlet} - \dot{m}_{evap}h_{evap} + \dot{m}_{cond}h_{cond} - P\frac{dV_{liq}}{dt} + \dot{Q}_{in,liq} \tag{2.27}$$

The outlet flow is assumed to be from the liquid node and $\dot{m}_{outlet}$ is computed via equation (2.7). The heat transfer terms are now a combination of interphase processes and convection to the tank walls.

To compute the heat and mass transfer between the phases, we assume the presence of an infinitesimal layer of saturated liquid between the bulk liquid and the vapor, defined by the pressure in the tank ullage. Natural convection transports heat from the bulk liquid to this surface and also from this surface into the vapor. If the heat transfer from the bulk liquid to the surface exceeds that from the surface to the vapor, the excess is used to vaporize liquid and yields mass transfer from the liquid to the vapor. Therefore:

$$\dot{m}_{evap} = \frac{\dot{Q}_{liq\rightarrow surf} - \dot{Q}_{surf\rightarrow vap}}{\Delta h_{LV} + (h_{sat,liq} - h_{liq})} \tag{2.28}$$

$\dot{Q}_{liq\rightarrow surf}$ and $\dot{Q}_{surf\rightarrow vap}$ are computed via (2.11) through (2.14), however Zilliac & Karabeyoglu multiplied $\dot{Q}_{liq\rightarrow surf}$ by an empirical factor E_{ZK} with a value on the order of 10^3 in order to match experimental results. Therefore $\dot{Q}_{liq\rightarrow surf} = E_{ZK}hA\Delta T$, in contrast to equation (2.11). Physically, they assumed that this corrected for a heat

transfer coefficient that was too low because it didn't include the effects of boiling, liquid layer motion, and blowing. Condensation is handled differently and occurs only when the pressure increases above the saturation pressure of the vapor. Then we assume that mass transfer from the vapor to the liquid occurs in the amount needed to bring the pressure to the saturation pressure in one time step:

$$\dot{m}_{cond} = \begin{cases} \dfrac{(P - P_{sat,vap})V_{vap}}{Z_{vap}R_{vap}T_{vap}\Delta t}, & \text{if } P > P_{sat,vap} \\ 0, & \text{if } P \leq P_{sat,vap} \end{cases} \tag{2.29}$$

The heat released from the condensation of this vapor is added into the vapor volume and is accounted for in the $\dot{Q}_{in,vap}$ term. Both the $\dot{Q}_{in,vap}$ and $\dot{Q}_{in,liq}$ terms also include heat transfer to/from the tank walls, which is computed via equations (2.11) through (2.14).

The work term ($P\frac{dV}{dt}$) presents a major problem because $\frac{dV}{dt}$ is not explicitly known. Zilliac & Karabeyoglu solved this problem by computing numerically via backwards differences, but this can introduce numerical instability in some situations and therefore a different procedure is desirable. One alternative developed by this author is to use the pressure and volume constraints (equations (2.2) and (2.3)) to derive an equation for $\frac{dV}{dt}$:

$$P_{vap} = P_{liq} \tag{2.30}$$

$$\frac{dP_{vap}}{dt} = \frac{dP_{liq}}{dt} \tag{2.31}$$

$$\left[\left(\frac{\partial P}{\partial T}\right)_\rho \frac{dT}{dt} + \left(\frac{\partial P}{\partial \rho}\right)_T \frac{d\rho}{dt}\right]_{vap} = \left[\left(\frac{\partial P}{\partial T}\right)_\rho \frac{dT}{dt} + \left(\frac{\partial P}{\partial \rho}\right)_T \frac{d\rho}{dt}\right]_{liq} \tag{2.32}$$

The thermodynamic partial derivatives $\frac{\partial P}{\partial T}$ and $\frac{\partial P}{\partial \rho}$ can be calculated from an

equation of state. The time derivative of temperature can be calculated from:

$$\frac{dU}{dt} = u\frac{dm}{dt} + m\frac{du}{dt} \tag{2.33}$$

$$= u\frac{dm}{dt} + m\left[\left(\frac{\partial u}{\partial T}\right)_{\rho}\frac{dT}{dt} + \left(\frac{\partial u}{\partial \rho}\right)_{T}\frac{d\rho}{dt}\right] \tag{2.34}$$

$$\frac{dT}{dt} = \frac{1}{c_V}\left[\frac{1}{m}\left(\frac{dU}{dt} - u\frac{dm}{dt}\right) - \left(\frac{\partial u}{\partial \rho}\right)_{T}\frac{d\rho}{dt}\right] \tag{2.35}$$

And finally $\frac{d\rho}{dt}$ is found from

$$\frac{d\rho}{dt} = \frac{1}{V}\frac{dm}{dt} - \frac{m}{V^2}\frac{dV}{dt} \tag{2.36}$$

$$\frac{dV_{liq}}{dt} = -\frac{dV_{vap}}{dt} \tag{2.37}$$

A value of $\frac{dV}{dt}$ must be chosen that solves (2.32), entering the equation via $\frac{d\rho}{dt}$. In order to compute various properties of the two phases, the thermodynamic state of each must be specified. Given that (2.35) must be computed to find $\frac{dV}{dt}$, it is convenient to integrate (2.35) for T_{vap} and T_{liq} rather than integrating (2.26) and (2.27) for U_{vap} and U_{liq}. The internal pressure of the tank is readily chosen as the second thermodynamic state variable and can be found by using another version of the tank volume constraint,

$$V_{tank} = \frac{m_{liq}}{\rho_{liq}} + \frac{m_{vap}}{\rho_{vap}} \tag{2.38}$$

where $\rho_{liq} = \rho(T_{liq}, P)$ and $\rho_{vap} = \rho(T_{vap}, P)$.

The Zilliac & Karabeyoglu model is then a set of six ordinary differential equations that must be integrated: (2.15) for $T_{w,vap}$, and (2.15) for $T_{w,liq}$, (2.24) for m_{vap}, (2.25) for m_{liq}, (2.35) for T_{liq}, and (2.35) for T_{vap}.

This model directly calculates the rates of heat and mass transfer between the phases and as a result at any given point in time one or both of the phases may be in a metastable state. Therefore, care is needed in calculating thermodynamic and transport properties.

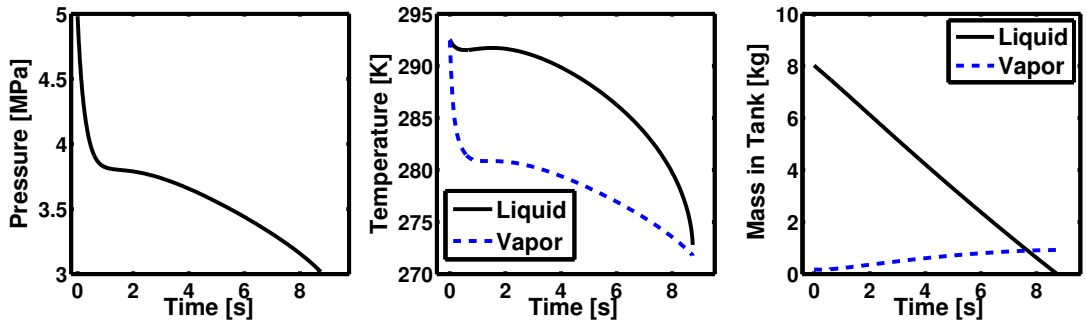

Figure 2.6: Pressure, temperature, and mass time histories from the ZK model using the conditions of Van Pelt et al [3]. Details of the conditions will be discussed later in section 2.5.

Figure 2.6 shows typical results from this model. Note that it does a much better job than the equilibrium model of capturing the non-linear nature of the pressure time history. Unlike the equilibrium model, these results do change character as experimental conditions are varied. To demonstrate one aspect of how the results change, figure 2.7 shows the variation seen in the pressure time history as E_{ZK} is varied. As E_{ZK} grows, it increases the amount of heat and mass transfer that occur for a given temperature difference. Therefore E_{ZK} can be viewed as a measure of how close the system is to an equilibrium solution. As will be shown later, E_{ZK} is system-dependent and is found by fitting the results of the model to experimental data.

2.4 Casalino & Pastrone Model

In a paper by Casalino & Pastrone [32], two different models for self-pressurizing propellant tank dynamics are presented. The first is an equilibrium model, and the second is what they termed a "two-phase lumped model" which will be described here. This model uses two non-saturated nodes similar to the Zilliac & Karabeyoglu model, nominally requiring four equations. However in this model a series of simplifying assumptions are made that allow for all properties to be found at the saturation state, removing the necessity for complex equations of state. The only modification

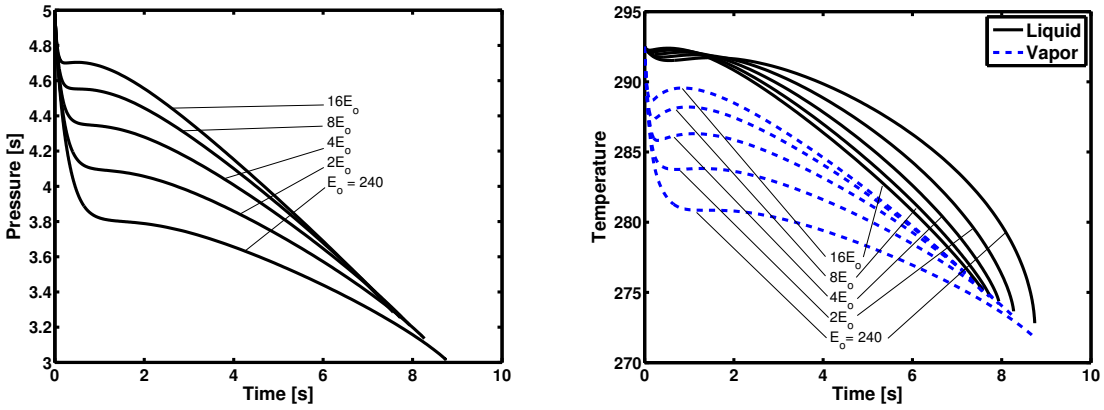

(a) Pressure (b) Temperature

Figure 2.7: Pressure and temperature time histories as E_{ZK} is varied. The Van Pelt et al [3] case is taken as a baseline and E_{ZK} is increased by a factor of 16.

made to the original model is the use of the Dyer flow model (equation (2.7)) in place of the SPI model (equation (2.8)). We begin by applying conservation of mass and energy to both the liquid and vapor nodes:

$$\frac{dm_{vap}}{dt} = \dot{m}_{evap} - \dot{m}_{cond} \tag{2.39}$$

$$\frac{dm_{liq}}{dt} = -\dot{m}_{evap} + \dot{m}_{cond} - \dot{m}_{outlet} \tag{2.40}$$

$$\frac{dU_{vap}}{dt} = \dot{m}_{evap}h_{evap} - \dot{m}_{cond}h_{cond} - P\frac{dV_{vap}}{dt} \tag{2.41}$$

$$\frac{dU_{liq}}{dt} = -\dot{m}_{outlet}h_{outlet} - \dot{m}_{evap}h_{evap} + \dot{m}_{cond}h_{cond} \tag{2.42}$$

where we've already assumed that the liquid is incompressible and there is no heat transfer between the phases or to the tank walls. By assuming that the vapor remains saturated, meaning all properties are functions only of temperature, equation (2.41) can be written as

$$m_{vap}\frac{du_{vap}}{dT_{vap}}\frac{dT_{vap}}{dt} - \dot{m}_{cond}\left[\Delta h_{LV}(T_{vap}) - \frac{P}{\rho_{vap}}\right] - \dot{m}_{evap}\left[h_{vap}(T_{liq}) - u_{vap}\right] = -P\frac{dV_{vap}}{dt} \tag{2.43}$$

Additionally we've assumed that condensing vapor leaves the ullage as saturated

liquid at T_{vap} and evaporating liquid enters the ullage as saturated vapor at T_{liq}. For the liquid, if we make the idealizing assumptions that $u = h = h(T)$, equation (2.42) can be written as

$$c_{liq} m_{liq} \frac{dT_{liq}}{dt} = \dot{m}_{cond} \left[h_{liq}(T_{vap}) - h_{liq}(T_{liq}) \right] - \dot{m}_{evap} \Delta h_{LV}(T_{liq}) \tag{2.44}$$

By assuming the liquid to be incompressible, the pressure constraint is no longer applicable because liquid properties are not functions of pressure. Therefore an expression different from equation (2.32) is needed. We can use the volume constraint to derive:

$$\frac{dV_{vap}}{dt} = -\frac{dV_{liq}}{dt} \tag{2.45}$$

$$= -\frac{1}{\rho_{liq}} \frac{dm_{liq}}{dt} + \frac{m_{liq}}{\rho_{liq}^2} \frac{d\rho_{liq}}{dT_{liq}} \frac{dT_{liq}}{dt} \tag{2.46}$$

Note that in Casalino & Pastrone's paper where this model was presented [32], there was a sign error in equation (2.46). The corrected version is shown above. In order to calculate the mass transfer from condensation and evaporation, we make some assumptions about both these processes. First, we assume that boiling does not begin until the pressure reaches a critical value, P_{lim}, which is a function of the liquid temperature and is midway between the saturation pressure and the spinodal. Before the pressure drops to this value, condensation occurs in the vapor in the amount necessary to maintain it at the saturation state. After P reaches P_{lim}, condensation ceases and then evaporation and/or boiling occurs in the amount needed to keep the pressure at P_{lim}. This is summarized as:

$$\frac{dP}{dt} = \begin{cases} \dfrac{dP_{sat}}{dT} \dfrac{dT_{vap}}{dt}, & \text{if } P > P_{lim} \\ \\ \dfrac{dP_{lim}}{dT} \dfrac{dT_{liq}}{dt}, & \text{if } P = P_{lim} \end{cases} \tag{2.47}$$

Where

$$P_{lim}(T_{liq}) = \frac{1}{2}\left[P_{sat}(T_{liq}) + P_{spin}(T_{liq})\right] \tag{2.48}$$

$$P_{spin}(T_{liq}) = (1.98\ bar/K)T_{liq} - (540\ bar) \tag{2.49}$$

Where equation (2.49) is a curve fit developed by Casalino & Pastrone. This does not directly yield an expression for $\dot{m}_{cond}$ or $\dot{m}_{evap}$, therefore we turn to the real gas equation of state in order to relate $\frac{dP}{dt}$ to $\dot{m}$. Differentiating $PV = ZmRT$ with respect to time and rearranging gives

$$\frac{dm_{vap}}{dt} = m_{vap}\left(-\frac{1}{Z_{vap}}\frac{dZ_{vap}}{dt} - \frac{1}{T_{vap}}\frac{dT_{vap}}{dt} + \frac{1}{P}\frac{dP}{dt} + \frac{1}{V_{vap}}\frac{dV_{vap}}{dt}\right) \tag{2.50}$$

Which can be simplified by assuming that the vapor remains saturated

$$\frac{dZ_{vap}}{dt} = \frac{dZ_{vap}}{dT}\frac{dT_{vap}}{dt} \tag{2.51}$$

This value of $\frac{dm_{vap}}{dt}$ is used in equations (2.43) and (2.44) by making the substitutions:

$$\dot{m}_{cond} = \begin{cases} -\dfrac{dm_{vap}}{dt}, & \text{if } P > P_{lim} \\ 0, & \text{if } P = P_{lim} \end{cases} \tag{2.52}$$

$$\dot{m}_{evap} = \begin{cases} 0, & \text{if } P > P_{lim} \\ \dfrac{dm_{vap}}{dt}, & \text{if } P = P_{lim} \end{cases} \tag{2.53}$$

We now have a system of four ODE's to integrate: (2.40) for m_{liq}, (2.43) for T_{vap}, (2.44) for T_{liq}, and (2.50) for m_{vap}. Unfortunately, unlike the previous models the ODE's are a system of algeabraic equations that must be solved simultaneously in order to calculate the derivatives. This adds some additional complexity to the implementation.

Sample results from this model are shown in figure 2.8. The pressure initially shows a steep drop followed by a linear decrease. This sudden change occurs when

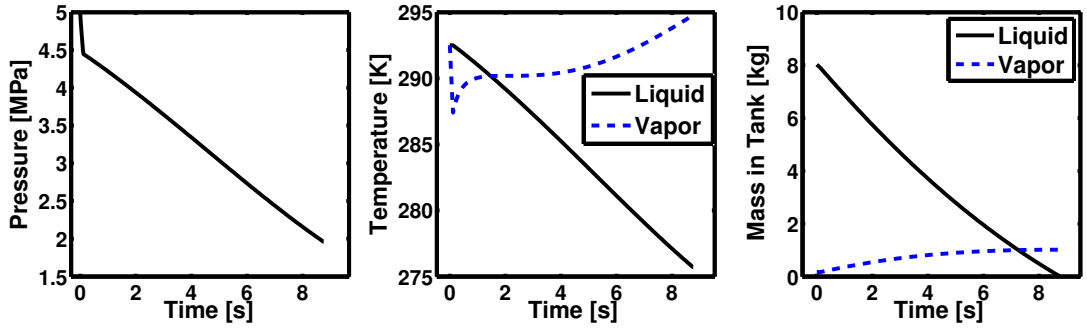

Figure 2.8: Pressure, temperature, and mass time histories from the CP model using the conditions of Van Pelt et al[3]. Details of the conditions will be discussed later in section 2.5.

condensation ceases and boiling begins. An interesting feature is seen in the temperature history: after boiling begins, the vapor temperature increases with time, eventually exceeding its initial value. This happens because the transfer of energy into the vapor is fixed by boiling, which is in turn fixed by $P_{lim} = P_{lim}(T_{liq})$. Energy flows into the vapor during this time at a rate that is only dependent on the liquid temperature, and without regard for the vapor temperature. The basic character of these plots does not vary significantly with initial conditions.

2.5 Model Evaluation

When these models were presented by their developers, they were each compared against a different set of experimental data. It is useful to evaluate each of them against a common array of experimental data to evaluate their performance and allow for direct comparisons. Here pressure and temperature traces taken from six experiments will be given, along with the predicted traces from the three models. Additionally, one set of data includes many tests with the same system over a range of mass flow rates. This set will be used to compare how the models' predictions change as this parameter is varied.

Table 2.2: Tank dimensions from each data set.

Data set	Volume $[m^3]$	Length $[m]$	Tank ID $[cm]$	Wall Thickness $[mm]$	Wall Material
Zilliac & Karabeyoglu	0.0354	1.652	19.05	3.18	Aluminum
Van Pelt et al	0.01128	1.582	9.525	3.18	Aluminum
Prince et al	$9.29 \cdot 10^{-3}$	0.813	12.07	3.18	Aluminum
Zimmerman	$1.80 \cdot 10^{-4}$	0.356	2.54	6.35	Polycarbonate

2.5.1 Overview and Procedure

The sets of experimental data that are used in this paper are summarized here:

1. One of the blow-down cold flow tests from Zilliac & Karabeyoglu [7], originally used to validate their model.

2. A hybrid motor firing performed by Van Pelt et al [3], from a class project at Stanford University in 2004 that was also used as validation data for Casalino & Pastrone's model.

3. Data from ground and flight tests performed by Prince et al [49], from a class project at Stanford University in 2013.

4. Two blow-down cold flow tests in a small scale visualization setup developed by this author and discussed in detail later in chapter 3 where it is referred to as the polycarbonate tube system.

The basic features of these data sets are summarized in tables 2.2 and 2.3. The subscript i refers to the initial value and LRO to the value at the liquid run out point, where the outlet flow transitions to vapor. These four data sets represent a range of experimental conditions, and include flight data in order to see any effects of enhanced acceleration or forced convection on the tank dynamics. For convenience the models will be abbreviated as EQ, ZK, and CP, referring to equilibrium, Zilliac & Karabeyoglu, and Casalino & Pastrone, respectively.

The initial conditions for the models are set by the values in these tables. It is assumed that the nitrous oxide liquid and vapor begin at saturation defined by the

Table 2.3: Experimental conditions from each data set.

Data set	Fill Level [%]	P_i $[MPa]$	T_i $[K]$	m_i $[kg]$	t_{LRO} $[s]$
Zilliac & Karabeyoglu	64	4.502	286.5	20.0	4.91
Van Pelt et al	90	4.999	292.5	8.2	8.74
Prince et al (Ground test)	95	4.777	290.7	7.2	5.56
Prince et al (Flight test)	85	5.452	296.5	6.3	4.85
Zimmerman (low $\dot{m}$)	87	4.091	282.7	0.14	19.88
Zimmerman (high $\dot{m}$)	87	3.763	278.8	0.14	4.86

initial pressure. In most cases this implies a temperature slightly different from the reported initial values, but since pressure measurements are frequently more accurate than temperature measurements, the pressure was chosen as more trustworthy. The initial amount of nitrous oxide in the tank, measured as m_i or fill level, is often a difficult measurement to make. Therefore we can assume that there is significant, although unquantified, uncertainty in these values in table 2.3. The exceptions to this are the data of Zilliac & Karabeyoglu, who used a load cell to measure the mass of propellant in the tank, and the tests performed by this author in the polycarbonate system where video imagery was used to locate the liquid level.

One parameter not chosen from the reported system configuration is the injector C_dA. Due to the uncertainty in modeling the flow of nitrous oxide through injectors and the variability of feed systems, instead an effective injector C_dA will be estimated. This is done by varying C_dA until the averaged mass flow rate (demonstrated by t_{LRO}) of the model matches that of the experiment. Therefore, each model uses a different C_dA for comparing to a given set of experimental data. The results are shown in table 2.4. Obviously this presents a problem for engineers who wish to predict performance without prior knowledge of either C_dA or t_{LRO}, but that task is outside the scope of this thesis.

For the ZK model, both E_{ZK} and C_dA affect t_{LRO} so the process is more complicated. The values of E_{ZK} and C_dA were chosen to minimize the integrated deviation between the modeled pressure history and the experimental pressure history, shown in equation (2.54). The denominator in this relation is included for normalization.

Table 2.4: Model parameters for each data set.

Data Set	C_dA $[mm^3]$			$E_{ZK,opt}$
	EQ	CP	ZK	ZK
Zilliac & Karabeyoglu	86.6	107	93.5	$1.3 \cdot 10^3$
Van Pelt et al	19.7	23.6	22.8	$2.4 \cdot 10^2$
Prince et al (Ground)	28.0	34.8	29.4	$5.3 \cdot 10^2$
Prince et al (Flight)	25.5	28.4	26.4	$1.0 \cdot 10^3$
Zimmerman (low $\dot{m}$)	0.155	0.236	0.156	$3.4 \cdot 10^2$
Zimmerman (high $\dot{m}$)	0.687	1.07	0.698	$7.5 \cdot 10^2$

This is of course still subject to the constraint that t_{LRO} is equal to the experimental value. The values of E_{ZK} determined in this way (designated $E_{ZK,opt}$) vary from 240 to 1300 and do not appear to be correlated with any parameters of the system. There are even large differences between two tests with the same system, indicating that it is not merely a function of tank dimensions.

$$P_{error} = \frac{\int_0^{LRO} |P_{model} - P_{exp}| dt}{\int_0^{LRO} P_{exp}\, dt} \tag{2.54}$$

2.5.2 Evaluation of Time Histories

We begin by comparing each model to the data of Zilliac & Karabeyoglu[7]. In figure 2.9, the three models are compared against the experimental pressure time history. The ZK model clearly outperforms either the EQ or CP models, with each respectively over- and under-predicting the pressure. This is consistent with the variation in C_dA in table 2.4, where the CP model has a larger value to compensate for the lower pressure and the EQ model has a higher value. The EQ model does reproduce the slope of the pressure trace in the linear region after $t = 2s$, and the CP model is fairly accurate before the linear region begins.

Next we compare the models to the pressure data of Van Pelt et al[3] in figure

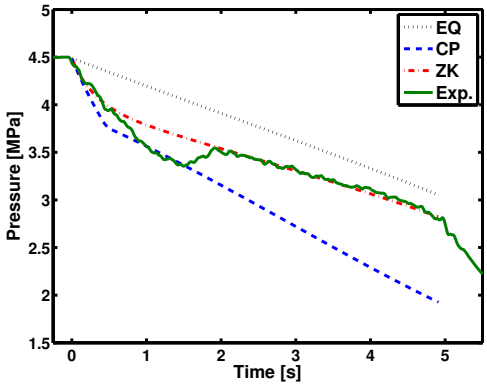

Figure 2.9: Comparison of model results to the experimental data of Zilliac & Karabeyoglu [7].

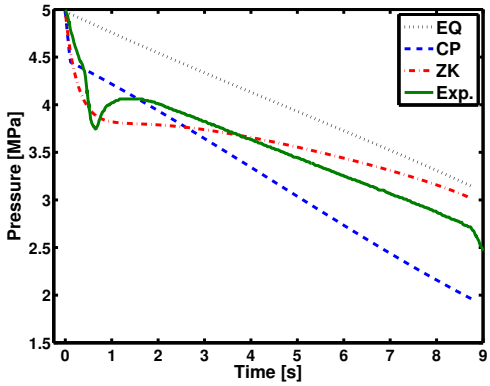

Figure 2.10: Comparison of model results to the experimental data of Van Pelt et al [3].

2.10. Physically this data set utilized a tank that was about one third the size of the previous experiment by Zilliac & Karabeyoglu. None of the models do particularly well here, although the ZK model does the best of the three. Again, the EQ model reproduces the slope of the linear region well.

In Casalino & Pastrone's paper they showed better results when comparing their model to these data, possibly because they used a different source for nitrous oxide physical properties. In equation (2.44) the rate of change of liquid temperature is scaled by the liquid specific heat capacity, which was shown in figure 2.4 to have significant variation depending on the source of the data. Furthermore, most of the time is spent in the boiling/evaporation region, where the tank pressure is dictated by the liquid temperature.

As a demonstration of this effect, figure 2.11 shows the pressure traces generated by the CP model as the thermodynamic variables h, u, and c_P are scaled. The variation in pressure that results is significant, increasing or decreasing the value by up to 0.5 MPa. The variation in thermodynamic properties needed to produce this change in results is well within the range seen in figure 2.4.

Now we compare to the ground and flight test data of Prince et al in figure 2.12. The size of this system is similar to the previous test of Van Pelt et al. In this case, with the exception of the initial drop and recovery the EQ model predicts the

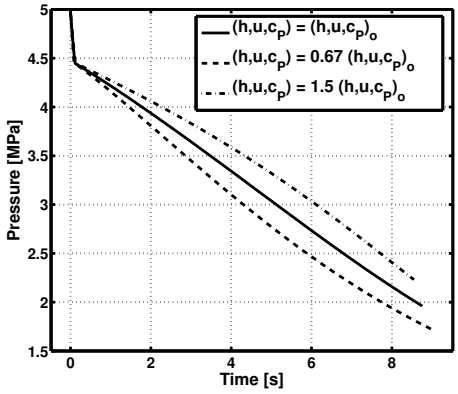

Figure 2.11: Pressure time histories from the CP model, showing effects of varying thermodynamic properties. Results are shown for the nominal values of h, u, c_P and also when they are multiplied by 1.5 and 0.67.

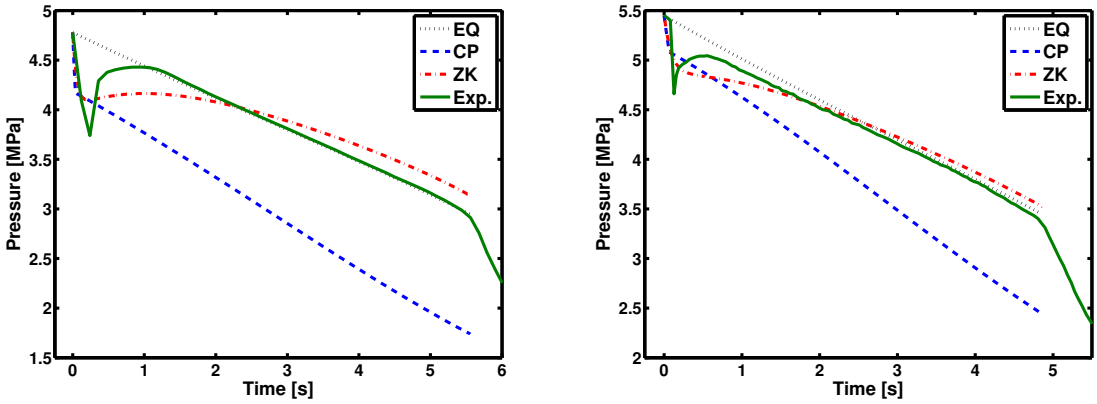

(a) Ground (b) Flight

Figure 2.12: Comparison of model results to the ground and flight test data of Prince et al [49].

pressure history quite well for both the ground and flight test. The ZK model also does relatively well, with better accuracy than EQ during the initial transient and worse performance in the linear region. The CP model performs poorly here and under-predicts the pressure for the full extent of the tests. The similarity between the ground and flight experimental data suggests that the effects of acceleration (approximately 4 to 7 g in this flight [49]) on the fluid and forced air convection on the tank walls are not significant. This result suggests both test data and tank models used in ground testing can be used for flight without loss of accuracy.

It is worthy of note that in figure 2.12 the experimental data were only sampled at about 15 Hz. Given the short time scale of the initial drop and recovery seen in self-pressurizing propellant tanks, it's possible that some features were not accurately captured in this region.

The tests performed by this author in the polycarbonate tube system are convenient to use as test cases because numerous experiments were performed with the same system over a range of mass flow rates (ie t_{LRO} or C_dA). Here we chose two tests to examine, one at a high flow rate and one at a low flow rate. The system used in these tests is much smaller than those in the data sets mentioned previously, holding only about $140g$ of nitrous oxide. The initial temperature was also lower, causing the initial pressure to be lower as well. This system was equipped with a thermocouple positioned in the outlet flow from the tank, upstream of the "injector," to obtain a measure of the effluent but it was found that this measurement was distorted by bubble nucleation within liquid and merely reproduced the saturation value. A thorough discussion of this phenomenon is given later in chapter 3 but for now we merely note that these temperature data will not be used for model evaluation here. The low mass flow rate data are shown in figure 2.13a, and the high mass flow rate data are shown in figure 2.13b.

Beginning with the low mass flow rate data, the pressure is predicted best by the ZK model although the overall slope is incorrect. The EQ model does somewhat worse, under-predicting the pressure for more than half of the time span. The CP model significantly under-predicts the pressure here. One possible reason for the CP model's deficiency is the linear fit for the pressure along the spinodal line, equation

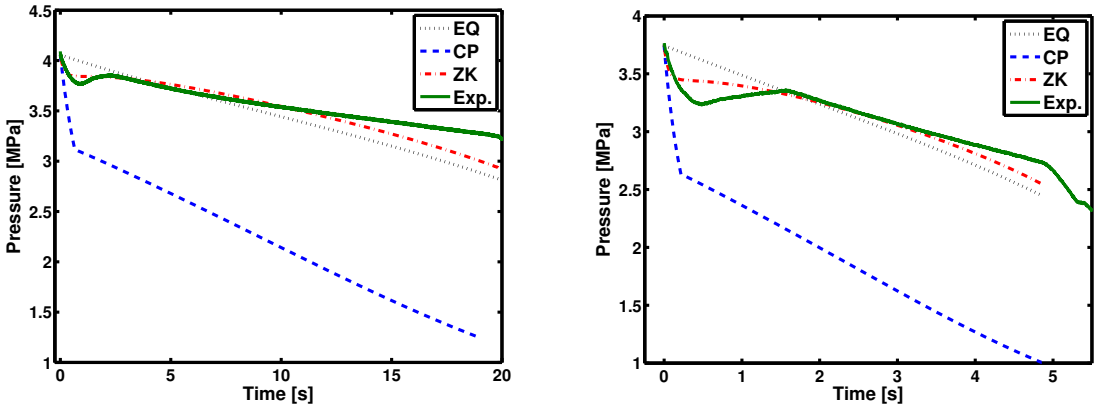

(a) Low flow rate. (b) High flow rate.

Figure 2.13: Comparison of experimental pressure to the results of models. Data are from the high and low flow rate tests in the polycarbonate tube system.

(2.49). It is unknown how accurate this fit is and over what temperature range it is appropriate. The tests in the small scale system had significantly lower initial liquid temperatures when compared to the other tests and this corresponds to a much lower spinodal pressure predicted by equation (2.49).

The CP model, unlike the EQ and ZK models, assumes an adiabatic tank. This could be a second possible cause for the CP model's inaccuracy in the polycarbonate tube tests because at small size scales the ratio of surface area to volume increases, and therefore heat transfer through the tank walls may be a more significant effect than in the larger tanks. This can be evaluated by looking at the ratio of the heat transfer rate from the wall into the liquid to the liquid mass, $\dot{Q}/m_{liq}$. This ratio is proportional to the increase of the liquid temperature caused by heat transfer from the wall. In figure 2.14, this ratio is plotted versus time for two cases, the high mass flow rate test in the polycarbonate system and the test of Zilliac & Karabeyoglu. The Zilliac & Karabeyoglu test clearly shows a much larger value, indicating that in the polycarbonate tube test the wall heat transfer term is not as important than in the Zilliac & Karabeyoglu test. We can therefore conclude that the assumption in the CP model of an adiabatic tank is not a likely cause of its inaccuracy here. This is a result of the thick polycarbonate tank wall, which with its very low thermal conductivity is

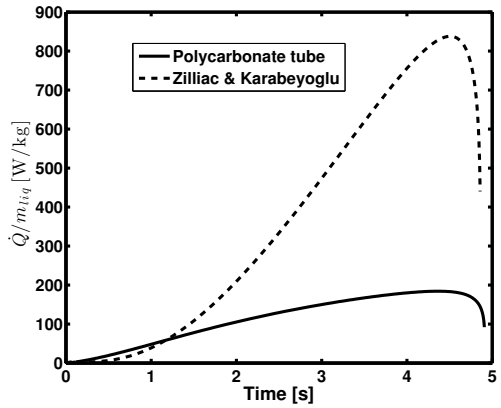

Figure 2.14: Specific heat transfer rate from tank wall into liquid, as predicted from ZK model. Results shown for the high mass flow rate test in the polycarbonate tube system and for the blow-down test of Zilliac & Karabeyoglu.

a good insulator.

In figure 2.13b the pressure data are shown from the high mass flow rate test. The ZK model does a good job of reproducing the pressure here, although it does not fully capture the initial transient. The EQ model also performs reasonably well although it under-predicts the pressure during the linear region. The CP model fairs poorly and significantly under-predicts the pressure.

The results here can be discussed quantitatively by calculating the error in predicted pressure history (equation (2.54)) for each of the three models and each of the six experimental data sets. This is done in table 2.5. Of the three models, the ZK model performs the best, with errors consistently less than 5%. The EQ model is next, with errors under 15% for all cases, and as low as 1.69% for one test. The CP model performs the worst, with errors ranging from 9.68% to 39.5%. Again, this could be a result of using a different source for thermodynamic properties than what Casalino & Pastrone used in developing the model.

An important issue for those who wish to use the ZK model without prior measurements of E_{ZK} is the sensitivity of P_{error} to E_{ZK}. To that end, a modeling test was performed on the six experiments used in this work: E_{ZK} was fixed to the average of the six $E_{ZK,opt}$ ($E_{ZK,ave} = 693$) and then C_dA was solved for again in order to match

Table 2.5: Normalized error in pressure histories, calculated via equation (2.54). Values are in percent.

Data Set	Pressure Error, %				Model with Minimum Error
	EQ	CP	ZK, $E_{ZK,opt}$	ZK, $E_{ZK,ave}$	
Zilliac & Karabeyoglu	10.8	12.2	1.91	2.67	ZK
Van Pelt et al	14.6	9.68	4.61	9.69	ZK when $E_{ZK} = E_{ZK,opt}$, CP when $E_{ZK} = E_{ZK,ave}$
Prince et al (Ground)	1.69	21.7	3.63	3.70	EQ
Prince et al (Flight)	2.44	11.9	1.99	2.38	ZK
Zimmerman (low $\dot{m}$)	4.27	34.9	2.21	2.86	ZK
Zimmerman (high $\dot{m}$)	4.66	39.5	1.97	2.00	ZK

the experimental t_{LRO}. The pressure histories were recomputed and the resulting errors as calculated by equation (2.54) for each case are listed in table 2.5. In most cases errors only increased slightly, but for the data of Van Pelt et al, it increased to 9.69%, making it slightly less accurate than the CP model. Note that in figures 2.9 through 2.13b $E_{ZK,opt}$ was used rather than $E_{ZK,ave}$.

2.5.3 Evaluation of Parameter Variations

These figures are useful in evaluating the general predictive ability of the three models for a given oxidizer feed system. Another test of the models is possible by looking at how the results change as parameters are varied. In other words, instead of looking at the pressure time history that a given model predicts, it is also useful to look at how the pressure trace changes when initial conditions change. The polycarbonate tube system experiments allow for this comparison because many tests were done with the same experimental setup at a range of mass flow rates.

To evaluate the models, the quantity P_{LRO}/P_i is evaluated. This is the pressure at the end of the liquid portion of the test, normalized by the initial value. This is plotted in figure 2.15 as a function of $1/t_{LRO}$ which is effectively the average mass flow rate because each test began with the same mass of nitrous oxide. Also shown in these figures are the experimental results.

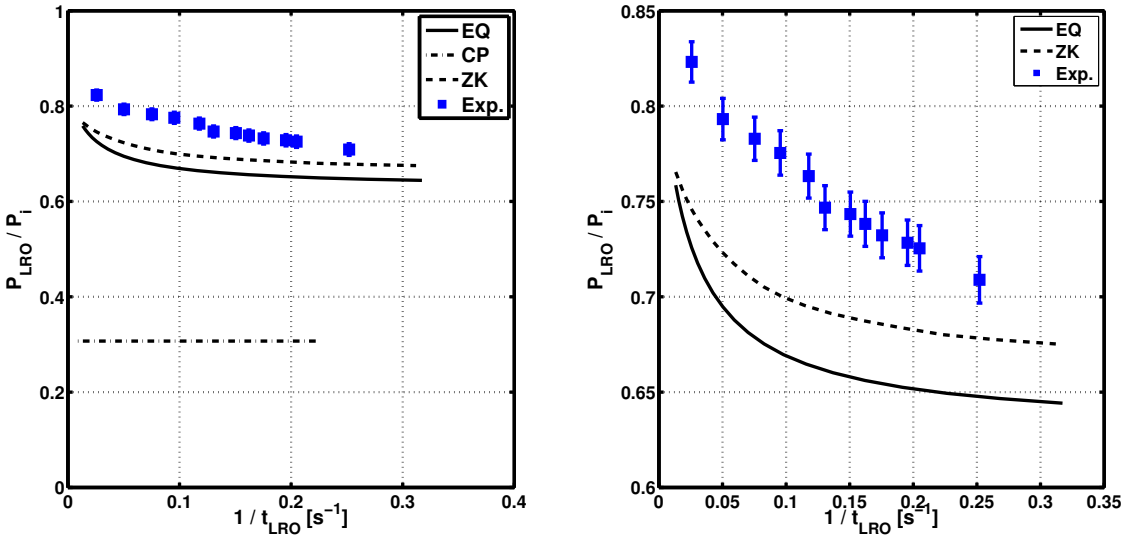

(a) All data (b) Zoomed to region near experimental data

Figure 2.15: Normalized pressure at the liquid run out point as a function of $1/t_{LRO}$. Shown are the results of the three models and the experimental findings from the polycarbonate tube system.

There are several implications of these results. First, the CP model in the pressure (figure 2.15) plot is constant as t_{LRO} changes. This means that the CP model results are not dependent on the test time scale, and one set of results can be remapped to another set with a different t_{LRO} (and hence C_dA) by simply stretching or compressing the time axis.

Physically, these constant values imply that in the development of the CP model we've assumed that processes within the tank are much faster than the rate at which mass is removed via the tank outlet. The key part of the model where this takes place is described by equation (2.47). This states that initially, condensation occurs at *the rate required to maintain the vapor at saturation.* Then, once the limit pressure is reached, boiling occurs at *the rate required to keep the pressure at the limit pressure.* In other words, boiling and condensation are occuring at a time scale much smaller than that of mass exiting the tank and the processes are unaffected by the change in flow rate.

The EQ model makes a similar assumption by stating that all propellant in the tank is at a uniform temperature and remains in phase equilibrium. However, the inclusion of heat transfer from the tank walls creates a dependence on mass flow rate and therefore it shows different values of P_{LRO}/P_i as the flow rate changes. In essence, as t_{LRO} drops there is less time for heat to flow into the nitrous oxide from the walls.

Figure 2.15 also shows us that the EQ model and ZK model both predict the trend in pressure variations as mass flow rate changes, but under-predict the value. Additionally, they seem to show more curvature at low mass flow rates than the experimental data. The ZK model is closer in value to the experimental data than the EQ model. The CP model gives pressures that are much lower than seen in the experiments, consistent with the pressure time history plots of this system (figures 2.13a and 2.13b).

2.6 Summary and Conclusions

To summarize, in this chapter we have taken three models (equilibrium, Casalino & Pastrone, and Zilliac & Karabeyoglu) for self pressurizing propellant tank dynamics

and compared them to a wide variety of experimental data. This was done with the goal of identifying the relative advantages and disadvantages of each of the models and developing a quantitative understanding of the conditions under which they are the most or least accurate. The key results for each model can be listed as:

Equilibrium Model The equilibrium model is by far the easiest to implement and solve, with the simplest differential equations and requiring properties only at saturation. Sometimes it accurately predicts the pressure time history, and other times it gives values higher than experimental data show. It cannot capture the initial transient. It does predict the variation in P_{LRO} fairly well as t_{LRO} changes, although it's values are offset from experimental results.

Zilliac & Karabeyoglu Model This model is the hardest to implement and requires an equation of state in order to calculate properties away from saturation. Solution times are also the longest of the three models. Its accuracy at reproducing experimental pressure traces is the most consistent out of the three models, but requires determination of E_{ZK}. Values for this parameter range from 240 to 1300 and have no known relationship to experimental parameters. An average value of $E_{ZK} = 693$ was shown to give good results in most cases. The ZK model does a good job of estimating the changes in P_{LRO} as t_{LRO} changes.

Casalino & Pastrone Model In terms of implementation and solution, the CP model is a compromise between the EQ and ZK models. It has more complex differential equations than the EQ model, but only needs properties at saturation and hence does not require a full equation of state. When compared to the experimental data used in this paper, the CP model did not do a particularly good job of accurately reproducing pressure. It is possible that the original authors used a different source for fluid properties which could have a significant impact on the results. A key physical assumption in the model makes its results functionally independent of t_{LRO} except for a scale factor, so it cannot predict the changes that occur as t_{LRO} varies. On the other hand, this allows a single

set of results to be used for many different values of t_{LRO}, simplifying design studies.

Based on these results, the ZK model is recommended when there is prior knowledge of the value of the empirical factor E_{ZK}, and computational effort and complex implementation are acceptable in return for increased accuracy. In all other situations, the EQ model is recommended. Ultimately though in many cases the accuracy of these models both in calculating pressure is unacceptable for practical design purposes. This effectively underscores the need for a robust and accurate tank model that can be used in a wide variety of systems to accurately predict experimental results.

Chapter 3

Experimental Systems

While previous researchers have developed models for self-pressurized nitrous oxide tanks, these models used differing fundamental assumptions in their foundations and as was shown earlier in chapter 2 these models generally have limited accuracy. Therefore it is likely that one or more of these models' basic assumptions were incorrect, a result of the fact that there exists little knowledge about the phenomena that take place within a self-pressurized propellant tank.

Therefore, a series of experiments were performed in order to gain the insight needed to establish a correct model foundation. These experiments focused on visualizing and identifying the heat and mass transfer processes inside the tank such as boiling, condensation, evaporation, convection, and motion of the liquid level. To this end, a series of experimental systems were developed with similar basic concepts: small-scale pressure vessels with optical access that could replicate the conditions of a rocket motor firing without requiring hot-fire testing.

Experimental work for this thesis spanned four years and over that time the system evolved based on insight gained from experiments. Originally, testing was performed in the Stanford Propulsion and Space Exploration Lab in room 051 of the Durand Building at Stanford University. Later, testing was relocated to the Outdoor Aerodynamic Research Facility (OARF) at NASA Ames Research Center in order to minimize any possible risks to personnel. The data and results that are presented here were gathered from three distinct versions of the system, all situated at the OARF.

The first is a setup that utilized a thick-walled polycarbonate tube as a transparent pressure vessel. Later a new system using quartz tubing was developed, in parallel with a much larger system using a stainless steel vessel with glass windows. These last two systems were used in parallel and there are many common elements to those two setups.

These three experimental systems will be described here, with particular attention given to the design of the quartz tube system. The polycarbonate vessel was repurposed from some injector visualization testing performed by Greg Zilliac at NASA Ames Research Center and there was relatively little design work involved. The stainless steel vessel with glass windows was an off-the-shelf component and was designed to be a visual liquid level gauge for high pressure vessels, known as a flat glass gauge. Some modifications were made in order to incorporate additional instrumentation but again there was little design work done on the vessel itself. The quartz tube system however was a completely new design by the author.

Nitrous oxide is in some ways a problematic fluid to work with and therefore this section begins with a discussion of its negative aspects and establishes carbon dioxide as a simulant fluid that can be used for cold flow testing. Then, the experimental systems that were used in this work are detailed. Finally, a brief description is given of some difficulties encountered when attempting to make pressure and temperature measurements with this system.

3.1 Carbon Dioxide as a Simulant

The most serious problem with using nitrous oxide as a working fluid for non-combustion testing is its positive heat of formation: $N_2O \rightarrow N_2 + \frac{1}{2}O_2 + 82.05\ kJ/mol$. This inherent chemical energy of the fluid allows nitrous oxide to be used as a monopropellant, with applications in small thrusters, gas generators, and igniters for larger rocket motors [1, 50]. However, this exothermic decomposition reaction can take place within nitrous oxide storage containers, causing a chain reaction that can cause pressure vessels or other components to explode [51, 52, 53, 54, 55, 56]. Although the reaction rate for this decomposition reaction in N_2O is approximately 10^4 smaller

Table 3.1: Estimates of chemical atmospheric lifetimes and global warming potentials [57].

Chemical	Lifetime in Atmosphere (years)	Global Warming Potential (100-year time horizon, molar basis)
Carbon Dioxide	50-200	1
Methane	12	21
Nitrous Oxide	120	310
Hydrofluorocarbons	1-270	140-11,700
Perfluorocarbons	800-50,000	6,500-9,200
Sulfur Hexafluoride	3,200	23,900

than that for hydrogen peroxide and hence in some ways it is a safer propellant, explosions have previously been observed in hybrid rocket propulsion systems and have even caused fatalities [51]. As a result, due to the potential hazard to personnel it is unfeasible to perform tests with N_2O in a university laboratory not designed for work with materials that present explosive hazards.

An additional concern with nitrous oxide arises when it is vented to the atmosphere, as is typically done with non-combustion testing. This is in contrast to use in a rocket motor where it would react with the fuel and exit the motor mostly in the form of species like N_2, CO_2, and H_2O. Unfortunately nitrous oxide is a potent greenhouse gas and thus venting in this way presents environmental concerns. For a 100-year time horizon, nitrous oxide has 310 times the global warming potential of carbon dioxide and 15 times that of methane [57]. A comparison of the global warming potential of N_2O with other greenhouse gases is given in table 3.1 To illustrate, this implies that venting a cylinder containing 25 kg of nitrous oxide to the atmosphere has approximately the same impact as burning 3000 L of gasoline.

For the testing required to investigate self-pressurizing propellant tank dynamics, an ideal simulant fluid would have identical thermodynamic and transport properties as nitrous oxide, yet would not possess explosion or environmental hazards. Carbon dioxide will be shown to present as a nearly ideal simulant fluid, with the added benefit of low cost, few health hazards, and extreme ease of handling. To explore the possibility of using CO_2 in place of N_2O in self-pressurized propellant tank dynamics

Table 3.2: Overview of thermodynamic similarity of nitrous oxide and carbon dioxide, with data from REFPROP [2]. Note that some parameters have been determined to different levels of precision and so there are different numbers of digits for the two fluids in some cases. The difference shown here is calculated as $(x_{CO_2} - x_{N_2O})/x_{N_2O}$.

Property	Nitrous Oxide	Carbon Dioxide	% Difference
Molecular Weight $[kg/kmole]$	44.0128	44.0098	-0.0068
Critical Temperature $[K]$	309.52	304.1282	-1.7
Critical Density $[kg/m^3]$	452.0	467.6	3.4
Critical Pressure $[MPa]$	7.245	7.3773	1.8
Triple Point Temperature $[K]$	182.33	216.592	19
Triple Point Pressure $[kPa]$	87.84	517.96	490
Normal Boiling Point $[°C]$	184.7	194.7	5.5
Acentric Factor	0.1613	0.22394	39

testing, a detailed comparison of the two fluids' properties is presented in this section. An overview comparison of various thermodynamic properties of the two chemicals is given in table 3.2, using data from the computer program REFPROP that has been developed by the National Institute of Standards and Technology [2]. With the exception of the triple point and the acentric factor, all the properties are within 5.5% of each other.

The acentric factor is a means of characterizing how different a fluid behaves compared to simple monatomic fluids such as argon or krypton and is closely related to the nonsphericity of a molecule's potential field [58]. It is defined as $\omega = -\log_{10}(P_{r,sat}(T_r = 0.7)) - 1$ and is close to zero for the simple monatomic fluids. The differing acentric factors suggest that some deviations in thermodynamic properties could be expected, as evidenced by the triple point properties. While the triple point may be reached during a propellant tank blowdown, it would only be long after the liquid is entirely expelled from the tank and only a small amount of vapor remains. This condition is not generally of importance to propulsion applications and in fact it is the time when liquid is being expelled from the tank that is what concerns us most. Therefore this divergence is not expected to hinder the use of CO_2 as an analog for N_2O in this work. Nevertheless, further analysis is required to make a conclusion.

To explore the differences between nitrous oxide and carbon dioxide in greater

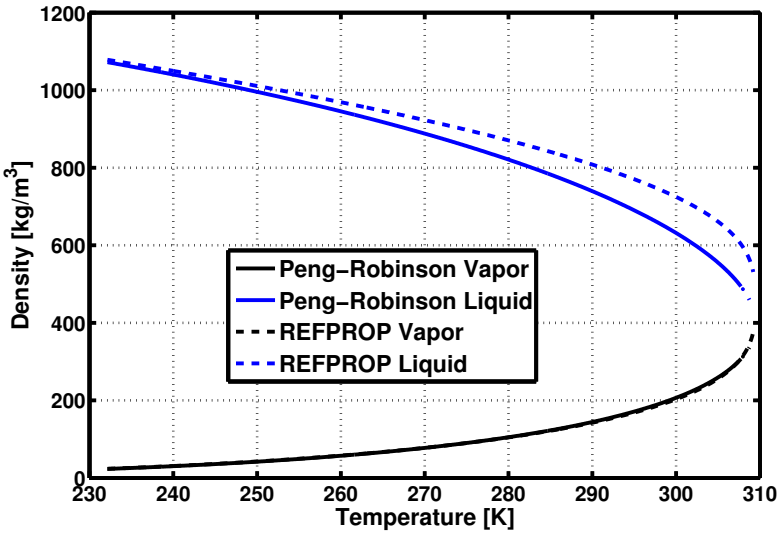

Figure 3.1: Comparison of Peng-Robinson and REFPROP saturated N_2O density calculations.

detail, extensive data is needed on their thermodynamic and transport properties. The difficulty in this is that standard operating conditions at ambient temperatures are very close to both fluids' critical points. Near this point properties become very sensitive to temperature and hence great care must be exercised in calculating fluid properties. As an example, figure 3.1 shows the density of N_2O as a function of temperature for both the saturated liquid and vapor, calculated with a cubic equation of state (Peng-Robinson [44]) and the REFPROP program. Note that while the vapor densities are nearly identical between the two programs, the liquid densities differ by more than 20% near the critical point.

In place of comparatively simple cubic relations such as Peng-Robinson, REFPROP utilizes technical equations of state that contain more than a dozen terms. Technical equations of state are created by fitting these terms to numerous experimental data sets in order to achieve accuracies better than 1% for many properties over wide ranges of temperature and pressure. While one technical equation of state can calculate all thermodynamic properties for a fluid, no such single source exists for the transport properties and instead a collection of theoretical predictions and

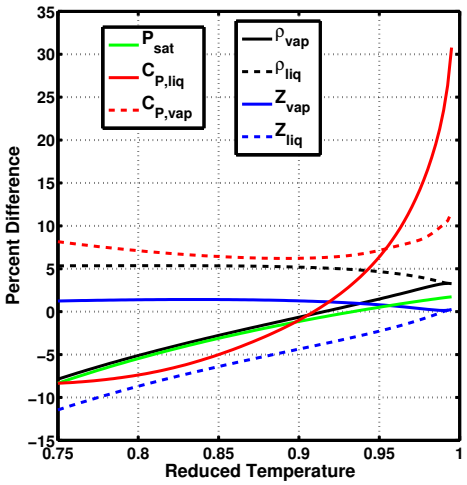

(a) Pressure (P), liquid and vapor isobaric specific heat capacities (C_P), liquid and vapor densities (ρ), and liquid and vapor compressibility factors (Z).

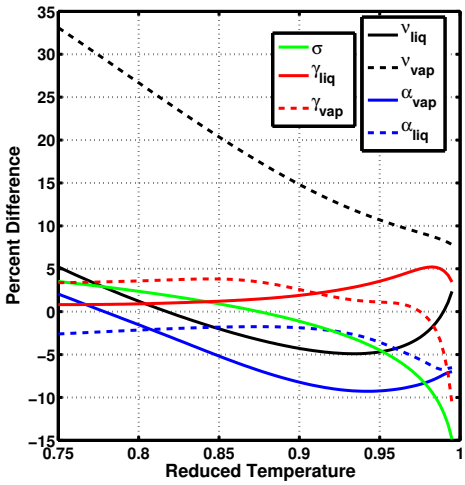

(b) Surface tension (σ), liquid and vapor ratios of specific heats (γ), liquid and vapor dynamic viscosities (ν), and liquid and vapor thermal diffusivities (α).

Figure 3.2: Relative difference in some properties of N_2O and CO_2 along the saturation line. Data are taken from REFPROP [2] and are plotted as a function of reduced temperature (T/T_c).

empirical correlations are used within REFPROP.

All tank tests begin with the liquid and vapor close to phase equilibrium at saturated states and equilibrium models assume that they remain saturated for the duration of the test. Therefore, the analysis begins by examining how properties of the liquid and vapor vary while maintaining a saturation state. Figure 3.2 shows the relative difference in nitrous oxide and carbon dioxide as expressed in various properties of the saturated liquid and saturated vapor. These are calculated simply as $(x_{CO_2} - x_{N_2O})/x_{N_2O}$ where x is the property being evaluated. These comparisons are plotted as a function of reduced temperature ($T_r = T/T_c$). While the critical temperatures of N_2O and CO_2 are only different by 5.4 $°C$, properties become extremely sensitive to temperature near the critical point and by using reduced temperature as the independent variable a fairer comparison of properties is possible.

In the temperature range of interest ($T_r = 0.75 \rightarrow 1.0, T_{N_2O} = 232\ K \rightarrow$

310 K, $T_{CO_2} = 228\ K \rightarrow 304\ K$) none of the thermodynamic properties differ between the two fluids by more than 30% and most differ by less than 10%. Note that the high compressibility of liquid N_2O and CO_2 creates significant differences in the isobaric and isochoric specific heat capacities. While most of the transport properties show differences of less than 10%, the liquid viscosity shows differences of more than 30% at very low temperatures.

From these plots it is possible to conclude that most properties of the two fluids are similar to within 10%, except for liquid viscosity, liquid enthalpy, and vapor isobaric specific heat capacity which all vary up to 30%. Therefore if the dynamics are sensitive to changes in these properties, differences between nitrous oxide and carbon dioxide tank testing behavior may be evident.

While saturation properties are the sole data required for an equilibrium model, it is also possible that the liquid and vapor are not maintained in phase equilibrium. Therefore, properties away from the saturation state must also be examined. To this end, an array of properties of the two fluids is compared over a wide range of temperature and pressure. In figure 3.3, the phase boundary between liquid and vapor is plotted versus reduced temperature. Below this line are the liquid states while above it are the vapor states. While curves for N_2O and CO_2 are very similar, it is important to note that they differ slightly. In the region near this phase boundary very large differences between the two fluids are expected and therefore this region will not be included in the calculations.

In figure 3.4, the absolute magnitude of the relative differences between N_2O and CO_2 density, compressibility factor, isobaric specific heat capacity, ratio of specific heats, kinematic viscosity, and thermal diffusivity are given. The differences plotted here are calculated in the same manner as those in figure 3.2. In each plot the two independent variables are reduced temperature and reduced pressure ($P_r = P/P_c$). The temperature and pressure ranges extend from the triple point to just past the critical point. The contours and colors show the relative difference, in percent. The thick red line running from the bottom left towards the upper right of each figure highlights states near saturation that were not evaluated.

For density, compressibility factor, isobaric specific heat capacity, and the ratio of

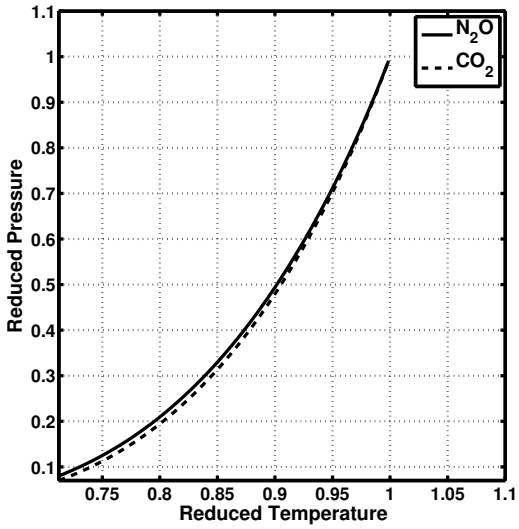

Figure 3.3: Phase boundaries for carbon dioxide and nitrous oxide.

specific heats the maximum difference between the two fluids is 5.4% over a very wide range of temperature and pressure. For thermal diffusivity and kinematic viscosity the deviations rise to 16% and 30%, respectively. For kinematic viscosity however the areas where N_2O and CO_2 diverge are at low temperatures in the vapor region. This region is only reached during the gas phase of tank blowdown, a situation that is relatively easy to accurately model when compared with the liquid phase. Therefore this divergence will likely not impact tank testing and modeling.

However, thermal diffusivity shows differences of 10-15% for liquid near saturation, a region that is commonly encountered in the liquid phase of tank testing. This is possible evidence that the two fluids may behave differently in some aspects of propellant tank dynamics.

When comparing N_2O and CO_2 using REFPROP, it is important to note the uncertainty in REFPROP's outputs. The program itself gives the uncertainties in several quantities for each fluid, calculated by comparing the output with experimental data. These are shown in table 3.3 along with the maximum deviations between CO_2 and N_2O both at saturation (figure 3.2) and away from saturation (figure 3.4). For the thermodynamic properties, REFPROP's uncertainty is much less than the

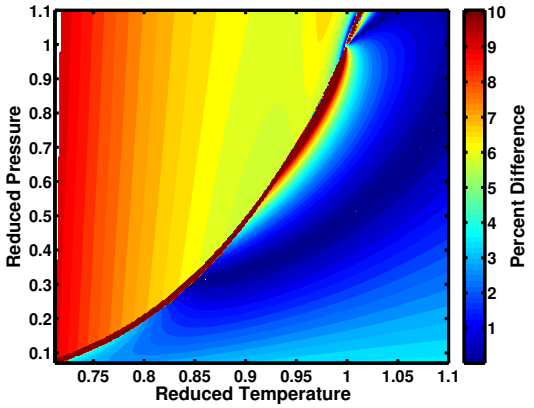

(a) Isobaric specific heat capacity

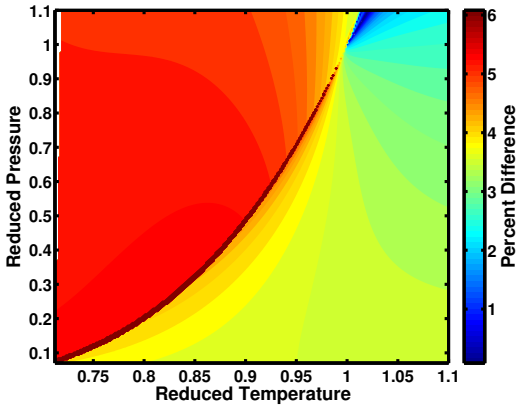

(b) Density

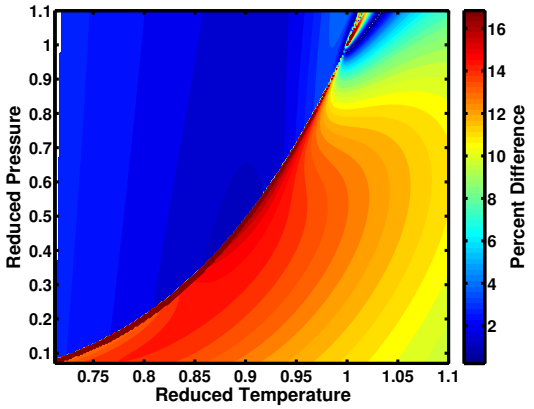

(c) Thermal diffusivity

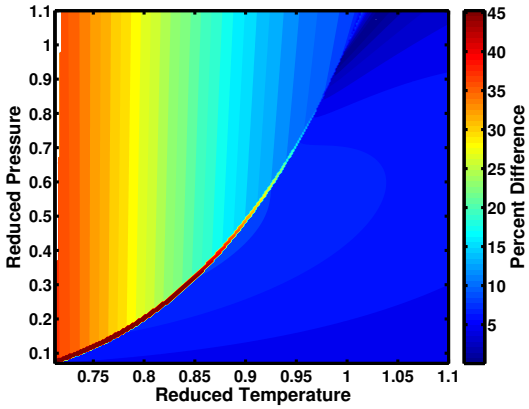

(d) Kinematic viscosity

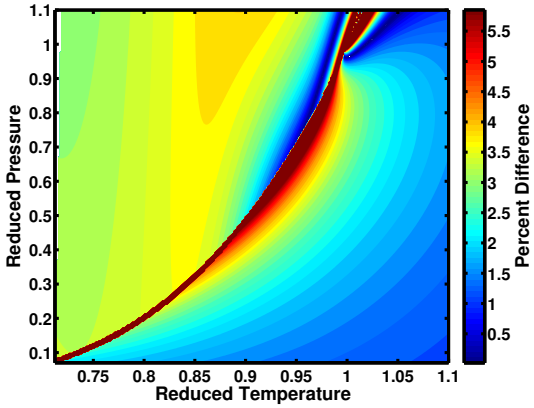

(e) Ratio of specific heats

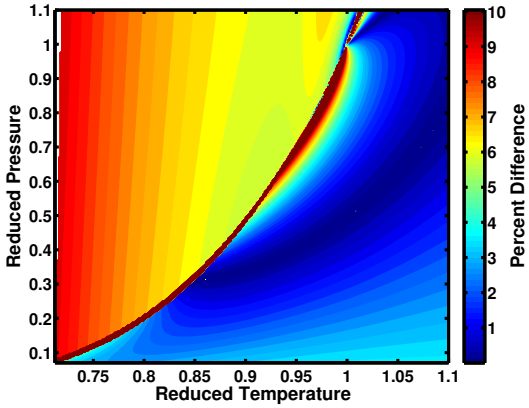

(f) Isobaric specific heat capacity

Figure 3.4: Comparison of N_2O and CO_2 properties away from saturation line.

Table 3.3: Comparison of REFPROP uncertainty and maximum differences between nitrous oxide and carbon dioxide.

Property	REFPROP Uncertainty		Maximum Difference	
	CO_2 [%]	N_2O [%]	Along Saturation [%]	Away From Saturation [%]
ρ_l	0.05	0.25	5.4	4.6
ρ_v	0.05	0.25	7.9	5.4
Z_l	0.5	5	11.4	1
Z_v	1	0.05	1.4	1.7
$c_{p,l}$	1.5	3	11	10
$c_{p,v}$	0.15	3	30	9.2
ν	5	10	33	30
α	10	10	9.3	16

maximum deviations with the exception of the liquid and vapor compressibility factor where they are of similar size. The uncertainty in kinematic viscosity is also substantially less than the calculated differences between carbon dioxide and nitrous oxide. For thermal diffusivity however they are again of similar size. There is no uncertainty information on other quantities such as surface tension, or the ratio of specific heat capacities.

The fundamental limitation of this type of analysis is that without an existing model for self-pressurizing propellant tank dynamics, it is unknown which fluid properties or groups of properties are important to match and also how close they need to be to reproduce the relevant behavior. However, it is important to note all properties examined here are relatively close when compared with other fluids. To illustrate, while ethane is a fluid with a similar vapor pressure to nitrous oxide its liquid and vapor densities are roughly 50% those of nitrous oxide. Propane on the other hand has similar density but a vapor pressure that is only about 20% that of nitrous oxide.

The similarity between the CO_2 and N_2O has been leveraged in other industries. In supercritical fluid extraction, a fluid that is heated and pressurized above its critical point is used as a powerful solvent to extract chemicals of interest. This is enabled by many supercritical fluids' extremely low viscosity and high density. Carbon dioxide has traditionally been used for this process, but nitrous oxide has also been evaluated

as a possible replacement because it has higher solubility for some components [59, 60]. N_2O is attractive in this regard because its fluid properties are very similar to those of CO_2 and hence could be a "drop-in" replacement, without needing new equipment.

3.2 Polycarbonate Tube System

The first experimental setup was based around a vessel designed and built by Greg Zilliac of NASA Ames Research Center, with the original purpose of visualizing the flow downstream of the injector plate in a hybrid rocket. These tests were completed in 2008 and so when the propellant tank research began in 2011 this vessel was available for use.

The test vessel used in this setup was a thick walled extruded polycarbonate tube purchased from K-Mac Plastics of Wyoming, MI. The tubing was captured on either end with aluminum end caps that formed o-ring seals on the outside of the tube. The top end cap has a single central port to allow fluid flow while the bottom contained three small side ports in addition to a central port similar to the top end cap. The polycarbonate tubing had an internal diameter of 25.4 mm, an outside diameter of 38.1 mm, and a length of 355.6 mm. The internal volume was then 0.1802 L without including any pipes or tubing that connect to the vessel. When completely filled with liquid at 20 $°C$, the vessel held 142 g of N_2O or 139 g of CO_2. A picture of this vessel is given in figure 3.5 and a plumbing and instrumentation diagram is shown in figure 3.6.

The tank was filled from a standard "K" size cylinder of CO_2 or N_2O using a pneumatic piston pump. From the pump the fluid enters the test vessel via the side of the bottom end cap. The fitting is visible on the lower right side of figure 3.5. Also present is a helium cylinder that can be used to pressurize the polycarbonate vessel from the top. All fluid handling (other than for valve actuation) is done via 1/4 in (6.35 mm) stainless steel tubing, and all flow control is achieved via pneumatically-actuated full-port ball valves. This not only allows for low pressure drops across the valves but also alleviates many material compatibility concerns as most commercial off-the-shelf solenoid valves contain elastomers that are not compatible with nitrous

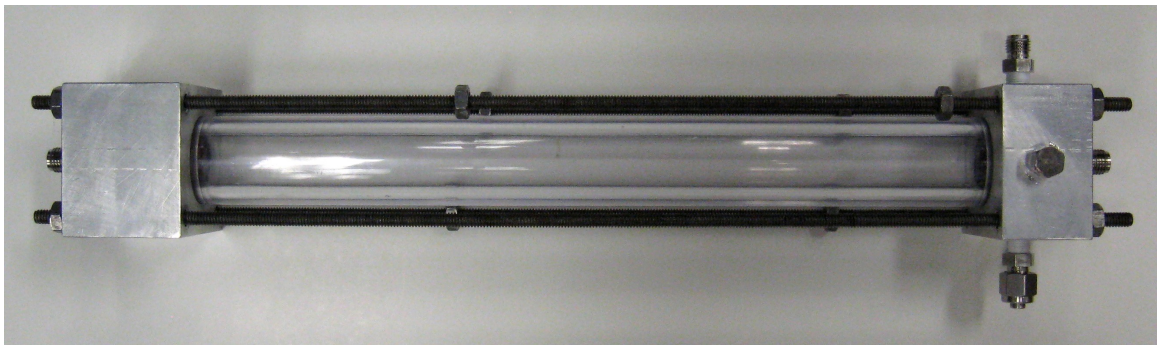

Figure 3.5: Picture of the polycarbonate tubing test vessel. The right side is the base and the left is the top.

oxide, carbon dioxide, or both. Ball valves however are easier to obtain with compatible elastomers.

Initially, hydraulic hoses were used to connect the helium cylinder to the test vessel because of their flexibility, high pressure rating, and extremely low cost. Although they were made from Buna-N rubber and hence not compatible with carbon dioxide or nitrous oxide, a check valve was used to prevent any back flow from the test vessel. However carbon dioxide vapor appears to have somehow traveled into the hose possibly caused by a leak in the check valve or diffusing through the helium when the valve was open, and eventually causing it to fail during testing. A picture of the failed hose is shown in figure 3.7.

A pneumatically actuated ball valve is located in the tubing below the test vessel and controls the flow of fluid out of the vessel. From there the liquid flows through a metering valve and then is vented directly to the atmosphere. This metering valve is used to control the mass flow rate, draining the tank in anywhere from 4 to 40 seconds. Slower mass flow rates were not possible because solid N_2O or CO_2 would form and block the metering valve. At the exit of the tank and upstream of the metering valve there is a K-type thermocouple that is used to measure the temperature of the fluid leaving the tank. The static pressure within the tank is also measured with a pressure transducer. This transducer is located in the exit line from the tank, but the low velocities present in this system minimize any difference between this pressure and the ullage pressure. This assumption is easily justified by noting that

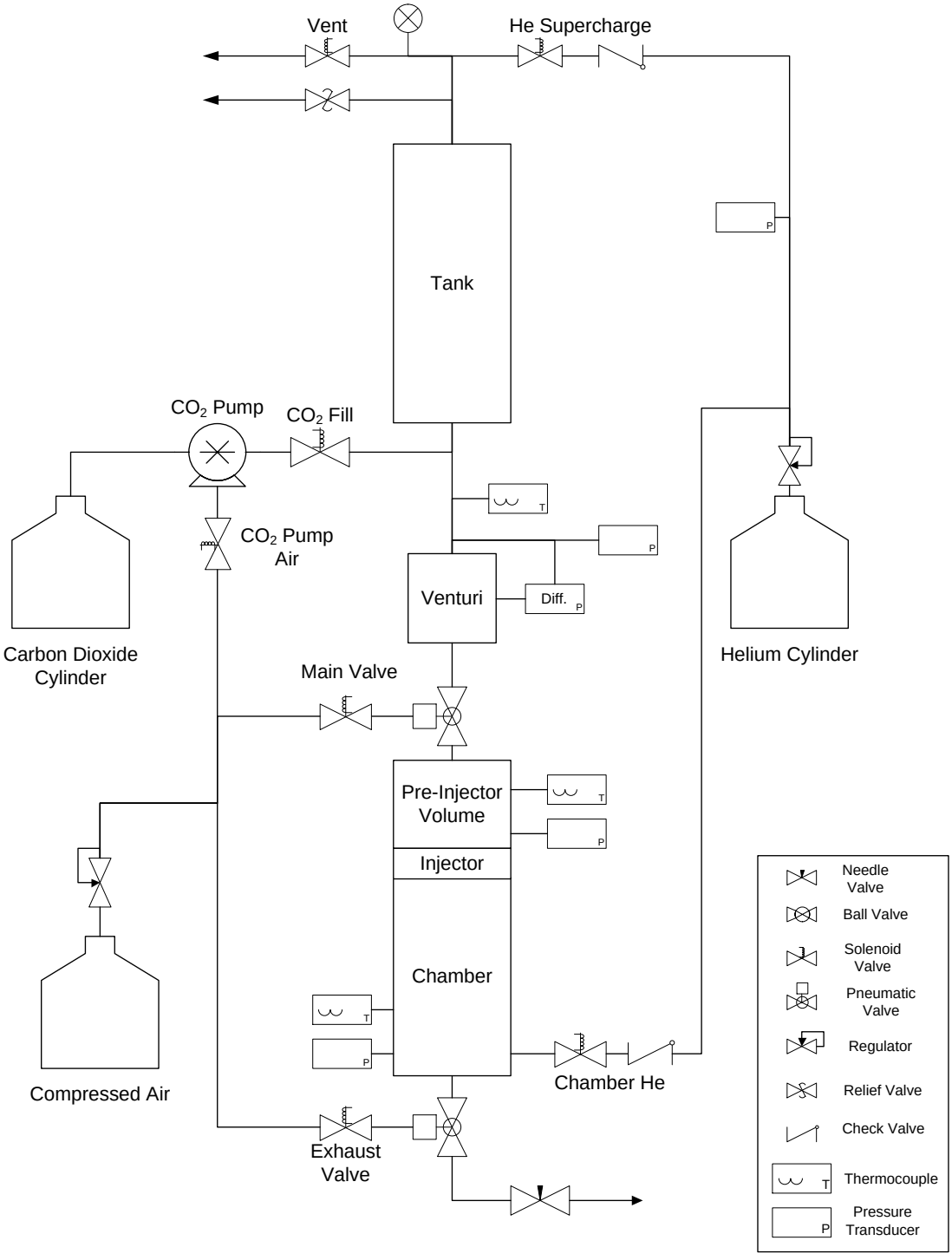

Figure 3.6: Plumbing and instrumentation diagram for the polycarbonate tubing system.

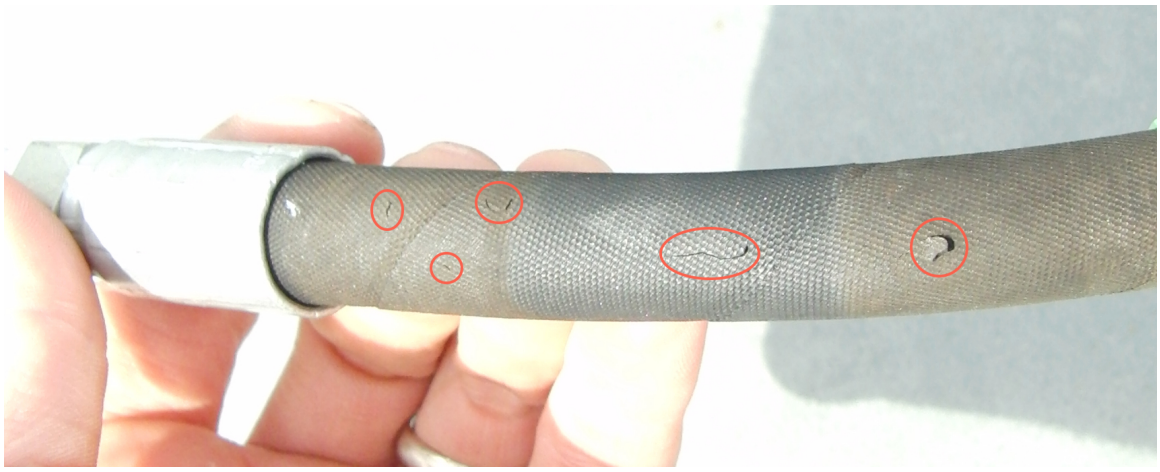

Figure 3.7: Failed hydraulic hose used for helium supply. Red circles highlight regions where the hose burst.

the pressure drops smoothly as the test begins; pressure changes due to fluid motion would by contrast be quite sudden. This will be proven later in the experimental results section when the effect of feed line length is shown.

A venturi flowmeter in conjunction with a differential pressure transducer is also situated in the piping downstream of the tank exit before the pneumatically actuated ball valve, however large amounts of unsteady two-phase flow make this measurement system unreliable. Therefore, an averaged mass flow rate is calculated based on the initial mass of liquid in the tank and the time required for the to be completely drained.

The transparent nature of the tank allows for the detection of boiling, convection cells, and other processes via video imagery. However the polycarbonate tubing used has relatively poor optical clarity and therefore simply illuminating the tank from the back or front is ineffective. Instead, a laser sheet illumination system is used and directed towards the centerline of the tank. The entire system is pictured in figure 3.8. Also visible in this image is a second polycarbonate vessel downstream of the tank, an injector testing system used by another researcher. This injector testing setup was removed during all tank testing and in its place the metering valve was installed.

The procedure for a test is as follows. First, the tank is filled to the desired

Figure 3.8: Picture of the polycarbonate tube setup. The system is mounted to a mobile cart at the Outdoor Aerodynamic Research Facility at NASA Ames Research Center.

level with liquid carbon dioxide or nitrous oxide. Once this condition is met, a pneumatically actuated ball valve is opened below the tank and the liquid begins to exit out the bottom of the tank. Eventually the liquid is completely depleted and gas flows out of the tank until the internal pressure reaches atmospheric pressure.

Early testing with this facility showed relatively poor repeatability, with tests that had ostensibly identical initial conditions giving variable results in terms of both the video imagery and the pressure data. This problem was eventually solved by establishing and strictly adhering to a set of experimental procedures, including venting the ullage repeatedly during the filling process and delaying the start of a test until the system has reached equilibrium. In every test, after the vessel is filled the ullage is vented until the entire tank can be seen to visibly boil. This ensures that there is a relatively uniform temperature field. In order to allow the system to reach equilibrium, the test is not allowed to begin until the rate of change of pressure within the tank is less than 700 Pa/s, which often required waiting 10 to 30 min.

Both liquid CO_2 and N_2O are strong industrial solvents and are known to damage many common sealing elastomers [61, 62, 63]. As a result, when comparing two tests that are performed at the same setting of the metering valve it is important to verify that the valve's condition is unchanged. Therefore, the gas portion of each test is used to estimate the valve's flow coefficient or C_v.

When the liquid has been completely expended gas is still present in the system and vents out the metering valve until the internal pressure reaches ambient. During this time the mass flow rate can be easily calculated using the measured temperature and pressure, and then the corresponding valve flow coefficient can be determined. While this procedure yields the gas C_v and not the liquid C_v, it is reasonable to assume that the two are directly related and if changes in gas C_v are detected it would be a sign that the valve has sustained damage.

The procedure to estimate the valve C_v begins with calculating the mass of gas in the system as a function of time,

$$m(t) = \frac{P(t)V_{tank}}{Z[T(t), P(t)]\ R\ T(t)} \tag{3.1}$$

and then differentiating it with respect to time. Note that while pressure and temperature are directly measured, the compressibility factor is calculated using REFPROP. Then, because of the large pressure drop across the metering valve the flow is assumed to be choked and the valve's C_v can be calculated [64] as

$$C_v = \frac{q\sqrt{(G_g T)}}{10.68P}, \tag{3.2}$$

where q is the mass flow rate in $SCFM$, G_g is the gas specific gravity, pressure is in $psia$ and temperature is in $^\circ R$. For the valve used in the tests presented in this thesis, the C_v ranges from 0.003 to 0.06.

3.3 Quartz Tube System

After a significant amount of testing was completed with the polycarbonate system, sufficient knowledge and experience was generated to identify its shortcomings. These included:

1. A low resolution camera and polycarbonate with poor optical clarity made it impossible to discern small features and required tests to be done in darkness with laser sheet illumination. This configuration made it difficult to accurately measure the liquid level before each test began to better than about ± 2%.

2. The polycarbonate was held by end caps that sealed on the outside diameter of the tube, thereby obscuring the top and bottom of the tank from view and making it impossible to determine if bubbles were originating on the surfaces of these end caps or within the exit flow tubing.

3. The temperature and pressure were measured only at the tank exit, with no knowledge of the temperature and pressure fields within the tank.

4. The flow out of the tank was metered with a needle valve that had poor repeatability and would become blocked with solid CO_2 or N_2O at low flow rates, limiting the range of flow rates that could be tested. The flow rate out through

this valve is also difficult to model when compared with a simpler restriction such as an orifice or nozzle.

5. Few system parameters could be controlled.

A new experimental system was designed to overcome these problems. This design began with a search for a new vessel wall material that had improved optical properties compared with the polycarbonate but still had high strength in order to function as a pressure vessel and was chemically compatible with nitrous oxide and carbon dioxide. Nearly identical internal dimensions were sought in order to make results with the new system directly comparable to the old system.

Unfortunately, after discussions with several manufacturers and machine shops specializing in plastics, polycarbonate was eliminated as a possibility because no manufacturer produced tubing with a more uniform surface than the previously used tubing, and polishing a tube of this length and internal diameter was not feasible (mechanically, chemically, or thermally).

Acrylic was the first option selected. When compared with polycarbonate, acrylic is more brittle (but still more plastic than glass or sapphire or quartz) but has a higher ultimate strength (77.6 *MPa* vs 65.5 *MPa*). In contrast to the polycarbonate tubing, a vendor (Spartech Townsend) was found that supplies cast acrylic tubing with high optical quality surface finish and in the size desired for this experiment. While the chemical compatibility of liquid CO_2 and N_2O with acrylic was somewhat unknown due to a lack of published data, the acrylic was low-cost, easily machinable, and therefore testing was a low-risk option.

Initial testing was performed with the acrylic tubing by pressurizing it with CO_2 to 5.5 *MPa* for 20 minutes. Unfortunately this short test resulted in crazing along the inside surface of the tube, as seen in figure 3.9. The crazing was likely caused by a combination of the tensile stresses from the internal pressure and the chemical attack from the carbon dioxide. The crazing also indicated that a complete structural failure was probable if the tube continued to be exposed to the fluid and high internal pressure. Therefore a new material was sought.

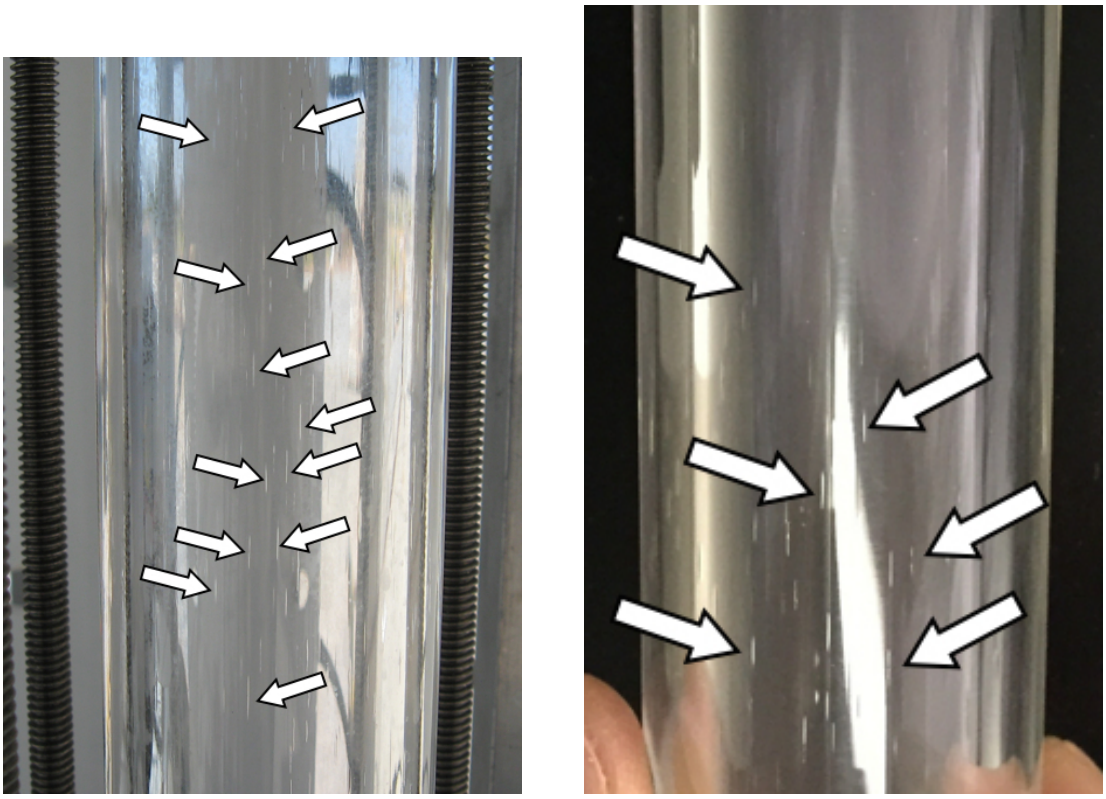

Figure 3.9: Pictures of acrylic tube showing crazing. White arrows show some crazing lines.

Various types of glass, quartz, and sapphire were all examined. Glass was found to have insufficient mechanical strength, with design tensile strengths of approximately 7 *MPa* quoted by manufacturers. For a pressure vessel with a nominal design pressure of 7 *MPa*, this was unacceptable. For sapphire, the vast majority of vendors and manufacturers reported that they could not produce tubing with dimensions anywhere near the required geometry (25.4 *mm* ID, 355 *mm* length). One vendor was found that could grow and polish the crystal in approximately the requested size, but the cost was unacceptable.

Quartz was found to have a good combination of reasonably low cost, high strength, resistance to thermal loads, and chemical resistance. A manufacturer was also found that could produce custom tubing in the sizes required (Wilmad-Labglass).

Probabilistic Failure Analysis Methods

A relatively modern method was used to determine the required wall thickness and this will be discussed in detail here. The basic foundation is taken from Harris [65], with further details from Yoder [66] and Salamin [67]. In contrast to the methods used with plastic materials, probabilistic failure models are well suited to brittle materials such as quartz.

Imagine a structure with volume V is composed of n volume elements of size δV and each with a probability of failure P_f. Then, the probability of survival of one element is $P_s = 1 - P_f$ and the probability of survival of the entire structure is $(1 - P_f)^n$. This can also be written as

$$P_s = \left(1 - \frac{VP_f}{V}\right)^n \tag{3.3}$$

$$= \left(1 - \frac{VP_f}{n\delta V}\right)^n \tag{3.4}$$

$$= \left(1 - \frac{V\phi}{n}\right)^n \tag{3.5}$$

where ϕ is the probability of failure per unit volume. Now, as $n \to \infty$, $P_s \to e^{-V\phi}$ using the limit definition of e^x. Different expressions have been developed for ϕ, but

the most widely used is $(\sigma/\sigma_o)^m$ where σ is the mechanical stress, σ_o is the Weibull scaling factor (often called the characteristic or nominal strength), and m is the Weibull modulus (often referred to as the shape factor or shape parameter). σ_o is a parameter that describes the range of σ at which specimens fail, while m describes the spread about that point.

Careful readers will note that this expression for ϕ does not appear to have the correct units in order to cancel the units of volume introduced by V. Therefore, a reference volume is introduced with the factor $1/V_o$ to produce the final expression for the probability of survival:

$$P_s = \exp\left[-\frac{V}{V_o}\left(\frac{\sigma}{\sigma_o}\right)^m\right] \tag{3.6}$$

If the stress state is not uniform throughout the structure, this expression becomes

$$P_s = \exp\left[-\frac{1}{V_o}\int\left(\frac{\sigma}{\sigma_o}\right)^m dV\right] \tag{3.7}$$

This expression is frequently expressed in terms the maximum stress in the structure, σ_{max}, and the effective volume kV. This effective volume is defined as the volume that the structure would have if $\sigma = \sigma_{max}$ everywhere and the probability of survival were identical. Therefore we write:

$$\begin{aligned} P_s &= \exp\left[-\frac{kV}{V_o}\left(\frac{\sigma_{max}}{\sigma_o}\right)^m\right] \\ kV &= \int\left(\frac{\sigma}{\sigma_{max}}\right)^m dV \end{aligned} \tag{3.8}$$

Often times there is a surface that contains the highest stress levels within the structure and this analysis is done in two dimensions on that surface alone. This is the most common method of analysis and as such most reported values for σ_o and m are calculated from this type of analysis, so it will be used here. The new expression

based on area is:

$$\begin{aligned} P_s &= \exp\left[-\frac{kA}{A_o}\left(\frac{\sigma_{max}}{\sigma_o}\right)^m\right] \\ kA &= \int\left(\frac{\sigma}{\sigma_{max}}\right)^m dA \end{aligned} \tag{3.9}$$

Now, to determine the probability of survival of a brittle structure we need to find the stress state σ, and the material properties σ_o and m. A complicating factor is introduced by the uncertainty reported in the values of σ_o and m (U_{σ_o} and U_m). Since we are discussing probabilistic methods for failure analysis, we must take into account the probability that σ_o and m take on a given set of values. This effect may be introduced in different ways and here we consider two.

The first is the traditional method for propagating uncertainties. Given uncertainties in independent variables x_i, it specifies the resulting uncertainty in a dependent variable y:

$$U_y = \sqrt{\sum_i \left(\frac{\partial y}{\partial x_i} U_{x_i}\right)^2} \tag{3.10}$$

Where for us y is the probability of success and x_i are σ_o and m. Note that we've implicitly assumed that k, A, A_o, σ_{max} can be calculated exactly. In essence what we seek to compute is:

$$\begin{aligned} P_s &= \exp\left[-\frac{kA}{A_o}\left(\frac{\sigma_{max}}{\sigma_o}\right)^m\right] \pm U_{P_s} \\ &= P_s(\sigma, \sigma_o, m) \pm U_{P_s} \end{aligned} \tag{3.11}$$

and we are really only interested in one side of the interval $P_s(\sigma, \sigma_o, m) - U_{P_s}$.

The approach of equation (3.10) makes two important assumptions. First, that the uncertainties in the dependent variables are independent, meaning that variations in x_1 have no effect on x_2. Second, it assumes that over the interval U_{x_i} the relationship between y and x_i is linear. For the situation here, both of these assumptions are incorrect.

The function to be evaluated (equation (3.9)) is highly non-linear in σ_o and m, even in small intervals. It will also be shown that doing a non-linear calculation instead of the traditional linear one doesn't complicate the procedure so there is little downside to using the more accurate method. The parameters σ_o and m define a fit to experimental data and therefore they are not independent. In other words, if a higher value of m were used in the fit, σ_o would change too in order to maintain the best fit possible to the data.

Therefore, because equation (3.10) may be inaccurate here, we use a more general expression:

$$U_y \leq \sum_i |y(x_i + \tfrac{1}{2}U_{x_i}) - y(x_i - \tfrac{1}{2}U_{x_i})| \tag{3.12}$$

Without further knowledge, the $\leq$ must be taken as $=$ and hence the maximum value for U_{P_s}. Therefore for our equation this becomes:

$$\begin{aligned} U_{P_s} = &|P_s(\sigma, \sigma_o + \tfrac{1}{2}U_{\sigma_o}, m) - P_s(\sigma, \sigma_o - \tfrac{1}{2}U_{\sigma_o}, m)| \\ &+ |P_s(\sigma, \sigma_o, m + \tfrac{1}{2}U_m) - P_s(\sigma, \sigma_o, m - \tfrac{1}{2}U_m)| \end{aligned} \tag{3.13}$$

Now, given values for U_{σ_o} and U_m, U_{P_s} can be calculated using equation (3.13). This completes the first method for incorporating uncertainties in the material properties and equation (3.13) will be referred to as the "traditional" approach.

The second approach leverages the fact that we are interested in the marginal probability of success and introduces probability density functions for m and σ_o. The result is

$$P_s(\sigma) = \iint P_s(\sigma|\sigma_o, m)P(\sigma_o, m)d\sigma_o dm \tag{3.14}$$

Where $P(\sigma_o, m)$ is the joint probability of σ_o and m, while $P_s(\sigma|\sigma_o, m)$ is the probability of success give the stress state and the material properties (σ_o, m) (in other words equation (3.9)). Determining the probability distribution for σ_o and m is another problem. Given an experimental data set it can be calculated numerically, but the quantities σ_o and m are only reported with some confidence intervals and usually

the entire data set used to find them is not given. Therefore we make the simplifying assumption that the two are independent and follow a Gaussian distribution:

$$P(\sigma_o, m) = P(\sigma_o)P(m) \tag{3.15}$$

$$P(\sigma_o) = \frac{1}{2s_{\sigma_o}\sqrt{2\pi}} \exp\left[-\frac{(\sigma_o - \mu_{\sigma_o})^2}{2s_{\sigma_o}^2}\right] \tag{3.16}$$

$$P(m) = \frac{1}{2s_m\sqrt{2\pi}} \exp\left[-\frac{(m - \mu_m)^2}{2s_m^2}\right] \tag{3.17}$$

Where s is the standard deviation and μ is the mean. This assumption should lead to a conservative estimate of the actual probability of survival because the worst case is at low values of both σ_o and m. Recall that these are found by fitting test data to equation (3.8) or (3.9) and therefore in reality a low value of σ_o will be associated with a high value of m for the same set of experimental data. For μ we take the reported best fit value of σ_o or m and for s we fit the Gaussian distribution to the reported confidence interval.

Equation (3.14) is the result of the second approach to incorporating uncertainties in material properties. It will be referred to simply as the "probabilistic" approach later.

For material properties we use values measured and reported by Klein [68]; based on this author's discussions with vendors, these properties are neither measured nor reported by most manufacturers. Klein's measurements produced: $\sigma_o = 117.6 \pm 20$ MPa, $m = 9.89 \pm 1.42$, where the bounds are at the 95% confidence level. These measurements are based on the area technique (equation (3.9)), with a reference area of 1 cm^2.

The 95% confidence interval values reported can be used to find s using the properties of a Gaussian distribution: $s = U_{95\%}/1.96$. Using these data and information about the stress state within the tube, the probability of survival of the tube can be computed with both the traditional and probabilistic approaches. For the case under consideration here, the stress state is generated by the internal pressure and any thermal strains.

Thermal and Mechanical Analysis

We begin with the stresses generated by thermal strains. We first assume that the thermal strains are small enough that they do not significantly deform the structure and hence the thermal problem will be decoupled from the mechanical one. In other words, we can solve the heat conduction by itself and then use the computed temperature field to determine the stresses introduced. This is in contrast to a coupled problem where the two must be solved simultaneously.

In this case due to symmetry we wish to solve the transient heat conduction equation in the radial direction alone:

$$\frac{\partial T}{\partial t} = \alpha \left[\frac{1}{r} \frac{\partial T}{\partial r} + \frac{\partial^2 T}{\partial r^2} \right] \tag{3.18}$$

We assume a uniform initial temperature field and convective boundary conditions at the inside surface and an insulated outside surface. The solution can be found via separation of variables:

$$\begin{aligned}
\Theta &= \frac{T - T_i}{T_i}, \quad \rho = r/r_o, \quad \tau = \frac{\alpha t}{r_o^2} \\
\Theta &= \sum_n^\infty \Theta_n \\
\Theta_n &= A_n e^{-\lambda_n^2 \tau} \left[Y_o(\lambda_n \rho) J_1(\lambda_n) - Y_1(\lambda_n) J_o(\lambda_n \rho) \right] \\
A_n &= \Theta(t=0) \frac{\int_{r_i/r_o}^1 \rho \left[Y_o(\lambda_n \rho) J_1(\lambda_n) - Y_1(\lambda_n) J_o(\lambda_n \rho) \right] d\rho}{\int_{r_i/r_o}^1 \rho \left[Y_o(\lambda_n \rho) J_1(\lambda_n) - Y_1(\lambda_n) J_o(\lambda_n \rho) \right]^2 d\rho}
\end{aligned} \tag{3.19}$$

Where T_i is the fluid temperature inside the tube, r_i and r_o are the inside and outside radii, α is the thermal diffusivity, and J_k and Y_k are Bessel functions of order k and of the first and second kind, respectively. The values of λ_n are the eigenvalues and are found by solving the characteristic equation

$$\begin{aligned}
&Bi \left[Y_o \left(\lambda_n \frac{r_i}{r_o} \right) J_1(\lambda_n) - Y_1(\lambda_n) J_o \left(\lambda_n \frac{r_i}{r_o} \right) \right] \\
&= \rho \left[-Y_1 \left(\lambda_n \frac{r_i}{r_o} \right) J_1(\lambda_n) + Y_1(\lambda_n) J_1 \left(\lambda_n r \frac{r_i}{r_o} \right) \right]
\end{aligned} \tag{3.20}$$

where Bi is the Biot number, hr_o/k. In order to complete the solution, a suitable value for the heat transfer coefficient at the inside surface is needed. Unfortunately though the nature of this heat transfer process is not generally known. Previous researchers assumed could be approximated using correlations for natural convection in the form $Nu = c(Ra)^n$, which produce values here on the order of $h = 500\ W/(m^2K)$. However it will be shown later that if boiling is occurring on the quartz tube wall the rate of heat transfer can be much higher. Therefore to be conservative we use a value of 10,000 $W/(m^2K)$. With h, we can now solve for $\Theta(\rho, \tau)$ and find the temperature profile as a function of space and time.

Temperatures for thermoelasticity problems such as this one are referenced to a stress-free temperature, taken here to be room temperature (ie $\Delta T = T - 25°C$). The basic thermoelastic equations for a thick-walled cylinder are [69]:

$$\begin{aligned} \sigma_r &= C_1 + \frac{C_2}{r^2} - \frac{\alpha E}{(1-\nu)r^2}\int_{r_i}^{r} \Delta T r dr \\ \sigma_\theta &= C_1 - \frac{C_2}{r^2} - \frac{\alpha E \Delta T}{(1-\nu)} + \frac{\alpha E}{(1-\nu)r^2}\int_{r_i}^{r} \Delta T r dr \end{aligned} \tag{3.21}$$

where μ is Poisson's ratio, E is the Young's modulus, α is the coefficient of thermal expansion, and C_1 and C_2 are constants of integration that are found from the boundary conditions ($\sigma_r(r = r_i) = -P_i$ and $\sigma_r(r = r_o) = 0$) to give

$$\begin{aligned} C_1 &= -P_i - C_2/r_i^2 \\ C_2 &= \frac{-r_o^2 r_i^2}{r_o^2 - r_i^2}\left(P_i + \frac{\alpha E}{(1-\mu)r_o^2}\int_{r_i}^{r_o} r\Delta T dr\right) \end{aligned} \tag{3.22}$$

These relations can now be used to find the stresses as a function of space and time, given the temperature profile. The stresses can then be used to find the probability of survival of the tube using equation (3.9) or (3.8).

We first examine some intermediate results from equation (3.21) to see how the material behaves with the internal pressure and thermal loading. For this example, we choose a wall thickness of 3.2 mm. Given the linearity of the problem, we can easily separate the internal stresses generated by the temperature profile and the internal

pressure. This allows a better understanding of the design drivers. The temperature profiles, thermal stresses, and mechanical stresses are shown in figures 3.10 through 3.12, respectively.

The temperature profiles in figure 3.10 begin at time $t = 0$ with a uniform temperature of 298 K. As time advances, convective cooling at the inside surface quickly drops the temperature there and heat diffusion slowly drops the temperature throughout the rest of the tube. At the final time, the entire tube is at the fluid temperature of 250 K.

The thermal stress profiles are less clear. At $t = 0$, the entire tube is at the stress-free temperature and hence there are no thermal stresses. As time goes on and the inside surface cools, this region of the material shrinks and tensile stresses are generated. To counteract these tensile stresses on the inside and maintain equilibrium, compressive stresses are generated on the outside of the tube. As time advances further and the temperature profile becomes more uniform these tensile stresses at the inside surface decrease and with them the compressive stresses at the outside also decrease. While difficult to see in figure 3.11, the steady state solution does leave some thermal stresses throughout the tube on the order of 1 kPa.

This behavior can be explained via the terms in equation (3.21). At early times at the inside surface, the $\alpha E \Delta T$ term is large at the inside surface and since $\Delta T < 0$, this drives $\sigma_\theta > 0$. At the outside surface however this term is small and instead the integral term dominates and drives $\sigma_\theta < 0$. At later times, ΔT becomes approaches a constant value throughout the tube wall and the integral term balances the $\alpha E \Delta T$ term, decreasing the thermal stresses.

A fortunate conclusion from these plots is that by far the highest thermal and mechanical stresses are at the inside surface. This means that the area method of calculating the probability of survival (equation (3.9)) can be easily used on this surface without concern for the stresses throughout the rest of the material. A secondary argument for this is seen by the large value of m (9.89), which means that stresses that are appreciably lower than σ_{max} will have little effect on the overall survivability.

Repeating this process over a range of wall thicknesses, we can determine the maximum thermal stress at the inside surface as a function of wall thickness. This

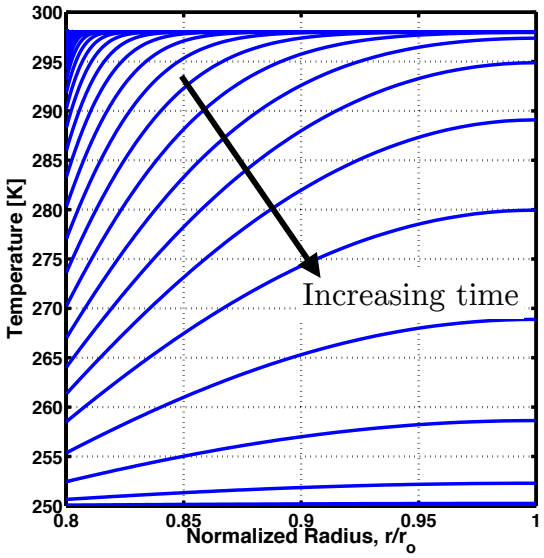

Figure 3.10: Temperature profiles. Each curve shows the profile at a different time.

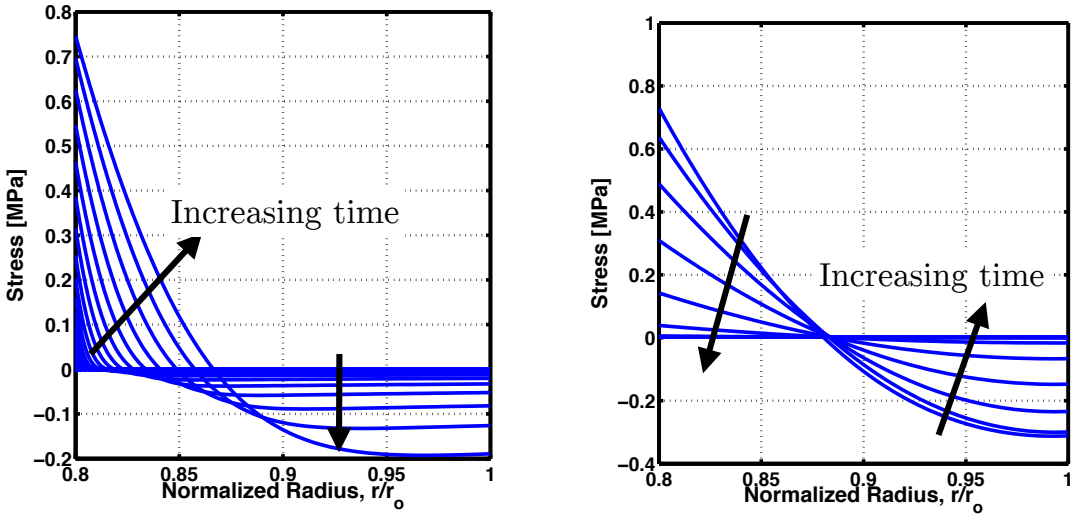

(a) Early times.

(b) Later times.

Figure 3.11: Thermal stresses. Each curve shows the profile at a different time.

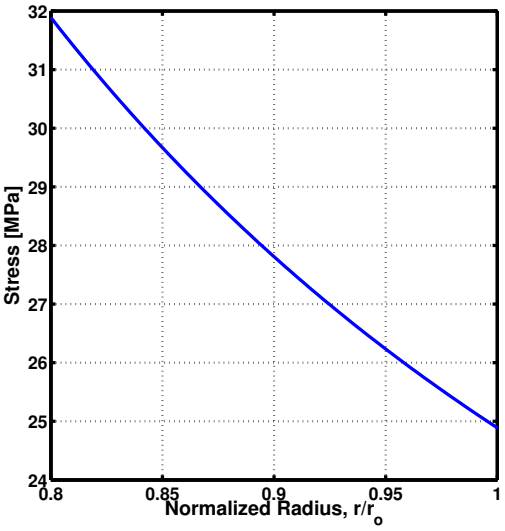

Figure 3.12: Mechanical stresses.

was done over the range of 1.3 to 13 mm, and the results were fitted to produce the following relation:

$$\sigma_{\theta,thermal,max} = -0.01998(r_o)^{-4.169} + 1.391 \cdot 10^6 \tag{3.23}$$

where the units of σ are Pa those for r are m. The uncertainty in the fit was 4.2 kPa at the 95% confidence level. Its clear from this fit that the thermal stresses appear to asymptote to a value of 1.391 MPa, a relatively small but significant value when compared with the internal pressure of the tube (7 MPa). Note that with other materials the thermal stresses can be much larger. For example, this type of analysis was performed for a sapphire test case and the thermal stresses were greater than 10 MPa.

This simple fit will be used to determine the thermal stresses as a function of the wall thickness in computing the overall probability of survival of the tube. To be conservative the fit uncertainty will be added to the computed thermal stress.

Now, we focus on the mechanical stresses at the inside surface. Equations (3.21), when the thermal terms are removed, produce the equations describing a thick-walled

pressure vessel:

$$\begin{aligned}\sigma_r(r) &= P_i \frac{r_i^2(r^2 - r_o^2)}{r^2(r_o^2 - r_i^2)} \\ \sigma_\theta(r) &= P_i \frac{r_i^2(r^2 + r_o^2)}{r^2(r_o^2 - r_i^2)}\end{aligned} \tag{3.24}$$

The stress is maximum at the inside surface and is

$$\sigma_\theta(r = r_i) = P_i \frac{r_i^2 + r_o^2}{r_o^2 - r_i^2} \tag{3.25}$$

The net maximum stress at the inside surface is a combination of the thermal and mechanical stresses:

$$\sigma_{\theta,max} = P_i \frac{r_i^2 + r_o^2}{r_o^2 - r_i^2} - \left[0.01998 Pa\ m^{4.169}\right](r_o)^{-4.169} + [1.395\ MPa] \tag{3.26}$$

We will use this value in the computation of the probability of survival in equation (3.9). For the stressed area (A), we will use the inside area of the tube (851.3 cm^2) and the reference area (A_o) is 1 cm^2, as that is the value used by Klein in calculating the values of σ_o and m. Given the geometry of the system we can conveniently assume that the entire area is stressed uniformly.

Probabilistic Failure Analysis Results

The results are shown in figure 3.13, in the form of the probability of failure $P_f = (1 - P_s)$. This metric was used because it shows more clearly the variation in the predictions of the different methods. Four lines are plotted: the result of equation (3.9) including only the mechanical stresses, the same equation with both the thermal and mechanical stresses, and then the modified probability of survival, with two different methods for capturing the uncertainty in the material properties. The traditional approach uses equation (3.11) and (3.13), while the probabilistic approach uses equation (3.14). Both of these last two include mechanical and thermal stresses.

Including the thermal stresses increases the probability of failure by roughly a factor of ten. Including the effect of uncertainty in material parameters adds another

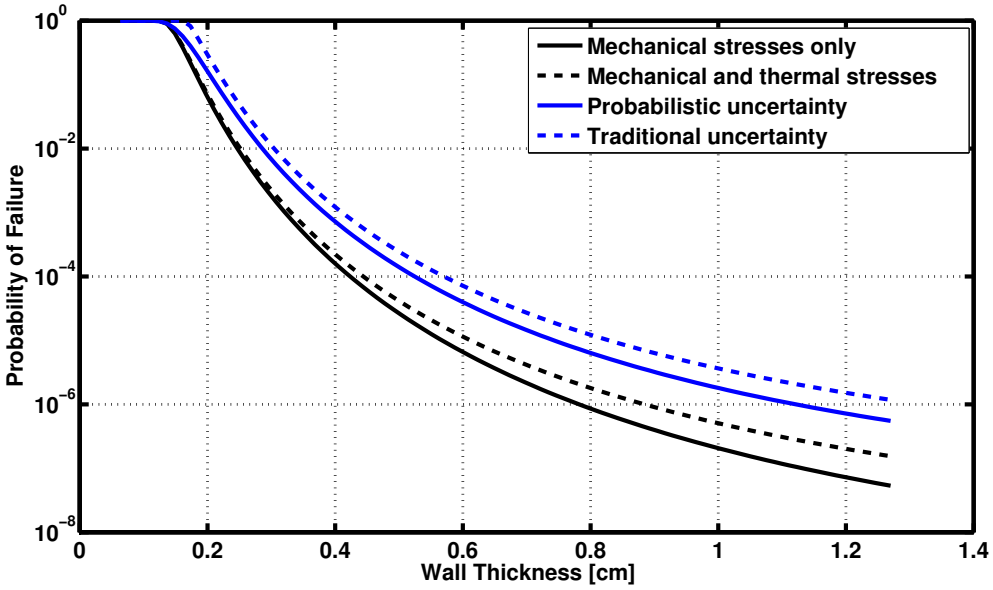

Figure 3.13: Probability of failure. Results are shown for four cases: 1 - only the stresses caused by the internal pressure are included, 2 - the thermal stresses are included with those from internal pressure, 3 - both mechanical and thermal stresses with probabilistic model of parameter uncertainty, 4 - both mechanical and thermal stresses with traditional model of parameter uncertainty.

order of magnitude according to the traditional model, while the probabilistic model adds significantly more. The reason that the probabilistic predicts such higher failure probabilities is that by integrating over the entire (assumed) distribution for σ_o and m, it captures extremely rare situations where the two are both very low. The traditional approach does not capture this effect because it is giving us the upper bound on the 95% confidence interval on P_f.

Crack Growth Rate Analysis

A second concern with brittle materials is crack growth over time. All materials contain imperfections, but with a brittle materials the growth rate of these imperfections with time is a potential failure mode. This is sometimes referred to as a static fatigue failure.

A common model for the crack growth rate is

$$v = A\left(\frac{K_I}{K_{IC}}\right)^n \tag{3.27}$$

Where v is the crack growth velocity, A and n are constants related to the growth rate, and K_I is the stress intensity and K_{IC} is the critical stress intensity or simply the fracture toughness. The stress intensity is defined as $Y\sigma\sqrt{a}$, where Y is a shape factor that is usually between 1.1 and 1.3, σ is the nominal stress in the material, and a is the flaw or crack size. Under a constant stress, the crack grows at an increasing rate until K_I reaches K_{IC}, at which point the part fails. We are dealing in this case with type I or "opening mode" cracks and this is why there is a subscript I on K. Other types of cracks include sliding or tearing, but these are not encountered in this situation and hence will not be studied.

To determine the time to failure, we must integrate equation (3.27) from the initial flaw size to the size at the critical stress intensity:

$$\begin{aligned} dt &= \frac{da}{v} \\ t_{fail} &= \int_{a_o}^{a_{IC}} \frac{da}{v} \end{aligned} \tag{3.28}$$

To integrate, we need to rearrange this equation:

$$\begin{aligned} K_I &= Y\sigma\sqrt{a} \\ dK_I &= Y\sigma\frac{1}{2\sqrt{a}}da \\ t_{fail} &= \int_{K_{Io}}^{K_{IC}} \frac{2\sqrt{a}}{Y\sigma}\frac{dK_I}{v} \\ &= \frac{2}{\sigma^2 Y^2}\int_{K_{Io}}^{K_{IC}} \frac{K_I}{v}dK_I \end{aligned} \tag{3.29}$$

This equation can now be integrated upon substitution of equation (3.27) for v. The result is

$$t_{fail} = \frac{2K_{Io}^2}{\sigma^2 A Y^2(2-n)}\left[\left(\frac{K_{IC}}{K_{Io}}\right)^2 - \left(\frac{K_{IC}}{K_{Io}}\right)^n\right] \tag{3.30}$$

Using the stress computed in equation (3.26), we can now compute the predicted time to failure given an initial flaw size and as a function of wall thickness. For the parameters needed, we use the values measured by Armstrong: $A = 0.2019\ m/s$, $n = 25$, $K_{IC} = 0.75\ MPa\sqrt{m}$, $Y = 1.16$. The results are shown in figure 3.14 for initial crack sizes ranging from 1 μm to 100 μm.

From this plot, it is clear that an initial flaw size on the order of 10 μm is entirely acceptable for any practical wall thickness. The vendor of the quartz tube stated that the surface finish would produce surface flaws less than this value, so as a result crack growth is not a concern with this system.

A wall thickness of 6.35 mm was selected to give a good compromise on failure probability and cost.

3.3.1 End Plug Design

Other than the quartz tube itself, the other principal components of this system are the end plugs that mate and seal with the tube. The primary goals for these were:

1. Seal with the tube on the inside surface so that the entire length of the tube will be accessible for imaging

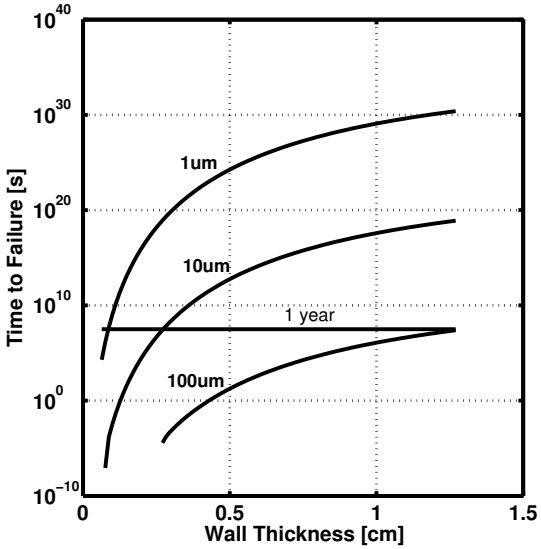

Figure 3.14: Time to failure. Lines are shown for three different initial flaw sizes $(1, 10, 100\mu m)$. A horizontal line showing 1 year of operation is also shown for reference.

2. Prevent any metal from contacting the quartz tube and producing stress concentrations that could lead to fracturing of the quartz

3. Allow for inclusion of thermocouple probes within the tube

4. Allow for pressure measurements inside the tube

5. Minimize other volumes not visible from the camera

6. Allow for heat transfer fluid to be circulated within the end plugs (not in contact with the CO_2 or N2O) and establish temperature control

The design process here did not follow a well-laid path as it did with the quartz tube and there were fewer simple trade studies that could be performed. Therefore only the final design will be presented.

Sealing with the quartz tube is done via two O-rings along the inside diameter. The glands are custom, but use standard O-ring sizes. Custom glands were used to increase the clearance between the quartz and the aluminum to help prevent any

contact that could cause stress concentrations. The second O-ring is important not only as a back up seal, but also as a way to keep the quartz tube concentric with the plug surface and prevent any metal from contacting the quartz. The two O-rings have different widths as a result of the presence of the holes in the end plugs for the thermocouple probes. An expanded PTFE cushion is used to protect the end of the quartz tube from the aluminum surface.

One initial concern with the O ring seals was the expansion of the quartz tube when pressurized. If it expanded too much, the seals could fail. A simple analysis is possible using the stresses reported earlier in equation (3.21), combined with the thermoelastic stress-strain relations for plane strain:

$$\varepsilon_r = \frac{1-\nu^2}{E}\left(\sigma_r - \frac{\nu}{1-\nu}\sigma_\theta\right) + (1+\nu)\alpha\Delta T - \nu\varepsilon_o \tag{3.31}$$

Where ε is the strain and ε_o is the longitudinal strain, taken to be constant in order to use the plane strain formulation. Here it will be taken as 0 since the loads on the end of the tube are minimal. This equation can be evaluated at r_i to determine the expansion of the inside diameter of the tube and hence the effect on the O ring seal. The result is that the maximum value of ε_r at r_i is $1.71 \cdot 10^{-4}$, meaning that the gap at the seal will widen by 2.2 μm, an insignificant amount. The thermoelastic component of this strain is also only about 10% so different temperatures will not significantly alter the expansion of the gap.

The two end plugs are connected via four $1/4-20$ stainless steel tie rods. These are tightened to 1.1 Nm. This value was chosen in order to establish a compressive force on the quartz tube when it is unpressurized that would match the force generated by the internal pressure when it is pressurized. Initially, these tie rods were only finger-tight with the expectation that once the system was pressurized they would be in tension and therefore tightening them beforehand served little purpose. However, during initial testing two quartz tubes developed small cracks near where the end plug protrudes into the quartz tube.

This was possibly caused by uneven finger tightening of the tie rods leading to an out-of-plane torque being applied to the end plug once it was pressurized and

therefore contacting the quartz tube. Using a torque wrench to establish a uniform initial tension in the tie rods was conceived of as a way to counteract this problem and no tubes cracked once this was implemented.

In order to prevent any torques perpendicular to the tube's longitudinal axis from being applied to the end plugs, the top plug is left "floating" and is supported only by the quartz tube itself. This was initially of some concern because the valves and fittings connected to the top plug weigh approximately 10 kg and it seemed imaginable that this force on the quartz tube could cause damage. However, when the tube is pressurized the upwards force on the top plug is approximately $3,000$ N, and so this downwards force is quite small in comparison. However, this was another reason to keep the tie rods torqued when the system is unpressurized - tension in the tie rods helps keep the top plug straight, even with a downward load on it that is not aligned with the tube centerline.

The end plugs each contain four ports for thermocouples and/or pressure sense tubes. They have a diameter of 1.613 mm and are each angled at 13.5° relative to the tube centerline in order to allow space for the fittings on the back side of the end plug.

The thermocouple probes have exposed junctions and are sheathed in 1/16 in (1.588 mm) diameter stainless steel tubing. This tubing is convenient because it can be used with ferrule tube fittings (eg Swagelok) to form pressure-tight seals. This was done with adapter fittings that thread into the end plug and form an O-ring seal.

3.3.2 Summary of Quartz Tube System Design

In this section the final quartz tube system design will be summarized. The pressure vessel is a custom manufactured thick walled quartz tube from Wilmad Labglass, shown in figure 3.17. It has in internal diameter of 25.4 mm, a length of 387.4 mm, and an external diameter of 38.1 mm. On either end identical aluminum plugs seal along the inside diameter of the tube, restricting the internal open length of the tube to 356.9 mm and a nominal volume of 0.1808 L (when the exit and entrance tubing volumes are included it grows to 0.1845 L). These aluminum plugs contain a

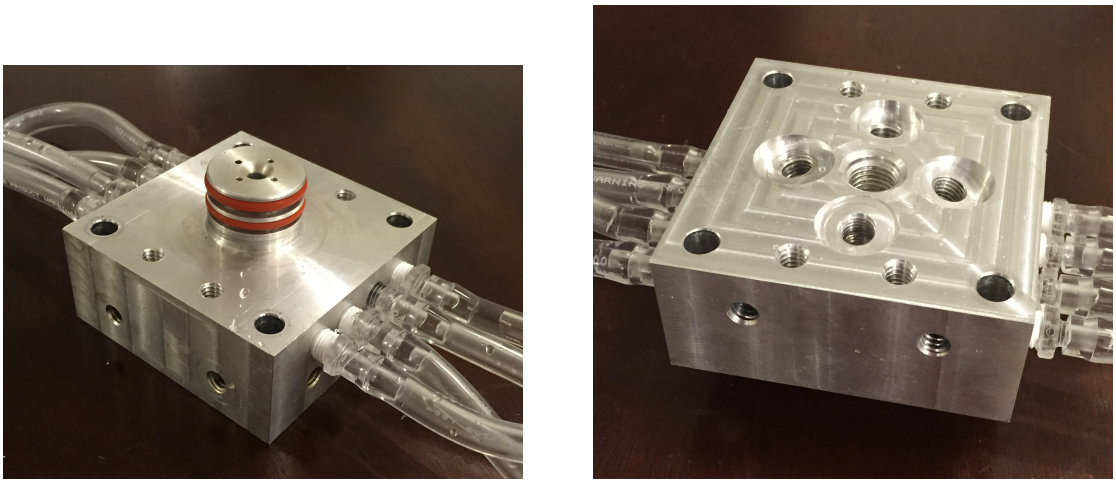

Figure 3.15: Images of the top and bottom of the end plug. Visible are the plastic tube fittings and hose used to circulate the heat transfer fluid within the end plug.

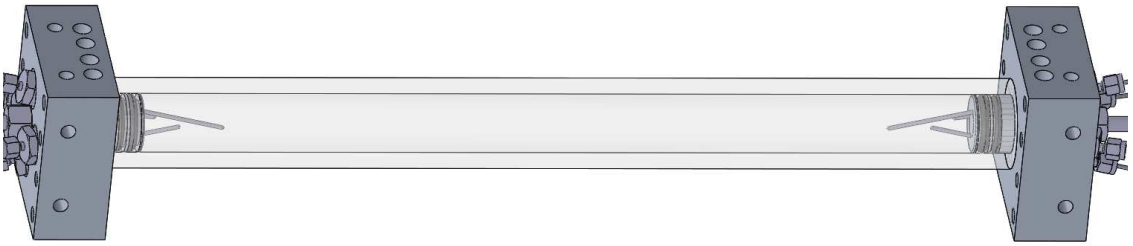

Figure 3.16: CAD model of the quartz tube with end caps. Also visible are the thermocouple probes protruding from one end cap into the tube.

central port with a rounded opening for fluid flow and four additional ports to allow thermocouple probes to be inserted into the interior of the tank. One of these four ports was left open and used as a sense tube for a pressure transducer. Passages were also drilled through the base of the aluminum plugs to allow for the flow of a heat transfer fluid, thereby heating or cooling the piece and enabling another method of temperature control. The six thermocouple probes in the vessel are spaced more closely near the top and bottom of the tank to get higher resolution in the regions where there might be higher temperature gradients. Tie rods connect the top and bottom end plugs. A still image from one of the tests is shown in figure 3.18 with relevant features identified.

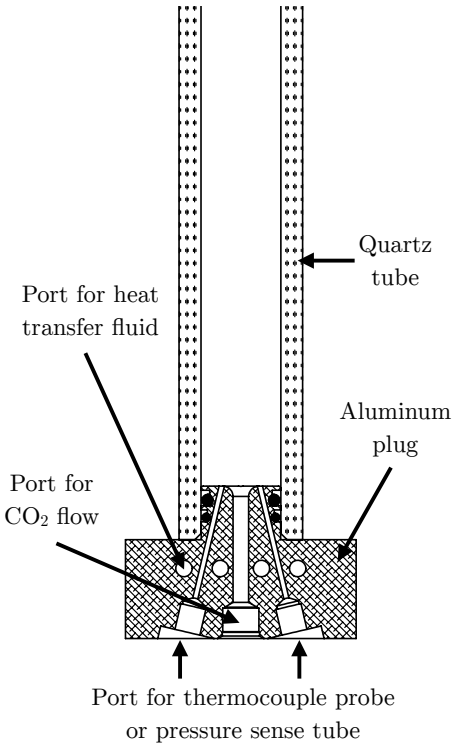

Figure 3.17: Drawing of longitudinal section of quartz tube apparatus. Only the bottom half is shown as the top is identical. Not shown in this diagram are the tie rods that connect the top and bottom plugs as well as thermocouple probes and sense tubes. Also not shown are the various fittings used to connect tubing, thermocouple probes, and pressure transducer sense tubes to the vessel.

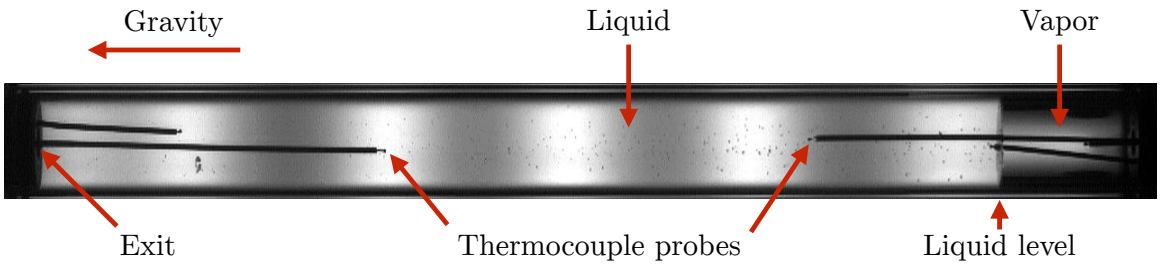

Figure 3.18: Annotated still image from high speed video of quartz tube apparatus. Image has been rotated 90° from its original appearance such that gravity acts to the left.

3.4 Flat Glass Gauge

The flat glass gauge is an off-the-shelf component purchased from Pentair Penberthy (model 2TLC8), and is marketed as a visual liquid level gauge for pressurized tanks. It is made from a 316 stainless steel pipe with borosilicate glass windows on two opposite sides running nearly the full length of the gauge as shown in figure 3.21. Its internal cross section is not circular due to the slots cut for the windows however the average cross sectional area is 1,103 mm^2 giving an equivalent circular diameter of 49.0 mm. This area also varies with length because the window slots are not continuous. The nominal internal volume is 1.233 L, and 1.239 L when the entrance and exit tubing are accounted for.

The wall thickness varies but is approximately 12 mm, the internal length is 641 mm, and the vessel is rated by the manufacturer to 10.9 MPa at room temperature. The end connections are 1 in NPT and two custom plugs were manufactured to each allow the inclusion of five thermocouple probes and one pressure sense tube within the tank. The ten thermocouple probes are equally spaced within the tank while the sense tubes protrude only 6 mm. A still image from one of the tests is shown in figure 3.22 with relevant features identified.

The flat glass gauge will only be used briefly in this work for three primary reasons. First, the reduced window area makes visualization more difficult than in the quartz tube. Second, the increased size results in a lowered physical resolution in terms of the effective size of each pixel in the video data, making small features less identifiable. Third, the large thermal mass and high thermal diffusivity of the stainless steel when compared to the quartz makes temperature control nearly impossible. Therefore, the majority of this work will discuss results with the quartz tube.

Figure 3.19: Image of the flat glass gauge. Also visible is the aluminum adapter mount and the steel strut stand.

Figure 3.20: Image of the two pipe plugs used to allow for instrumentation access within the flat glass gauge. The blue connectors are for the thermocouples, and the small tube with a right angle bend in it is the pressure transducer sense tube.

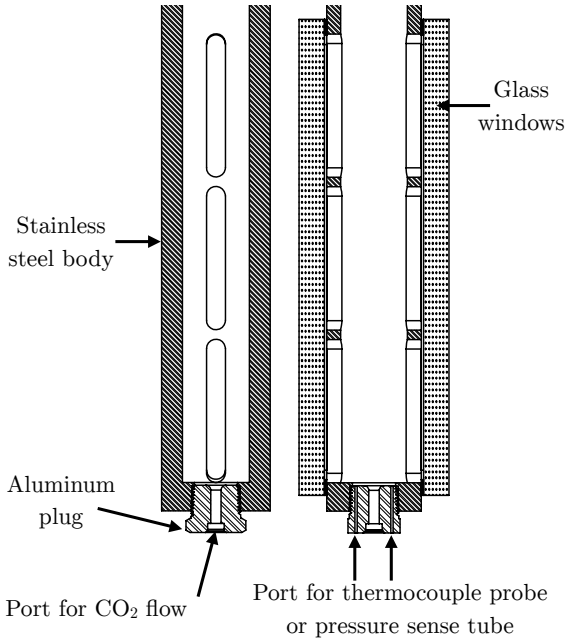

Figure 3.21: Drawings of longitudinal sections of flat glass gauge apparatus. Only the bottom half of the vessel is shown as the top is identical. The two sections are 90°apart. Not shown in this diagram are the retaining plates that hold the windows onto the vessel, the fitting at the exit of the aluminum plug, thermocouple probes, and pressure transducer sense tube.

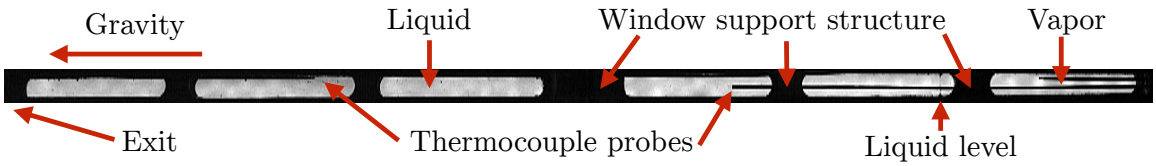

Figure 3.22: Annotated still image from high speed video of flat glass gauge apparatus. Image has been rotated 90° from its original appearance such that gravity acts to the left.

3.5 Common Components of Flat Glass Gauge and Quartz Tube Systems

The flat glass gauge and quartz tube systems were developed in parallel and share many common components. To increase operational simplicity the video, data acquisition, control, and feed systems are all nearly identical for both systems and these common features will be discussed here.

Data acquisition: All temperature measurements were made with exposed junction T type thermocouples from Omega Engineering, Inc. (TMQSS-062E) and a Measurement Computing USB-2416 data acquisition board, with a net uncertainty of approximately $\pm 0.9\ ^{\circ}C$. This uncertainty combines the thermocouple accuracy and accuracy of the data acquisition board but does not include effects related to conduction errors or thermal inertia (time response). Pressure measurements were made with Measurement Specialties MSP-600 series pressure transducers and a National Instruments USB-6210 data acquisition board, with a net uncertainty of approximately 45 kPa. Sample rates for both boards were identical, at 90 Hz for the flat glass gauge and 170 Hz for the quartz tube systems. The low sample rate was a limitation of the thermocouple data acquisition board, however previous experimental work with higher sample frequencies did not reveal any behavior of interest at higher frequencies and thus this low sample rate is acceptable for this work. Two pressure transducers are connected to the test vessel, one at the top and one at the bottom, via 1.6 mm diameter sense tubes roughly 10 cm long. Signal distortion caused by the sense tubes was checked for by replacing one sense tube with 3.2 mm tubing and comparing the

Orifice Diameter	0.201	0.279	0.406	0.559	0.813	1.092	1.321	1.524	0.787	2.260	3.048
Orifice Length	0.407	0.430	0.467	0.515	0.584	0.664	0.730	0.789	0.786	1.212	1.439
Exit Diameter	2.301	2.301	2.301	2.301	2.301	2.301	2.301	2.301	4.803	4.803	4.803
Orifice L/D	2.025	1.541	1.150	0.921	0.718	0.608	0.553	0.518	0.999	0.536	0.472

Table 3.4: Orifice dimensions. All dimensions in mm.

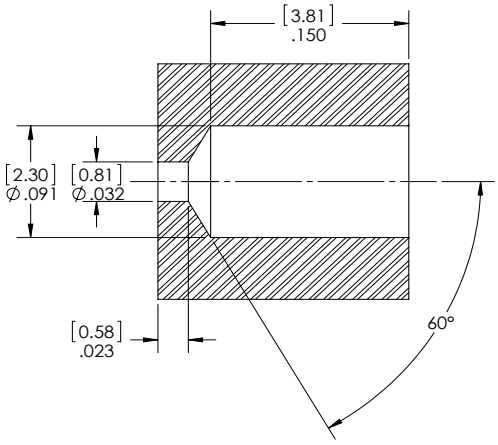

Figure 3.23: Sample of orifice dimensions. Dimensions in inches, with bracketed dimensions in mm. Flow is from left to right.

Figure 3.24: Picture of some of the orifices used in this work. The upstream side is facing the camera.

readings from the two transducers. The pressure transducers were also heated to prevent condensation and flashing of fluid on the diaphragm. See the appendix for more details.

Visualization: An IDT Motion Pro X3 Plus was used for high speed imaging, at frame rates of 50-2500 Hz. Most tests used a 50mm Nikon lens with f/1,2, f/2.0, or f/2.8 while some used a 105mm Nikon lens with f/2.8. The video data are used to determine the initial liquid fill level. The camera is triggered using a digital signal from one of the data acquisition boards. Illumination is provided by back lights constructed using high power white LEDs (CREE XML-T6) mounted on an aluminum base. Regulated switching power supplies are used to power the back lights, as commercial constant-current LED drivers were found to cause flickering that became visible at high frame rates.

Orifices: Many hybrid rockets using liquid N_2O effectively contain a choked orifice as the injector because the chamber pressure is significantly below the tank pressure. The choking effect (also commonly referred to as critical flow in multiphase flow literature) makes the mass flow rate insensitive to the downstream pressure, and so a tank being drained through a choked orifice directly to the atmosphere has the same downstream boundary condition as an actual rocket propellant tank. For this work a set of orifices were purchased from O'Keefe Controls ranging in size from 0.201 to 3.048 mm diameter and press fit into stainless steel tubing. An example of the orifice dimensions are shown in figure 3.23 with details for all orifices in table 3.4. The orifices are located immediately downstream of the valve at the bottom of the test vessel and vent directly to the atmosphere.

Feed system: A simplified plumbing and instrumentation diagram is shown in figure 3.25. The CO_2 is fed from the source cylinder into the test vessel using a piston pump (Sterling Pressure Systems, model PTF-400A). Most fluid handling is done with 1/4 in (6.35 mm) and 3/8 in (9.53 mm) stainless steel tubing, and flow control is achieved via pneumatically-actuated full-port ball valves. Two valves control flow into and out of the test vessel, one at the top and one at the bottom. The vessel is filled from the top and drained from the base. Care was taken in the design of the exit flow path in order to minimize pressure drop between the test vessel and the orifice entrance that might cause further flashing. For both vessels, this path begins with a well rounded entrance that constricts to a port bored in the aluminum plugs. This port matches the internal diameter of the tubing to which it connects, and from there the fluid enters a full port ball valve (4.83 mm for the quartz tube system, 7.04 mm for the flat glass gauge). Once it flows through the valve it then immediately encounters the orifice. The total length from the base of the tank to the orifice is 114 mm for both the quartz tube system and the flat glass gauge. This design required filling to be done from the top of the vessel, which is unlike most propellant tanks.

All control for the system is manual. All solenoids operate off of 120V AC, which is controlled via a set of relays. These relays are in turn controlled using a set of manual switches, shown in figure 3.26.

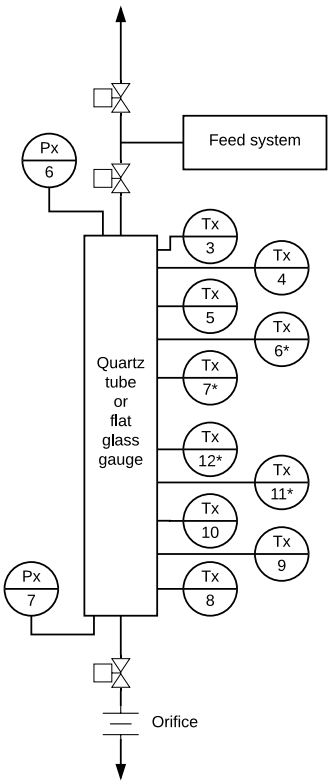

Figure 3.25: Simplified plumbing and instrumentation diagram. Px: pressure transducer. Tx: thermocouple (asterisk indicates presence on flat glass gauge only). In reality the thermocouples enter the system from the top and bottom of the test vessel, but have been illustrated on the side here for clarity.

Figure 3.26: Picture of the control box.

Temperature control: Several different strategies are used for achieving temperature control of the carbon dioxide. One involves heating or cooling the source cylinder by flowing heat transfer fluid through copper tubing wrapped around the cylinder. A second method uses a cross flow heat exchanger (NALCO, model 500-531062.88) placed downstream of the pump. To provide the hot or cold fluid, two recirculating water baths are used (Neslab model RTE-100, VWR model 1140) with a potassium formate solution heat transfer fluid (Dynalene HC-50) for both of these methods. Another simple way of cooling the CO_2 after it has been pumped into the test vessel is to vent from the ullage and cause the liquid to boil, converting heat into the enthalpy of vaporization. Venting vapor in this may is also an effective way of establishing a relatively uniform temperature profile within the tank, however it has a tendency to create a region of colder fluid at the base of the tank. In general it was often difficult to repeatably establish any specific temperature profile within the tank and as a result there is a large variety of temperature profiles presented in this work. However when two tests are compared care was taken to chose tests that had similar temperature profiles.

Procedures: The general procedure for tests is as follows. All valves between the source cylinder and the test vessel are opened and the pump is used to fill the vessel to the desired level. In some cases when low temperature tests were being performed, the pump was not used to avoid the increase in fluid temperature it caused as a result of compression work. In those cases, the source cylinder was heated and the test vessel was periodically vented in short bursts, causing mass transfer due to both pressure differential and condensation. Once the desired temperature profile and fill level have been established, all valves are closed. Then, after the data acquisition system and camera are started the valve at the base of the test vessel is opened and the fluid begins to flow out the bottom of the test vessel through this valve and then out through the orifice to the atmosphere.

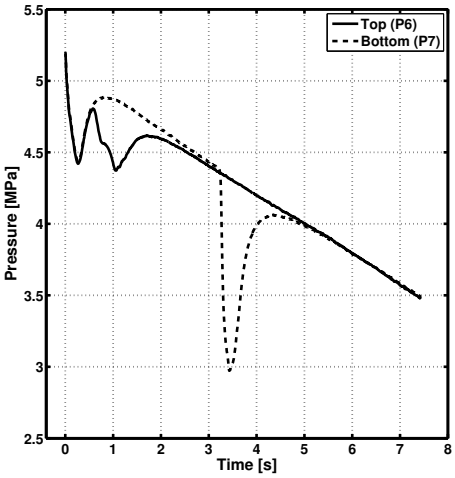

Figure 3.27: Bad pressure transducer data

3.6 Temperature and Pressure Measurements with Saturated Fluids

Temperature and pressure measurements of boiling or condensing fluids can be difficult. The reason for this is that the phase change can release or absorb large amounts of energy and if this occurs near a sensor it can distort the measurement significantly. One problem frequently encountered with pressure transducers in this system and others with saturated fluids is the presence of flashing liquid on the transducer diaphragm, which rapidly cools the front of the diaphragm [70]. The resulting thermal strains are measured by the strain gauge within the transducer and produces spurious pressure measurements (typically pressures lower than actual are reported). An example of this phenomenon is shown in figure 3.27. This is also not specific to one model of pressure transducer, and in this system multiple models from different manufacturers were tested with similar results.

To counteract this phenomenon, several approaches may be used. Long sense tubes (also known as standoff tubes) will help to prevent the flow of flashing liquid from encountering the pressure transducer. Keeping the transducer vertically oriented will help prevent liquid from pooling at the diaphragm, where it may later boil if the

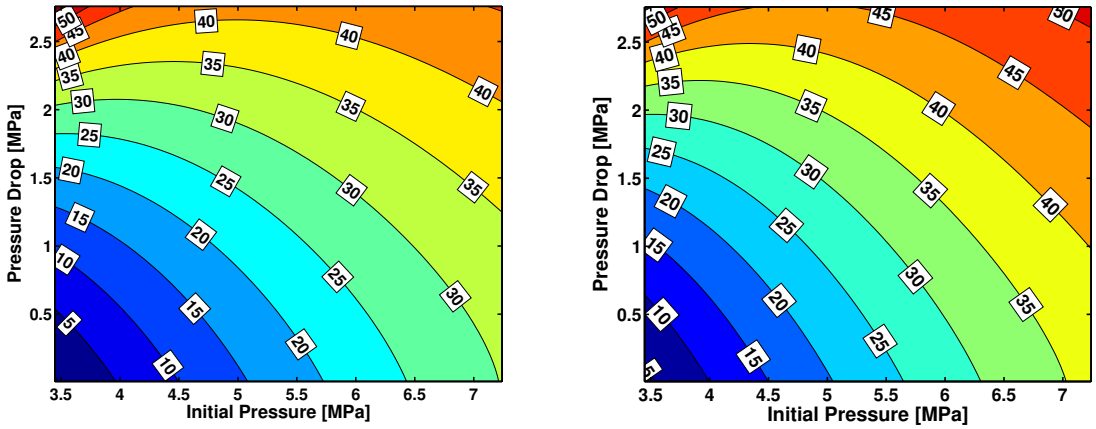

(a) Carbon dioxide.

(b) Nitrous oxide

Figure 3.28: Pressure transducer heating requirements. Plotted are contours of the required initial temperature in °C to ensure that no condensation occurs given an initial pressure and pressure drop. Values shown for carbon dioxide and nitrous oxide.

pressure drops. Thermal insulation of the diaphragm is also possible using grease or similar substances. In this work these countermeasures were all attempted but were found to be insufficient. This was especially problematic during tests at elevated temperatures as hot vapor would condense on the transducer diaphragms because they were removed from the test vessel by $\sim 15\ cm$ via the sense tubes and hence stayed close to ambient temperature.

A new solution to this problem was found by heating the pressure transducers to $\sim 40\ °C$, which is about $10\ °C$ above critical point of the fluid ($31.1\ °C$). By doing so, no fluid could condense on the diaphragm and boil at a later time. The necessary temperature can be found by assuming an isentropic expansion of the superheated vapor from the initial temperature and pressure, and finding the pressure at which the vapor would condense. If that pressure is higher than the minimum pressure that must be measured accurately, then the initial temperature must be increased. In reality the expansion will not be isentropic and heat will be absorbed by the vapor from the surroundings, so this analysis predicts the worst case. The results of this type of analysis are shown in figure 3.28.

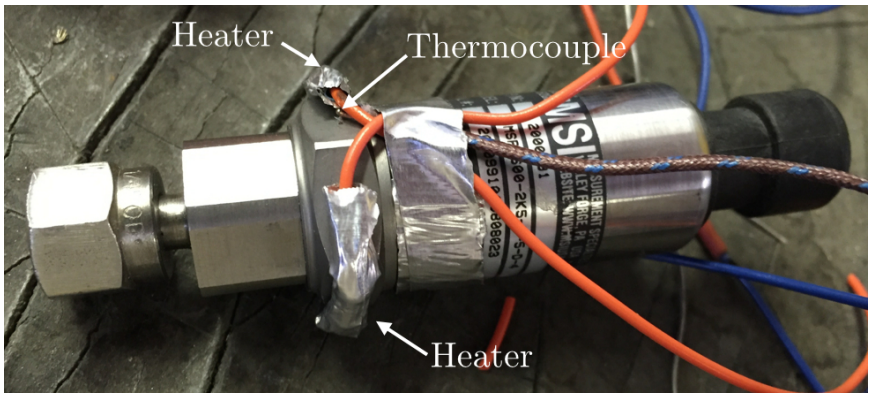

Figure 3.29: Pressure transducer with heaters and thermocouple installed.

The downside to this procedure is that the pressure transducers must be recalibrated at the higher temperature, and care must be taken to ensure that they are at the proper temperature prior to running a test. Heating was accomplished via two small 3 W heaters (ie 100 Ω resistors with a 24 V power supply) placed on the transducer near the diaphragm location. The temperature was measured with a thermocouple on the body of the transducer near the heaters, and the whole assembly was wrapped in insulation. The insulation was then trimmed to establish the desired temperature. An image of the transducer with the heaters and thermocouple installed but prior to being wrapped with insulation is given in figure 3.29.

Temperature measurements present another problem in this system. Within the test vessel, the liquid is often boiling while the vapor is condensing. The thermocouple probes can act as nucleation sites for both of these processes, and as a result the enthalpy of vaporization is absorbed or released into the thermocouple, driving its temperature towards the saturation value. This has been directly measured in the quartz tube system by using the high speed camera focused on a thermocouple probe junction.

While in the condensing vapor, a liquid film on the bead is visible and it reports a temperature close to the saturation value but as soon as the film evaporates the temperature quickly rises. This is shown in figures 3.30 and 3.31. In figure 3.30, the liquid film can be seen evaporating from the thermocouple bead during $t = 27 \rightarrow 31s$, while in figure 3.31 the measured temperature from this thermocouple is plotted along

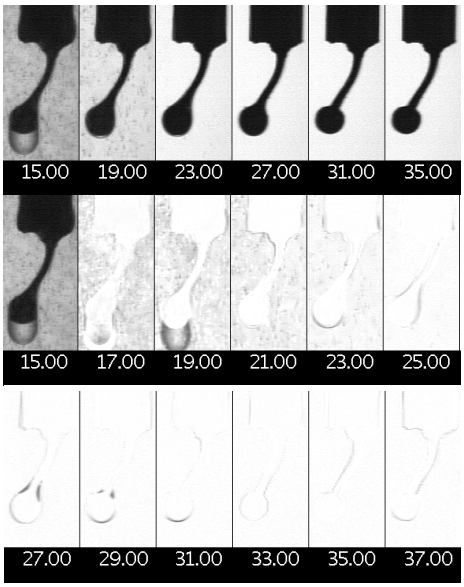

Figure 3.30: Image sequence showing presence and evaporation of film of liquid carbon dioxide on thermocouple bead. The numbers below each frame indicate the time in seconds since start of test. The first row shows the original images, while the second two rows show the change in gray scale pixel intensity between each frame.

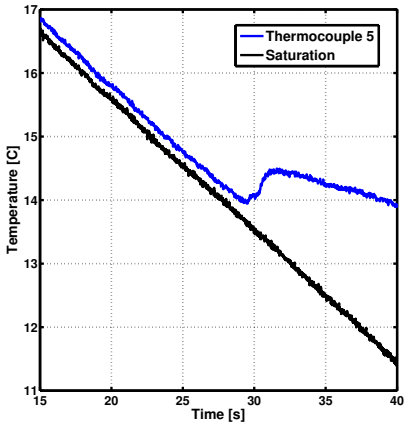

Figure 3.31: Temperature time history, showing measured values from thermocouple 5 as well as the saturation temperature calculated from the pressure.

with the saturation value. Once the film completely evaporates around $t = 30s$, the temperature suddenly increases and departs from the saturation value.

When submerged in liquid carbon dioxide, boiling can be clearly seen on the bead itself, as shown in figure 3.32. A plot corresponding to figure 3.31 cannot be produced in this case because it occurred earlier in the test when there are expected to be rapid changes in the temperature. As a result of this behavior of the thermocouples to effectively read the saturation value, they are primarily used in this thesis to determine the initial temperature profile, rather than the temperature time history during a test.

A second example of this behavior is given in figure 3.33, where the data from the

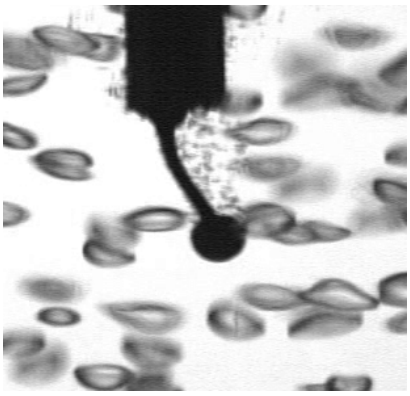

Figure 3.32: Still image showing boiling on thermocouple bead. The large bubbles were nucleated near the base of the tank and have had time to grow significantly by the time they reach this thermocouple, while the smaller bubbles are nucleating directly on the bead.

full array of thermocouples is shown for an entire test, including the time after t_{LRO}. The thermocouples can be seen following the saturation line for varying amounts of time, each departing once its film of liquid CO_2 has fully evaporated. The thermocouples depart from saturation in order of height, with the top thermocouples (# 3 and 4) being the first and the bottom thermocouples (#9 and 8) being the last. The thermocouple data from the polycarbonate system, where the probe was located in the exit tubing just downstream of the tank, closely resembles the data of the lower thermocouples here, suggesting that this behavior was prevalent in that earlier experimental system as well.

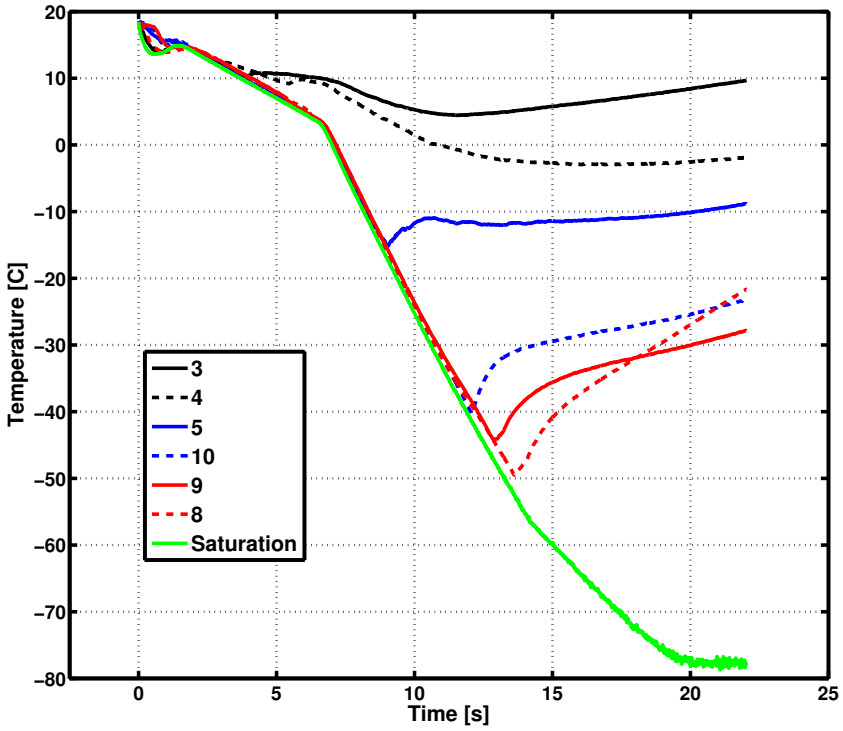

Figure 3.33: Temperature histories from all 6 thermocouple probes during a test, including the time after liquid runout where only gas remains in the tank. The saturation temperature based on the measured pressure is also given.

Chapter 4

Experimental Results

This chapter will present and discuss results of numerous visualization experiments and is divided into four sections. It will begin with a thorough description of a single test using carbon dioxide, and then a series of tests examining the effect of system parameter variations is given. Then, tests comparing the behavior of nitrous oxide and carbon dioxide will be shown. Finally, tests with multiple components are presented.

The high speed videos presented in this chapter are all available for download from the Stanford Propulsion and Space Exploration Research Group website:

http://spase.stanford.edu/Self-Pressurizing_Propellant_Tank_Dynamics_Videos.html

4.1 Basic Behavior

Typical results with the quartz tube system are presented here in order to a) explain basic features seen in the video, temperature, and pressure data, and b) provide a baseline for the later sections showing the effect of parameter variations. "Typical" is taken here to mean: ambient temperature (18.5 $°C$), a fill level of 91%, and an orifice sized to drain the tank in 7.16 s (0.813 mm diameter).

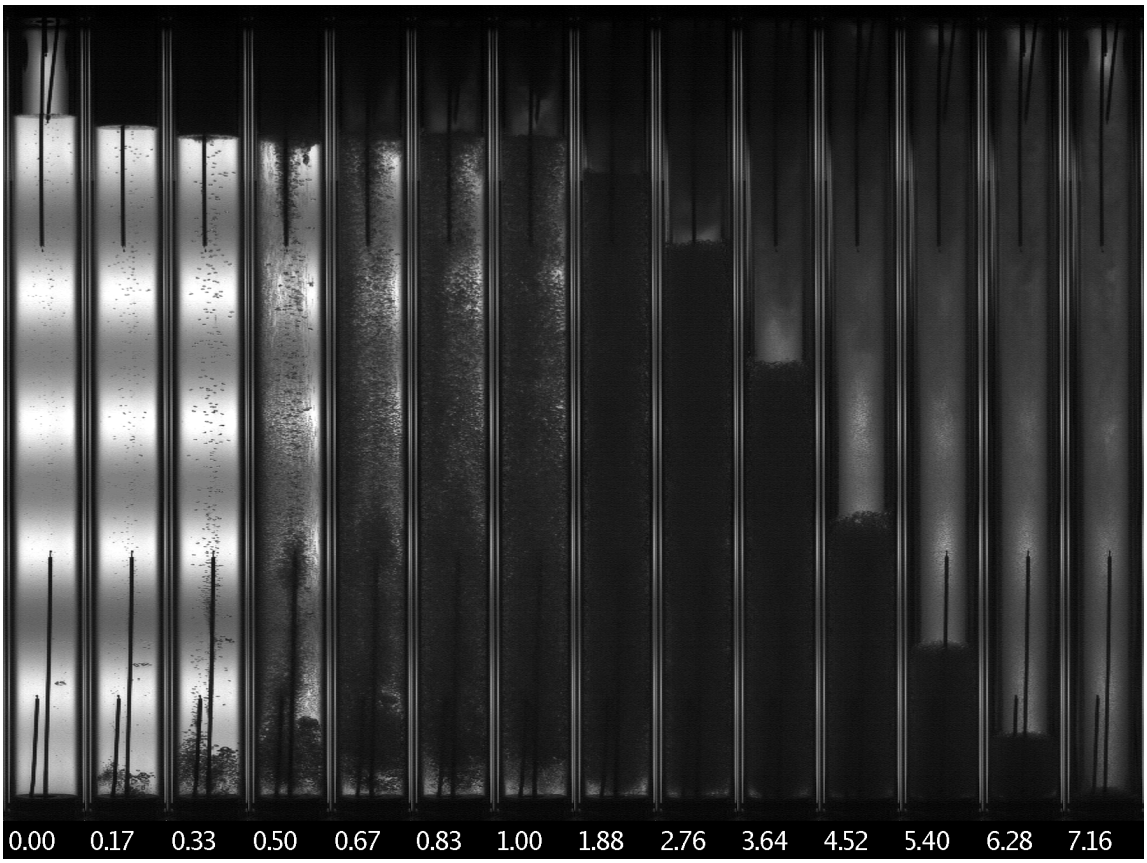

Figure 4.1: Image sequence from high speed video. Numbers below frames indicate time in seconds from start of test. Note that the time step between images is not uniform: the first 7 images are spaced 167 ms apart, while the last 8 images are spaced 880 ms apart. Test performed with CO_2.

4.1.1 Results

An image sequence from the high speed video from this test is shown in figure 4.1 and the pressure and temperature traces are shown in figure 4.2. The non-uniform time spacing of the images in figure 4.1 was done in order to highlight the changing physical timescale of the test - in early times there are rapid changes in temperature, pressure, and the video data while in later times these changes are much slower. Nearly all the image sequences presented in this paper will be broken up in this way.

Examining the high speed video data, the first visible feature is the condensation of the vapor with a rapid transition from clear to opaque happening in less than 167

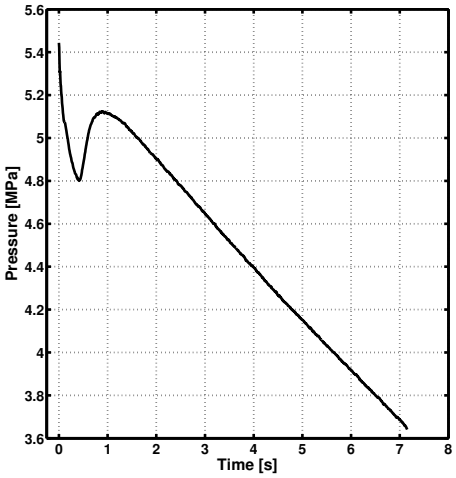

(a) Pressure time history. Only the data from one transducer is shown because there were no discernible differences between the two.

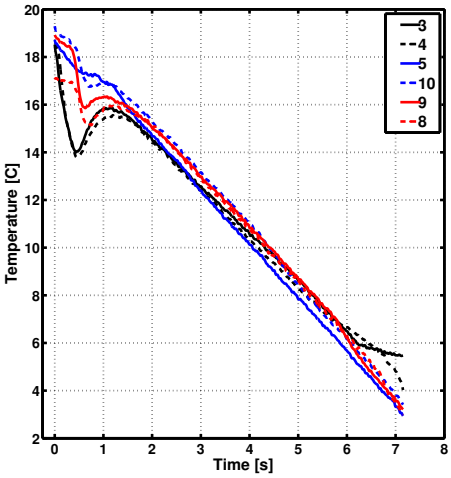

(b) Temperature time history. The thermocouple numbering is shown in figure 3.25.

Figure 4.2: Pressure and temperature histories. Test performed with CO_2.

ms and caused by the formation of droplets in the vapor. These droplets make the ullage appear darkened because they reflect the light from the back light away from the camera. Later, bubble nucleation begins at the base of the tank (see the image at 0.17 *s*) and is followed by nucleation occurring throughout the liquid (0.50, 0.67 *s*). Similar to the droplets, these bubbles also appear dark because they reflect light away from the camera. The initial nucleation at the base of the tank is originating at many points on the surface of the aluminum end plug, and not in the ext flow tubing. Shortly afterwards, the liquid has become densely and uniformly populated with bubbles and appears to be a homogeneous two phase mixture (0.83, 1.00 *s*). Similarly, the condensation in the vapor has caused it to also become a homogeneous mixture. At this point the details become harder to distinguish as the entire tank appears dark, however the general situation remains unchanged for rest of the duration of the test: the liquid and vapor both remain fairly homogeneous mixtures and the liquid level drops as the tank is drained.

Examining the pressure trace in figure 4.2, we can establish connections between

the pressure and features seen in the video. The pressure trace begins with a sharp drop and recovery finishing around a time of 1 s, which corresponds to the time required for the vapor to condense and the liquid to become a homogeneous mixture. Then, the pressure drops in a nearly linear fashion until the tank has been drained of liquid at 7.16 s. This is the time during which the video shows the liquid and vapor maintained as homogeneous mixtures and the liquid level steadily dropping. The portion of the test after all liquid has left the tank is not shown.

Now the temperature data can be examined within the context of both the pressure data and video imagery. The thermocouples within the ullage (3 and 4) show a drop and recovery during the first 1 s similar to that seen in the pressure data, again corresponding to the transient bubble nucleation and condensation processes seen in the video. The thermocouples in the middle of the tank (5 and 10) show very little variation, while those nearest the base of the tank (9 and 8) show a drop and recovery that is similar in character but smaller in magnitude than that seen in the ullage. After this point however all of the thermocouples give nearly identical values that drop in a linear fashion similarly to how the pressure data behave. Unfortunately, due to bubble nucleation in the liquid and vapor condensation in the ullage both occurring on the thermocouple probes, the probe temperature is driven to the saturation temperature, which may be quite different from the bulk liquid or vapor temperatures. This phenomenon is discussed in detail in the appendix, but the key result is that the thermocouple data are likely inaccurate during much of the test and hence they will primarily be used to establish the initial temperature field, not show its evolution with time.

4.1.2 Discussion

In this section, some basic theoretical concepts will be used to develop and present a conceptual understanding of the physical processes underway in the tank and observed in the video, temperature, and pressure data. The ullage will be examined first followed by the liquid. The ideas discussed here will be revisited in later sections when parameter variations are introduced to understand which aspects are affected.

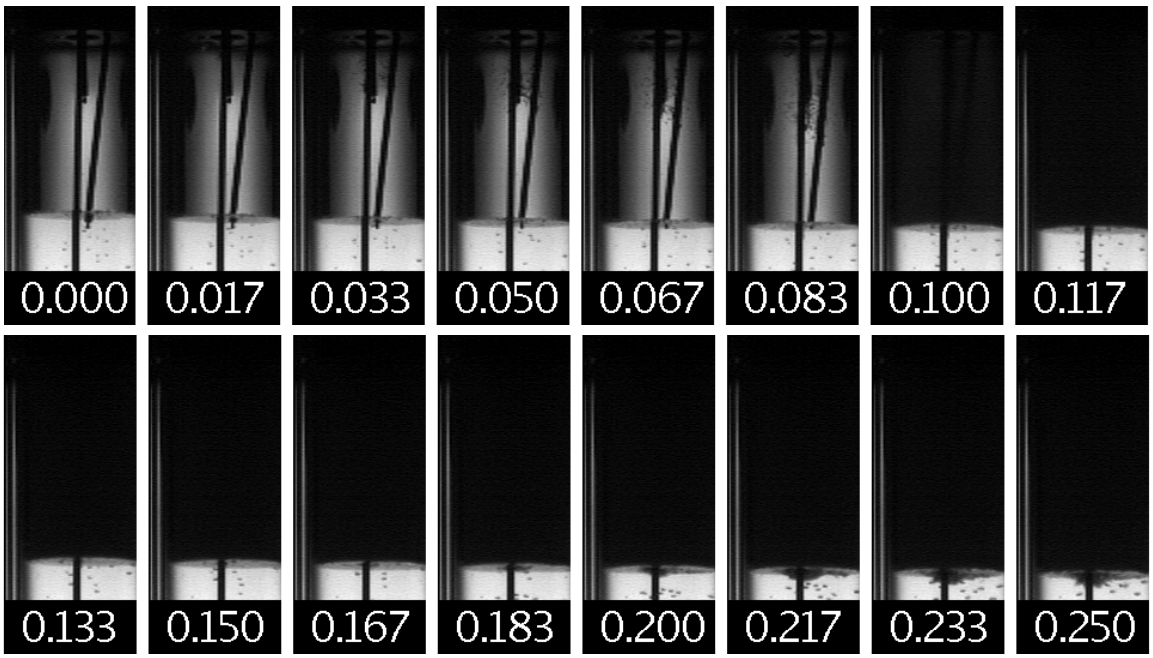

Figure 4.3: Still images of the ullage for the early times. Numbers below the frames indicate the time in seconds from the start of the test. Images are equally spaced in time. Test performed with CO_2.

Ullage

We begin by examining the vapor condensation that was visible in the second frame of figure 4.1. Another set of images showing just the ullage volume in the first 250 ms of the test are shown in figure 4.3. From this we can see the ullage vapor appears to condense in less than 17 ms beginning at a time of 83 ms. The recorded pressure during this period is shown in figure 4.4.

A slight discontinuity in slope of the pressure is visible around 100 ms, coinciding with the vapor condensation. This change in slope can be understood by approximating the process that the ullage undergoes as an isentropic expansion and tracing it on a Pv diagram, shown in figure 4.5. In the early times considered here, the process should be accurately approximated as an isentropic expansion but the quality of this assumption will no doubt decrease with time as heat and mass transfer occur between the ullage and the walls and liquid.

The ullage begins at point A where it is slightly superheated. As the liquid is

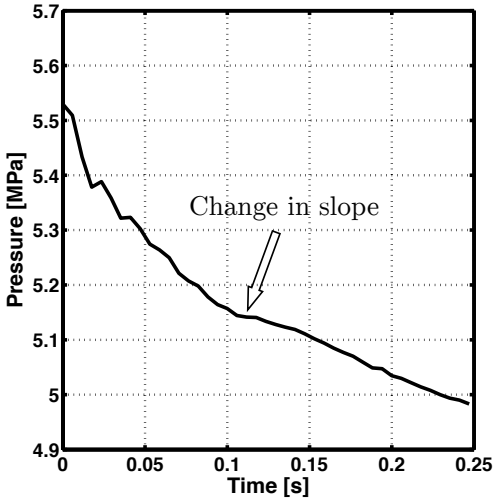

Figure 4.4: Pressure time history for the first 250 ms. Test performed with CO_2.

drawn out of the tank the ullage expands isentropically and crosses the saturation line without condensing, becoming metastable and reaching point B. Thermodynamic metastability refers to non-equilibrium states that a fluid can attain when the activation energy needed for a phase transition is absent (such as superheated liquid or subcooled vapor). Here the vapor is subcooled by 0.6 °C, measured as the difference in pressure between point B and a point on the equilibrium isentrope at the same specific volume, and then converted from pressure to temperature. This conversion is done with REFPROP: $P(s, v) \rightarrow T(s, v)$. At this point, the ullage suddenly condenses and travels to the equilibrium isentrope at point C before continuing to expand. This transition from the metastable to stable state corresponds to the change in pressure slope and the visual appearance of condensation around 100 ms.

To determine the validity of this proposed path, we can turn to classical homogeneous nucleation theory [71] to see if this metastable state is likely. This theory assumes that droplets nucleate only due to statistical thermodynamic fluctuations of energy within the vapor, and only when these fluctuations can overcome the work needed to form a droplet. This theory tends to under-predict the actual droplet production rates because it does not consider the catalytic effect that impurities, solid bodies, and existing droplets have. The droplet generation rate predicted by this

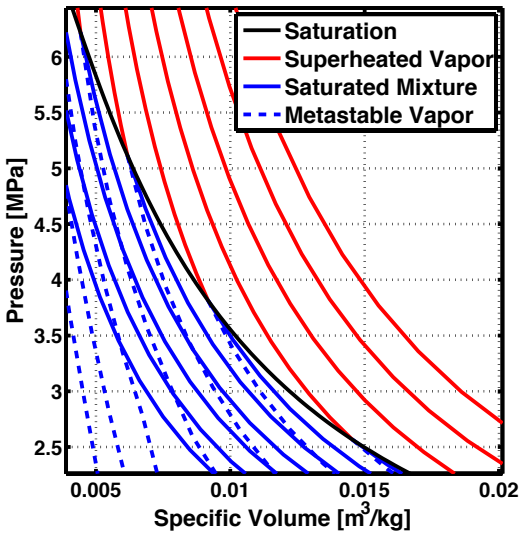

(a) Pv diagram for carbon dioxide showing isentropes, including superheated vapor, saturated mixtures, and metastable (ie supercooled or subcooled) vapor.

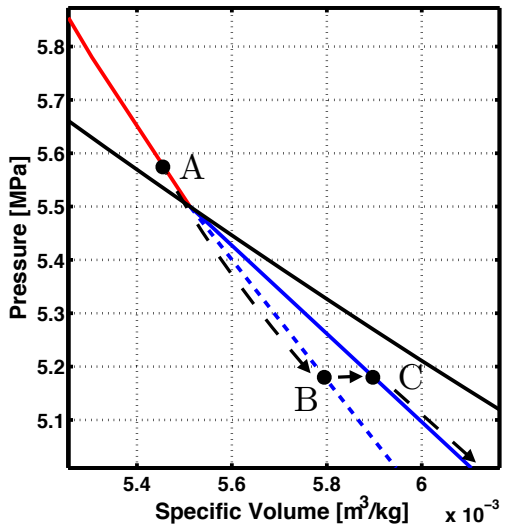

(b) Pv diagram for carbon dioxide showing possible isentropic expansion paths for the ullage.

Figure 4.5: Pressure-volume diagrams for the expanding ullage. Data from REFPROP [2].

theory can be calculated as:

$$\frac{dn}{dt} = N_{M,v}\frac{v_l}{v_v}\sqrt{\frac{2\sigma}{\pi m_M}}\exp\left[-4\pi\sigma\frac{r^{*2}}{3k_BT_v}\right] \tag{4.1}$$

Where r^* is the critical radius and is the size at which the droplet is at equilibrium with the surrounding vapor:

$$r^* = \frac{2\sigma v_l}{RT_v \ln\dfrac{P_v}{P_{sat}}} \tag{4.2}$$

The droplet nucleation rate is plotted as a function of both temperature and level of subcooling in figure 4.6. The nucleation rate increases rapidly with temperature and precipitously with the level of subcooling. For the conditions here ($T \sim 17°C$ and $\Delta T_s = 0.6°C$), the predicted nucleation rate is $\mathcal{O}(10^{18})^{Hz}/_{m^3}$. Ghiaasiaan [71] recommends as a rule of thumb that nucleation should be considered significant if

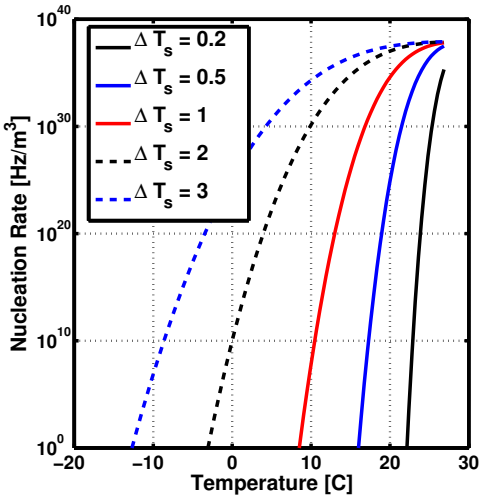

Figure 4.6: Droplet nucleation rate versus temperature for CO_2 for several levels of subcooling, according to classical homogeneous nucleation theory.

it reaches $\mathcal{O}(10^{17} - 10^{22})^{Hz}/_{m^3}$, which corresponds well to the value calculated here. The strong dependence on the level of subcooling, combined with the uniformity of the condensation in the image sequence (figure 4.3) suggests that the temperature field within the ullage volume is uniform.

This large nucleation rate produces significant interfacial area for heat and mass transfer to occur between the bulk vapor and liquid droplets. Once this area has been established, we do not expect that any significant level of subcooling could be maintained and hence an assumption of phase equilibrium within the ullage is valid. This is why the path from point C onward in figure 4.5 follows an equilibrium isentrope.

At later times, the ullage remains condensed but the vapor mass fraction varies across the length, as seen in figure 4.1 from $t = 2.76\ s$ onward. The ullage is more transparent closer to the liquid suggesting that the vapor mass fraction is lower here. This gradient is likely caused by heat and mass transfer from the liquid into the ullage. The boiling process produces saturated vapor that is transferred from the liquid to the ullage, which would produce a region of vapor in the ullage adjacent to the liquid

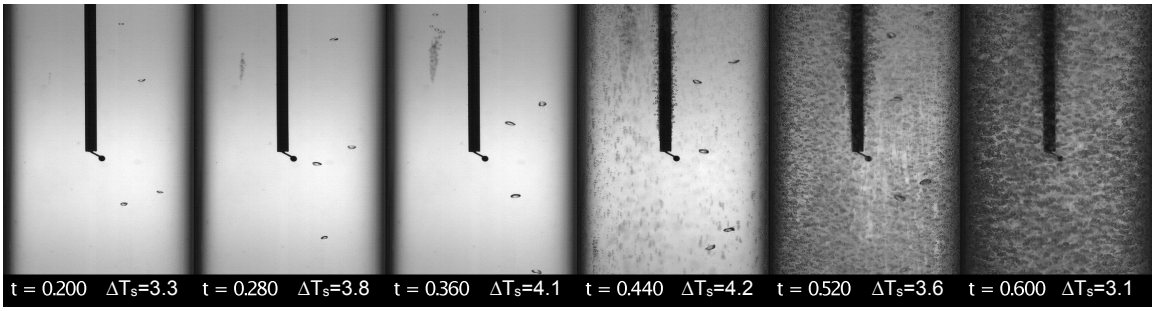

Figure 4.7: Still image sequence. Below each image, the time since the start of the test and the instantaneous value of the superheat reported by the thermocouple are shown. Images are equally spaced in time. Test performed with CO_2.

level with a vapor mass fraction ~ 1. As the pressure continues to drop this vapor will also condense, but the vapor near the top of the tank has been condensing since almost the start of the test and will have a lower vapor mass fraction. This vapor mass fraction gradient also indicates limited mixing within the ullage, making temperature gradients also quite possible. Vertical temperature gradients in the ullage (or liquid) is commonly referred to as stratification.

Liquid

The nucleation behavior observed in the liquid is heterogeneous rather than homogeneous and as a result this same theory cannot be directly applied to assess the bubble nucleation rate (homogeneous nucleation theory here predicts very low nucleation rates, $< 1^{Hz}/_{m^3}$). Instead of forming in the bulk of the liquid, the bubbles appear to form on surfaces such as the walls of the quartz tube, thermocouple probes, and the aluminum end plug as seen in figure 4.1. To get more information about the nucleation process, this experiment was repeated with a 105mm lens (a 50mm lens was used earlier) focused on thermocouple #5 in the upper part of the liquid. The resulting image sequence is shown in figure 4.7 along with the measured level of superheat.

This is one instance where the thermocouple probes can provide valuable data because as long as little or no nucleation is observed and they report significant superheat, it is unlikely that bubble nucleation is distorting their readings (see the appendix for more detail). The values were compared with those predicted based on

the measured pressure and an assumed isentropic expansion and found to be in good agreement up to $t \sim 0.6\ s$. Alternatively, a more conservative interpretation would be that the values of superheat measured are in reality a lower bound on the actual value, with the isentropic expansion as an upper bound.

The general location of the bubble nucleation within the tank can be predicted accurately with a knowledge of the initial temperature field and the surface materials. This initial temperature profile is shown in figure 4.8 and the liquid appears to be relatively uniform with the base of the tank somewhat cooler. With all other factors equal, nucleation will favor the regions with higher temperatures and hence higher saturation pressures as the system pressure drops. However, in this system the surface materials also play a significant role. While the base of the tank is colder, the machined aluminum of the end plug is much more conducive to bubble nucleation than the smooth quartz. Therefore as the pressure drops, bubbles nucleate first at the bottom of the tank before nucleating along the walls.

In general heterogeneous nucleation varies grossly based on the surface geometry, fluid, and other conditions and as such there are no widely accepted expressions to determine the generation rate. However, many sources of experimental data suggest that the nucleation rate behaves qualitatively similar to that for homogeneous nucleation: it is very low at small levels of superheat but increases rapidly as the superheat increases. This is illustrated in figure 4.9, which shows both the nucleation site density and the bubble departure frequency as a function of the level of superheat. The departure frequency is defined as the rate at which bubbles depart from a single nucleation site. When compared to homogeneous nucleation, the nucleation site density is now an additional important parameter - for a large number of bubbles to nucleate both the departure frequency and nucleation site density must be sufficiently large.

As the superheat grows in figure 4.7 to 4.2 $^{\circ}C$, we cross the "knee" of the curve for the nucleation site density causing significant bubble nucleation to now begin and ΔT_s begins to decrease. Once bubbles depart from the nucleation site, they grow and rise to the free surface, eventually giving up their volume of vapor to the ullage. Since bubbles generally nucleate at very small sizes, the growth process as they rise through the liquid is the primary mechanism for liquid-to-vapor mass transfer and is

essentially a diffusion-limited process. It is controlled by the rate of heat conduction from the bulk liquid to the bubble surface where the liquid is vaporized [74]. A simple approximation for this growth rate that assumes constant properties and a small thermal boundary layer is

$$\dot{r} = k_s Ja \sqrt{\alpha_l t} \tag{4.3}$$

Where k_s is a shape factor of order 1 and Ja is the Jakob number:

$$Ja = \frac{\rho_l c_{P,l} \Delta T_s}{\rho_g c_{P,g}} \tag{4.4}$$

Therefore the volume growth rate is $\dot{V} \sim r^2 Ja \sqrt{\alpha_l t}$, which in turn implies that small bubbles contribute very little to the overall rate of vapor production. This represents an inherent time lag in the boiling process: as the superheat increases, eventually significant nucleation begins according to figure 4.9, but significant vapor production doesn't begin until either a very large number of bubbles are present or the bubbles have grown so that the r^2 term is not small. This time lag is the fundamental cause for the pressure drop and subsequent recovery, which can alternatively be thought of as an overshoot similar to that displayed by an underdamped first order system given a step disturbance.

In figure 4.10, the images from later times ($t = 1.88 \rightarrow 7.16\ s$) in figure 4.1 have been reproduced with different pixel intensity levels. The lower 30% of the intensity range has now been mapped to the full gray scale, magnifying differences between dark pixels and causing light pixels to become saturated. This effect allows us to visualize the temporal and spatial uniformity of the liquid volume in terms of its bubble population. Due to the strong dependence of the nucleation rate on ΔT_s, this can also be an indirect measurement of the temperature field.

The images in figure 4.10 show that the appearance of the liquid is uniform in space and time, suggesting that the temperature field and the bubble population are both relatively uniform. Due to the finite lifetime of the bubbles, new bubbles must be continually generated throughout the test and therefore if the appearance of the liquid is approximately constant with time (and we take this to mean that the bubble

population is also roughly constant) the level of superheat is also a constant. This can be justified theoretically by considering a gross idealization of this system.

As the liquid drains out the net volume of the liquid in the tank will drop, which in turn causes the ullage to expand and the tank pressure to drop. Most models for mass flow through an orifice predict $\dot{m}_{orifice} \sim \sqrt{\Delta P}$ and since the pressure during the later times drops quite slowly, we can consider ΔP to be approximately constant and therefore this $\dot{m}_{orifice}$ is also approximately constant. This constant pressure implies that there is sufficient mass transfer from the liquid into the vapor to make up for the rate of change of the liquid volume. Therefore, if the volume rate of change of the liquid is constant and the tank pressure is constant, the production rate of vapor via bubble nucleation and growth is constant and we expect the level of superheat to be constant. In reality of course none of these quantities are constant, but given that the pressure drops by only 29% during this time these general conclusions are likely first order accurate.

As these bubbles vaporize liquid, significant amounts of energy are absorbed by Δh_{LV}, which causes the liquid temperature to drop with time. If the superheat is approximately constant, this would imply that the pressure in the system is $P = P_{sat}(T_l - \Delta T_s)$ and therefore as the temperature drops the pressure will drop as well. The strong dependence of the saturation pressure on temperature means that for the pressure drop seen here ($5.226 \rightarrow 3.742\ MPa$) a liquid temperature change of only 13.4 °C is required.

4.1.3 Summary and Conclusions

We now summarize the physical processes within the tank and establish some nomenclature that will be used to describe tests presented in subsequent sections of this thesis.

The early times of the test will be referred to as the "transient regime[1]." Initially as the liquid begins to drain out of the tank the ullage rapidly expands, briefly becoming slightly subcooled before undergoing homogeneous condensation and establishing a

[1] the term regime is used to avoid confusion with other uses of "region" or "phase"

equilibrium homogeneous two-phase mixture that continues to expand. In contrast, once the liquid becomes sufficiently superheated by the decreasing system pressure, heterogeneous nucleation begins on the vessel walls and not homogeneously within the bulk of the liquid. Bubbles are generated at these sites and break off, rising and growing in the bulk liquid until they reach the free surface. The inherent lag between the establishment of a sufficient level of superheat and the vapor generation from boiling accounts for the drop and recovery in pressure commonly observed during vessel blowdown. Eventually, a large and stable population of bubbles is formed in the liquid, balancing birth of new bubbles at wall nucleation sites and death of existing bubbles at the free surface, and transforming the liquid into a homogeneous two-phase mixture.

Once both the liquid and vapor have become these homogeneous mixtures, the system enters a "steady state regime" and the timescale of physical changes increases from $\sim$100 ms to $\sim$1 s and the liquid and vapor remain largely unchanged in general character and composition. At this point the bubble population has reached an approximately constant value implying in turn an approximately constant level of superheat that drives the transfer of heat and mass to the ullage. This establishes a region of pure vapor near the liquid surface while the vapor throughout the ullage continues to condense. As energy is absorbed from the liquid to produce the phase change, the temperature of the liquid and the system pressure steadily drop. The continual condensation of the ullage maintains its temperature close to the saturation value.

4.2 Parameter Variations

In this section, the effect of parameter variations on the overall system dynamics as described in the previous section will be evaluated. The purpose is to help improve our understanding of self-pressurizing propellant tank dynamics and identify the features that would need to be included in a model. A key component of that process is knowing whether a model generated from one set of experimental data can be expected to predict results from experimental systems that have different parameters. The

parameters studied here are: flow rate, fill level, initial temperature, initial bubble population, and vessel size.

These parameter variations are studied primarily via comparisons between two tests: a baseline and a test with a single parameter altered. Each subsection will focus on one of these comparisons and will present the pressure data, initial temperature fields, and still images from the high speed videos. Some discussion of these results is included to provide possible explanations for observed differences between tests.

To facilitate comparison of test data, we define normalized pressure and time such that pressure travels from 1 to 0 and time travels from 0 to 1 between the start and the liquid runout (LRO) point:

$$P_n = \frac{P - P_{LRO}}{P_i - P_{LRO}}, \quad t_n = \frac{t}{t_{LRO}} \tag{4.5}$$

Other quantities of interest are the minimum pressure reached during the transient regime as well as the maximum pressure at the subsequente recovery. These quantities will be referred to as P_{min} and P_{max} with associated times t_{min} and t_{max}. Detailed data for each of the tests presented in this work are given in the appendix.

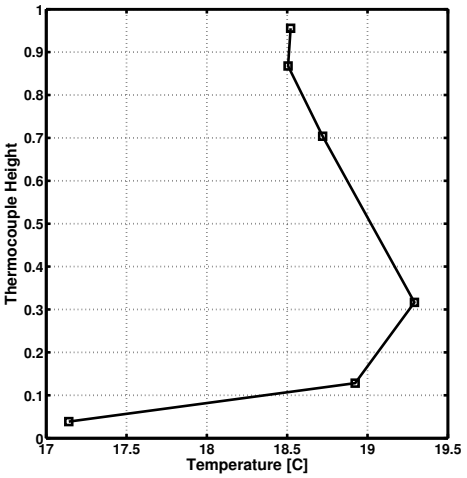

Figure 4.8: Initial temperature profile. Test performed with CO_2.

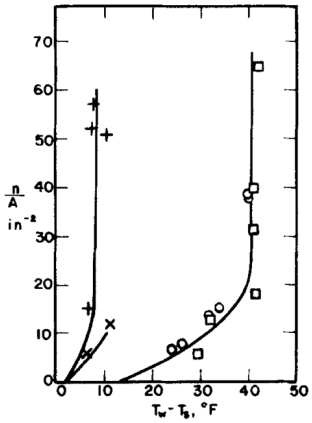

(a) Active nucleation site density versus liquid superheat. Symbols: X - methanol, + - ethanol, □ - water, O - water. Data from Griffith and Wallis [72].

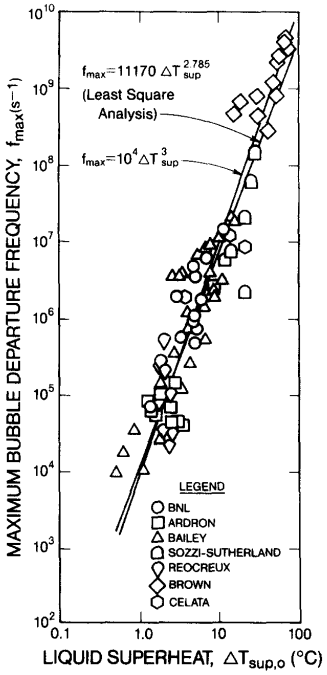

(b) Departure frequency versus liquid superheat for water. Note both axes are using a log scale. Data from numerous researchers, compiled by Shin and Jones [73]. Reprinted with permission.

Figure 4.9: Experimental data on the nucleation site density and departure frequency for heterogeneous nucleation of bubbles in liquid.

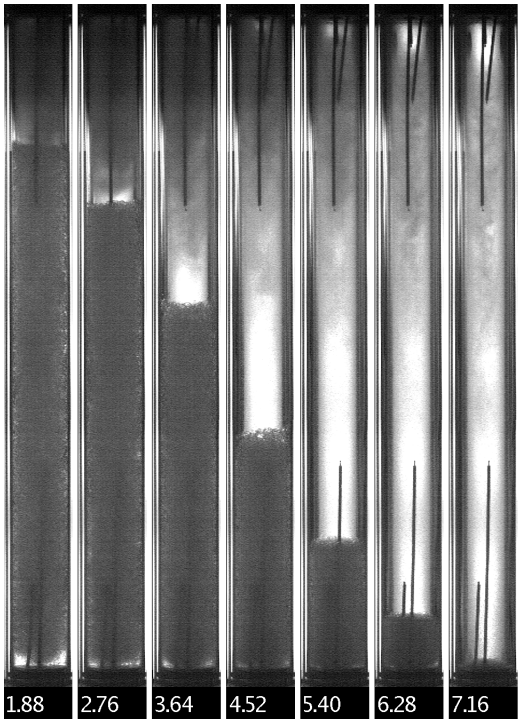

Figure 4.10: Image sequence with altered pixel intensities. Numbers below indicate the time in seconds since the start of the test. Test performed with CO_2.

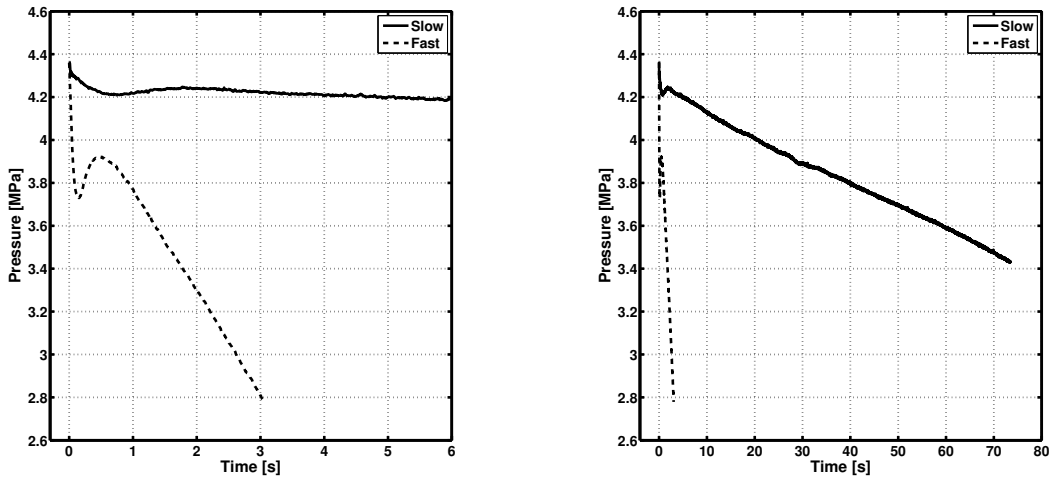

Figure 4.11: Pressure time histories for the slow and fast tests. Tests were performed with CO_2.

4.2.1 Flow Rate

The flow rate is varied by performing tests with different orifices. Here, two tests using the quartz tube system with different orifices (0.279, 1.321 mm) and test times ($t_{LRO} = 73.5, 3.0s$) are compared. They will be referred to simply as the "slow" and "fast" tests. All other features of the two tests were matched, including the fill level (85%), mean initial temperature (10.1 $°C$) and initial temperature profiles. The data from these two tests are shown in figures 4.11 to 4.15. Figure 4.11 shows the pressure traces and the normalized pressure traces are shown in figure 4.12, while figure 4.13 shows the initial temperature profiles. Figures 4.14 and 4.15 show a comparison of the still image sequences from these two tests. Several frames are missing from the slow test in figure 4.15 because the camera was unable to record the full duration of the test due to its finite internal memory.

We begin by examining the pressure traces in figure 4.11. The fast test more closely resembles the data shown in earlier sections, while the slow test at first appears quite different. However upon detailed inspection the slow test still exhibits the basic features: pressure drop and recovery followed by a linear decrease. In this case however the linear portion is the vast majority of the test and the earlier features are

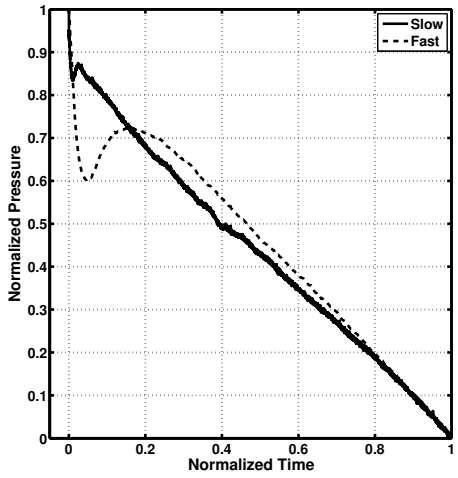

Figure 4.12: Normalized pressure time histories from the slow and fast tests. Tests were performed with CO_2.

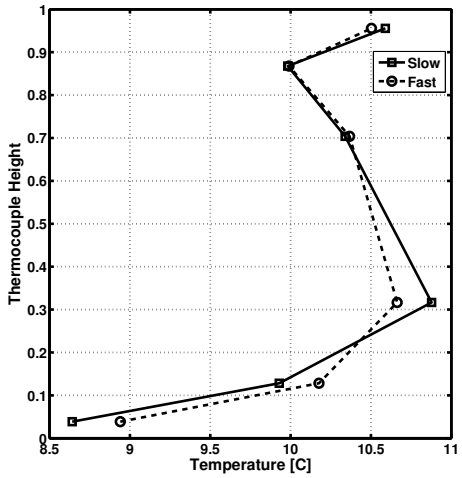

Figure 4.13: Initial temperature profiles from the slow and fast tests. Tests were performed with CO_2.

difficult to distinguish. The slow test also clearly maintains a much higher pressure than the fast test, with a P_{LRO} 0.650 MPa greater.

The similarity between the two tests in the normalized pressure trace in figure 4.12 is quite striking. The fast test clearly reaches a much lower pressure during the initial drop, and the early transient portion of the fast test is a much larger fraction of the entire test. This is also visible in figure 4.11, where the duration of the transient portion of the slow test is four times longer than that of the fast test ($t_{max} = 1.918, 0.482\ s$), despite t_{LRO} being 24 times longer. However the slopes of the two tests during the steady state portion of the test are quite similar. There are some slight fluctuations in the pressure data for the slow test. These were observed to coincide with nucleation beginning in a new region of the vessel. For example, the slight increase in pressure at $t_n = 0.40$ occurred when some bubbles began to nucleate from the base of the vessel, visible in the $t_n = 0.39$ image in figure 4.15.

Looking at the image sequence for the early portion of the tests in 4.14, the slow test does not show many of the typical features shown earlier. The ullage does not condense, and the bubble nucleation within the liquid occurs gradually over the course of several frames ($t_n = 0.02 \rightarrow 0.09$). The fast test however does appear more similar

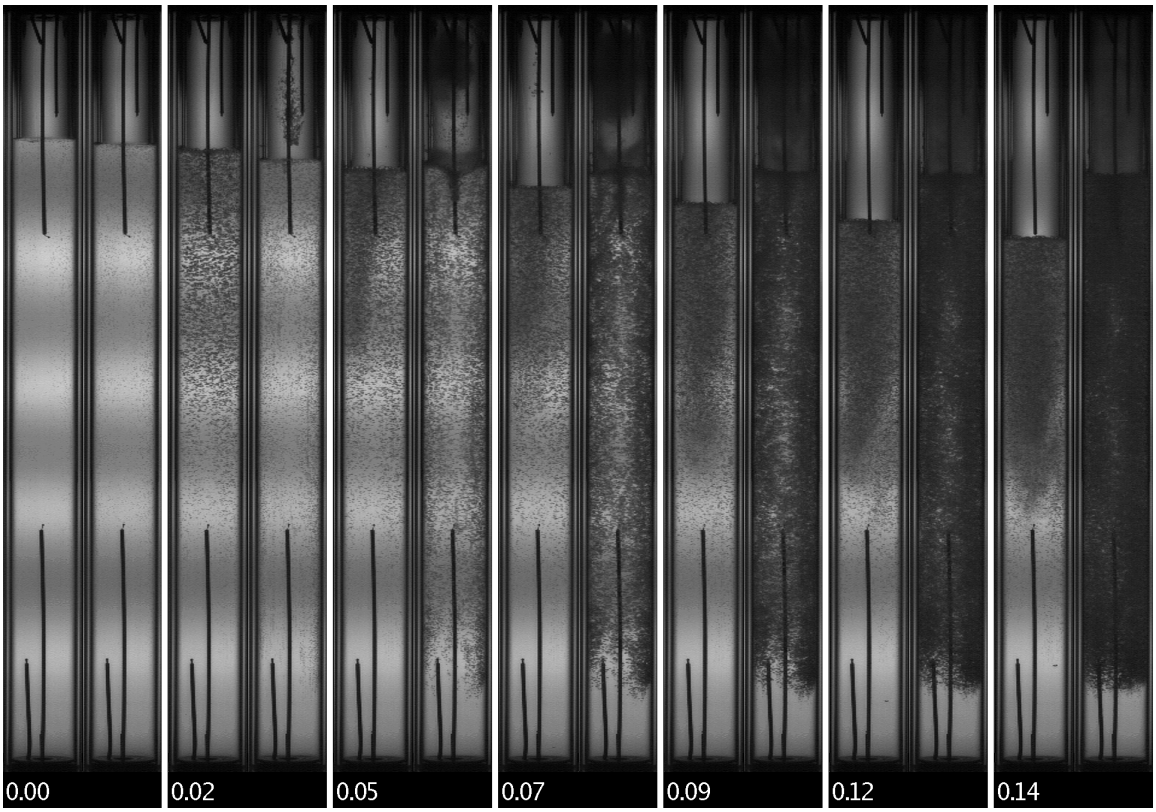

Figure 4.14: Image sequence comparison for early times from the slow (left) and fast (right) tests. Each pair of frames are taken from the two tests at the same normalized time, indicated by the number below. Tests were performed with CO_2.

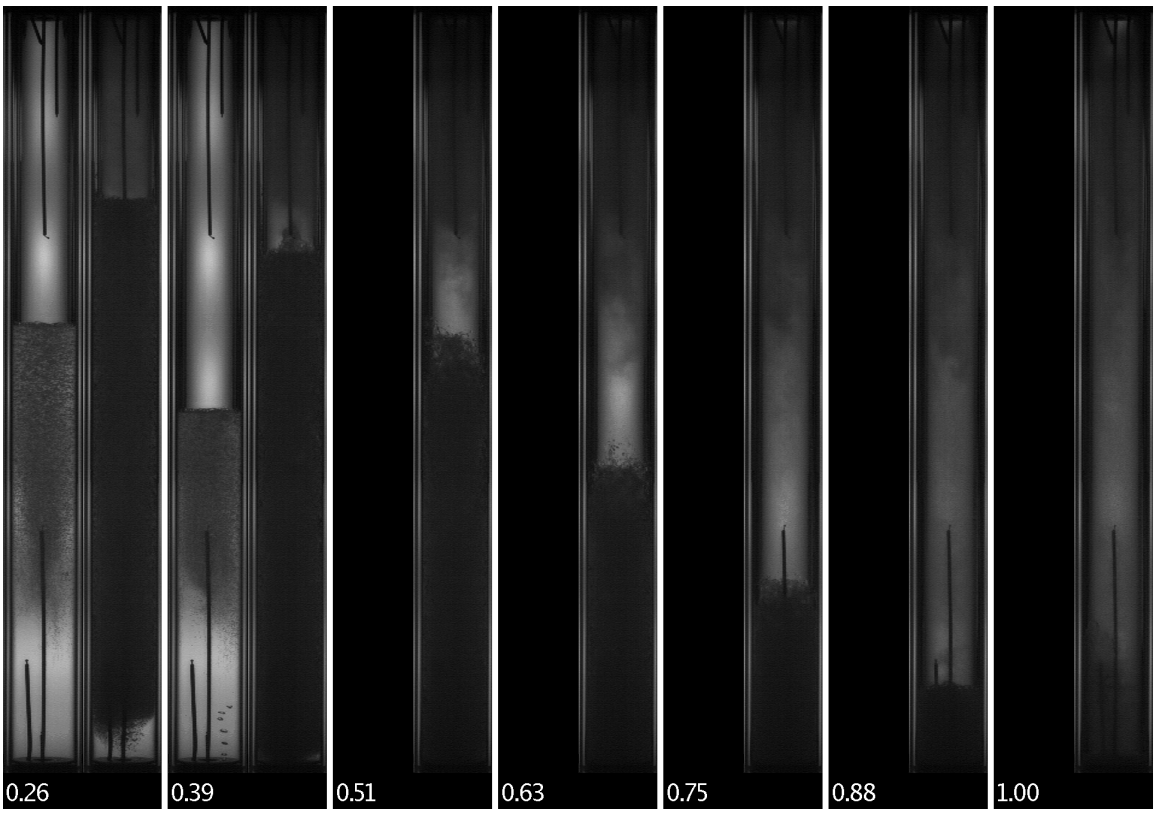

Figure 4.15: Image sequence comparison for later times from the slow (left) and fast (right) tests. Each pair of frames are taken from the two tests at the same normalized time, indicated by the number below. Some frames from the slow test are missing because the camera's internal memory was insufficient to capture the entire test. Tests were performed with CO_2.

to that shown in figure 4.1. The ullage condenses and bubble nucleation in the liquid is rapid and spans nearly the entire length. A region of pure liquid is maintained at the very base of the tank until $t_n \sim 0.39$ as seen in figure 4.15. This is likely caused by the low temperature at the base of the tank visible in the initial temperature profiles. Looking at later times in figure 4.15, the slow test's behavior is unchanged while the fast test does reach the steady state portion of the test with the liquid and vapor appearing as somewhat homogeneous mixtures.

As mentioned earlier, the final pressure reached by the slow test is much higher than the fast test ($P_{LRO} = 3.530, 2.880\ MPa$). This can be explained using the theory presented earlier in section 4.1-4.1.2-4.1.2. At higher flow rates, there must be accordingly a much higher level of superheat in the liquid, and given the same liquid temperature the system pressure is reduced. It is difficult to predict the actual difference in superheats due to the complex relationship between bubble nucleation rates and ΔT_s.

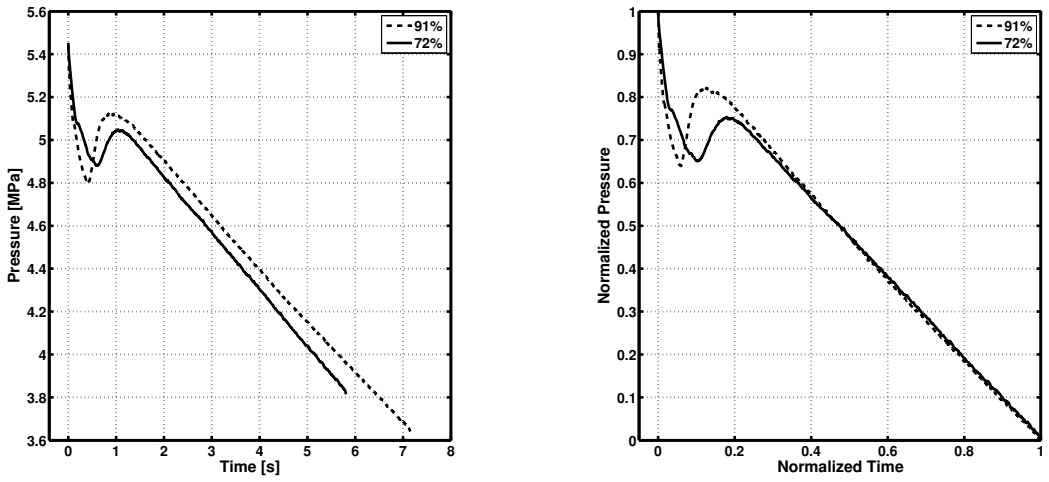

Figure 4.16: Pressure and normalized pressure time histories for the 91% and 72% fill level tests. Tests were performed with CO_2.

4.2.2 Fill Level

The fill level is easily varied by pumping different amounts of carbon dioxide into the test vessel. Here, two tests with different fill levels (91%, 72%) are compared. All other parameters of the two tests were matched, including the mean initial temperatures (18.5, 19.2 $°C$), the initial temperature profiles, and orifice diameters (0.813 mm). The differing fill levels resulted in different test times for the two tests, $t_{LRO} = 7.16, 5.82\ s$ for the 91% and 72% tests respectively. The data from these two tests are shown in figures 4.16 to 4.19. Figure 4.16 shows both pressure traces and the normalized pressure traces, while figure 4.17 shows the initial temperature profiles. Figures 4.18 and 4.19 show a comparison of the still image sequences from these two tests.

Beginning with the pressure traces in figure 4.16, several features are evident. The 91% test shows a more rapid initial drop in pressure and also reaches a lower pressure ($P_{min} = 4.906, 4.982\ MPa$) before beginning to increase once again. It then peaks higher than the 72% test and at an earlier time ($P_{max} = 5.226, 5.146\ MPa$, $t_{max} = 0.877, 1.071s$). From this point on ($t = 1.5s$) however the two appear quite similar, with nearly identical slopes. The 91% test continues longer and reaches a

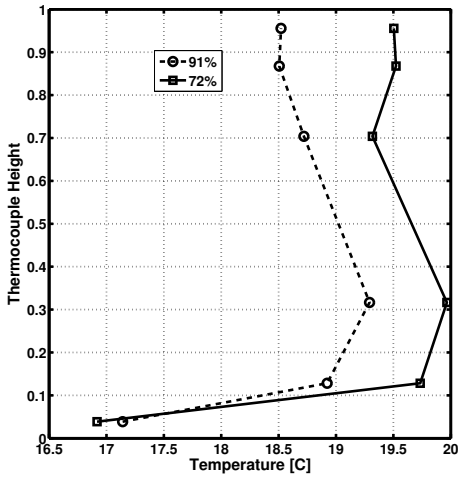

Figure 4.17: Initial temperature profiles from the 91% and 72% fill level tests. Tests were performed with CO_2.

lower ending pressure ($P_{LRO} = 3.742, 3.916\ MPa$). When the normalized pressure traces are examined the differences in the later times ($t_n > 0.2$) disappear completely. In the earlier times we see the two tests reach the same normalized minimum pressure, but the 91% test reaches it earlier ($t_{n,min} = 0.054, 0.087$) and peaks to a higher value that occurs earlier as well ($P_{n,max} = 0.823, 0.751$, $t_{n,max} = 0.112, 0.157$).

Examining the image sequence from the early test times in figure 4.18, we see features that correlate with the behavior of the pressure traces. Beginning with the ullage, the 72% test takes much longer to condense, with full condensation not appearing until $t_n = 0.05$, compared to $t_n = 0.02$ for the 91% test. Large scale bubble nucleation also takes much longer ($t_n = 0.12$ vs $t_n = 0.07$) and no bubbles are seen nucleating at the bottom of the tank in the 72% test.

In fact, when the later times image sequence is viewed (figure 4.19) the 72% test maintains a region of pure liquid at the base of the tank until $t_n = 0.51$, unlike the 91% test in which the entire liquid appears uniformly populated with bubbles by $t_n = 0.14$. In the later times though the two test do appear much more similar than in the early times, especially after $t_n = 0.51$. This connects with the behavior seen in the pressure traces, where the 91% test showed more rapid development and reached

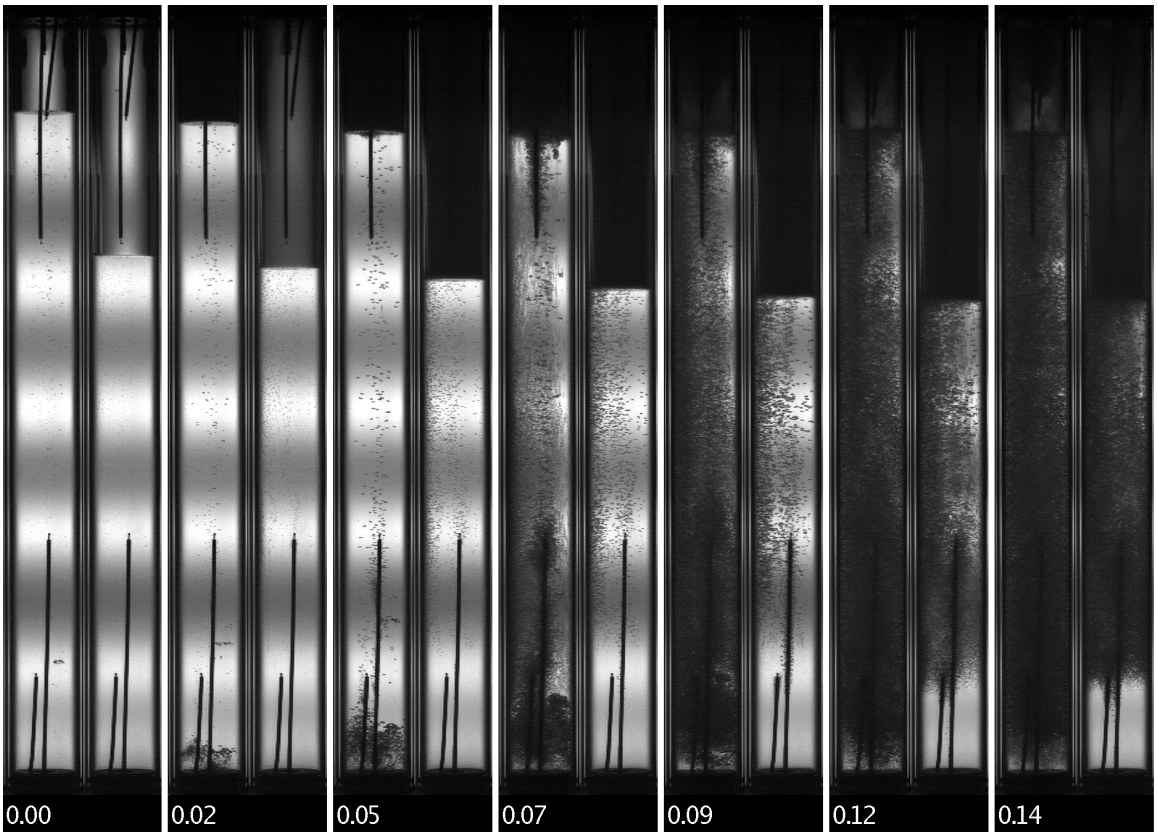

Figure 4.18: Image sequence comparison for early times from the 91% (left) and 72% (right) fill level tests. Each pair of frames are taken from the two tests at the same normalized time, indicated by the number below. Tests were performed with CO_2.

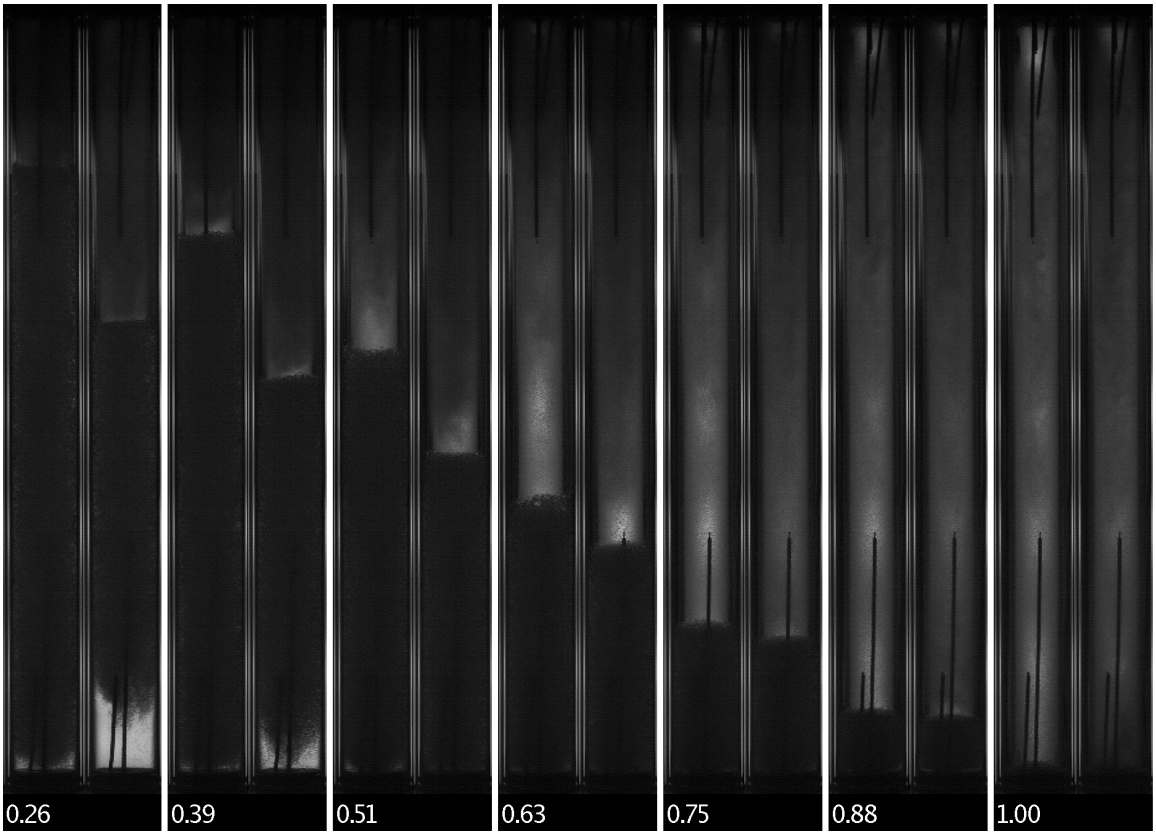

Figure 4.19: Image sequence comparison for later times from the 91% (left) and 72% (right) fill level tests. Each pair of frames are taken from the two tests at the same normalized time, indicated by the number below. Tests were performed with CO_2.

the steady state portion of test more quickly.

This can be explained with simple reasoning. During the early portion of the test as the liquid drains from the base of the vessel the ullage volume expands and the pressure drops according to its rate of volume expansion. In the 72% test the ullage is 3.1 times larger and so for the same flow rate out of the tank we would expect the pressure to drop to be much slower. Looking at just the first 100 ms to avoid any complications from condensation, the corresponding values are ${}^{dP}/_{dt} = 3.65, 2.51 MPa/s$. If we assume a simple isentropic expansion, the 72% test's value of ${}^{dP}/_{dt}$ should be a lower by a factor of 0.67, which matches well with the experimental value (0.69).

Also, the slower pressure drop results in a more gradual superheating of the liquid, allowing a more bubbles to nucleate and grow at low levels of superheat. This results in fewer nucleation sites being activated, directly resulting in a region of pure liquid at the base of the tank. This region of pure liquid may suggest that single phase liquid is exiting the tank in this case, while in the 91% test a two-phase mixture is exiting. Existing models and experimental evidence suggests that this will have a significant effect on the flow rate through the orifice which one would expect to have a correspondingly significant effect on the overall system behavior [75, 35]. Interestingly however the behavior of the tests in terms of the pressure traces is quite similar.

One possibility is that the pressure drop between the base of the tank and the entrance of the orifice caused by the increasing flow velocity combined with frictional losses causes significant vapor production. If this vapor production were large enough, a small change in the vapor fraction at the base of the tank would have little effect on the vapor fraction at the entrance of the orifice. Therefore the flow rates in the two cases would be similar.

4.2.3 Temperature

The fluid temperature is controlled in a variety of ways as discussed earlier. Here, three different comparisons will be made. The first two involve shifting the mean initial temperature without altering the shape of the initial temperature profile. This will be presented as a comparison between tests at ambient temperature and elevated temperature, and then a second comparison between ambient temperature and reduced temperature. Lastly, the effect of changes in the shape of the initial temperature profile while maintaining its mean value will be discussed. Temperature can be expected to play a strong role in the system dynamics due to the proximity of the critical point ($T_{c,N_2O} = 309.52K, T_{c,CO_2} = 304.13K$), which results in rapid changes in fluid properties as any state variable is adjusted.

Elevated Temperature

Here, two tests with similar temperature profiles but different mean temperatures ($\bar{T}_i = 18.3, 24.1°C$), hereafter referred to as "ambient" and "hot" tests for brevity, will be compared. All other parameters of the two tests were matched, including the fill levels (82, 81%), shape of the temperature profiles, and orifice diameters (0.818 mm). The differing temperatures and hence initial pressures resulted in different test times for the two tests, $t_{LRO} = 6.61, 6.21s$ for the ambient and hot tests respectively. The data from these two tests are shown in figures 4.20 to 4.23. Figure 4.20 shows both pressure traces and the normalized pressure traces, while figure 4.21 shows the initial temperature profiles. Figures 4.22 and 4.23 show a comparison of the still image sequences from these two tests.

Beginning with the pressure traces in figure 4.20, the higher saturation pressure of the hot test has elevated the initial pressure by 0.69 MPa. The typical features are still present in this hot test including the pressure drop, recovery and the establishment of the steady state regime. The transient regime is a relatively shorter portion of the test however and the pressure drop is much smaller ($P_{n,min} = 0.349, 0.227$), as is the recovery ($[P_{n,max} - P_{n,min}] = 0.089, 0.13$). Nonetheless in the steady state regime the slopes of the linear portions of both the ambient and hot tests are nearly

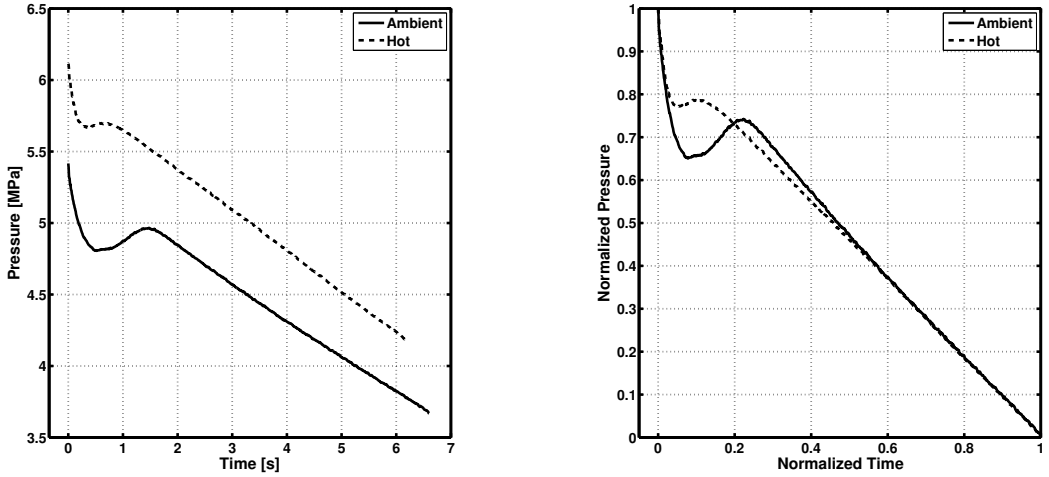

Figure 4.20: Pressure and normalized pressure time histories for the ambient and hot tests. Tests were performed with CO_2.

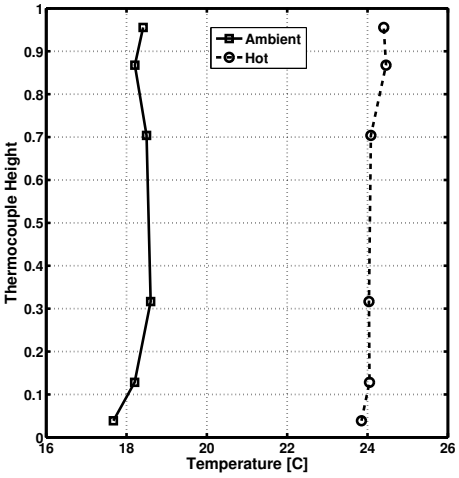

Figure 4.21: Initial temperature profiles from the ambient and hot tests. Tests were performed with CO_2.

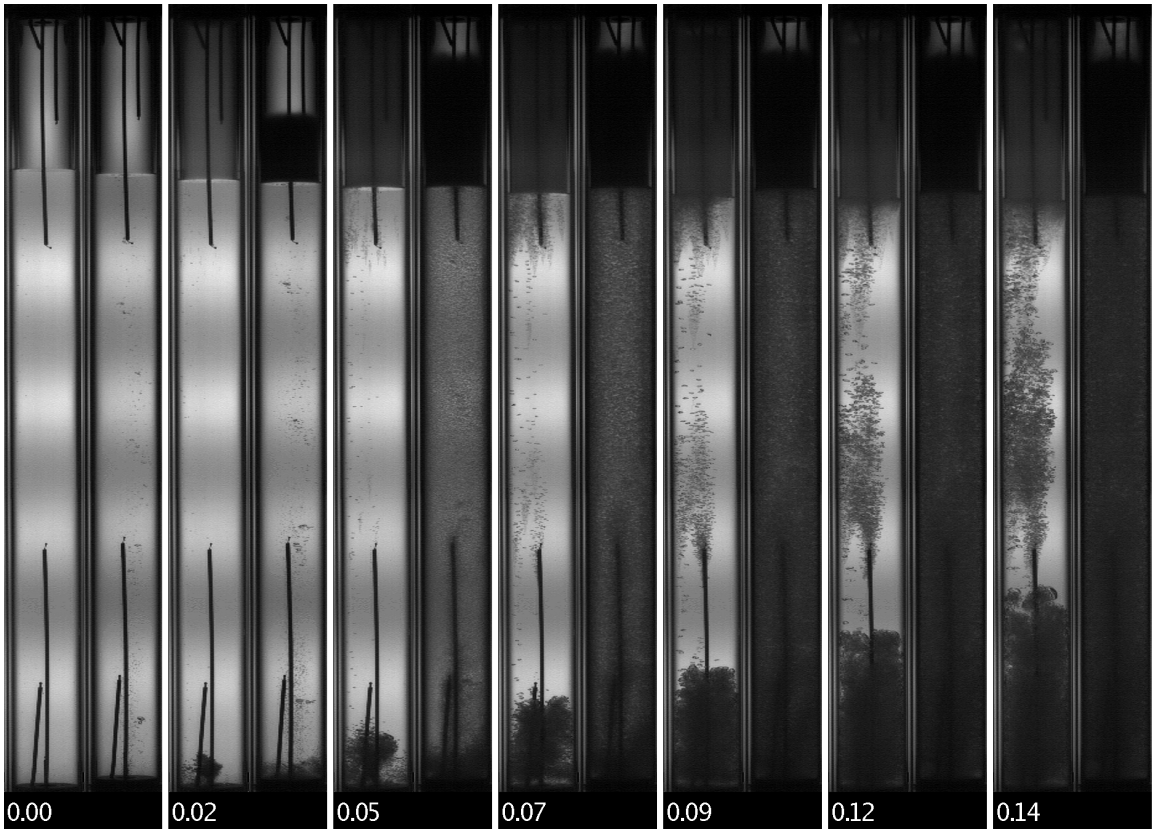

Figure 4.22: Image sequence comparison for early times from the ambient (left) and hot (right) tests. Each pair of frames are taken from the two tests at the same normalized time, indicated by the number below. Tests were performed with CO_2.

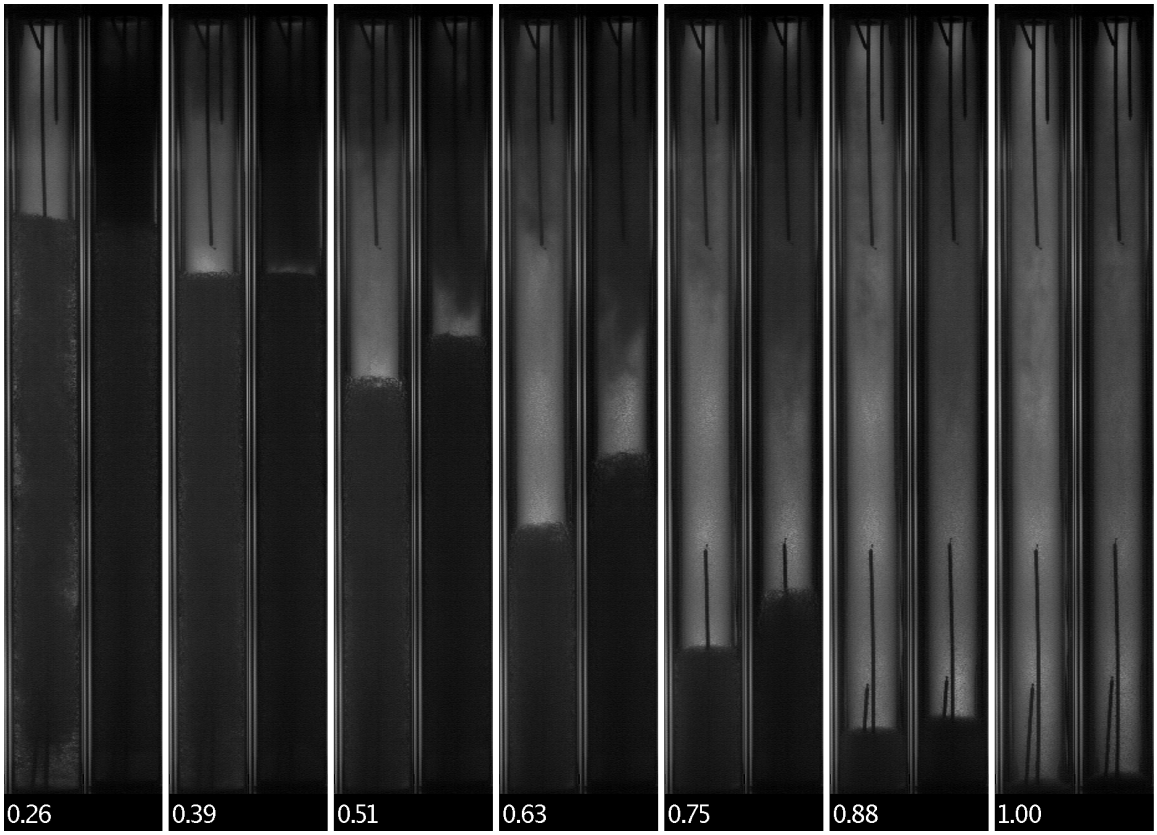

Figure 4.23: Image sequence comparison for later times from the ambient (left) and hot (right) tests. Each pair of frames are taken from the two tests at the same normalized time, indicated by the number below. Tests were performed with CO_2.

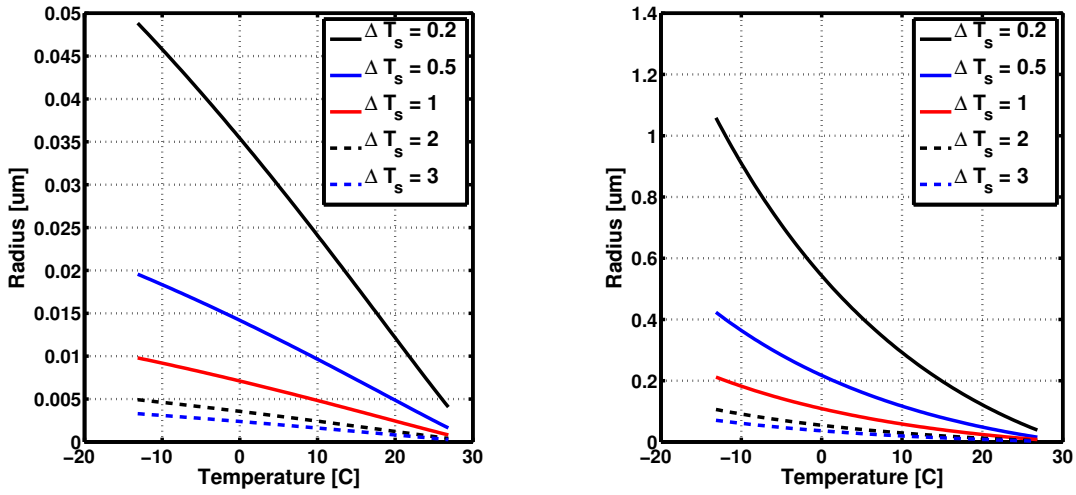

(a) Homogeneous droplet nucleation size for. (b) Heterogeneous bubble nucleation size.

Figure 4.24: Nucleation sizes as a function of temperature for different levels of superheat/subcooling, for CO_2 and expressed in $°C$.

identical. The normalized pressure trace highlights this fact, showing that nearly all the differences between the two tests are restricted to the initial transient.

The still images from the early portion of the tests shown in figure 4.22 are quite striking. Both the condensation in the ullage and bubble nucleation in the liquid are quite different for the hot and ambient tests. In the hot test the condensation appears as an upward moving wave that never reaches the top of the tank, unlike the ambient test where the condensation is uniform in the ullage. Conversely, bubble nucleation in the liquid appears much more uniform, with bubbles forming along the entire depth of the liquid simultaneously.

The images from the later times shown in figure 4.23 show fewer differences, especially near the end of the test. This corroborates the features of the normalized pressure trace, where the two tests behave similarly after $t_n \sim 0.25$. It seems that in both cases the liquid and ullage have been established as homogeneous two phase mixtures.

Interestingly, both the liquid and ullage in the hot test appear darker than in the light test despite identical optical parameters (back light output, aperture, exposure

time, sensor gain, lens, etc.). One possible explanation of this would be a reduced nucleation size, both for the droplets in the ullage and bubbles in the liquid. Smaller droplets and bubbles would be more effective at reflecting light away from the camera, rendering the images darker.

A decrease in droplet size can be predicted using the theory presented earlier in the relation given for the critical droplet radius (equation (4.2)), which is plotted versus temperature in figure 4.24. As the temperature increases, r^* drops rapidly. For the liquid, the heterogeneous bubble nucleation size can be estimated as[76]

$$r^* = \frac{2\sigma T}{\rho_g \Delta h_{LV} \Delta T_s} \tag{4.6}$$

This is also plotted versus temperature in figure 4.24 and shows a similar drop as temperature is increased. Therefore it is likely that in the hot test we are indeed seeing the formation of smaller bubbles and droplets.

The smaller pressure drop and recovery can also be predicted to a degree from theory. One relation proposed for calculating heterogeneous nucleation rates is[76]

$$\frac{dn}{dt} \sim N_{M,l}^{2/3} \sqrt{\frac{2\sigma}{\pi m_M F}} \exp\left[\frac{-16\pi\sigma^3 F}{3k_B T(P_{sat} - P_l)^2}\right] \tag{4.7}$$

The primary difficulty with this equation is that the term F relates to the contact angle and hence the specific geometry of an activation site, which is difficult to predict for practical systems and can vary from near 1 to 10^{-7}. This in turn can change the resultant nucleation rate by tens of orders of magnitude[77]. However between the hot and ambient tests we might expect F to be similar enough that the primary variations in equation 4.7 will be caused by other terms' temperature dependence. This relation is plotted in figure 4.25 for $F = 10^{-3}$.

While specific values from figure 4.25 cannot be used quantitatively, the clear qualitative result is that an increase in temperature of only 5.8 $°C$ as present here between the ambient and hot tests would result in a massive increase in the bubble nucleation rate ($\mathcal{O}(10^{100})$ at constant ΔT_s), and accordingly much higher vapor production at lower levels of superheat. The result is that the superheat reached during the hot test should be much lower and hence we can reasonably expect the drop and

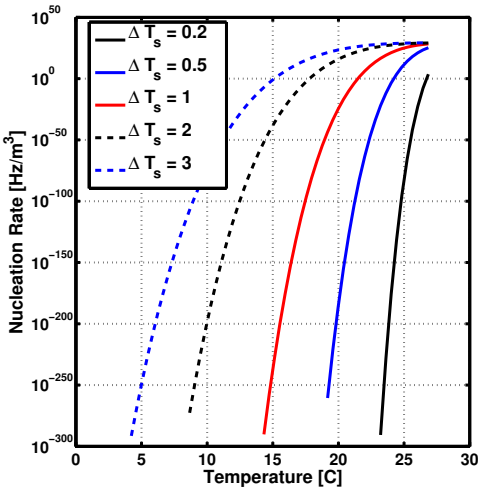

Figure 4.25: Heterogeneous bubble nucleation rate for CO_2.

recovery in pressure during the transient regime to be much smaller in magnitude.

Reduced Temperature

While the previous section compared an ambient test with an elevated temperature test, here an ambient and reduced temperature test will be compared ($\bar{T}_i = 16.2, -8.2°C$). These two will be referred to as "ambient" and "cold" tests for brevity. All other parameters of the two tests were matched, including the shape of the temperature profiles, fill levels (83%), and orifice diameters (0.559 mm). The differing temperatures and hence initial pressures resulted in different test times for the two tests, $t_{LRO} = 14.15, 19.49s$ for the ambient and cold tests respectively. The data from these two tests are shown in figures 4.26 to 4.29. Figure 4.26 shows both pressure traces and the normalized pressure traces, while figure 4.27 shows the initial temperature profiles. Figures 4.28 and 4.29 show a comparison of the still image sequences from these two tests.

The pressure traces in figure 4.26 are interesting because of the differences seen here compared to the earlier comparison between hot and ambient tests. In the normalized pressure trace, the cold test shows a larger drop and recovery yet the peak

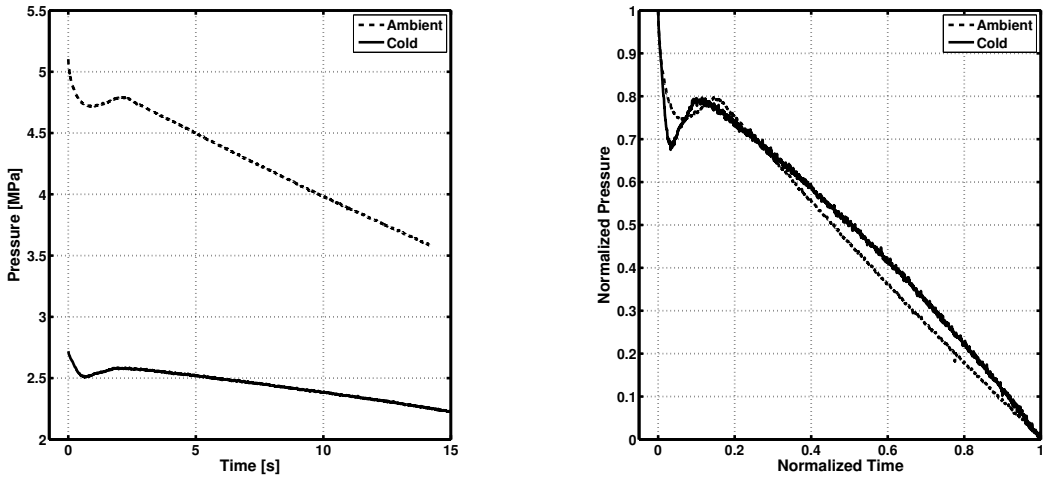

Figure 4.26: Pressure and normalized pressure histories for the ambient and cold. Tests were performed with CO_2.

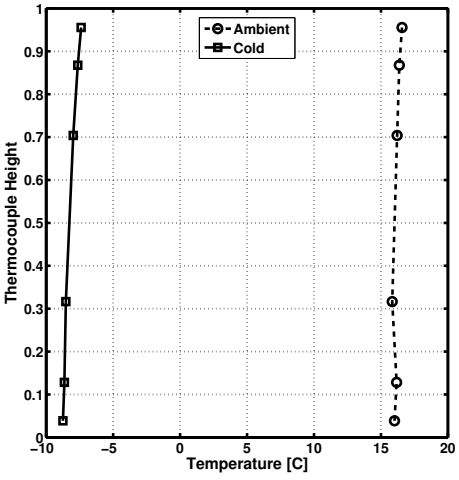

Figure 4.27: Initial temperature profiles from the ambient and cold tests. Tests were performed with CO_2.

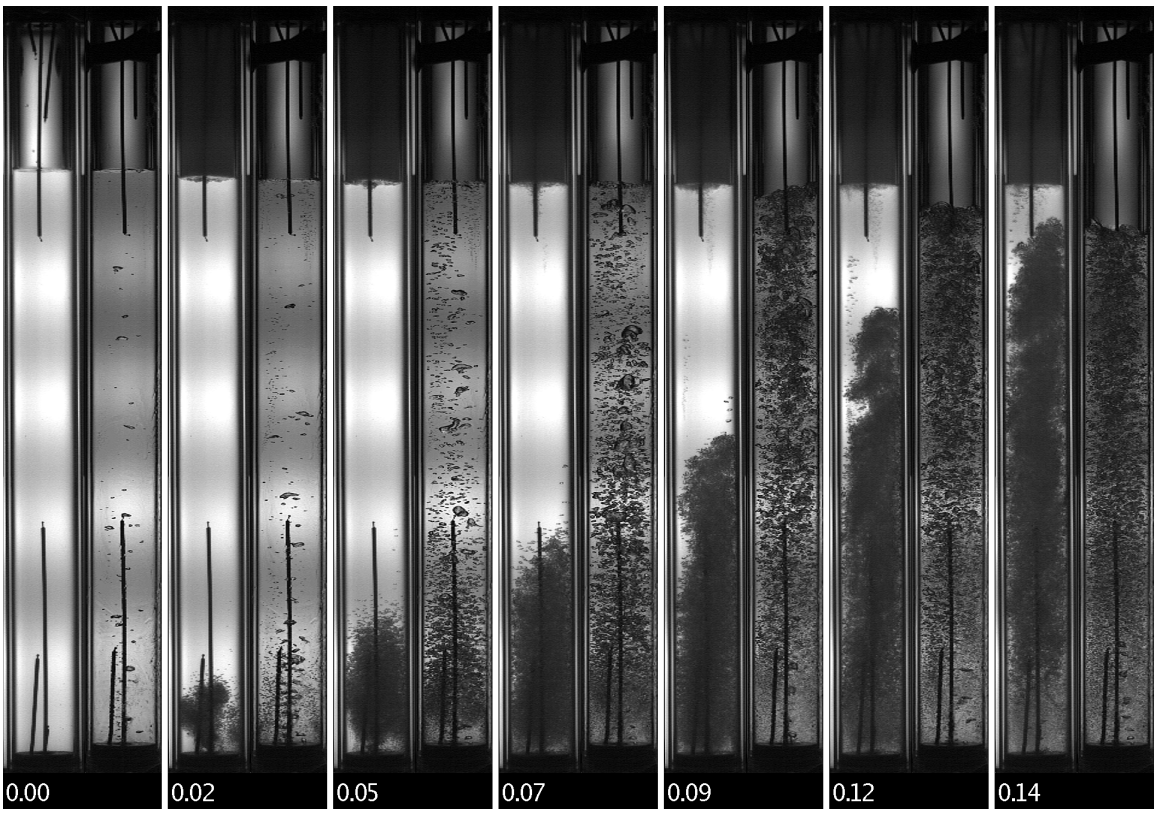

Figure 4.28: Image sequence comparison for early times from the ambient (left) and cold (right) tests. Each pair of frames are taken from the two tests at the same normalized time, indicated by the number below. In the cold test, a hose is partially obstructing the view of the ullage. Tests were performed with CO_2.

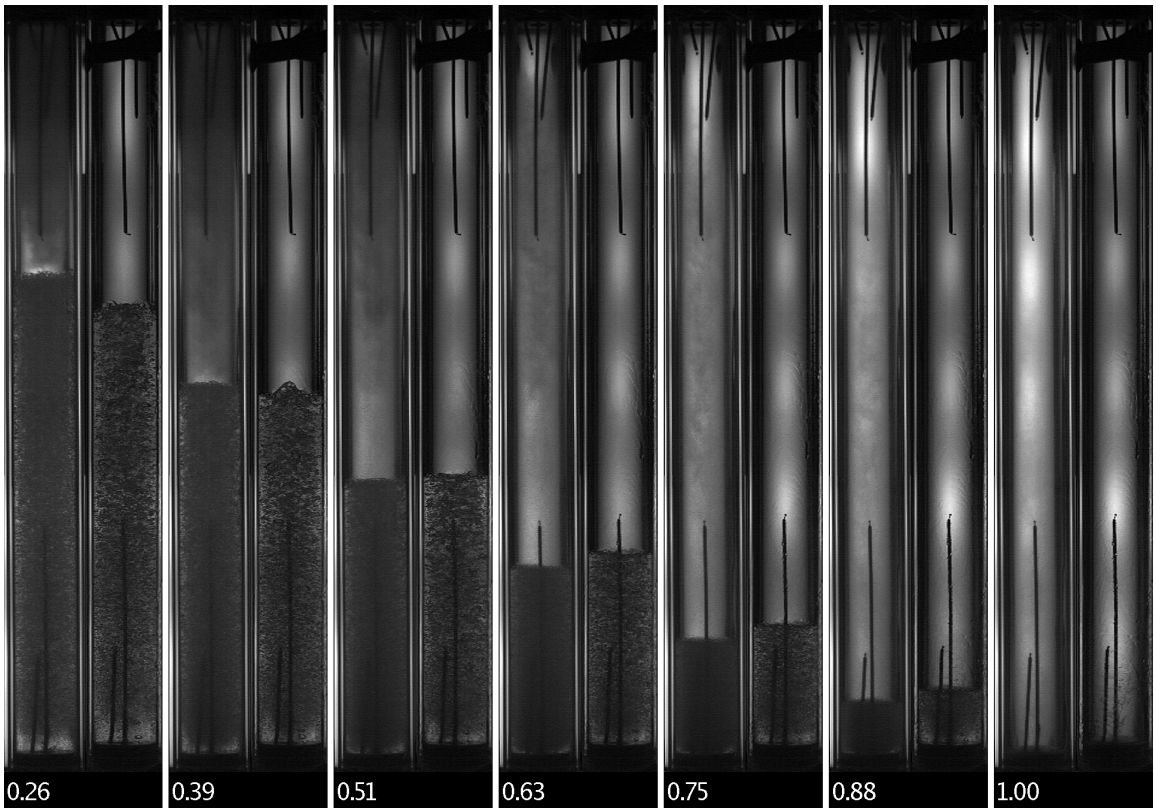

Figure 4.29: Image sequence comparison for later times from the ambient (left) and cold (right) tests. Each pair of frames are taken from the two tests at the same normalized time, indicated by the number below. In the cold test, a hose is partially obstructing the view of the ullage. Tests were performed with CO_2.

pressure achieved is similar to that of the ambient test. The time required for the drop and recovery is slightly less than that of the ambient test as well ($t_{n,max} = 0.115$ vs 0.140). Additionally, the linear portion of the cold test shows more curvature than the ambient test.

One possible explanation for the curvature during the steady state regime is an increase in the amount of heat transferred into the CO_2 from the vessel walls caused by the lower fluid temperature. The slope in the steady state regime also appears to begin relatively straight before slowly increasing in curvature after $t_n \sim 0.6$. As the test progresses the liquid temperature is dropping and one would expect the heat transfer from the vessel walls to therefore increase with time. In addition the liquid volume's surface area-to-volume ratio would increase as well, contributing to the relative effects of wall heat transfer.

Further evidence that suggests that wall heat transfer is to blame can be found in a simplified model of self-pressurizing propellant tanks known as the equilibrium model. This model assumes that the liquid and vapor remain in phase equilibrium throughout the duration of the test. This model has shown to be inaccurate in predicting the exact pressure time history, but is qualitatively correct in several respects and can capture the trends caused by some parameter variations, as described earlier in chapter 2.

In figure 4.30, an equilibrium model was used to assess the effect of varying amounts of wall heat transfer into the liquid. The conditions of the quartz tube test were used as an initial condition, and the wall heat transfer was varied from an adiabatic case up to 100 times greater than the nominal value predicted from free convection correlations. The results clearly show an increase in positive curvature as the wall heat transfer is increased, similar to that of the cold test in figure 4.26.

Perhaps the largest difference between the two tests in the images shown in figures 4.28 and 4.29 is in the bubble sizes. The bubbles in the cold test are clearly much larger than those in the ambient test, both during the transient phase in figure 4.28 and the steady state linear phase in figure 4.29. This can be explained using the theory presented in the previous section.

Other than the bubble size, the two tests only show only minor differences, and these are restricted to the early times. The cold test shows no condensation in the

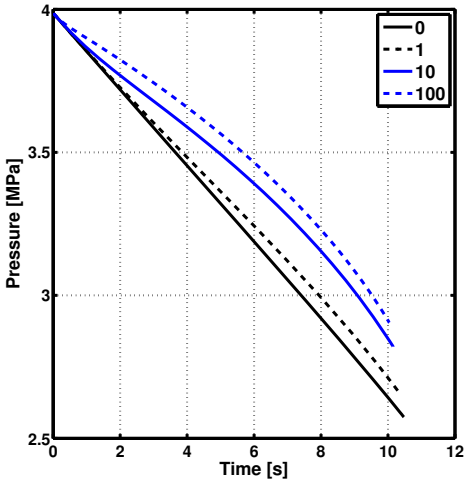

Figure 4.30: Equilibrium model predictions with varying wall heat transfer into the liquid. Legend shows the factor by which wall heat transfer has been scaled by. Simulation performed for CO_2.

ullage but has some boiling before the test begins. This is caused by heat transfer into the vessel from its surroundings, which was minimized by circulating cold heat transfer fluid through the aluminum end caps but could not be stopped completely. These preexisting bubbles may be a cause for the transient pressure drop and recovery of the cold test being similar to the ambient test, in contrast to the results of the hot/ambient comparison. This topic is covered in detail later in section 4.2.4.

Temperature Stratification

The effect of altering the shape of the initial temperature profile while maintaining its mean value is presented in this section. Three tests are compared: one baseline test with a fairly uniform initial temperature profile, one test where the ullage and upper part of the liquid is roughly 4 $°C$ warmer than the base of the tank, and a third where the very bottom of the tank has been cooled to roughly 5 $°C$ below the rest of the tank. See the initial temperature profiles in figure 4.31. For simplicity, these tests will be referred to as the "uniform", "top hot", and "bottom cold" tests respectively.

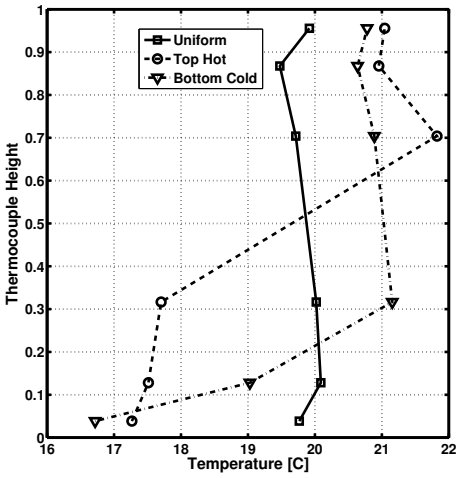

Figure 4.31: Initial temperature profiles from the uniform, top hot, and bottom cold tests. Tests were performed with CO_2.

In each test, all factors other than the shape of the initial temperature profile were matched, however the process used to generate these profiles resulted in less control over the fill level and hence there is more variation (87%, 86%, 90% for uniform, top hot, and bottom cold) than in the previous comparisons between tests. This should not be a concern as the main goal of this section is to highlight different possible behaviors than to make specific direct quantitative comparisons. The three tests all used a 0.559 mm orifice and had test times of 14.64, 14.23, and 14.45 s respectively.

The data from these three tests are shown in figures 4.32 to 4.34. Figure 4.32 shows both pressure traces and the normalized pressure traces while figures 4.33 and 4.34 show a comparison of the still image sequences from these three tests.

The pressure traces in figure 4.32 show very interesting differences in behavior. All three tests have very similar slopes in the linear steady state regime as well as end times, however the initial transients are quite distinct. The uniform test shows the typical behavior seen throughout this chapter. The bottom cold test appears similar at first, however at $t_n \sim 0.3$ the pressure drop halts momentarily before resuming once again at the same slope. The top hot test shows a very different initial transient, with the pressure dropping by 1.10 MPa almost linearly until $t_n \sim 0.2$ before showing a

recovery and transitioning to the steady state regime. As a result of this large pressure drop the steady state pressure is 0.26 MPalower than both the uniform and top hot tests.

The image sequence from early times in figure 4.33 are also quite interesting. The baseline test resembles others, with rapid condensation in the ullage and bubble nucleation first at the base of the tank and later throughout. The top hot test has significant condensation and bubble nucleation, however the bubbles are limited to the upper $\sim 20\%$ of the liquid. The bubble nucleation occurs extremely rapidly however and much faster than either the uniform or bottom cold tests. The bottom cold test also shows condensation and bubble nucleation, but now in the upper $\sim 60\%$ of the liquid and on a timescale similar to the uniform test.

In the later times in figure 4.34 the three tests appear more similar. The bottom cold test shows a region of pure liquid at the base of the tank that disappears around $t_n \sim 0.3$, but other than that all three tests appear to have liquid and vapor that are homogeneous mixtures.

Basic theory can once again explain much of the behavior seen here. In the top hot test the temperature profile shows that the upper part of the liquid (thermocouple

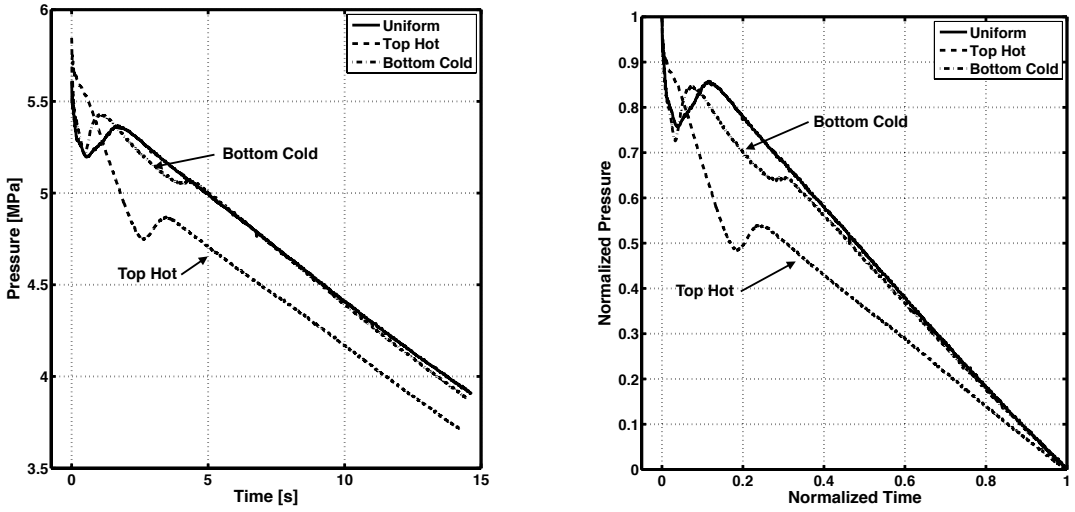

Figure 4.32: Pressure and normalized pressure histories for the uniform, top hot, and bottom cold tests. Tests were performed with CO_2.

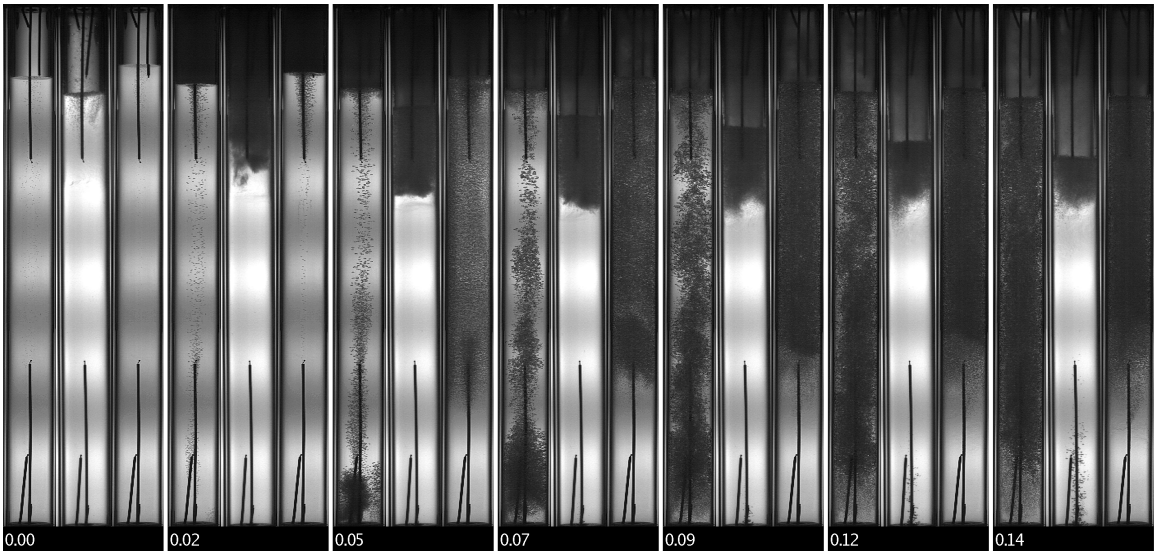

Figure 4.33: Image sequence comparison for early times from the uniform (left), top hot (middle), and bottom cold (right) tests. Each trio of frames are taken from the two tests at the same normalized time, indicated by the number below. Tests were performed with CO_2.

5) is significantly warmer than the rest of the liquid. Therefore as the pressure drops, this region will become superheated and boil before the rest of the tank. Due to the large amount of bubble nucleation occurring in this region seen in the video data, it appears that the tank reaches a linear steady state regime with solely this upper part of the liquid boiling. Once the temperature in this region has dropped low enough to be similar to the liquid below it, the rest of the tank becomes superheated and bubbles begin to nucleate there. This is beginning at $t_n \sim 0.14$, where some bubbles can be seen rising from the base of the tank. This is a new transient regime being established, complete with a pressure recovery and second steady state linear region.

In the bottom cold test, the behavior can be understood as essentially the same, with relatively different amounts of the hot and cold liquid. In top hot test the hot part of the liquid was only 20%, but in the bottom cold test it is the majority.

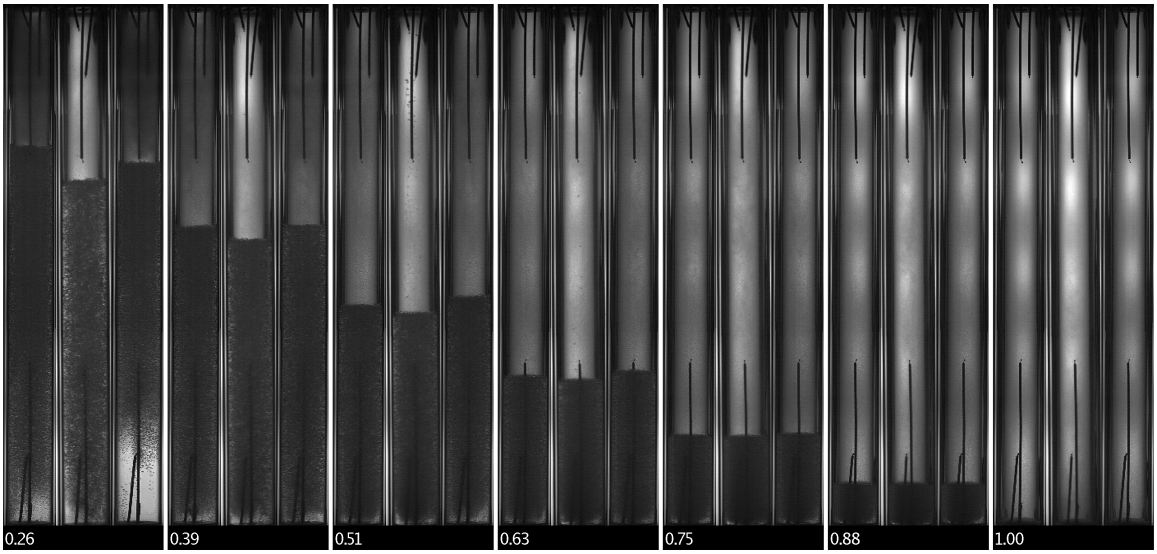

Figure 4.34: Image sequence comparison for later times from the uniform (left), top hot (middle), and bottom cold (right) tests. Each trio of frames are taken from the two tests at the same normalized time, indicated by the number below. Tests were performed with CO_2.

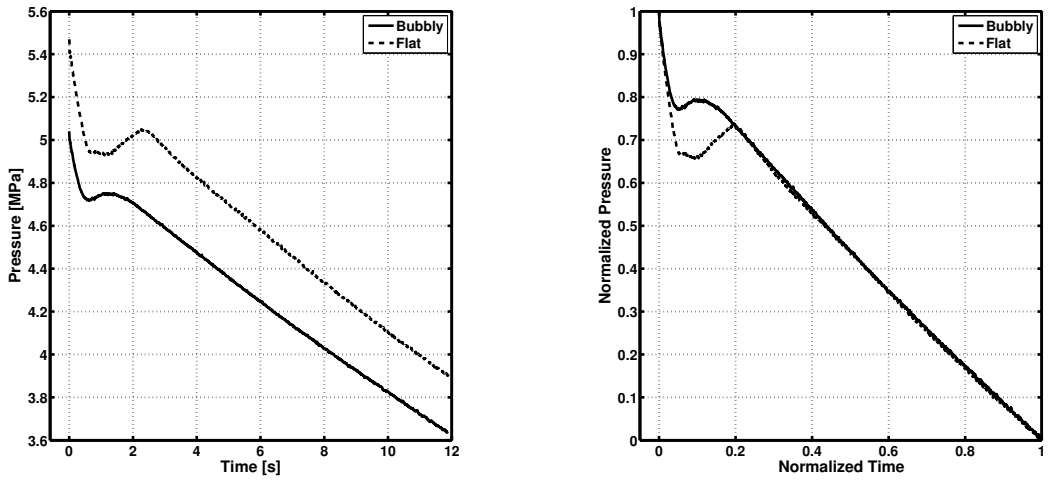

Figure 4.35: Pressure and normalized pressure histories for the flat and bubbly tests. Tests were performed with CO_2.

4.2.4 Initial Bubble Population

An initial bubble population can be established in two primary ways: either venting the ullage until the liquid begins to boil or heating the liquid directly. In this section two tests are compared that have different initial bubble populations, one with few bubbles initially and a second with a large population established by venting the ullage. To be clear, the ullage was vented prior to the start of the test and not during the test. For simplicity these two tests will be referred to simply as "flat" and "bubbly."

All other parameters of the two tests were reasonably matched, including the fill levels (71%), mean initial temperatures (17.4, 19.4°C), the initial temperature profiles, and orifice diameters (0.559 mm). While the temperature profiles were similar for these two tests, they were slightly different and resulted in different initial pressures and test times for the two tests, $t_{LRO} = 11.87, 11.93$ for the flat and bubbly tests respectively. The data from these two tests are shown in figures 4.35 to 4.38. Figure 4.35 shows both pressure traces and the normalized pressure traces, while figure 4.36 shows the initial temperature profiles. Figures 4.37 and 4.38 show a comparison of the still image sequences from these two tests.

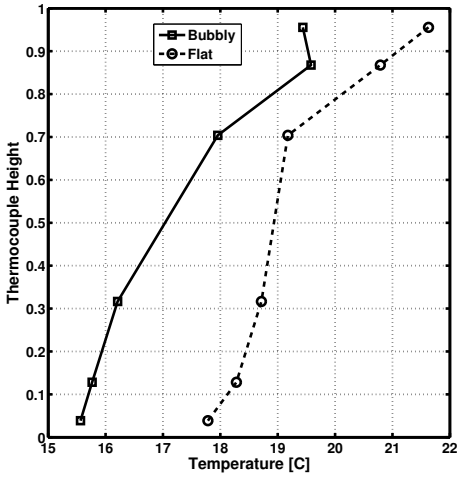

Figure 4.36: Initial temperature profiles from the flat and bubbly tests. Tests were performed with CO_2.

The pressure traces in figure 4.35 primarily show differences in the initial regime and not in the subsequent steady state regime. For the flat test a much larger pressure drop and recovery is evident ($P_{n,min} = 0.660, 0.771$, $P_{n,max} = 0.729, 0.794$) however once the steady state regime is entered the two appear quite similar.

The images from the early portion of the tests shown in figure 4.37 show significant differences. The existing bubbles are seen to grow immediately after the pressure drops, while bubbles are not seen in the flat test until $t_n \sim 0.07$. This results in the establishment of a uniform mixture much earlier than in the flat test, also evidenced by the pressure traces discussed previously. In the images from the later portion of the test (figure 4.38) the two appear quite similar.

The cause for this difference in behavior lies in the bubble nucleation process. In the flat test, a large number of bubbles are not present until the superheat builds to a relatively large value. However in the bubbly test, a population already exists and as the superheat begins to build these bubbles can respond by growing and expanding, thereby slowing the drop in pressure and increase in superheat. One unfortunate result of this study is exemplified by the first frame in figure 4.37, where the bubbles are not yet visible in the bubbly test. Effectively this means that a key part of the initial condition (the presence of a large initial bubble population) is not discernible

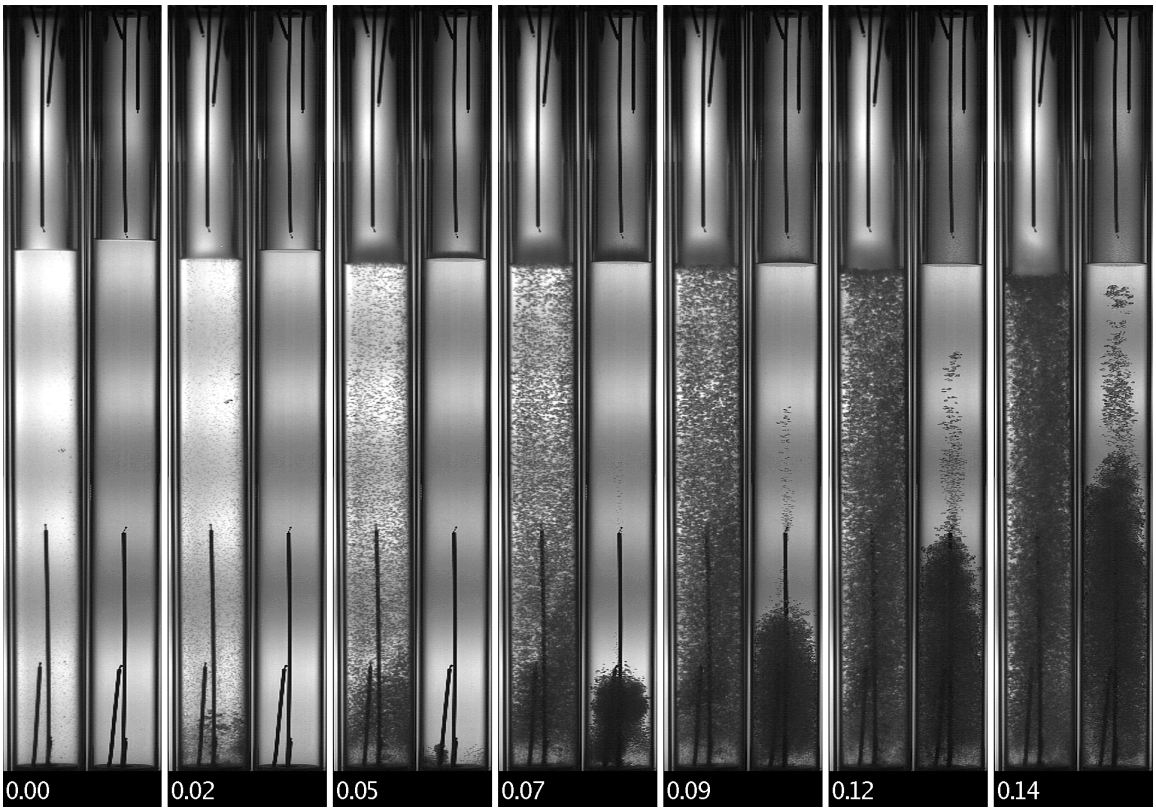

Figure 4.37: Image sequence comparison for early times from the flat (right) and bubbly (left) tests. Each pair of frames are taken from the two tests at the same normalized time, indicated by the number below. In the cold test, a hose is partially obstructing the view of the ullage. Tests were performed with CO_2.

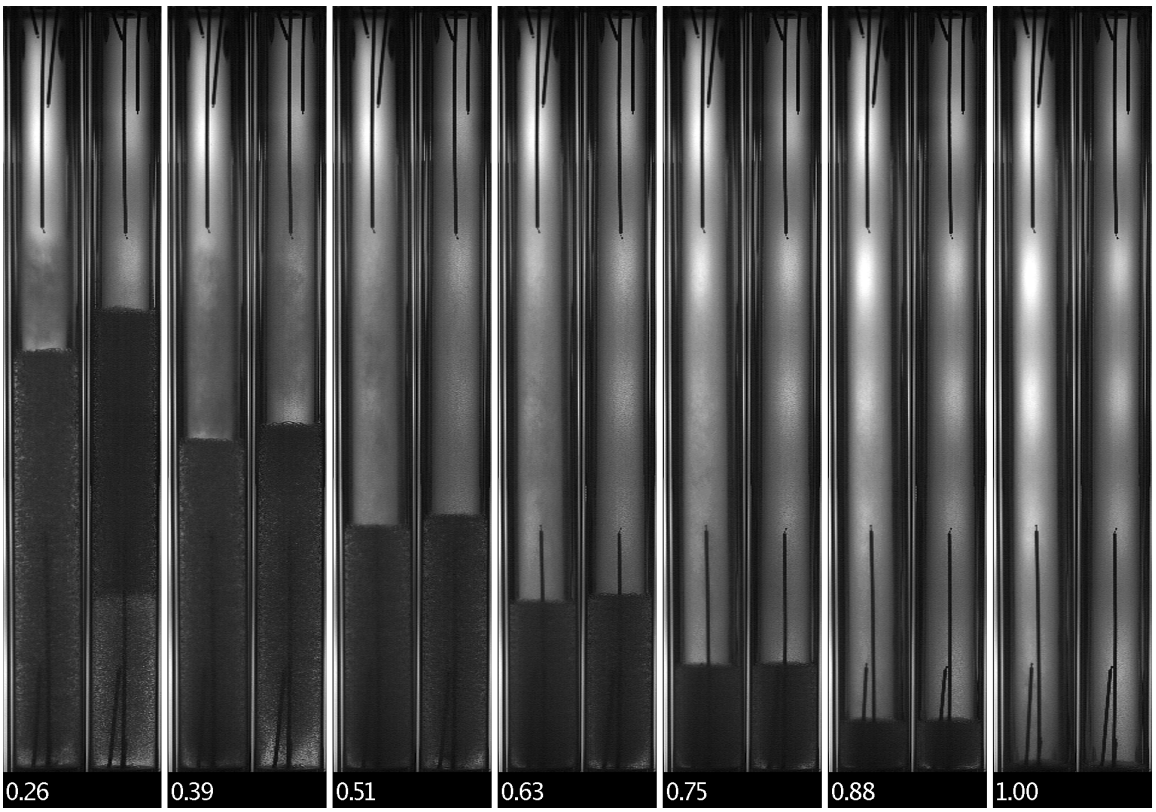

Figure 4.38: Image sequence comparison for later times from the flat (right) and bubbly (left) tests. Each pair of frames are taken from the two tests at the same normalized time, indicated by the number below. In the cold test, a hose is partially obstructing the view of the ullage. Tests were performed with CO_2.

from the video data alone, and information about the filling history is also required, namely whether or not the ullage was vented enough to cause bubble nucleation.

4.2.5 Feed System Length

One difference between the experimental systems used here and real propulsion systems is the extremely short distances from the tank to the main valve and from that valve to the orifice. On a rocket these distances may be considerably longer. While changing the distance from the tank to the main valve with this system was not feasible, adding additional tubing length between that valve and the orifice was trivial. Therefore, in this section three tests will be compared: one baseline similar to the tests shown earlier, one with an additional 24 cm of tubing, and one with an additional 52 cm of tubing. These will be referred to simply as the 0 cm, 24 cm, and 52 cm tests, respectively.

Other than the additional tubing the other parameters of these tests were close to identical: mean initial temperatures (20.6, 20.0, 20.7 $°C$), fill levels (83, 84, 83%), test times (14.2, 14.3, 14.6 s), and the orifice diameters (0.559 mm). The data from these three tests are shown in figures 4.39 to 4.42. Figure 4.39 shows both pressure traces and the normalized pressure traces while figures 4.41 and 4.42 show a comparison of the still image sequences from these three tests.

The pressure time histories show very different transient regimes while in contrast the steady state regimes are quite similar for the three tests. Interestingly, the 52 cm test shows quite different behavior from the 24 cm test. The two tests with additional feed line length both show a pressure that drops much more rapidly in the transient regime than the 0 cm test. The 52 cm test goes on to reach a pressure maximum and enter the steady state regime much sooner than the other two tests. The 24 cm test has a pressure minimum and maximum similar to the 0 cm test but shifted downwards. The normalized pressure traces again emphasize that after the transient regime the three tests are quite similar.

The image sequences for the early times show significant differences in behavior, while the later images from the later times show again that after the transient regime

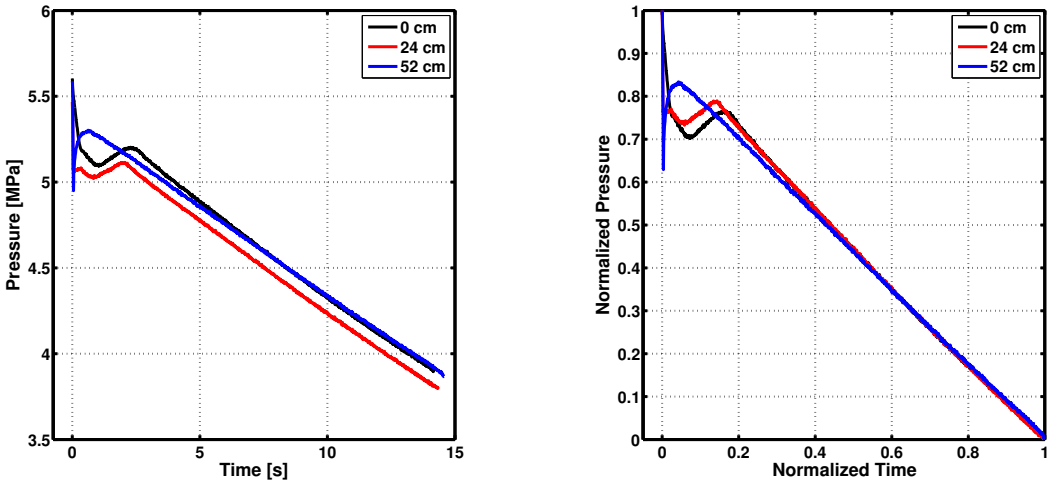

Figure 4.39: Pressure and normalized pressure histories for the tests with different feed line lengths. Tests were performed with CO_2.

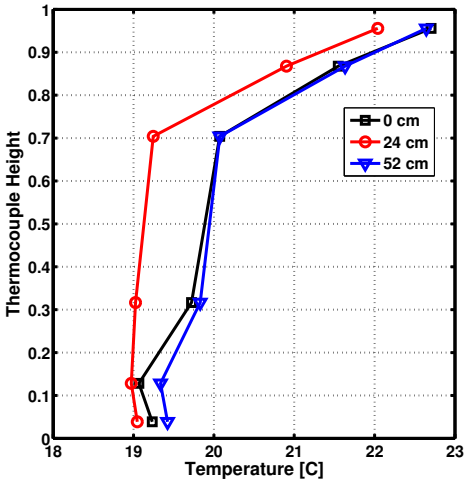

Figure 4.40: Initial temperature profiles from the tests with different feed line lengths. Tests were performed with CO_2.

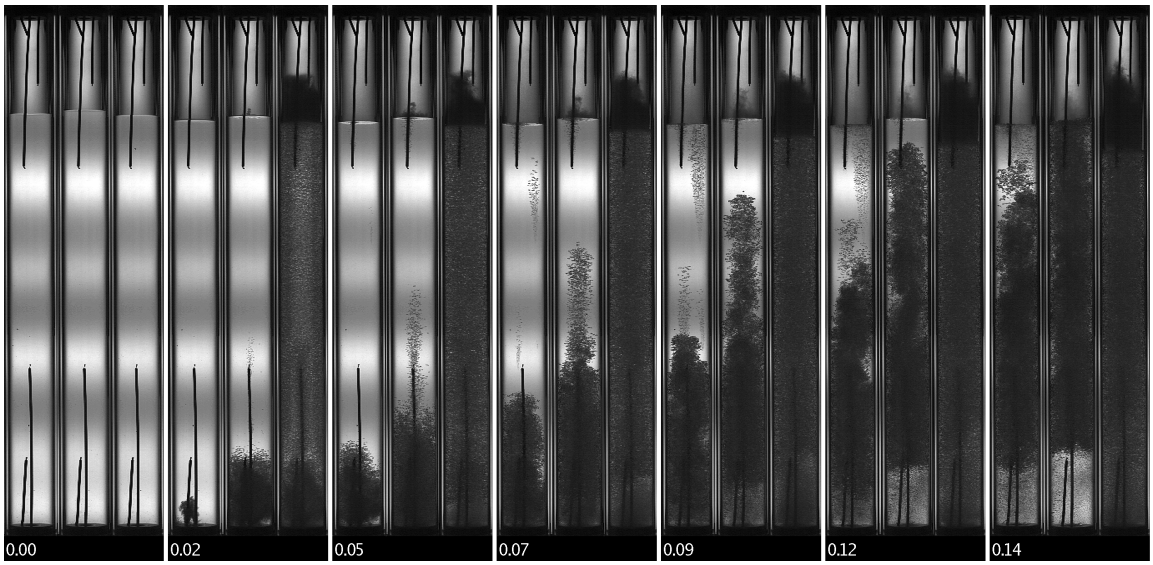

Figure 4.41: Image sequence comparison for early times from the different feed line length tests. The left image shows the baseline with no additional tubing, the middle image shows the test with 24 *cm* of additional tubing, and the right shows the test with 52 *cm*. Each trio of frames are taken from the two tests at the same normalized time, indicated by the number below. Tests were performed with CO_2.

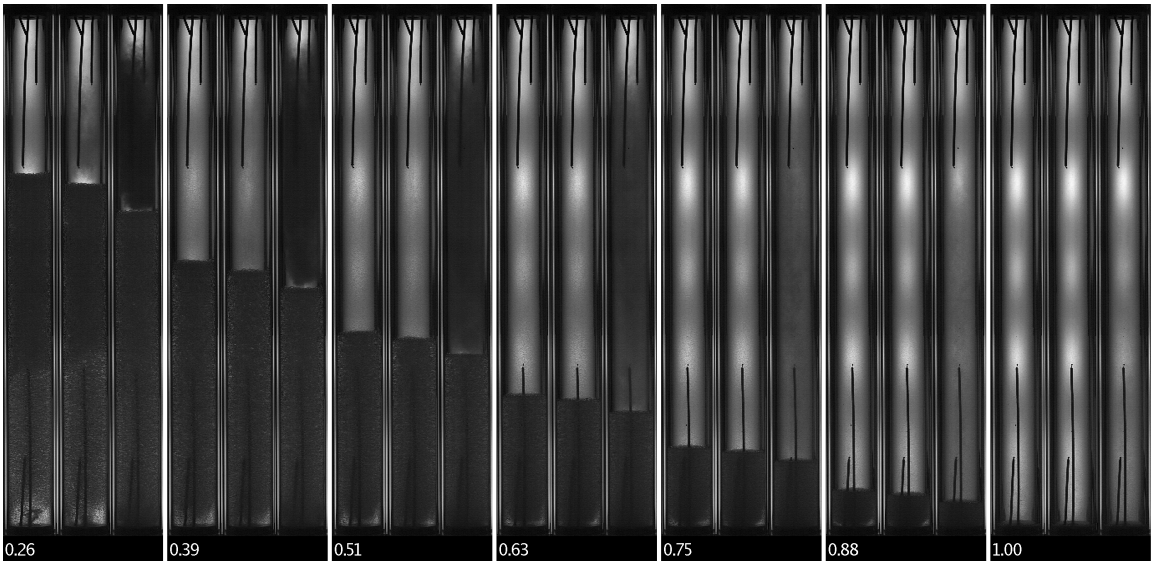

Figure 4.42: Image sequence comparison for later times from the different feed line length tests. The left image shows the baseline with no additional tubing, the middle image shows the test with 24 *cm* of additional tubing, and the right shows the test with 52 *cm*. Each trio of frames are taken from the two tests at the same normalized time, indicated by the number below. Tests were performed with CO_2.

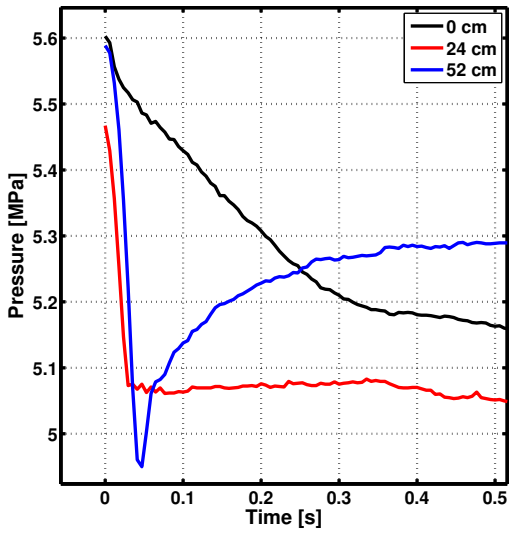

Figure 4.43: Pressure time histories for the 0 *cm*, 24 *cm*, and 52 *cm* tests. Tests were performed with CO_2.

the three tests behave similarly. In the early times for the 52 *cm* test we see nucleation throughout the quartz tube at $t_n = 0.02$, with nucleation limited to the bottom of the tank in the 24 *cm* test and even less nucleation in the 0 *cm* test. As time progresses the 52 *cm* test appears unchanged up through $t_n = 0.14$ while the other two tests progress similarly to other tests, with nucleation proceeding up the liquid towards the ullage. In the later times the only difference of note is in the ullage: the 52 *cm* test shows significant condensation while the other two tests show little or none.

When the test begins and the valve opens, fluid rushes out of the tank to fill the volume between the valve and the orifice. In this brief time the orifice is not restricting the flow rate and so it can be quite high. In the tests with additional tubing, there is a larger volume to fill and so this initial rush of liquid CO_2 is larger. To give more detail, figures 4.43 and 4.44 show the pressure time histories and image sequence for these very early times.

Both the 24 *cm* and 52 *cm* have rapid initial pressure drops and in fact the 52 *cm* test has a pressure that drops and recovers so fast that the sample rate of 200 Hz is insufficient to resolve the minimum. The minimum pressure measured is 5.066 MPa,

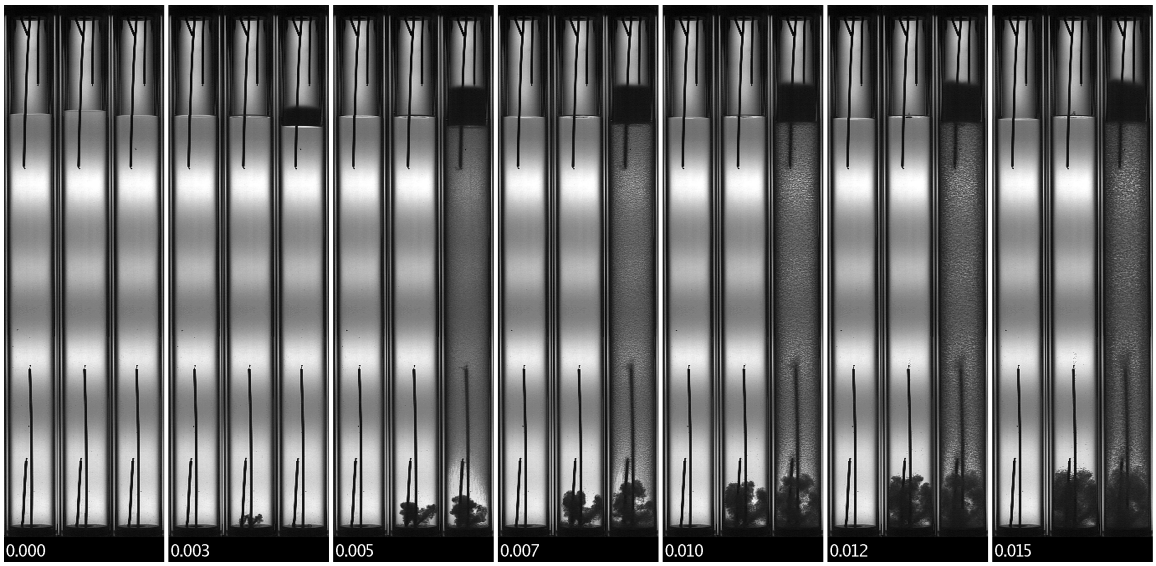

Figure 4.44: Image sequence comparison for very early times from the different feed line length tests. The left image shows the baseline with no additional tubing, the middle image shows the test with 24 *cm* of additional tubing, and the right shows the test with 52 *cm*. Each trio of frames are taken from the two tests at the same normalized time, indicated by the number below. Tests were performed with CO_2.

which corresponds to a superheat of $4.9°C$ in the liquid. In the 24 cm test the pressure drops almost as rapidly but the minimum is much higher, and in fact the pressure stays nearly constant for about 250 ms. In this case the maximum superheat is only $3.4°C$.

The image sequence from these early times shows more similarities between the two tests with additional tubing. At $t_n = 0.003$ we see in both that the liquid level has dropped and at $t_n = 0.005$ there is a burst of bubbles formed at the base of the tank. There are differences too, with significant condensation in the 52 cm test and condensation in the ullage as well. As time goes on the bottom of the tank in both tests appears identical, with the initial burst of bubbles growing and rising. However the rest of the tank is of course quite different.

We can conceptualize the processes seen here in the following manner: As the valve opens and the fluid rushes out to fill the tubing, the sudden superheat causes nucleation at the base of the tank and a sudden jet of bubbles is formed. In the 24 cm test the tubing volume is filled soon after this and the fluid flow rate suddenly *decreases* which causes the nucleation of new bubbles to slow or stop. The existing bubbles grow and cause the pressure to stay relatively constant.

In the 52 cm case however the flow rate remains high and the pressure continues to drop, causing bubble nucleation on less favorable sites along the wall of the quartz tube. After this however the tubing has been filled and the flow rate decreases as well, yet leaving a huge population of bubbles that have just been nucleated. These bubbles all grow, increasing the system pressure and establishing the steady state regime.

4.2.6 Valve Opening Time

Given that much attention is being paid to the transient period at the beginning of a test, one potential controlling factor is the speed at which the valve opens to let the CO_2 flow out of the test vessel. In this system, this valve is a normally closed pneumatically actuated quarter-turn ball valve (Swagelok SS-42GS4-33) that requires roughly 200 ms to open. To determine the effect that the valve speed has on the system dynamics, tests were completed at reduced air pressure on the pneumatic actuator.

First, the valve speed was measured as a function of the driving air pressure. This was accomplished by using the high speed camera to observe the valve's rotational position as it actuated, with the results are shown in figure 4.45. In these tests the test vessel was pressurized with CO_2 at normal test pressures of approximately 5.5 MPa to replicate the correct loading conditions on the valve. From this plot it is clear that as the driving air pressure is reduced, the valve turns more slowly and at the lowest driving pressure the valve never achieves its fully open position.

In figure 4.46, the time required for the valve to sweep the center $\pi/4$ rad of its rotation is plotted as a function of the driving pressure. This metric is used rather than the full $\pi/2$ rad because it is often difficult to determine the exact time at which the valve begins or stops moving, however because the plots of 4.45 are roughly linear we can expect the total valve rotation time to be about twice the time required for $\pi/4$ rad. For all other tests reported in this thesis the driving pressure was between 750 and 850 kPa and no significant differences in test results were found in the range of 860 to 620 kPa.

Here, two tests will be compared with high and low driving pressures (689 and 414 kPa respectively) and based on figure 4.46 are expected to have valve opening times that differ roughly by a factor of three. They will be referred to as the "fast" and "slow" tests for simplicity. All other features of the two tests were matched, including the orifice diameter (0.813 mm), fill level (79, 81%), mean initial temperature (17.2, 19.2 $°C$) and initial temperature profiles. The test times were also quite similar: 6.44 and 6.64 s.

The data from these two tests are shown in figures 4.47 to 4.50. Figure 4.47 shows

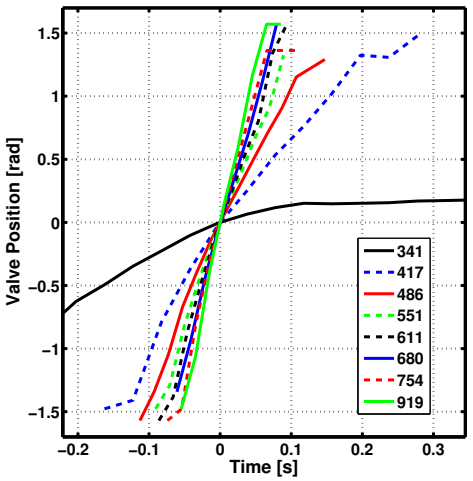

Figure 4.45: Valve position versus time for various driving air pressures. Legend shows the air pressure in kPa.

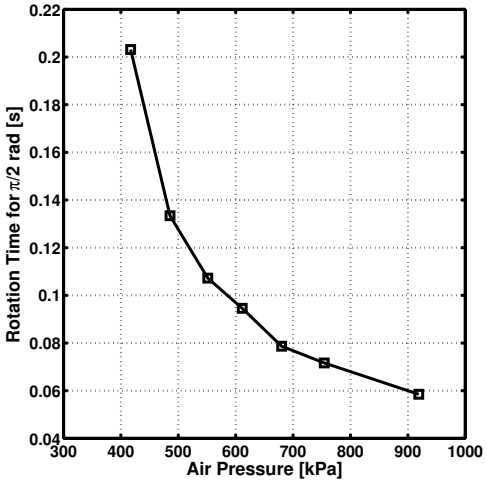

Figure 4.46: Valve rotation time versus the driving air pressure. Rotation time is measured as the time required for the middle $\pi/4$ rad of the total $\pi/2$ rad.

the pressure traces and the normalized pressure traces, while figure 4.48 shows the initial temperature profiles. Figures 4.49 and 4.50 show a comparison of the still image sequences from these two tests.

The pressure traces of the two tests are shifted vertically from each other, but this is merely result of the slightly different starting temperatures. The normalized pressure traces are however very similar, with only slight differences visible during the transient regime. The image sequences in figures 4.49 and 4.50 are also quite similar. In the early times the condensation of the ullage in the fast test is uniform while that of the slow test is limited to the region close to the liquid. We can also see beginning at $t_n = 0.07$ that thermocouple #5 is an active nucleation site in the fast test but not in the slow test, with a steady stream of bubbles rising from it. In the later times the two tests do not show any significant difference.

The similarity of these two tests suggests that the valve opening time is not an important factor, at least as long as the valve opens relatively quickly ($t_{valve} \lesssim 0.4$ s). This may be explained by the fact that the valve used here is a full-port ball valve

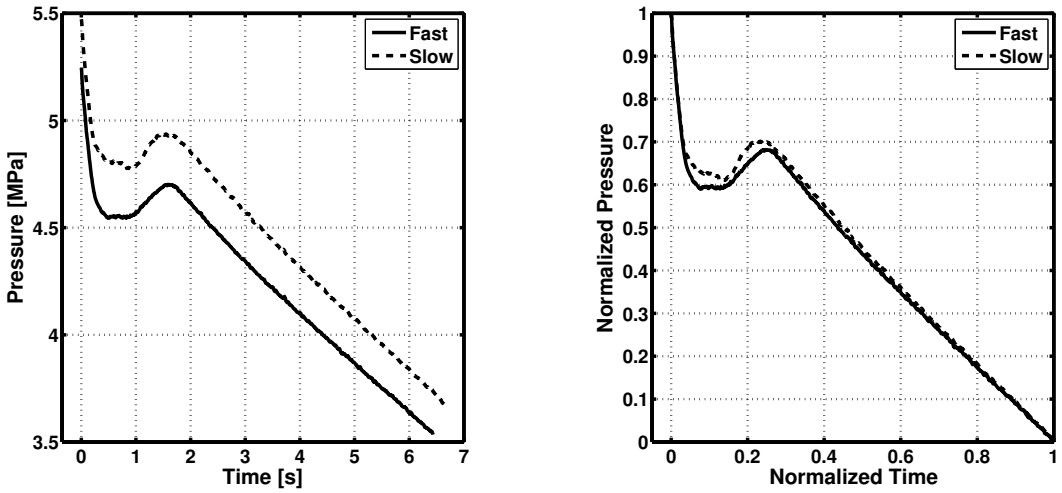

Figure 4.47: Pressure and normalized pressure histories for the fast and slow valve speed tests. Tests were performed with CO_2.

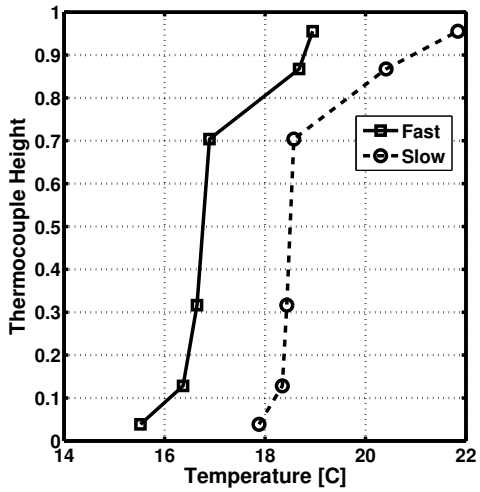

Figure 4.48: Initial temperature profiles from the fast and slow valve speed tests. Tests were performed with CO_2.

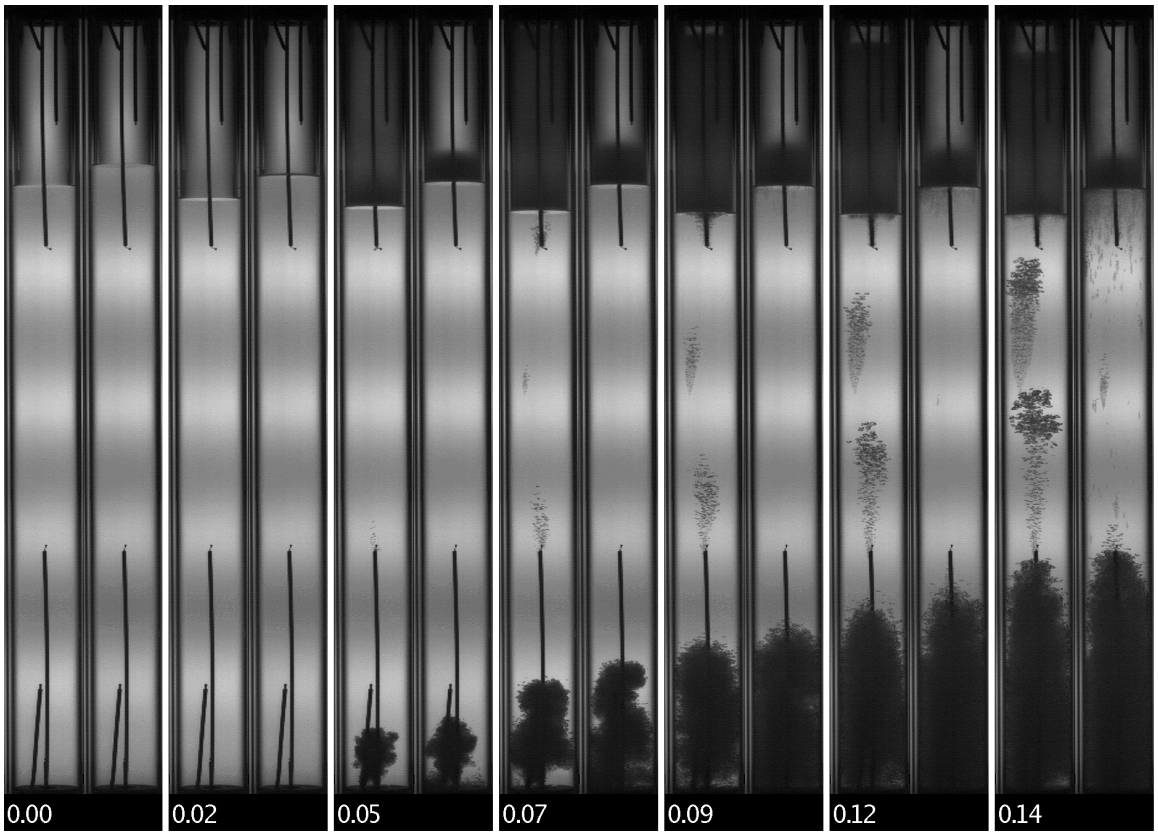

Figure 4.49: Image sequence comparison for early times from the tests with fast (left) and slow (right) valve speeds. Each pair of frames are taken from the two tests at the same normalized time, indicated by the number below. Tests were performed with CO_2.

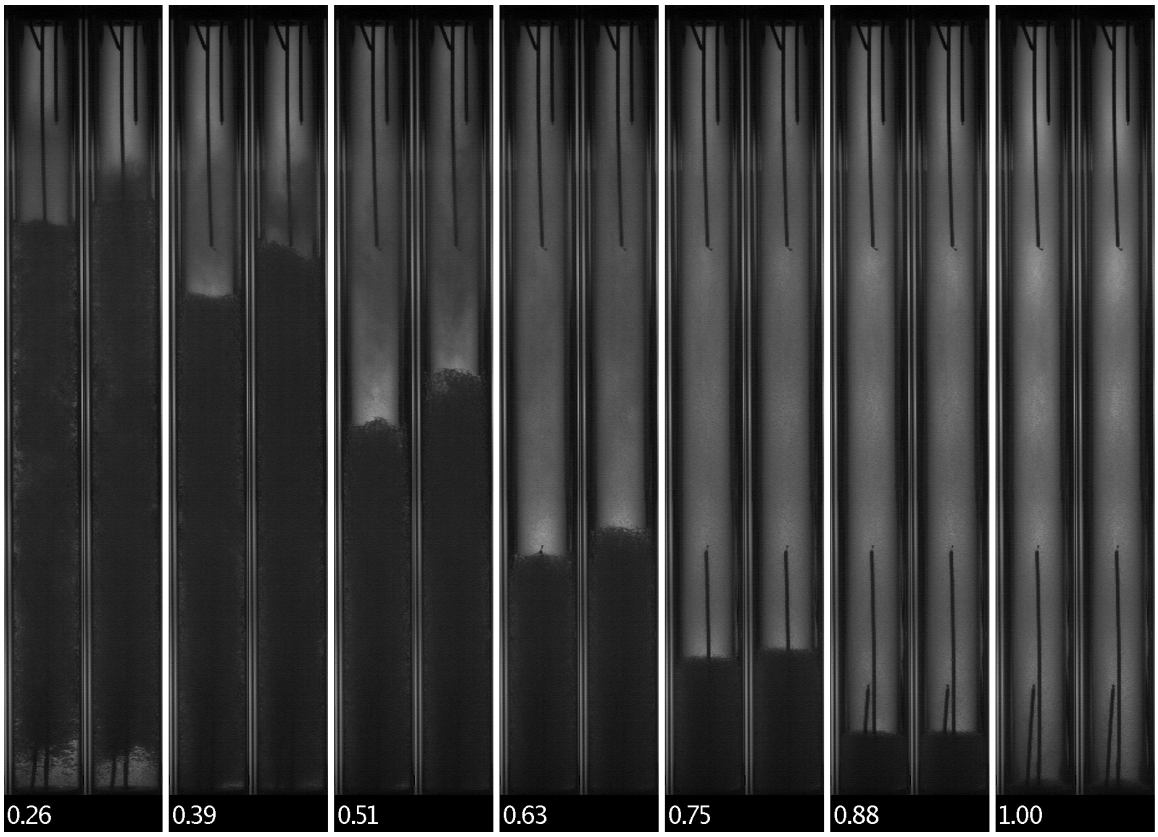

Figure 4.50: Image sequence comparison for later times from the tests with fast (left) and slow (right) valve speeds. Each pair of frames are taken from the two tests at the same normalized time, indicated by the number below. Tests were performed with CO_2.

and the orifices used are quite small in comparison, meaning that even if the valve were only partially opened it would be a negligible flow restriction when compared to the orifice.

4.2.7 Vessel size

The primary purpose of the flat glass gauge system is to evaluate scaling effects by doing comparisons with the quartz tube system. When compared with the quartz tube, it is approximately a factor of 1.9 larger in each dimension and has a volume 6.72 times larger. The primary differences in terms of recorded data are the smaller window area (12.7 mm wide) and increased number of thermocouples within the vessel (10 equally spaced probes). In this section a test from the flat glass gauge is compared with one from the quartz tube to see how the results differ in the larger vessel. All experimental parameters were matched, including fill level (80, 82%), mean initial temperature (18.7, 17.6 $°C$), and initial temperature field. Values given are for the quartz tube test and flat glass gauge test respectively. The orifice used in the flat glass gauge test was selected to give a similar t_{LRO} to the quartz tube test (6.59, 5.96 s). Parameters could not be as well matched as with the earlier comparisons between quartz tube tests.

The data from these two tests are shown in figures 4.51 to 4.54. Figure 4.51 shows both pressure traces and the normalized pressure traces, while figure 4.52 shows the initial temperature profiles. Figures 4.53 and 4.54 show a comparison of the still image sequences from these two tests. It may be useful to review the annotated still images presented earlier (figures 3.18 and 3.22) before examining the image sequences.

Beginning with the video data, in the transient regime condensation of the vapor is similar between the two tests and occurs as an upward-moving wave like that of the hot test (figure 4.22) shown earlier. Bubble nucleation in the liquid is quite different however with bubbles nucleating uniformly along the entire length of the flat glass gauge at $t_n = 0.05$, while the quartz tube test shows nucleation limited to the bottom during this time and significant nucleation on the walls not happening until $t_n \sim 0.11$. In the later times shown in figure 4.54 the same basic features are visible in both tests, however the flat glass gauge's liquid level appears substantially higher than that of the quartz tube. In addition while the ullage in the quartz tube appears to have condensed throughout the entire length by $t_n = 0.48$, in the flat glass gauge this does not occur until $t_n = 0.65$.

The pressures traces shown in figure 4.51 also show much similarity between the

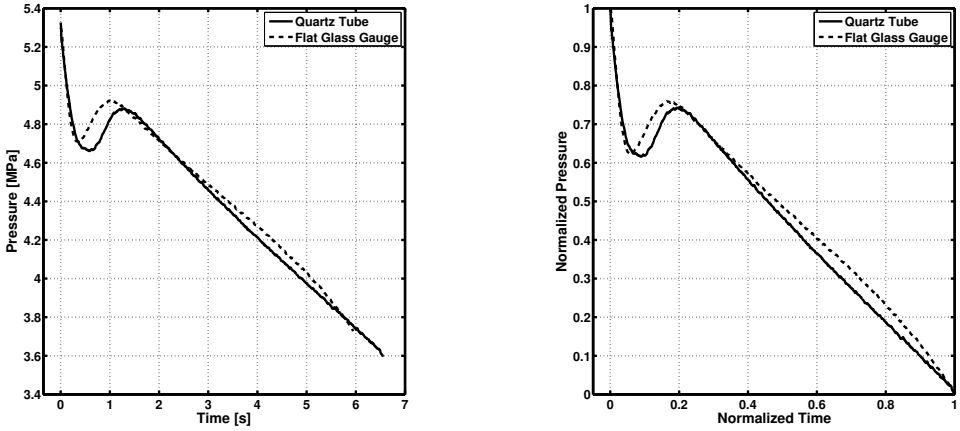

Figure 4.51: Pressure and normalized pressure time histories for quartz tube and flat glass gauge tests. Tests were performed with CO_2.

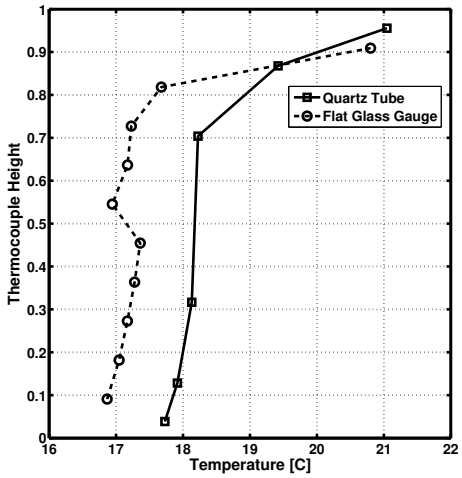

Figure 4.52: Initial temperature profiles for the quartz tube and flat glass gauge tests.

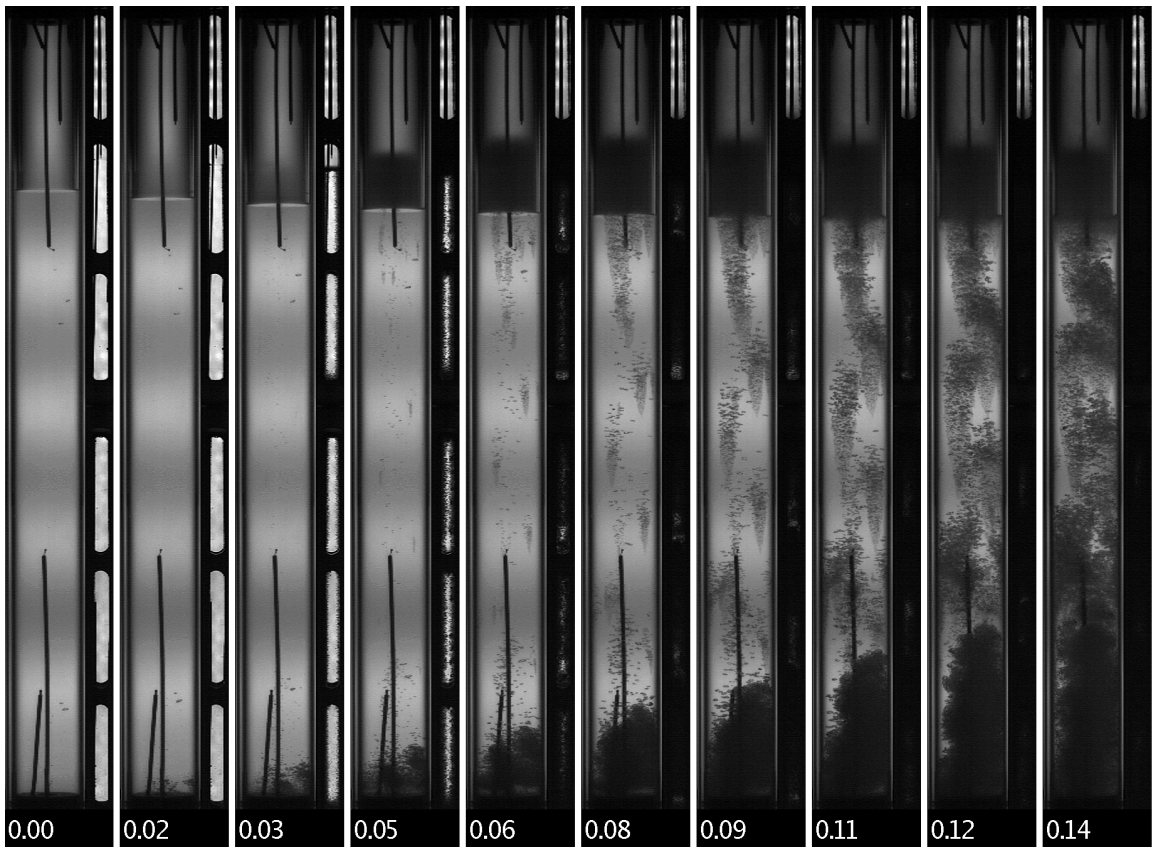

Figure 4.53: Image sequence comparison for early times from the quartz tube (left) and flat glass gauge (right) tests. Each pair of frames are taken from the two tests at the same normalized time, indicated by the number below. Tests were performed with CO_2.

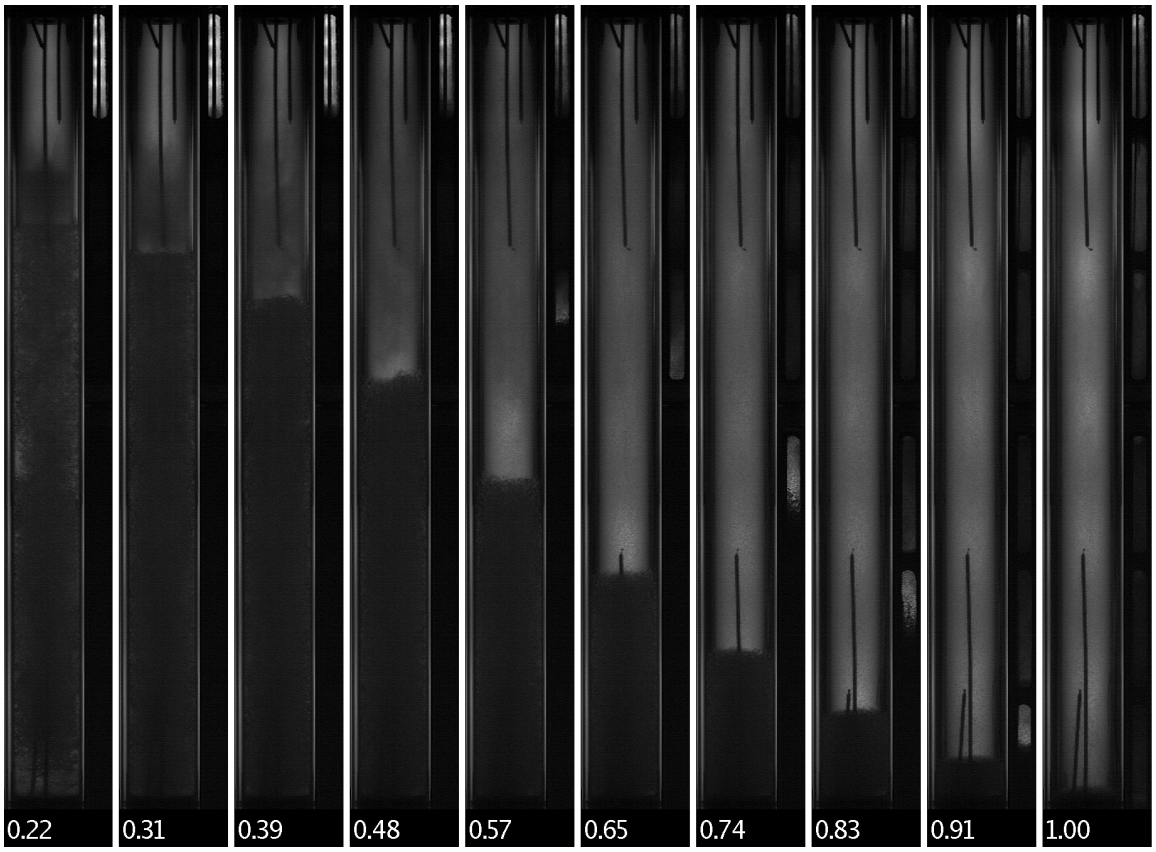

Figure 4.54: Image sequence comparison for later times from the quartz tube (left) and flat glass gauge (right) tests. Each pair of frames are taken from the two tests at the same normalized time, indicated by the number below. Tests were performed with CO_2.

two vessels' results. Due to slight differences in the initial temperature and pressure and t_{LRO}, the two are best compared using the normalized pressure histories. In the transient regime the pressure drops are nearly identical, while the quartz tube recovers to a lower pressure than the flat glass gauge ($P_{n,max} = 0.741, 0.759$). The flat glass gauge pressure history recovers more quickly than the quartz tube ($t_{n,max} = 0.180, 0.218$) as well. In the steady state regime the slopes are similar, but the flat glass gauge's data show positive curvature while the quartz tube data shows none.

This curvature was also seen in the reduced temperature test's pressure trace (figure 4.26) and may be a result of heat transfer into the vessel. In this test the heat transfer rate was enlarged due the high thermal inertia and thermal diffusivity of the stainless steel relative to the quartz, while previously the increased temperature differential between the CO_2 and the ambient contributed.

4.2.8 Exotic Conditions

In this section we briefly examine several conditions that are of little importance for most propulsion applications, but are still interesting for their thermodynamic or fluid mechanic behavior. First, an extremely high flow rate test will be discussed, followed by two tests at elevated temperature. The first of these has an initial temperature just below the critical point while the second's is above it.

Extremely High Flow Rate

To examine the effects of extremely high flow rates, a test was done in which no restriction orifice was used in the tubing downstream of the tank. After the CO_2 flowed through the main valve, it was exhausted directly to the atmosphere. The valve used is "full port," meaning that when open the flow path is the same as the tubing and so there is no restriction between the exit of the tank and the end of the tube (11.4 cm). This produced a large flow rate and a test time of only $t_{LRO} = 0.62$ s. This short time is impractical for propulsion applications.

The basic parameters of the test are as follows: fill level of 84%, mean initial temperature of 12.0 $°C$. The data from this test is shown in figures 4.55 through

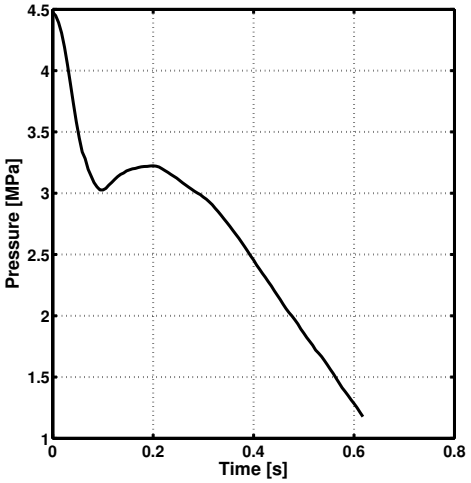

Figure 4.55: Pressure time history for the extremely high flow rate test. Test performed with CO_2.

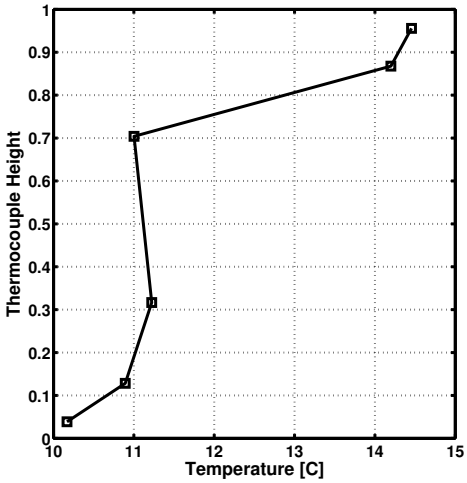

Figure 4.56: Initial temperature profile from the extremely high flow rate test. Test performed with CO_2.

4.59. Figure 4.55 shows the pressure time history and figure 4.56 shows the initial temperature profile. An image sequence from the early test times is shown in figure 4.57 while one for the later times is shown in figure 4.58.

Beginning with the pressure trace in figure 4.55, it is perhaps remarkable that the features are similar to most of the previous test results, with a transient drop and recovery followed by a linear steady state. In this case though the transient regime is nearly equal in length to the steady state. The temperature profile in figure 4.56 shows that the liquid was somewhat cold ($\sim$ 11 $^{\circ}C$), while the ullage was warmer at around 14.5 $^{\circ}c$. This is reflected in the early time image sequence (figure 4.57) where the ullage does not condense appreciably until $t_n = 0.09$. We also have little or no bubble nucleation till this time, a result of the initial pressure being above the liquid's saturation pressure.

When bubble nucleation begins, it is clearly forming on the walls of the tube as well as the thermocouple probe. Another image sequence is given in figure 4.59 to show more detail of this bubble nucleation process. One feature not observed in other tests is the downward velocity of bubbles after they have departed. This is most clearly seen in the lower thermocouple probes - although bubbles are visible on

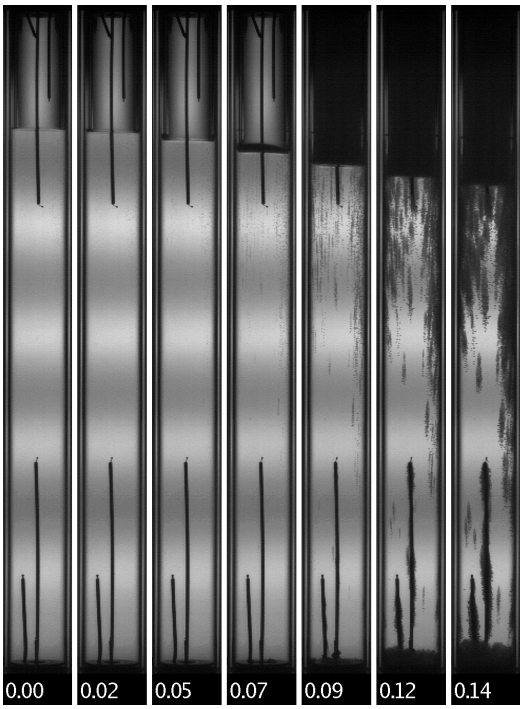

Figure 4.57: Image sequence of early times from the extremely high flow rate test. The number below each frame denotes the normalized time. Test performed with CO_2.

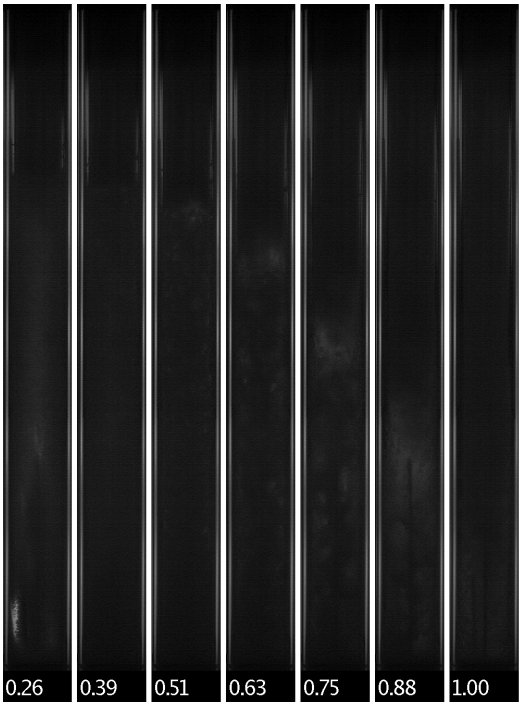

Figure 4.58: Image sequence of later times from the extremely high flow rate test. The number below each frame denotes the normalized time. Test performed with CO_2.

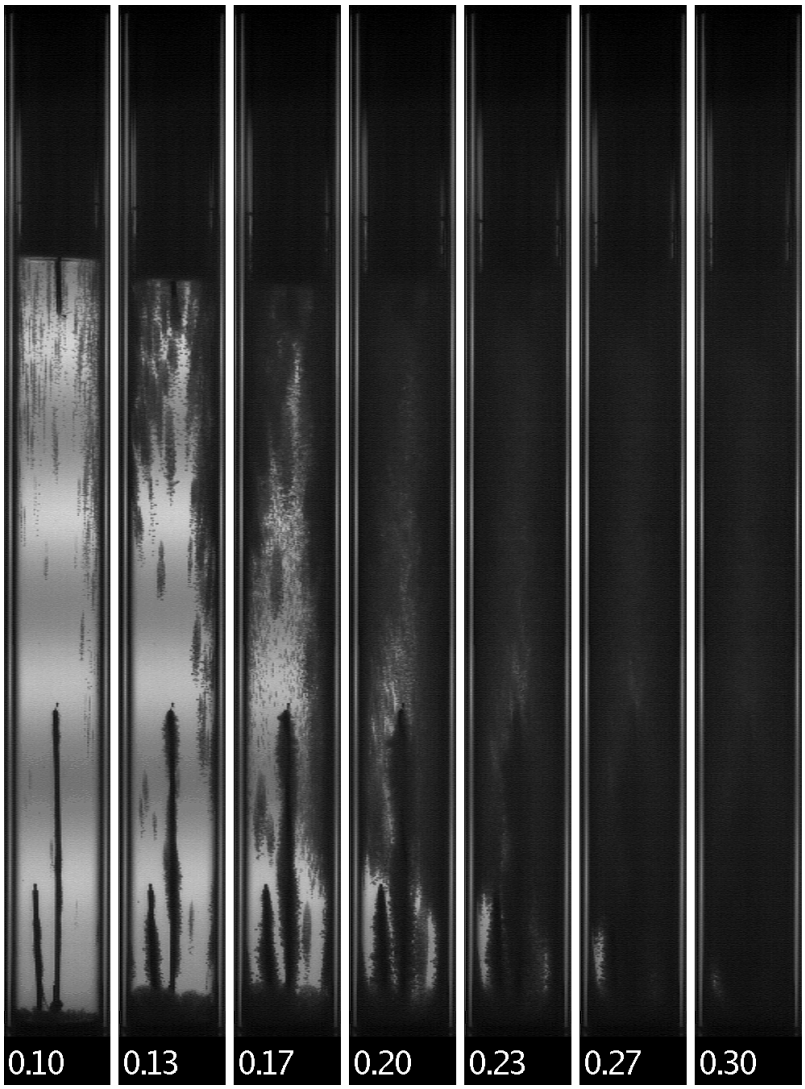

Figure 4.59: Image sequence highlighting bubble nucleation in the extremely high flow rate test. The number below each frame denotes the normalized time. Test performed with CO_2.

them as early as $t_n = 0.10$, they do not rise above the probe junction but instead form a downward-moving wake. This is because the liquid flow rate is so high that it is greater than the rise velocity caused by the bubbles' buoyancy.

In later times, unfortunately very little is visible. The high flow rate has generated a high level of superheat within the liquid and subcooling in the vapor, in turn causing massive amounts of bubble and droplet nucleation that turn the liquid and vapor into homogeneous mixtures with qualities far from 0 and 1.

A boiling liquid expanding vapor explosion (BLEVE) is a concept somewhat related to self-pressurizing propellant tanks. In a BLEVE a tank of liquid at equilibrium with its vapor is ruptured and the sudden pressure decrease causes the liquid to become highly superheated. This high superheat causes the liquid to rapidly vaporize and the resulting expansion of the fluid generates a strong pressure wave that can cause significant damage. There are numerous occasions in which BLEVEs have occurred with flammable chemicals such as propane or methane, which can cause additional damage from the formation of a large fireball as the vapor burns with the air.

The extremely high flow rate test described in this section somewhat resembles the conditions of a BLEVE however there was no detected overpressure and hence the CO_2 did not undergo a BLEVE. This may be a result of the relatively low volume ratio between the liquid and vapor. For CO_2 in this test at 11 $°C$, the ratio $v_{vap}/v_{liq} = 6.1$, while for propane at similar conditions it is 36.2, and for methane at standard storage conditions (-160 $°C$) it is 242. Therefore, for CO_2 to BLEVE a much larger amount of liquid must vaporize than for propane or methane.

Near-Critical Point Temperatures

While the effect of elevated temperatures was discussed earlier, higher temperatures near the critical point were also investigated to see if there were any additional effects introduced by the large changes in fluid properties that occur in that region. In this section, a test is presented with a mean initial temperature of 29.5 $°C$ ($T_r = 0.995$). The other parameters of this test are: a 0.813 mm diameter orifice and a fill level of 84%.

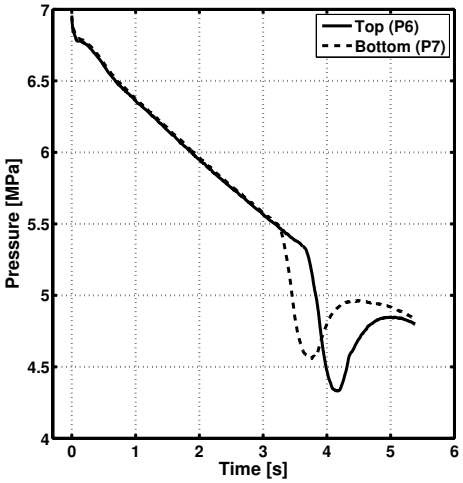

Figure 4.60: Pressure time history for the near critical point test. Test performed with CO_2.

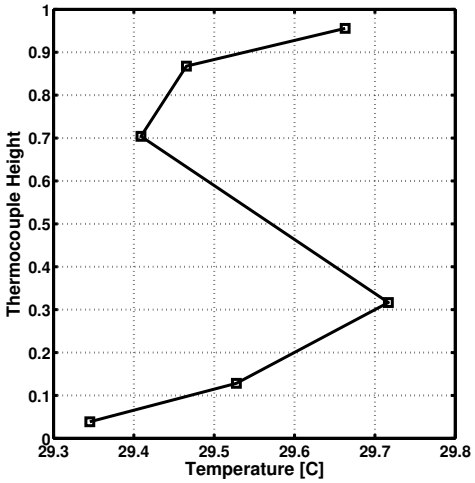

Figure 4.61: Initial temperature profile from the near critical point test. Test performed with CO_2.

The data from this test is shown in figures 4.60 through 4.64. Figure 4.60 shows the pressure time history and figure 4.61 shows the initial temperature profile. An image sequence from the early test times is shown in figure 4.62 while one for the later times is shown in figure 4.63.

A notable feature of the pressure time history in figure 4.60 is the dip at roughly $t = 4\ s$. This dip is a result of fluid flashing on the pressure transducer diaphragm, a phenomenon described earlier in chapter 3. Unfortunately this test was performed before the remedy of heating the pressure transducers was developed. The fact that this dip is an artifact and not a physical change in pressure can be verified in two ways. First, the data from the top and bottom pressure transducers can be compared and these are both given in figure 4.60. While the dip occurs in both sensors' data the dip occurs at different times and therefore there is a pressure difference of more than 0.5 *MPa* for an appreciable amount of time. This pressure difference would be very difficult to maintain within this system. Secondly, the video data do not suggest that anything new is occurring in this time period.

Therefore, if we ignore these spurious dips in the pressure data we observe that the pressure time history appears to have little or no transient regime, and the steady

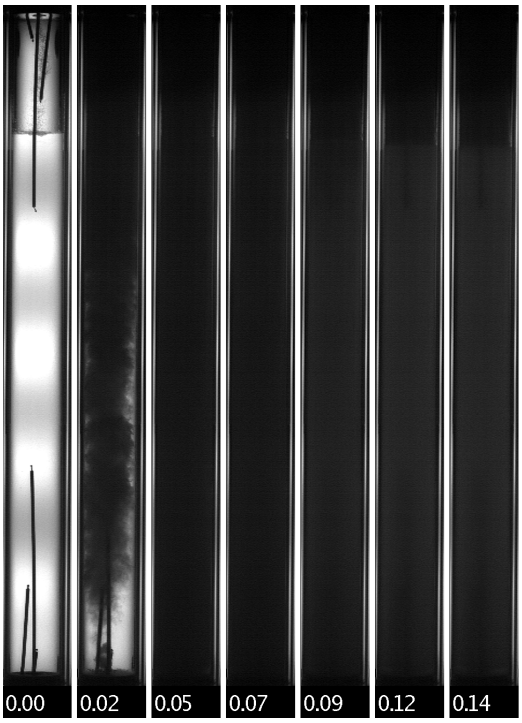

Figure 4.62: Image sequence of early times from the near critical point test. The number below each frame denotes the normalized time. Test performed with CO_2.

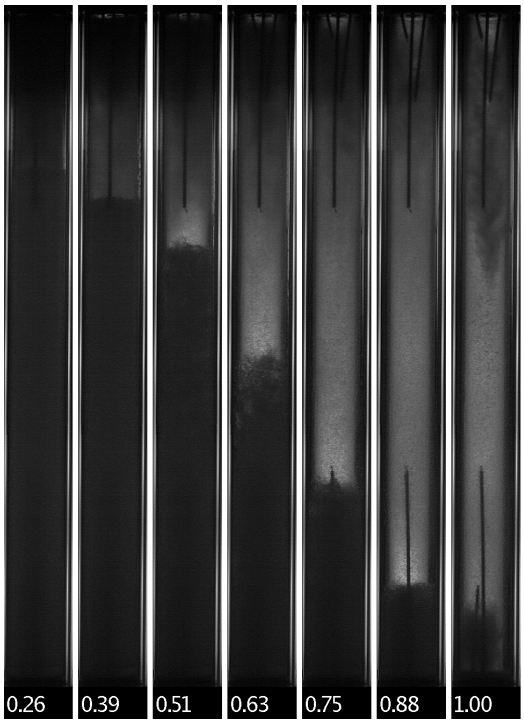

Figure 4.63: Image sequence of later times from the near critical point test. The number below each frame denotes the normalized time. Test performed with CO_2.

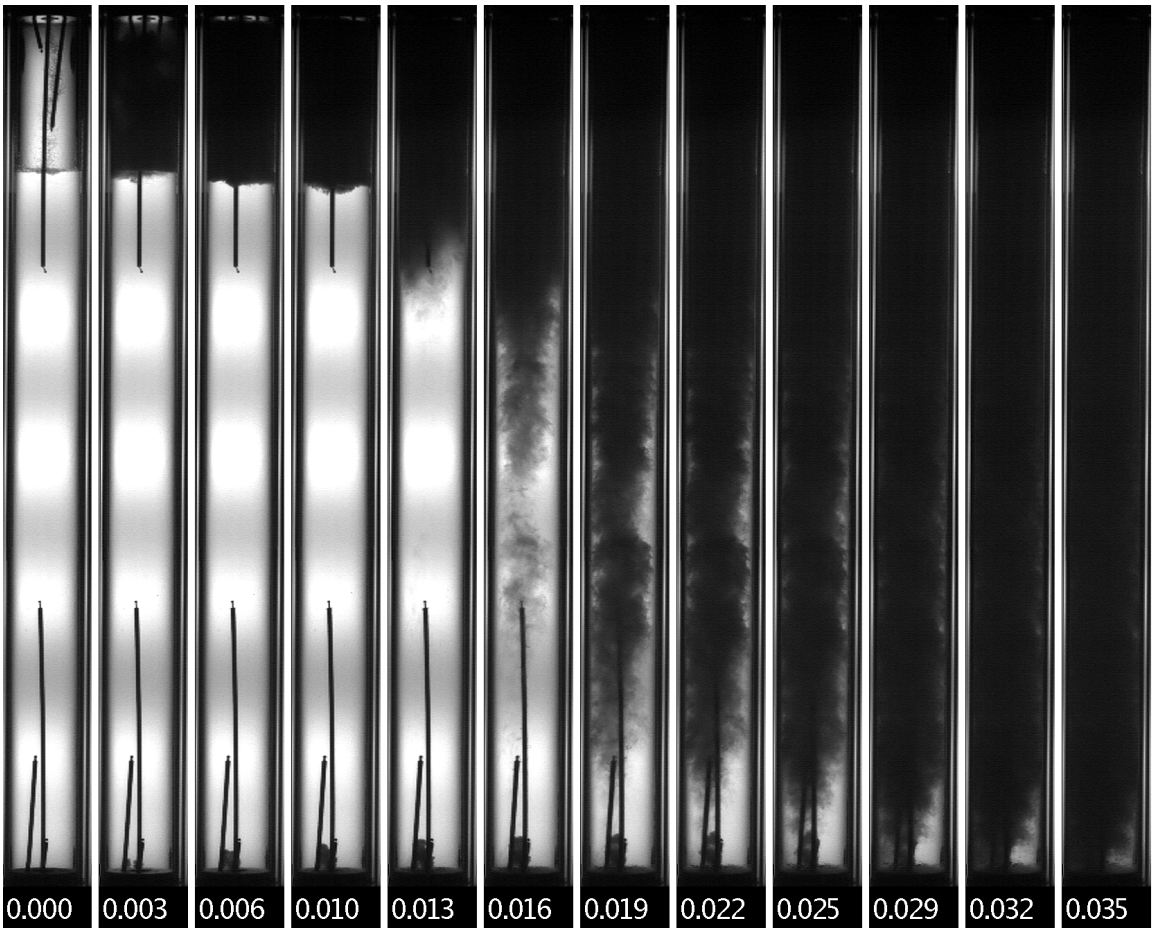

Figure 4.64: Image sequence highlighting bubble nucleation in the near critical point test. The number below each frame denotes the normalized time. Test performed with CO_2.

state spans nearly the entire test. This is perhaps a logical extension of the data presented earlier in subsection 4.2.3, where the length and magnitude of the drop and recovery was seen to decrease as temperature increased. Here we have reached the point where it has almost disappeared entirely, corresponding to a superheat of only about 0.5 $°C$ achieved within the liquid.

The temperature profile shown in figure 4.61 is exceptionally uniform, and in fact the variation is well within the thermocouple probes' measurement uncertainty. This uniformity can be explained via the Rayleigh number: for the same temperature difference and length scale, the Rayleigh number for liquid CO_2 is nearly a factor of 50 higher at 29.5 $°C$ than at 20 $°C$. It is worth noting however that as we approach the critical point the specific heat capacity of CO_2 increases dramatically ($c_p(29.5°C) = 22,714\ J/(kgK)$, $c_p(20.0°C) = 4,264\ J/(kgK)$) and so small changes in temperature can still represent large differences in thermal energy.

The image sequence from early times, shown in figure 4.62, shows rapid bubble and droplet nucleation and a homogeneous, nearly opaque test vessel by $t_n = 0.05$. In the later time image sequence in figure 4.63 the results appear more similar to other tests shown previously. To explore the rapid nucleation process, another image sequence is given in figure 4.64.

This image sequence shows how the ullage condenses extremely rapidly, by $t_n = 0.003$, and nucleation occurs throughout the liquid between $t_n = 0.013$ and 0.029. This rapid nucleation process accounts for the near disappearance of the transient regime. Here a significant difference between this test is visible that sets it apart from all other tests shown previously: the bubble nucleation in the liquid appears to be homogeneous rather than heterogeneous, with bubbles forming in the bulk of the liquid and not solely on solid surfaces. Some heterogeneous nucleation is visible at the base of the tank but the vast majority of bubble nucleation is happening in the interior of the liquid.

The reason for this change can be understood in two different ways, either by comparing models for heterogeneous and homogeneous bubble nucleation rates at this temperature or by resorting to simple thermodynamics. Here we use the latter argument. Figure 4.65 shows a $T - s$ diagram for CO_2 including the saturation and

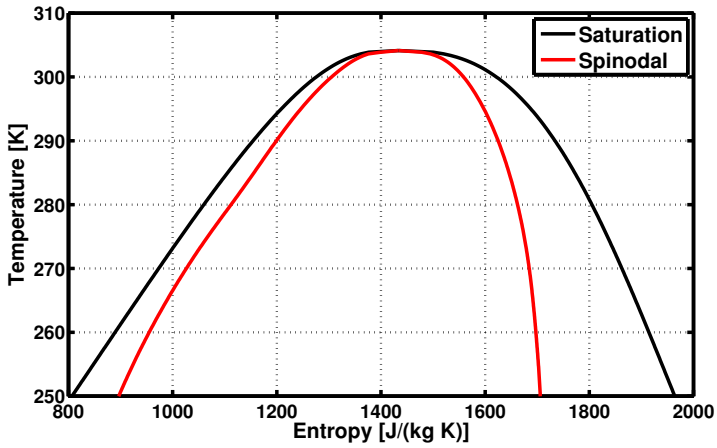

Figure 4.65: Temperature-entropy diagram for CO_2 showing the saturation and spinodal lines.

spinodal lines. During early times, the liquid is essentially undergoing an isentropic expansion, a downwards vertical path on this diagram. As the initial temperature is increased, the distance from the saturation line to the spinodal decreases. The spinodal represents the boundary between metastable and unstable thermodynamic states. At high temperatures only very small levels of superheat can be sustained before the liquid reaches an unstable thermodynamic state and rapid vaporization occurs.

Above the Critical Point

Out of curiosity, a test with CO_2 was performed with a supercritical initial state. At temperatures above the critical point, there ceases to be a distinction between the liquid and vapor phases. Therefore there is no saturation state, and Gibbs' Phase Rule allows for a second degree of freedom to control the $P\rho T$ behavior of the fluid. As a result, a single point in the supercritical region is insufficient to fully characterize the behavior of this system. With that in mind, this supercritical test will be described here.

The conditions of the test are: mean initial temperature of 34.3 $°C$ ($T_r = 1.011$), pressure of 7.851 MPa, and a 0.813 mm diameter orifice. The fill level is impossible

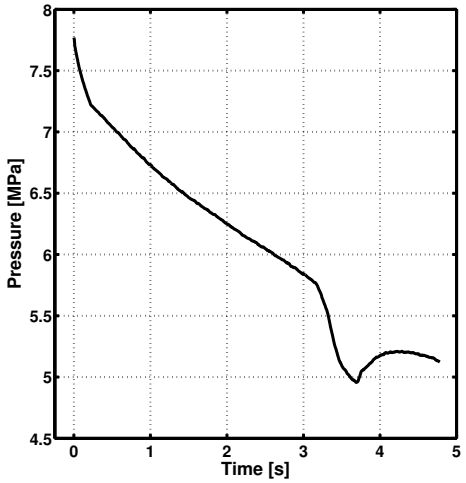

Figure 4.66: Pressure time history for the supercritical test. Test performed with CO_2.

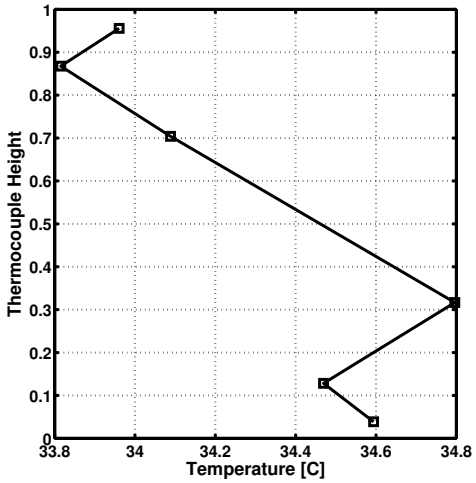

Figure 4.67: Initial temperature profile from the supercritical test. Test performed with CO_2.

to determine, but given the temperature and pressure we can calculate the density as 389.0 kg/m^3 and the initial mass of CO_2 as 71.8 g. The data from this test is shown in figures 4.66 through 4.70. Figure 4.66 shows the pressure time history and figure 4.67 shows the initial temperature profile. An image sequence from the early test times is shown in figure 4.68 while one for the later times is shown in figure 4.69.

The pressure time history in figure 4.66 shows a dip similar to that seen in the previous test and is again a result of liquid CO_2 condensing on the transducer diagram and flashing. The drop at the start of the pressure trace is much larger than that of the previous test just below the critical point, but this is most likely a result of this test being superheated by about 3.2 $°C$ above the critical point and hence a good distance from any saturation region. Once the test starts, the temperature must drop by this amount before any droplet nucleation can be expected to occur.

This behavior is seen in figure 4.68, where droplets do not nucleate until after $t_n = 0.05$, much later than in the previous test just below the critical point. When nucleation does occur, it is homogeneous nucleation and rapidly produces a large amount of liquid CO_2 such that in the later times in figure 4.69 a clear boundary between the liquid and ullage is established and the test begins to resemble those

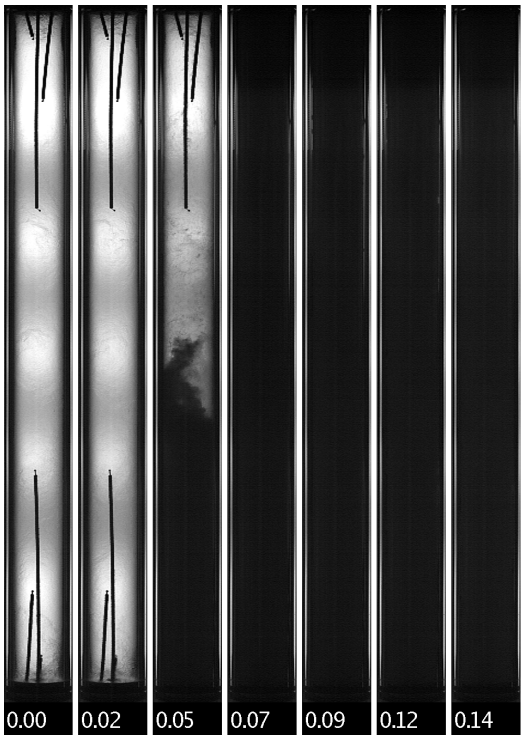

Figure 4.68: Image sequence of early times from the supercritical test. The number below each frame denotes the normalized time. Test performed with CO_2.

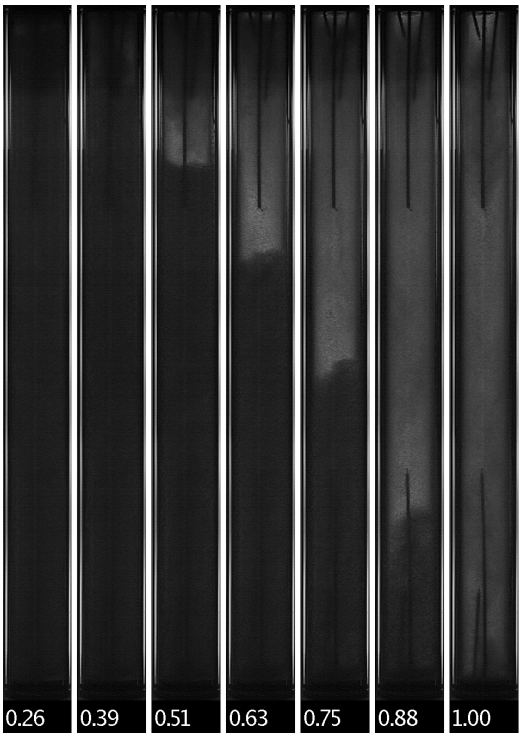

Figure 4.69: Image sequence of later times from the supercritical test. The number below each frame denotes the normalized time. Test performed with CO_2.

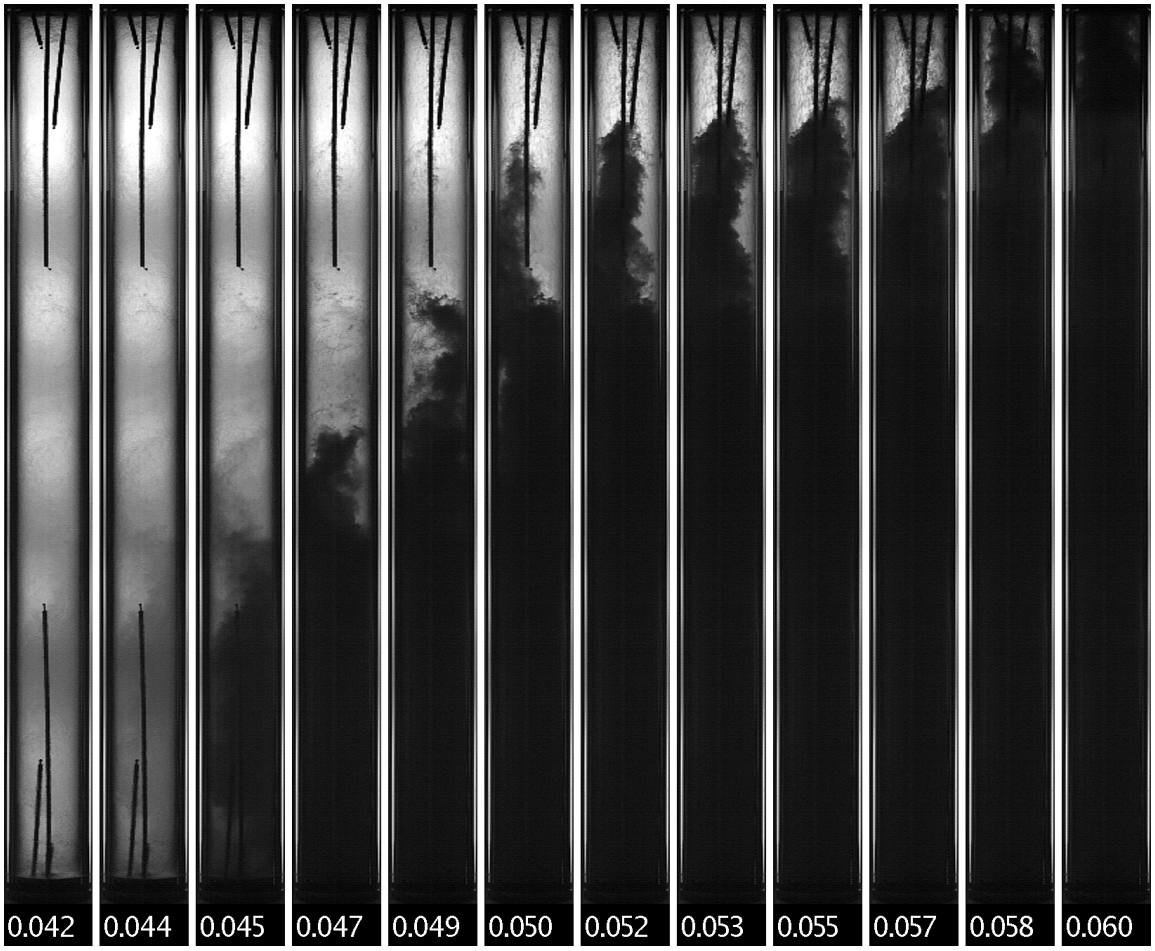

Figure 4.70: Image sequence highlighting bubble nucleation in the supercritical test. The number below each frame denotes the normalized time. Test performed with CO_2.

starting below the critical point.

Figure 4.70 shows the droplet nucleation process, noteworthy for its rapidity. In the later images in this sequence it also appears that there is some condensation occurring on the walls of the quartz tube in the upper regions.

4.2.9 Summary and Conclusions

In this section, the effect of a variety of parameter variations has been studied in the quartz tube and flat glass gauge experimental systems using carbon dioxide. We can summarize the findings as follows:

Flow Rate: The test time (t_{LRO}) was varied by a factor of 24 using different orifices. The transient regime only increased in length by 4 times and therefore was proportionally a much smaller part of the slow test. The fast test had a much larger pressure drop during the test as a result of the increased level of superheat that was needed to drive a higher level of vapor generation in the liquid.

Fill Level: The fill level was varied by a factor of 3. This primarily affected the transient regime, increasing P_{min} and decreasing P_{max} due to the slower superheating of the liquid that allowed more bubble nucleation to take place at lower values of ΔT_s.

Mean Initial Temperature: Tests at elevated and reduced temperature were presented. Increasing temperature decreased the bubble and droplet sizes and reduced the magnitude of the pressure drop and recovery in the transient regime, while decreasing the temperature had the opposite effect.

Temperature Stratification: Tests with different initial temperature fields were examined and found to have very different behavior. By establishing large regions of liquid at different temperatures, multiple transient and steady state regimes were found based on which portions of the liquid were currently boiling.

Initial Bubble Population: The initial bubble population significantly affected the magnitude of the pressure drop and recovery in the transient regime. The

existing bubbles were able to respond to the drop in pressure, expanding and decreasing the level of superheat reached.

Feed System Length: 24 and 52 cm lengths of tubing were added between the main valve and the orifice. When the valve opens, liquid briefly flows at a high rate into this volume and creates a sudden pressure drop in the tank. This sudden superheating of the liquid causes rapid bubble nucleation.

Valve Opening Time: The driving pressure to the pneumatic main valve was decreased in order to slow the valve rotation time from ~ 150 ms to ~ 400 ms. This did not appear to have a significant effect on the results.

Vessel Size: The vessel size was increased by a factor of 6.92 by using the two test apparatuses. No significant effects were found in the overall system behavior, while some effects of differences in vessel construction were detected including wall heat transfer and bubble nucleation locations.

The robustness of the general dynamics of the self-pressurizing propellant tank system has been demonstrated by the fact that few of these parameter variations caused substantial changes to the fundamental features that were discussed in detail in the last section. This conclusion is highly beneficial for modeling efforts, as it suggests that a single model should be capable of predicting the behavior of propellant tanks with different parameters or at different conditions.

4.3 Comparison of Carbon Dioxide and Nitrous Oxide

As was mentioned in the beginning of the previous chapter, experimental data is needed to prove that carbon dioxide functions as an accurate analog for nitrous oxide. To that end, several comparison tests have been performed to see if any differences in the two fluids' behavior as self-pressurizing propellants can be detected. This type of testing was a priority early in this research program, as it was truly unknown whether results from CO_2 could be used to learn about the behavior of nitrous oxide. If the two were found to be significantly different, it would have required all subsequent testing to be done with nitrous oxide.

Therefore a large number of tests were done in the polycarbonate system to compare the two fluids. Later, a handful of tests were conducted with the quartz and flat glass gauge systems to verify the earlier findings with the new systems that produced higher quality data and offered more options for parameter control. In this section these two test campaigns will be discussed.

4.3.1 Initial Tests in Polycarbonate System

A detailed series of tests were performed in the polycarbonate system at different flow rates, draining the tank in 4 to 40 seconds. By performing tests over such a wide range of flow rates, the physical phenomena that dominate at different time scales could be evaluated. In all, 12 tests were performed with each fluid and the test conditions are summarized in table 4.1. The liquid level could not be precisely measured because of the difficulty of identifying it in the video imagery before a test began, but was kept between 86% and 88% of the tank volume.

Shown in the table for each test is the metering valve setting, the calculated C_v, time required for liquid to be completely drained, averaged fluid mass flow rate, the initial reduced pressure, and the initial deviation in pressure from saturation. This last quantity is computed by comparing the measured pressure with the saturation pressure calculated from the temperature measured at the tank exit. It is a measure

Table 4.1: Test parameters for the nitrous oxide and carbon dioxide comparison tests in the polycarbonate system. N_{MV} is the metering valve setting.

	N_2O				CO_2			
N_{MV}	C_v	t_{LRO} [s]	$P_{r,i}$	$P_{r,i} - P_{r,sat,i}$	C_v	t_{LRO} [s]	$P_{r,i}$	$P_{r,i} - P_{r,sat,i}$
1	0.0031	38.72	0.586	0.0226	0.0057	29.66	0.594	0.0194
2	0.0083	19.87	0.565	0.0184	0.011	17.56	0.572	0.0099
3	0.014	13.27	0.540	0.0103	0.016	12.58	0.567	0.0117
4	0.016	10.48	0.525	0.0118	0.020	10.22	0.563	0.0133
5	0.023	8.49	0.530	0.0148	0.027	8.29	0.552	0.0106
6	0.026	7.66	0.529	0.0201	0.028	7.29	0.555	0.0150
7	0.030	6.64	0.531	0.0215	0.032	6.79	0.544	0.0163
8	0.033	6.16	0.521	0.0195	0.038	6.03	0.537	0.0125
9	0.035	5.70	0.522	0.0207	0.041	5.65	0.529	0.0112
10	0.045	5.12	0.519	0.0166	0.043	5.20	0.533	0.0113
11	0.041	4.88	0.519	0.0227	0.044	4.88	0.535	0.0243
25	0.051	3.97	0.515	0.0221	0.056	4.27	0.533	0.0227

of the uniformity of the temperature within the tank. This value is always less than 0.025, indicating that the temperature field was close to uniform when tests begin.

Examining the $P_{r,i}$ columns, it is evident that the initial pressure decreases as mass flow rate increases. The reason for this is that each test series was performed outdoors over the course of an evening. The tests were performed in order from lowest to highest mass flow rate and as the evening progressed the ambient temperature drops and thus with it the saturation pressure. Unlike the later quartz tube system, there was no thermal control capability with this system. Additionally, as was discussed in the previous chapter, repeatable results with this system were only able to be obtained when the test procedures were followed closely, including waiting for the system to reach thermal equilibrium with the ambient conditions before starting a test. In this way the initial fluid temperature was set by the outdoor temperature which unfortunately would not remain constant to the desired degree.

A second feature of this table is seen in the calculated metering valve flow coefficient. This is computed by averaging the C_v calculated throughout the gas portion of each test. The main purpose of this calculation, as described in chapter 3, is to verify

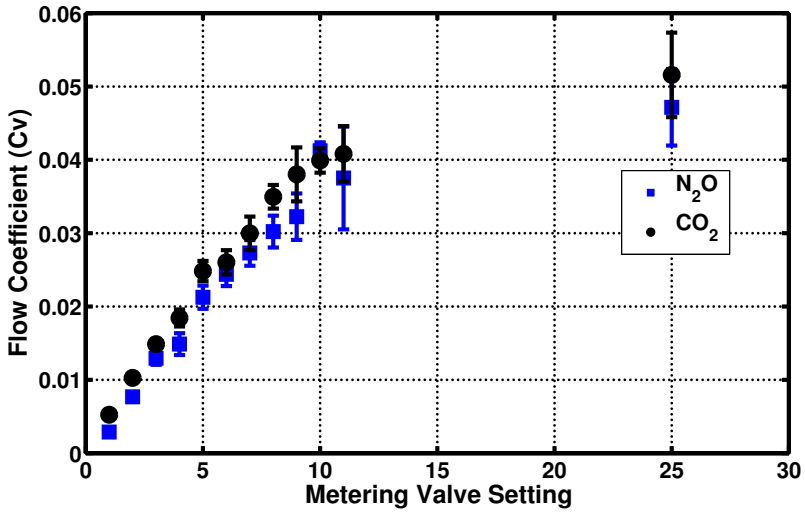

Figure 4.71: Measured metering valve flow coefficient versus the valve handle setting, for both N_2O and CO_2.

that the metering valve has not been damaged. When the C_v of N_2O and CO_2 tests performed at the same metering valve setting is compared there are noticeable differences. In figure 4.71, the calculated C_v is plotted versus the metering valve setting for both fluids. Here, it appears that the C_v's of the CO_2 tests are consistently higher than those for N_2O. One possible cause of this is damage to the metering valve by CO_2.

The N_2O tests were all performed after the CO_2 tests were completed, and if CO_2 had caused swelling or blistering of the elastomers within this valve the C_v may have been altered for subsequent testing with nitrous oxide. While the metering valve used has a metal seat, any swelling or blistering of the sealing elastomers could cause a shift in the position of stem tip and result in a different C_v. A second possibility is that solid carbon dioxide may have formed in this valve. However, the differences in most cases are small and therefore it is not expected that the internal geometry of the valve was altered sufficiently to affect its basic behavior.

Given that the normalization system used for pressure and time is based on the corresponding values at the liquid runout point, a first step towards characterizing the experimental differences between N_2O and CO_2 can be accomplished by comparing

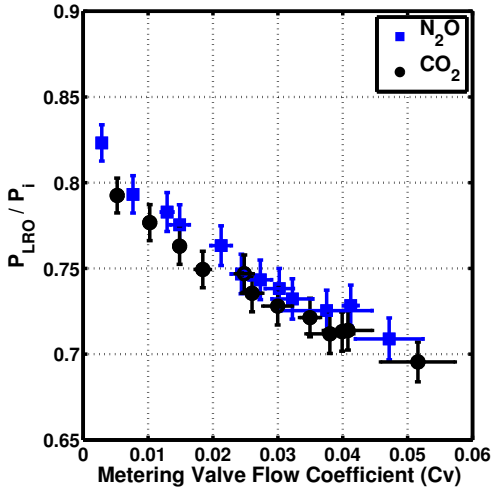

Figure 4.72: Pressure at the liquid runout point versus the valve flow coefficient for all CO_2 and N_2O tests.

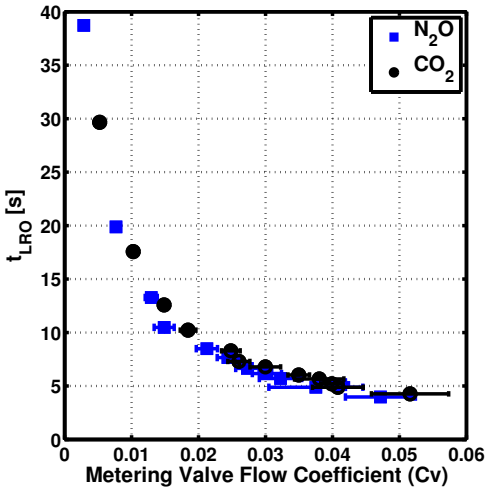

Figure 4.73: Time at the liquid runout point versus the valve flow coefficient for all CO_2 and N_2O tests.

these values for the two fluids. In figures 4.72 and 4.73 the time and pressure at this point are plotted as a function of the metering valve's flow coefficient. In both plots it is difficult to distinguish the CO_2 and N_2O data, although in figure 4.72 the nitrous oxide data appear to have slightly higher pressure at liquid runout. In both cases the two fluids do show similar trends and most differences are within the measurement uncertainty.

The pressure and normalized pressure traces from all tests performed with N_2O are shown in figure 4.75. Similar plots for CO_2 are given in figure 4.74. These plots are useful for observing how the character changes as mass flow rate is increased.

Several features are apparent and are similar to those presented earlier with the quartz tube system in section 4.2. As mass flow rate increases, the magnitude and duration of the initial drop and recovery increases. Additionally, the following section of the plots becomes more linear for the higher mass flow rate tests. One difference between the two fluids that is apparent from these plots is that at high mass flow rates, the recovery in pressure is flatter on the CO_2 plots than those for nitrous oxide. This feature will be discussed in greater detail when a high mass flow rate test is compared between the two fluids.

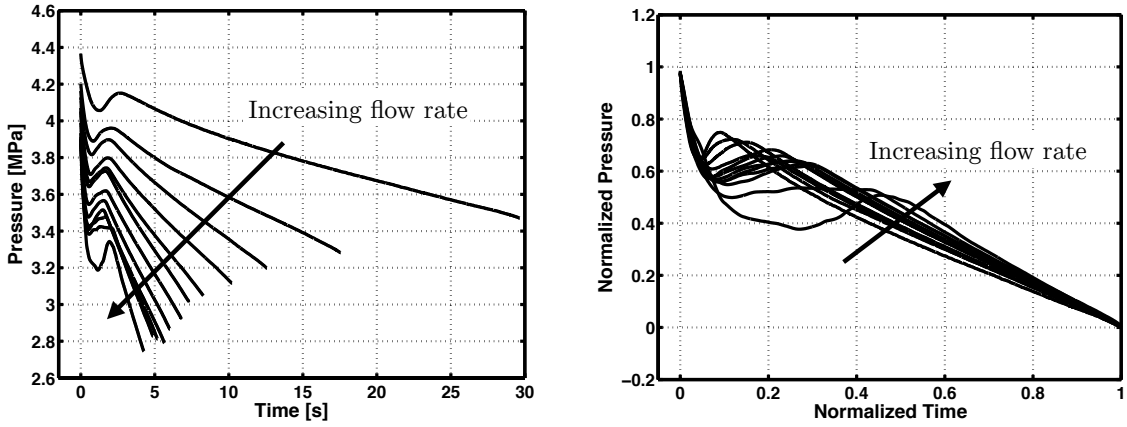

Figure 4.74: Pressure and normalized pressure histories for all CO_2 tests.

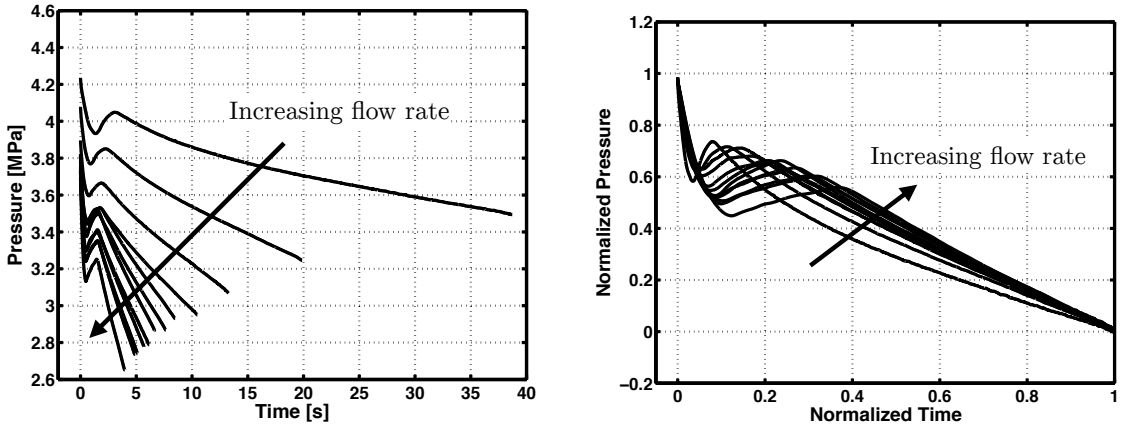

Figure 4.75: Pressure and normalized pressure histories for all N_2O tests.

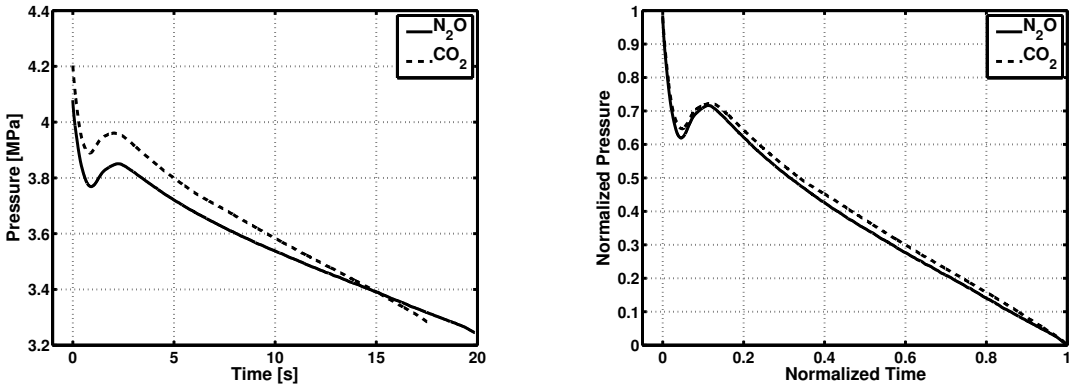

Figure 4.76: Pressure and normalized pressure histories for the low flow rate CO_2 and N_2O tests.

In order to directly compare the experimental data from the two fluids, six tests (3 pairs) will be examined in detail. These tests are those performed at metering valve settings 2, 5, and 11 in order to see a variety of mass flow rates. The tests performed at metering valve setting 1 are not used because of the large difference in calculated valve C_v. Tests performed at metering valve setting 11 are used rather than those at setting 25 in order to highlight a feature of the high mass flow rate videos that was more distinguishable at the slightly lower flow rate.

The pressure and normalized pressure time histories from the two low flow rate tests are shown in figure 4.76. In both cases the normalized traces are nearly on top of each other, although the carbon dioxide pressure trace is slightly higher.

Figure 4.77 shows the video imagery from this test. The white numbers denote the normalized time while the N and C denote nitrous oxide and carbon dioxide, respectively. Images from both tests were taken at the same normalized time point. Due to a slight misalignment of the laser sheet, the carbon dioxide stills appear darker near the bottom of the tank. The images, like the pressure plots, show little difference between the two fluids.

Tests performed at a metering valve setting of 5 are examined next. In figure 4.78, the pressure and normalized pressure time histories are shown. While the two fluids still show a great deal of similarity in the normalized pressure histories, larger differences are seen compared to the low flow rate test. In particular, the initial drop

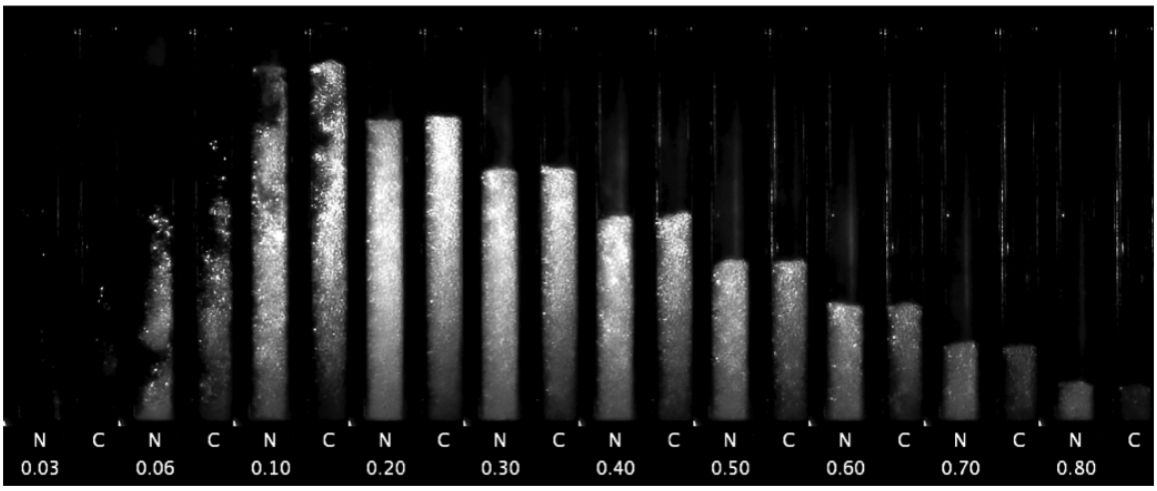

Figure 4.77: Image sequence for the low flow rate CO_2 and N_2O tests.

in both temperature and pressure around normalized time of 0.07 shows the largest differences between the two fluids. The video stills from this test are shown in figure 4.79. Here the two fluids are nearly indistinguishable.

The higher flow rate tests performed at a metering valve setting of 11 are now shown. In figure 4.80 the pressure and normalized pressure time histories are given. Larger differences between the CO_2 and N_2O data are apparent, especially in the normalized pressure history throughout the recovery between normalized times of 0.1 and 0.4. While earlier tests showed the largest differences at the minimum of the initial pressure drop, now the subsequent increase is different. The CO_2 trace falls below the N_2O during this time and similar behavior is seen in other tests at the upper range of mass flow rates.

The reason for this is seen in the video stills in figure 4.81. Between the start of the test and $t_n = 0.2$, the two fluids seem similar although condensation is visible in the ullage of the CO_2 test and not in the N_2O test. For the next stills at $t_n = 0.2$ and $t_n = 0.3$ the bubbles in the CO_2 stills appear lower than in the corresponding N_2O stills. After $t_n = 0.4$ the two fluids seem quite similar. From $t_n = 0.2$ to $t_n = 0.4$, a single large bubble appears at the top of the wave of bubbly liquid that is moving towards the top of the tank.

To make this feature more visible, figure 4.82 shows the portion of the CO_2 test

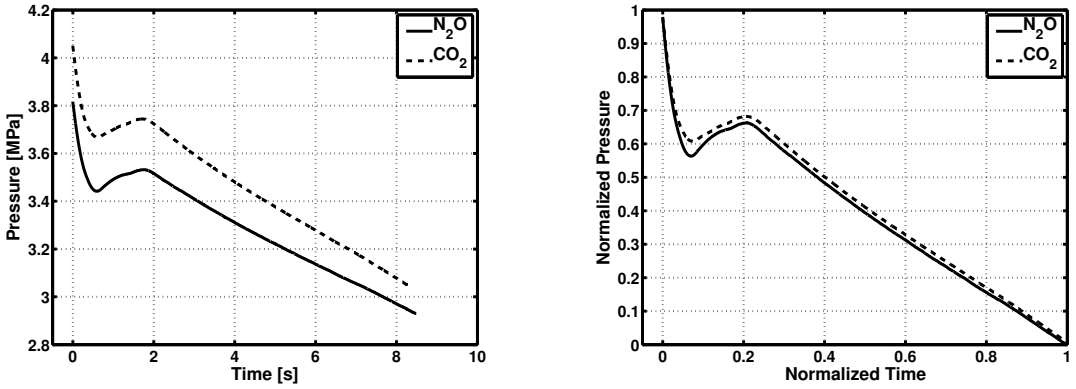

Figure 4.78: Pressure and normalized pressure histories for the medium flow rate CO_2 and N_2O tests.

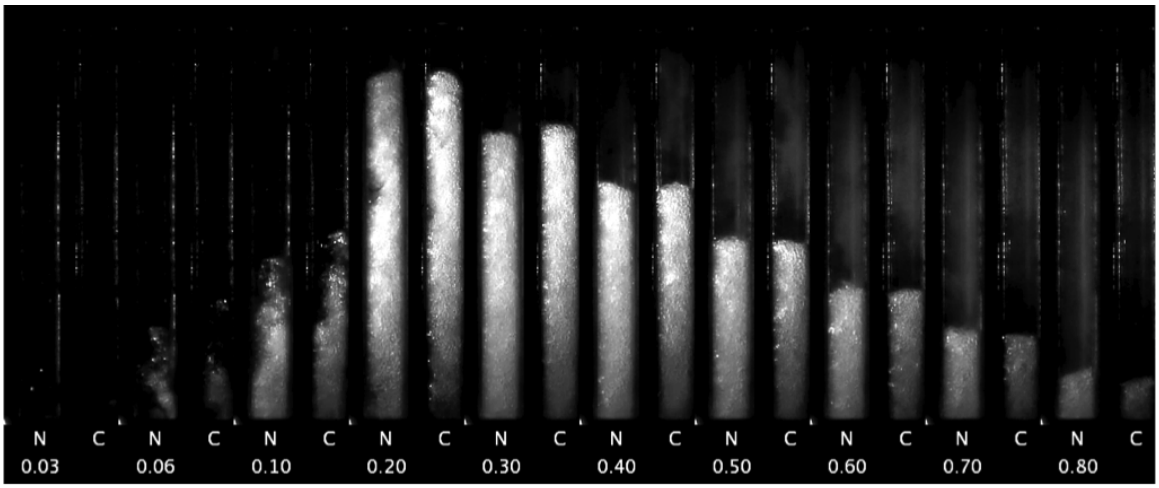

Figure 4.79: Image sequence for the medium flow rate CO_2 and N_2O tests.

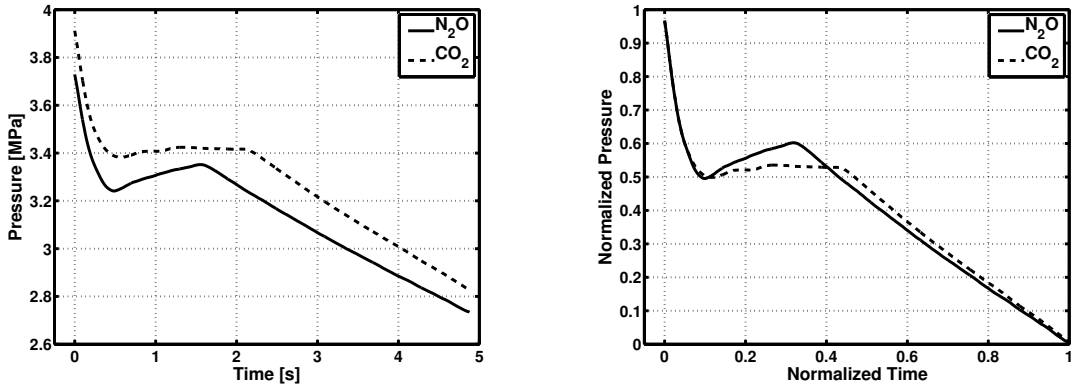

Figure 4.80: Pressure and normalized pressure histories for the high flow rate CO_2 and N_2O tests.

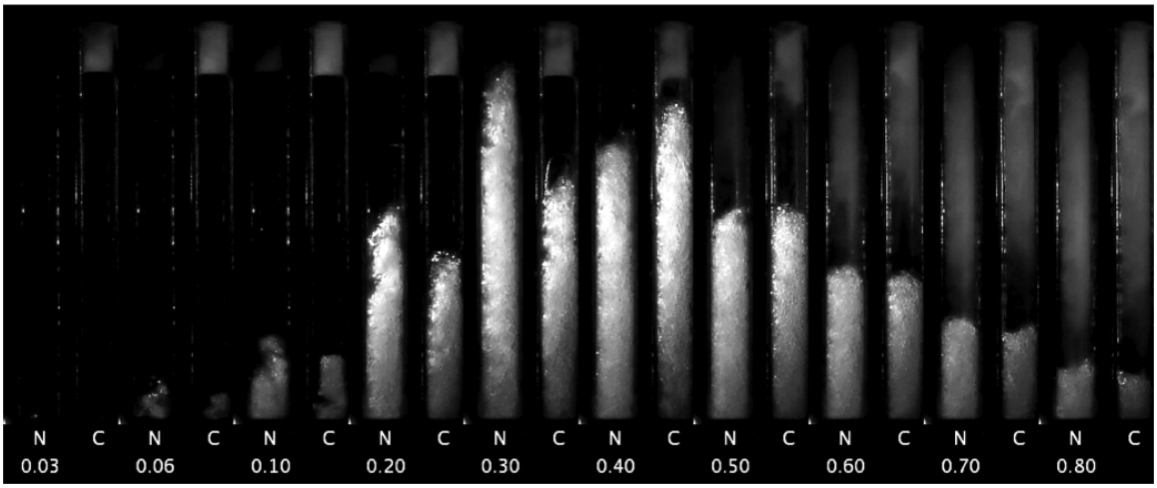

Figure 4.81: Image sequence for the high flow rate CO_2 and N_2O tests.

Figure 4.82: Image sequence from the high flow rate CO_2 test showing the single large bubble.

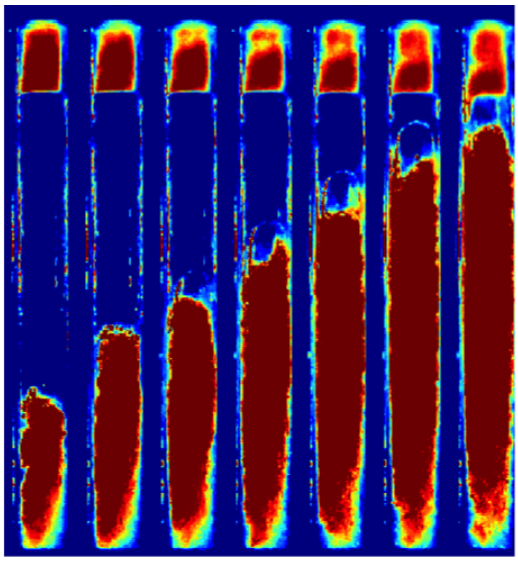

Figure 4.83: Image sequence shown in figure 4.82 but with the image intensity remapped to a range of colors to increase contrast.

where this bubble is visible, from $t_n = 0.16$ to $t_n = 0.4$. On the right hand side of this figure the video stills have been altered by remapping the gray scale pixel intensity onto a range of colors. By doing this, the bubble can be more clearly seen moving towards the top of the tank as time progresses. This phenomenon was observed in both of the highest mass flow rate tests of CO_2 (metering valve settings 11 and 25), but not in any N_2O tests.

A similar phenomenon has been studied by previous researchers in the context of cryogenic propellant system tubing, and is sometimes termed "geysering" (unfortunately this term also refers to an unrelated propellant slosh phenomenon seen during pulsed acceleration). When there are vertical tubes of cryogenic liquid and heat is transferred into them, the liquid will begin to boil. The subsequent processes have been described by Morgan and Brady [78]:

> "The ... effect is that the bubbles displace liquid from the line into the large reservoir, causing a decrease in hydrostatic pressure at any point below the bubbles. This decrease in pressure effectively superheats the

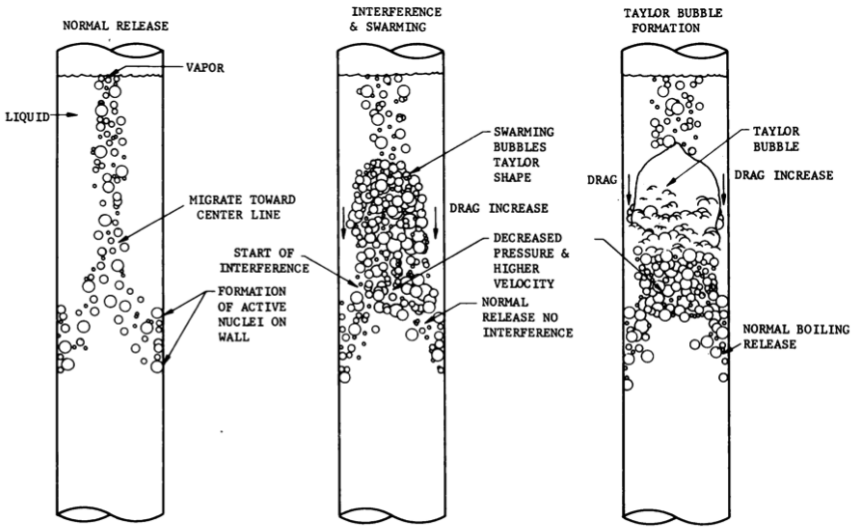

Figure 4.84: Diagram describing the geysering phenomenon, from Morgan [78]. Reprinted with permission.

> remaining liquid, causing it to release more vapor - which again decreases pressure, causing more superheat. The production of vapor bubbles is not serious until the population reaches the point where the bubbles interfere with each other in performing a release from the system ... The bubbles will begin to 'swarm,' causing the creation of a slow-moving mass or a single large bubble. Other bubbles below travel at a faster velocity and join the large bubble, causing it to grow at a very fast rate - and to decrease the column static pressure rapidly."

A diagram from this work is shown in figure 4.84. This description, although depicting a slightly different situation than that present in these N_2O and CO_2 tests, captures the main features observed here. A separate work by Murphy [79] studied geysering in a variety of fluids and a wide range of size scales and heat fluxes. They determined that the boundary between the conditions that produced geysering and

those that did not could be described as:

$$\begin{aligned} X &= \log_{10}\left[\frac{(q/A)L}{12\alpha Pr^{1/3}}\right] \\ Y &= \log_{10}([L/D]D^{-0.68}) \\ Y &= -0.05769X + 0.9923 \end{aligned} \tag{4.8}$$

where Y values greater than this result in geysering. Here, q is the heat transfer from the surroundings into the tube. For some tests Murphy used heaters and for the cryogenic tests he estimated the heat flux through different thicknesses of insulation from the ambient air.

From the small magnitude of the slope, it is clear that the presence of geysering has a strong dependence on the geometry of the system, and less so on the fluid properties and the heat transfer rate. Using the parameters of the experimental system used in the present work, $\log_{10}([L/D]D^{-0.68}) = 1.15in^{-0.68}$, which would place it in the geysering region. This suggests that self-pressurizing propellant tank tests at larger size scales and lower length-to-diameter ratios may eliminate geysering completely. However, this is a substantial extrapolation of Murphy's experiments that used significantly larger tubes and fluids dissimilar to either carbon dioxide or nitrous oxide. Additionally, this explanation does not account for the absence of geysering in the N_2O tests. In fact, there is a relatively weak dependence on fluid properties in Murphy's results, with the factor $\alpha Pr^{1/3}$ in the denominator of the horizontal axis value. This factor only differs by about 5% for nitrous oxide and carbon dioxide in the temperature range of interest.

The basic conclusion from this early work was that CO_2 seems to function as an accurate analog for N_2O in self-pressurized propellant tank testing, except in cases where geysering is observed. Since this phenomenon was not observed in N_2O tests, it must be assumed that results with CO_2 that show geysering do not reproduce the behavior of nitrous oxide. In testing described later in this section it will be shown that this conclusion is false, and in fact the lack of geysering in the N_2O tests was related to the different temperatures of the CO_2 and N_2O tests and not a result of the small differences in properties of the two fluids.

4.3.2 Follow-up Tests

Once the quartz and flat glass gauge systems were developed, the topic of comparing nitrous oxide and carbon dioxide was revisited. First, since the quartz system offered much better imaging capabilities than the polycarbonate system it was desirable to see if any differences between the two fluids would be evident at the small scales that could now be visualized. Additionally the array of thermocouples and the temperature control systems allowed for better control and determination of the initial condition, as well as enabling tests at elevated or reduced temperatures. The flat glass gauge was used to find if there were any obvious scaling effects with nitrous oxide that weren't present with carbon dioxide.

Ambient Temperature

We begin by comparing tests with nitrous oxide and carbon dioxide in the quartz tube system at "standard" conditions. All parameters of the two tests were reasonably matched, including the fill levels (83%), mean initial temperatures (20.6, 20.4 $°C$), the initial temperature profiles, test times (14.2, 14.6 s), and orifice diameters (0.559 mm) for the CO_2 and N_2O tests, respectively.

The data from these two tests are shown in figures 4.85 to 4.88. Figure 4.85 shows both pressure traces and the normalized pressure traces, while figure 4.86 shows the initial temperature profiles. Figures 4.87 and 4.88 show a comparison of the still image sequences from these two tests.

The large difference in starting pressure for the two tests seen in figure 4.85 is a result of the difference in saturation pressure as the initial temperatures were nearly identical. When the normalized pressure traces are compared the plots are quite similar, with the CO_2 test have a slightly lower P_{min} and P_{max}. This is likely caused by the different ullage temperatures visible in the initial temperature profiles shown in figure 4.86. The ullage of the CO_2 test was roughly 1.5 $°C$ warmer than that of the N_2O test despite the similar liquid temperatures. Therefore once the test began and the pressure began to drop, it took slightly longer for the pressure in the CO_2 test to cross the saturation line.

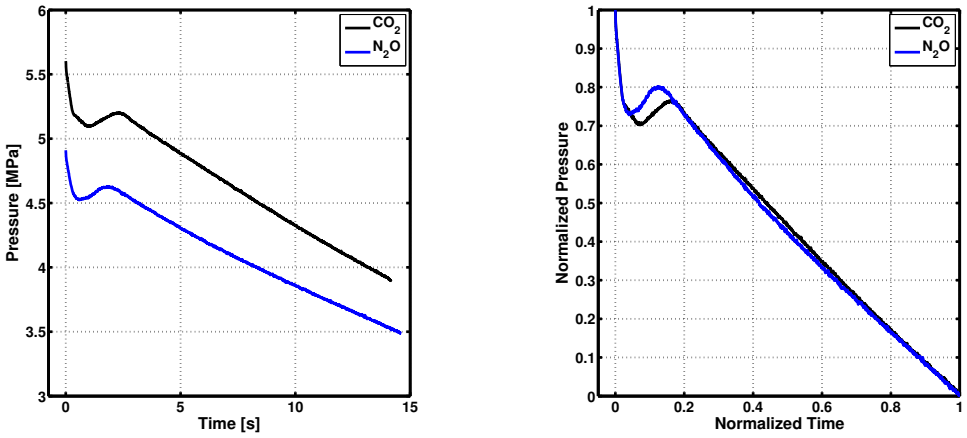

Figure 4.85: Pressure and normalized pressure time histories for CO_2 and N_2O tests.

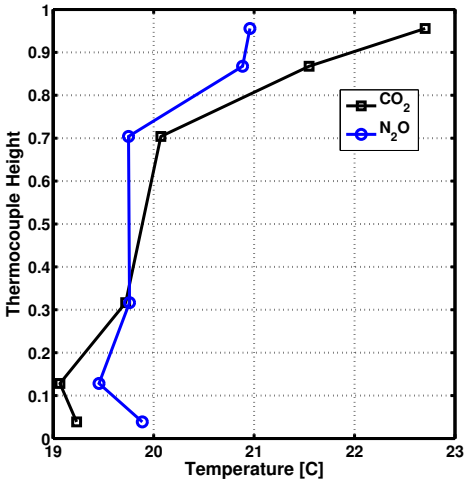

Figure 4.86: Initial temperature profiles for the CO_2 and N_2O tests.

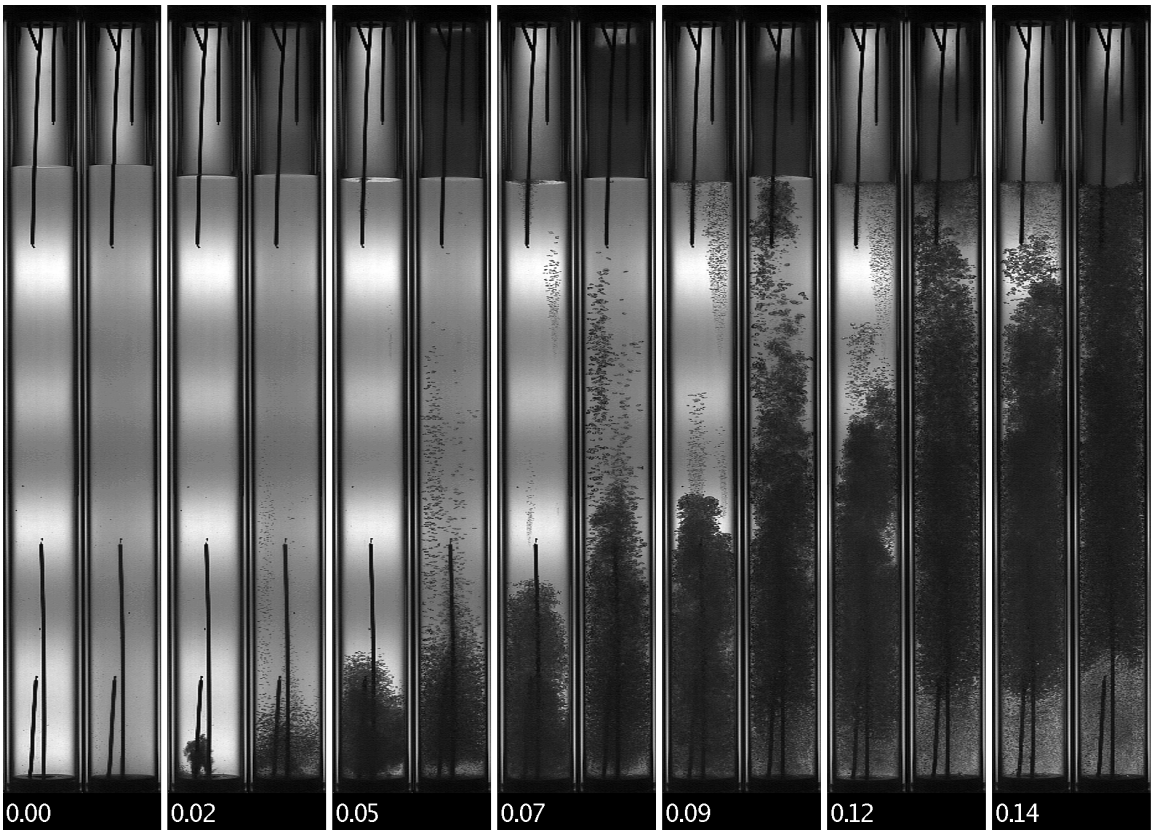

Figure 4.87: Image sequence comparison for early times from the CO_2 (left) and N_2O (right) tests. Each pair of frames are taken from the two tests at the same normalized time, indicated by the number below.

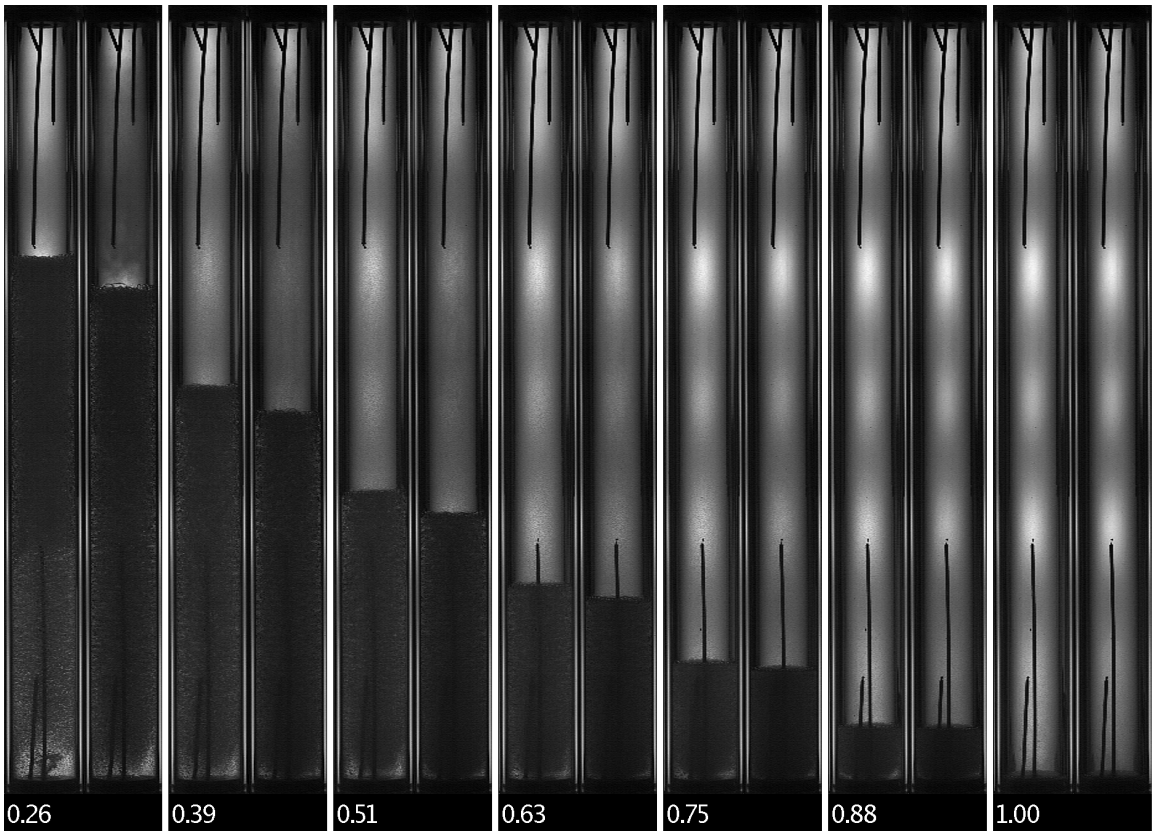

Figure 4.88: Image sequence comparison for later times from the CO_2 (left) and N_2O (right) tests. Each pair of frames are taken from the two tests at the same normalized time, indicated by the number below.

This feature is also seen in the early time image sequence in figure 4.87. While the ullage of the N_2O test condenses fairly uniformly around $t_n = 0.05$, the ullage of the CO_2 test never condenses. Other than this difference, the two tests appear quite similar in the early times with the only other difference being slightly more uniform bubble nucleation in the liquid of the N_2O test compared to the CO_2 test. This is most obvious in the still image at $t_n = 0.09$, where the N_2O test shows much more bubble nucleation in the upper regions of the liquid than in the CO_2 test. In the later times the two tests become even more similar, especially after $t_n = 0.39$ when quality of the N_2O ullage increases and resembles that of the CO_2 test.

These two comparisons have shown that there are no new features that we can identify as different between the two fluids that weren't detectable with the original polycarbonate system.

Elevated Temperature

In the testing done with CO_2 in the quartz system, it was shown that increasing temperature has significant effects on the overall system dynamics, despite maintaining the key features. Therefore testing is now reported at elevated temperatures with N_2O to verify that its response to increased initial temperature is similar to that of carbon dioxide. Similar to the comparison done earlier between ambient and elevated temperature CO_2 , two N_2O tests will now be compared that have similar temperature profiles but different mean temperatures (19.5, 28.4 $°C$), hereafter referred to as simply the "ambient" and "hot" tests. All other parameters of the two tests were matched, including the fill levels (83%), shape of the temperature profiles, and orifice diameters (0.813 mm).

The differing temperatures and hence initial pressures resulted in different test times for the two tests, $t_{LRO} = 7.17,\ 6.39\ s$ for the ambient and hot tests respectively. The data from these two tests are shown in figures 4.89 to 4.92. Figure 4.89 shows both pressure traces and the normalized pressure traces, while figure 4.90 shows the initial temperature profiles. Figures 4.91 and 4.92 show a comparison of the still image sequences from these two tests.

In general, the results mirror those shown earlier in subsection 4.2.3. Beginning

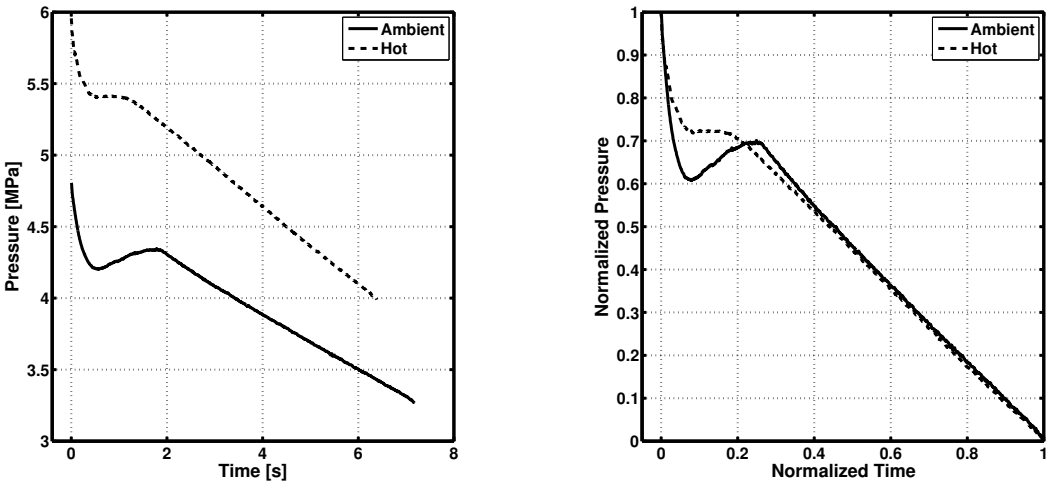

Figure 4.89: Pressure and normalized pressure time histories for the ambient and hot tests.

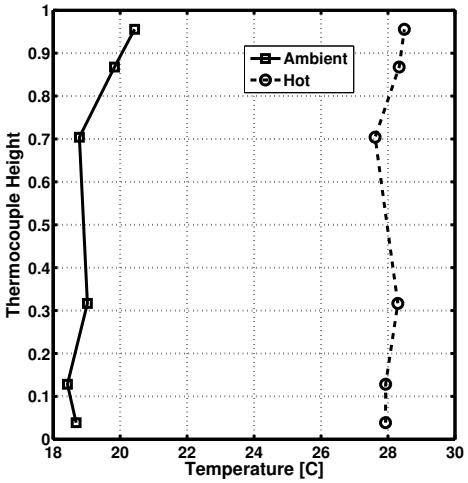

Figure 4.90: Initial temperature profiles from the ambient and hot N_2O tests.

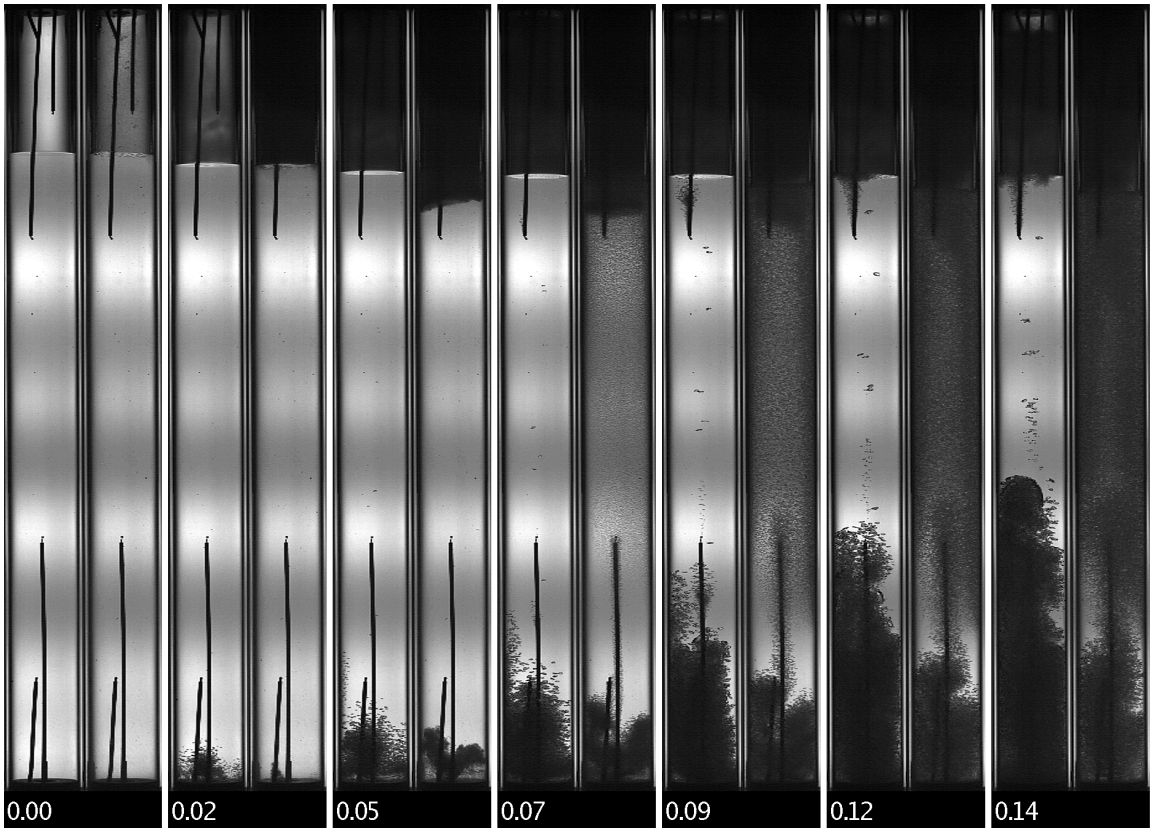

Figure 4.91: Image sequence comparison for early times from the ambient (left) and hot (right) N_2O tests. Each pair of frames are taken from the two tests at the same normalized time, indicated by the number below.

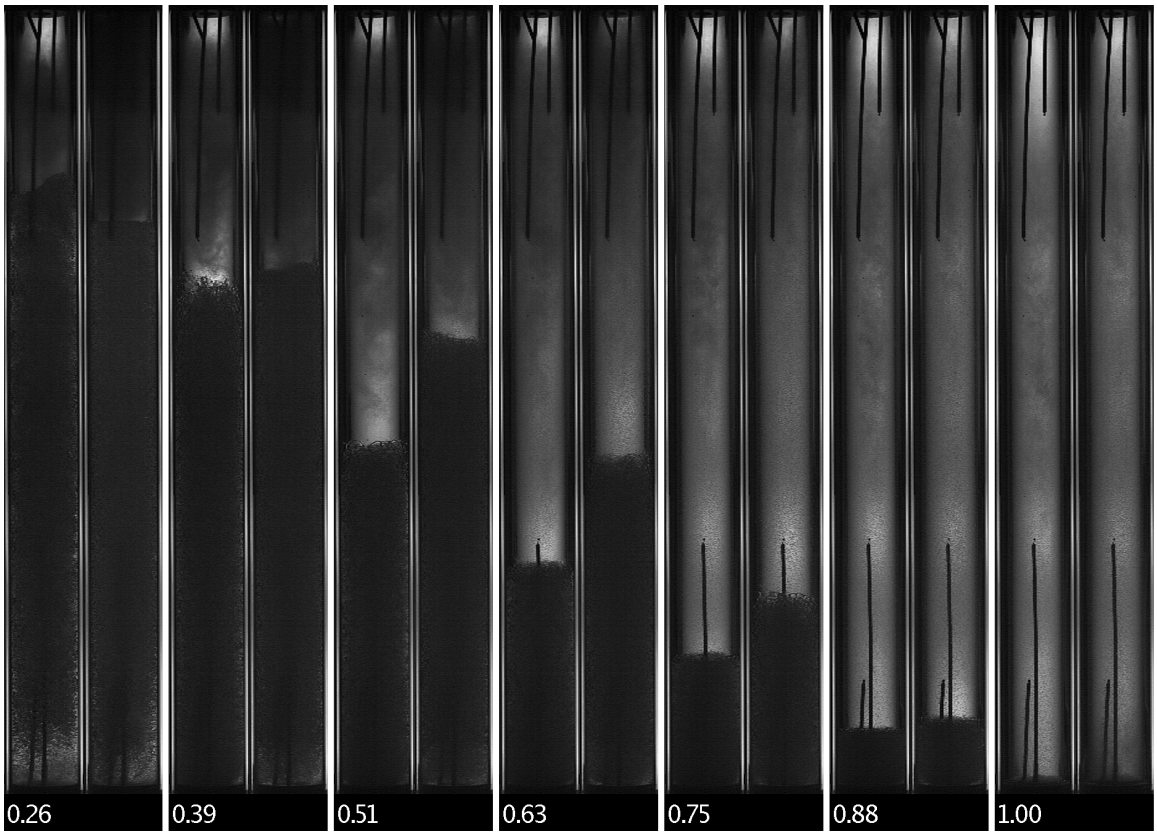

Figure 4.92: Image sequence comparison for later times from the ambient (left) and hot (right) N_2O tests. Each pair of frames are taken from the two tests at the same normalized time, indicated by the number below.

with the pressure histories in figure 4.89, the hot test has a transient drop and recovery which has decreased substantially in both magnitude and duration. The normalized pressure histories show that after this period the steady state regimes have nearly identical slopes. In the image sequence for the early times (figure 4.91) we see bubble nucleation occurring across the entire length of the quartz tube for the hot test while it's mainly limited to the bottom of the vessel for the ambient test. In later times we actually see larger differences, with the liquid level in the ambient test dropping much more rapidly than in the hot test.

Geysering with Nitrous Oxide and Carbon Dioxide

In the earlier polycarbonate system testing, geysering was observed in CO_2 tests at high mass flow rates but not in nitrous oxide. When testing with CO_2 in the quartz system geysering was again observed. Due to the higher level of control and measurement of the initial conditions, it was found that geysering occurred in tests with both low temperatures ($\leq$ 20 $°C$) and high mass flow rates ($t_{LRO} \leq 8$ s). Geysering was never observed in the flat glass gauge, even at initial temperatures of 4 $°C$ and $t_{LRO} = 4.1$ s. This result, combined with the data shown earlier in figure **??** suggests that the geysering is an artifact of the small size of the quartz and polycarbonate tube systems and therefore is not a concern to most propulsion engineers. Additionally, tests at low temperature and high mass flow rate in the quartz tube with a significant initial bubble population did not exhibit geysering. This may suggest that the smooth nature of the quartz tube is another factor that contributes to the presence of geysering and again suggests that geysering is unlikely in practical applications.

Never the less, several tests were performed with the goal of determining if geysering could occur with N_2O as well as CO_2 in the quartz tube system. It was found that N_2O does indeed exhibit geysering at similar conditions to CO_2 : low temperatures and high flow rates. Here, a test that shows geysering in CO_2 will be compared with one with N_2O that also showed geysering.

The parameters of the two tests were reasonably matched although perhaps not as well as in other test comparisons. The test parameters were: fill levels of 83%,

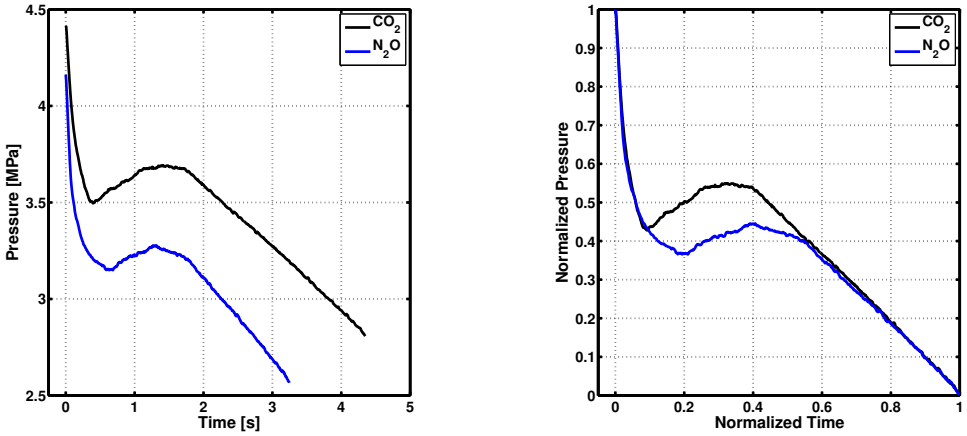

Figure 4.93: Pressure and normalized pressure time histories for CO_2 and N_2O tests.

mean initial temperatures of 9.1, 10.7 $°C$, similar initial temperature profiles, and orifice diameters of 1.092 and 1.321 mm. Different orifice diameters were used in an attempt to match the test times despite the different saturation pressures of the two fluids at identical temperatures. The resulting test times were $t_{LRO} = 4.35, 3.25$ s for the CO_2 and N_2O tests respectively.

The data from these two tests are shown in figures 4.93 to 4.97. Figure 4.93 shows both pressure traces and the normalized pressure traces, while figure 4.94 shows the initial temperature profiles. Figures 4.95 and 4.96 show a comparison of the still image sequences from these two tests. Figure 4.97 highlights the Taylor bubble in both tests.

The geysering effect is detectable in the pressure traces in figure 4.93 by the ragged nature of the pressure recovery in the transient regime. This was also demonstrated earlier in the results from the polycarbonate system in figure 4.80. The Taylor bubble cannot be seen in the early times in figure 4.95, only after $t_n = 0.15$ and also in the first few frames of the later times image sequence in figure 4.96. The geysering is more pronounced in the N_2O test here.

To show more detail of the geysering process figure 4.97 shows an image sequence during the time the Taylor bubble is most visible. In this image sequence it is clear why the N_2O geysering appears stronger: in the CO_2 test there is some amount of

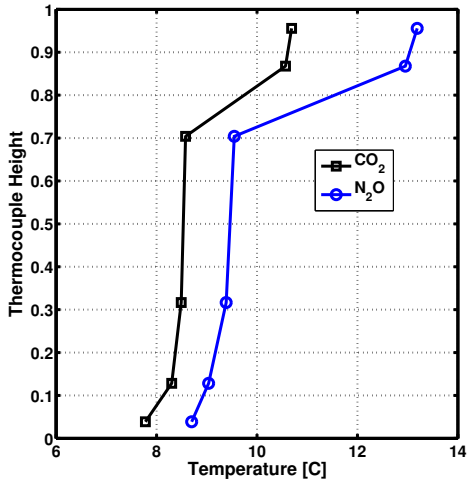

Figure 4.94: Initial temperature profiles for the CO_2 and N_2O tests.

bubble nucleation above the Taylor bubble, and once it rises and encounters this region of higher quality mixture the bubble bursts. In the N_2O test there is much less bubble nucleation above the Taylor bubble and hence it is longer lived, clearly visible at $t_n = 0.44$ while the CO_2 test has no visible Taylor bubble after $t_n = 0.32$.

The difference shown here in the geysering process and its strength should not be taken as a fundamental difference between the two fluids. The conditions for these tests were not perfectly matched, and the precise conditions that control the "strength" and time evolution of the geysering process have not been identified in this system. Additionally, geysering has been observed in this system at a variety of strengths. To illustrate, images 4.98 through 4.101 show Taylor bubble formation in four different tests, with strengths increasing from mild to very intense. Note that these descriptions are entirely qualitative.

These four tests were done with N_2O and the conditions are as follows. Mild geysering was observed in a test with $T_i = 18.1\ ^\circ C$ and $t_{LRO} = 7.0\ s$, while moderate geysering was observed in a test with $T_i = 13.4\ ^\circ C$ and $t_{LRO} = 3.1\ s$ and strong geysering was observed during a test with $T_i = 10.7\ ^\circ C$ and $t_{LRO} = 3.3\ s$. Very strong geysering was observed with initial temperature $T_i = 3.1\ ^\circ C$ and $t_{LRO} = 3.6\ s$. As noted earlier, short test times and low temperatures seem to be the conditions at

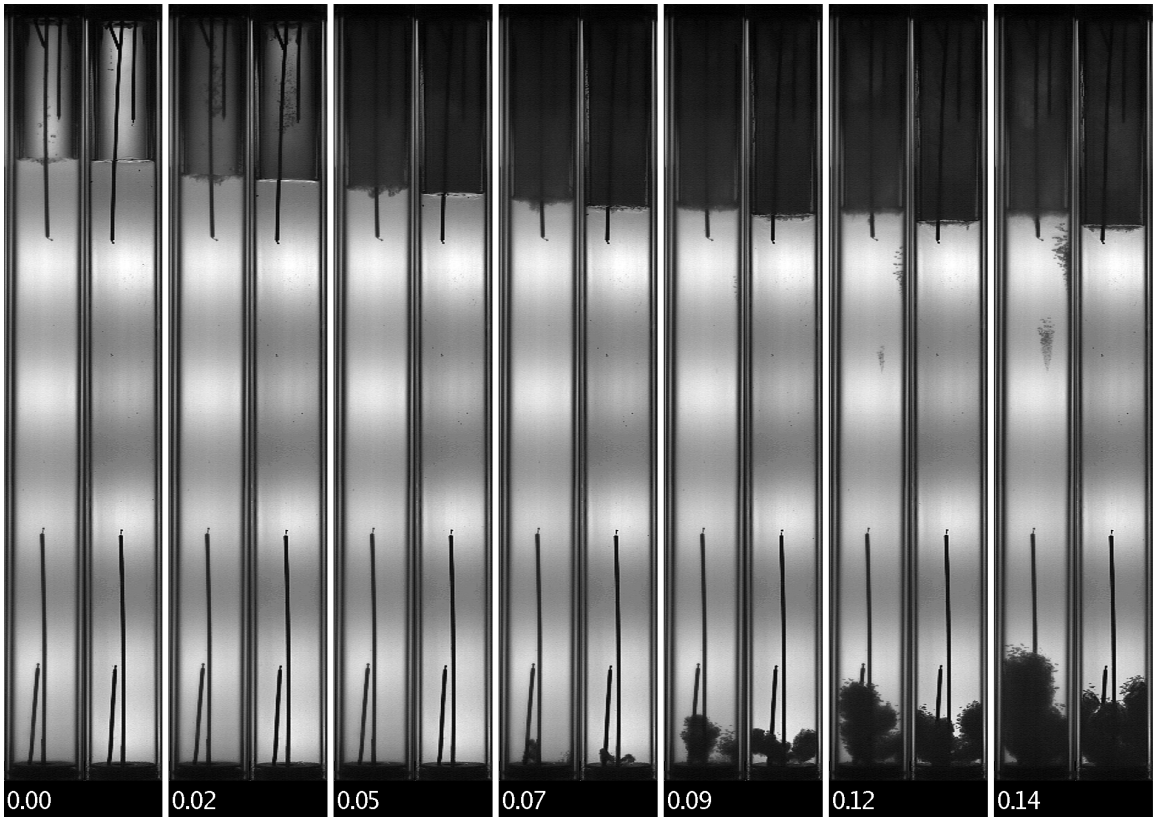

Figure 4.95: Image sequence comparison for early times from the CO_2 (left) and N_2O (right) tests. Each pair of frames are taken from the two tests at the same normalized time, indicated by the number below.

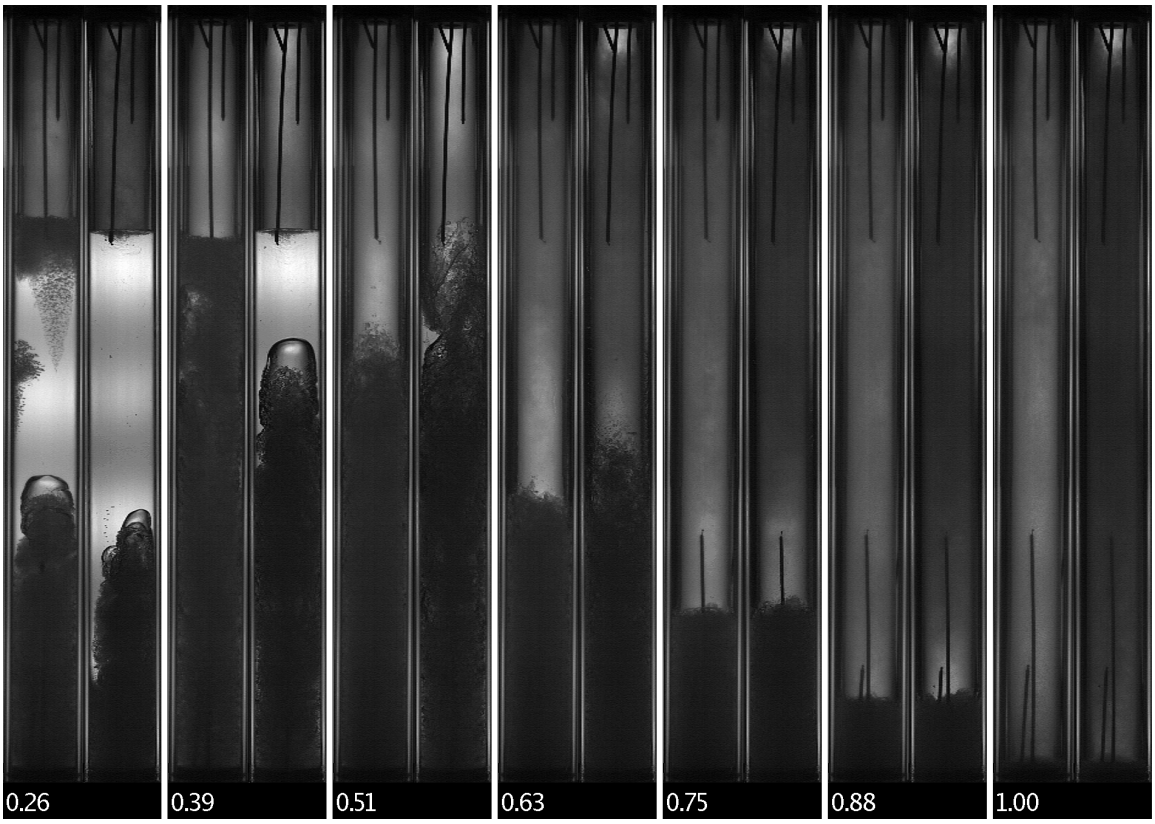

Figure 4.96: Image sequence comparison for later times from the CO_2 (left) and N_2O (right) tests. Each pair of frames are taken from the two tests at the same normalized time, indicated by the number below.

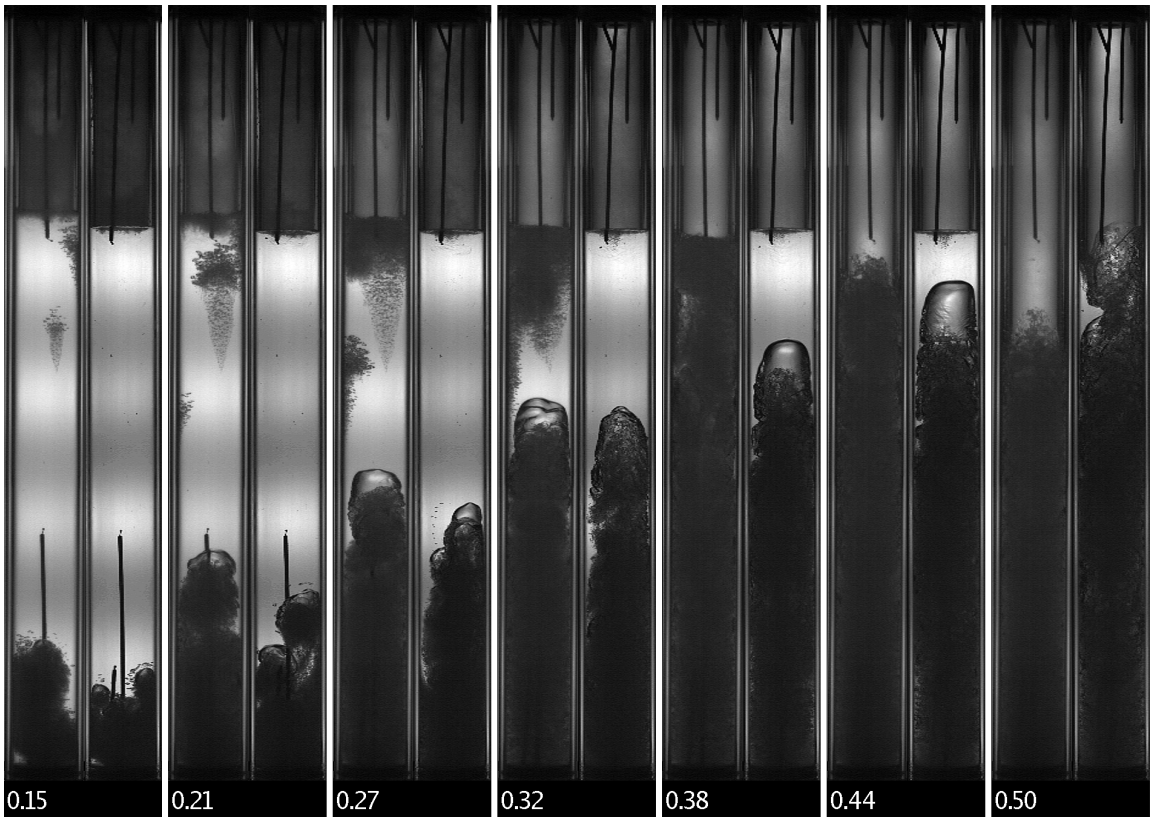

Figure 4.97: Image sequence comparison the times at which the Taylor bubble is most visible for the CO_2 (left) and N_2O (right) tests. Each pair of frames are taken from the two tests at the same normalized time, indicated by the number below.

Figure 4.98: Image sequence showing "mild" Taylor bubble formation in N_2O.

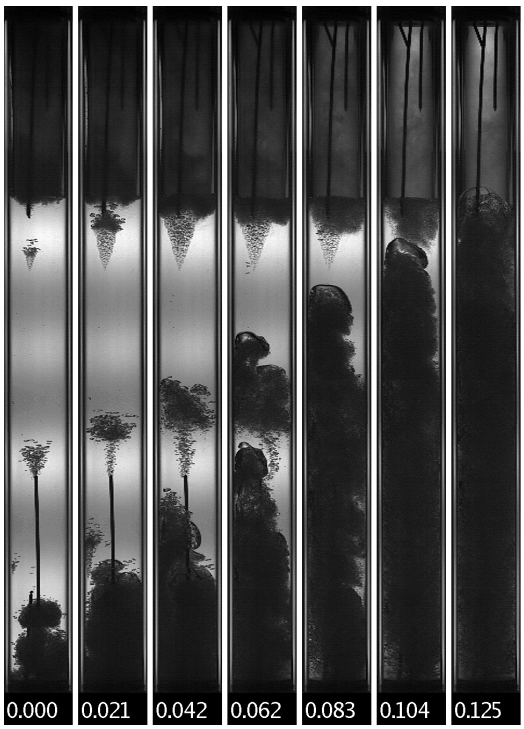

Figure 4.99: Image sequence showing "moderate" Taylor bubble formation in N_2O.

which geysering is most likely to occur.

Earlier it was mentioned that tests with a significant initial bubble population seemed to prevent geysering from occurring. To demonstrate, two tests will be briefly compared here, one that has an initial bubble population and one without. This was done in the same way that the tests shown previously in subsection 4.2.4, by venting the ullage. For simplicity these two tests will be referred to simply as "flat" and "bubbly."

All other parameters of the two tests were reasonably matched, including the fill levels (82, 83%), mean initial temperatures (18.3, 18.1 $°C$), the initial temperature profiles, orifice diameters (1.092 mm), and test times ($t_{LRO} = 3.94, 3.96\ s$) for the flat and bubbly tests respectively. The data from these two tests are shown in figures 4.102 to 4.104. Figure 4.102 shows both pressure traces and the normalized pressure traces, while figure 4.103 shows the initial temperature profiles and 4.104 shows a

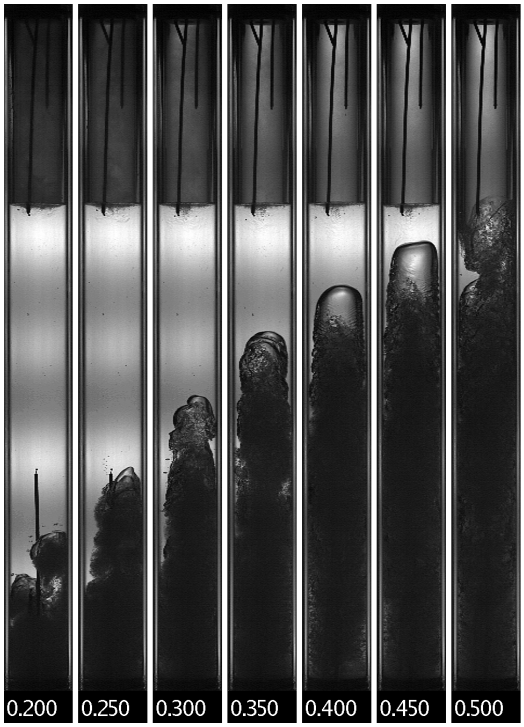

Figure 4.100: Image sequence showing "strong" Taylor bubble formation in N_2O.

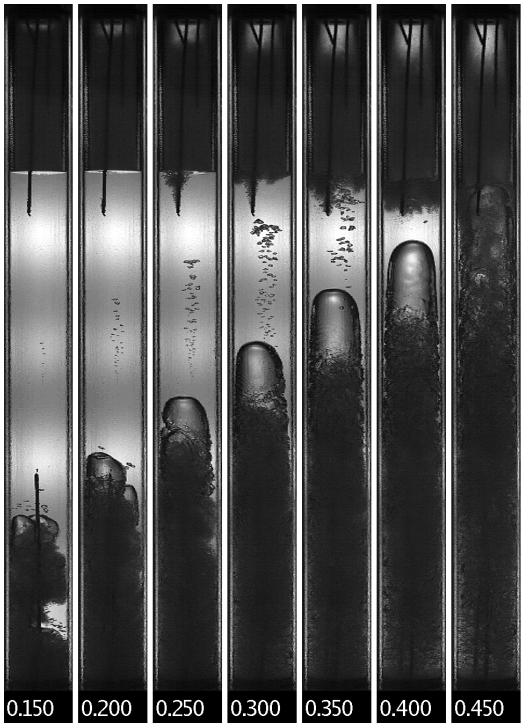

Figure 4.101: Image sequence showing "very strong" Taylor bubble formation in N_2O.

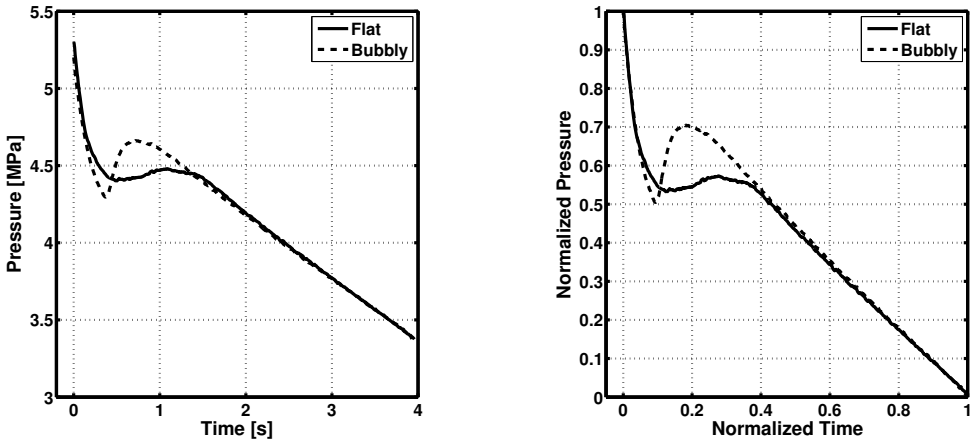

Figure 4.102: Pressure and normalized pressure time histories for the flat and bubbly tests. Tests performed with CO_2.

comparison of the still images during the early part of the test when the geysering effect is visible.

The large difference between these two tests in the pressure time histories are in stark contrast to the temperature profiles, which are nearly identical. This reiterates the concept that this system is sensitive to all aspects of the initial conditions, even those that cannot be easily measured such as the initial bubble population. In the flat test the pressure recovery in the transient regime has been completely suppressed however this does not affect the rest of the test, with the times before and after being nearly indistinguishable in terms of the pressure histories. The image sequence in figure 4.104 shows the Taylor bubble forming in the flat test around $t_n = 0.200$ while in the bubbly test there is much more uniform bubble nucleation throughout the tube, preventing a Taylor bubble from forming at all.

Geysering has traditionally been observed within cryogenic propellant feed lines and generally has a negative impact on the propulsion system by either disrupting the flow of propellant or damaging components via a water hammer effect after the Taylor bubble bursts. However, geysering in a self-pressurized propellant tank is less of a concern because its main effects are an increase in bubble nucleation below the Taylor bubble and reduction of the magnitude of the pressure drop and recovery. The

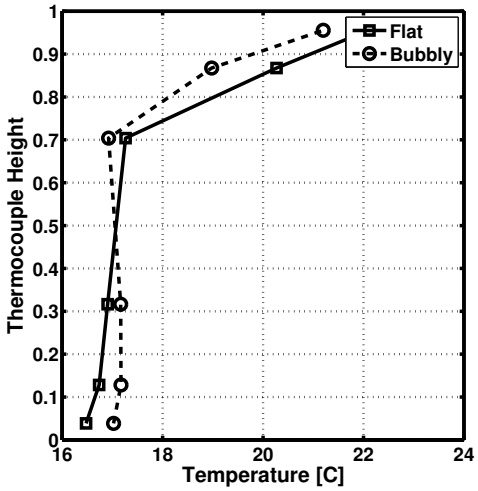

Figure 4.103: Initial temperature profiles for the flat and bubbly tests. Tests performed with CO_2.

flat and bubbly tests described in this section demonstrate this quite well, with no other differences visible in the pressure data.

Flat Glass Gauge

Here, tests in the flat glass gauge will be compared between the two fluids to determine the presence or absence of scaling effects that differ between carbon dioxide and nitrous oxide. All parameters of the two tests were reasonably matched, including the fill levels (83%), mean initial temperatures (CO_2 : 17.6, N_2O : 19.1 $°C$), test times (5.94, 5.92 s), the initial temperature profiles, and orifice diameters (2.261 mm). The data from these two tests are shown in figures 4.105 to 4.108. Figure 4.105 shows both pressure traces and the normalized pressure traces, while figure 4.106 shows the initial temperature profiles. Figures 4.107 and 4.108 show a comparison of the still image sequences from these two tests.

Beginning with the pressure time histories, the higher saturation pressure of CO_2 his increased the starting pressure by 0.35 MPa. With this exception, the curves are quite similar and the normalized pressure histories only show a slight difference during the transient regime, with the N_2O test having a lower P_{min} and P_{max} although

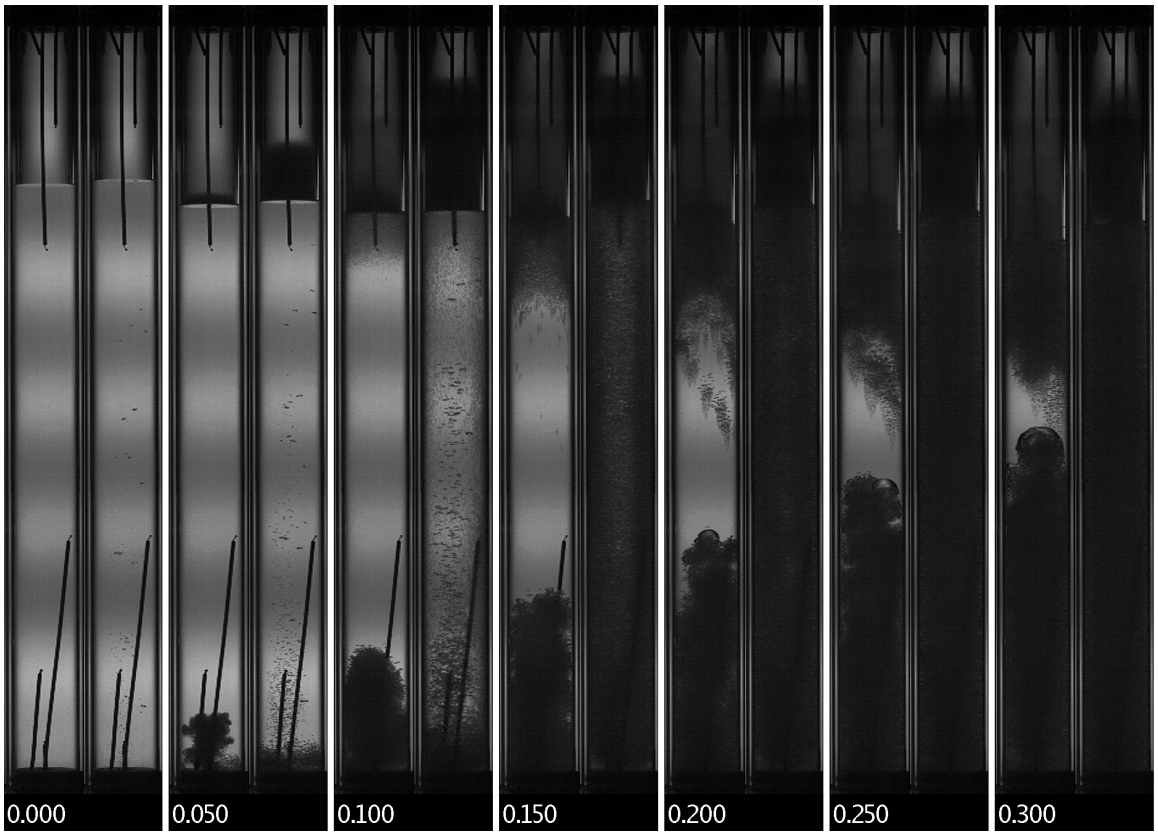

Figure 4.104: Image sequence comparison for early times from the flat (left) and bubbly (right) tests. Each pair of frames are taken from the two tests at the same normalized time, indicated by the number below. Tests performed with CO_2.

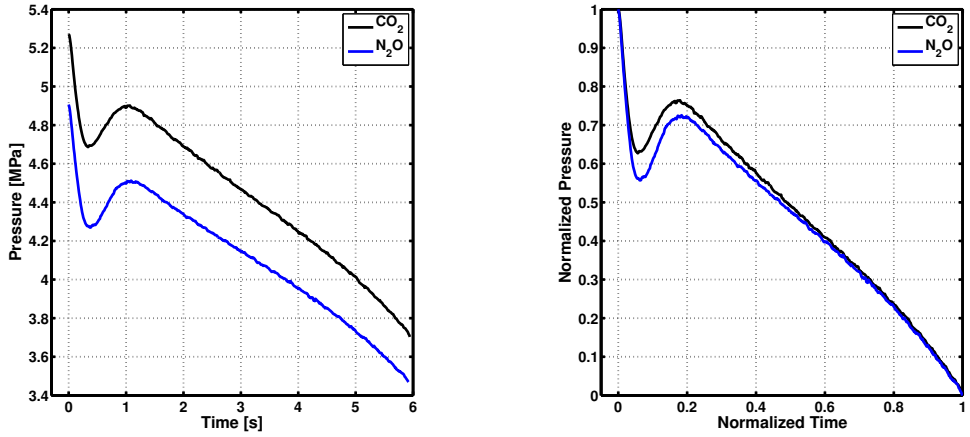

Figure 4.105: Pressure and normalized pressure time histories for CO_2 and N_2O tests.

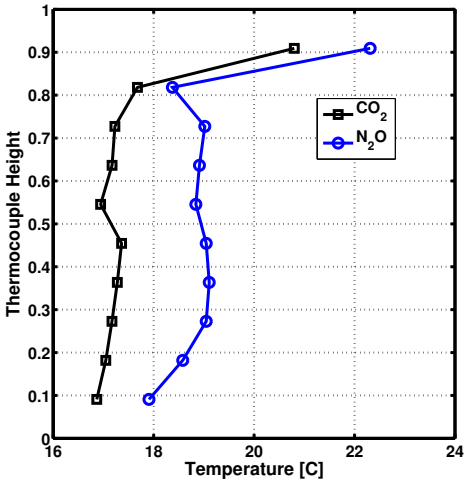

Figure 4.106: Initial temperature profiles for the CO_2 and N_2O tests.

the associated times are nearly identical. The image sequences in figures 4.107 and 4.108 are also quite similar although the condensation behavior of the ullage of the two fluids is different. In the N_2O test the ullage condenses rapidly and uniformly and staying condensed enough to render it nearly opaque for the entire test. In the CO_2 test however condensation is initially limited to the space immediately above the liquid level, and then gradually increases to reach the top of the ullage by about $t_n = 0.72$.

4.3.3 Summary and Conclusions

In this section a thorough experimental comparison of CO_2 and N_2O has been presented with the goal of demonstrating that carbon dioxide can be used as an accurate analog for nitrous oxide. The two were first compared with the early polycarbonate experimental system where they showed similar behavior at a range of mass flow rates but at the highest flow rates a geysering phenomenon was observed only in carbon dioxide. This phenomenon has been previously studied but empirical correlations show only a weak dependence on fluid properties.

Later a new test series was conducted with the quartz tube system that leveraged better instrumentation and control of the initial conditions to show that geysering

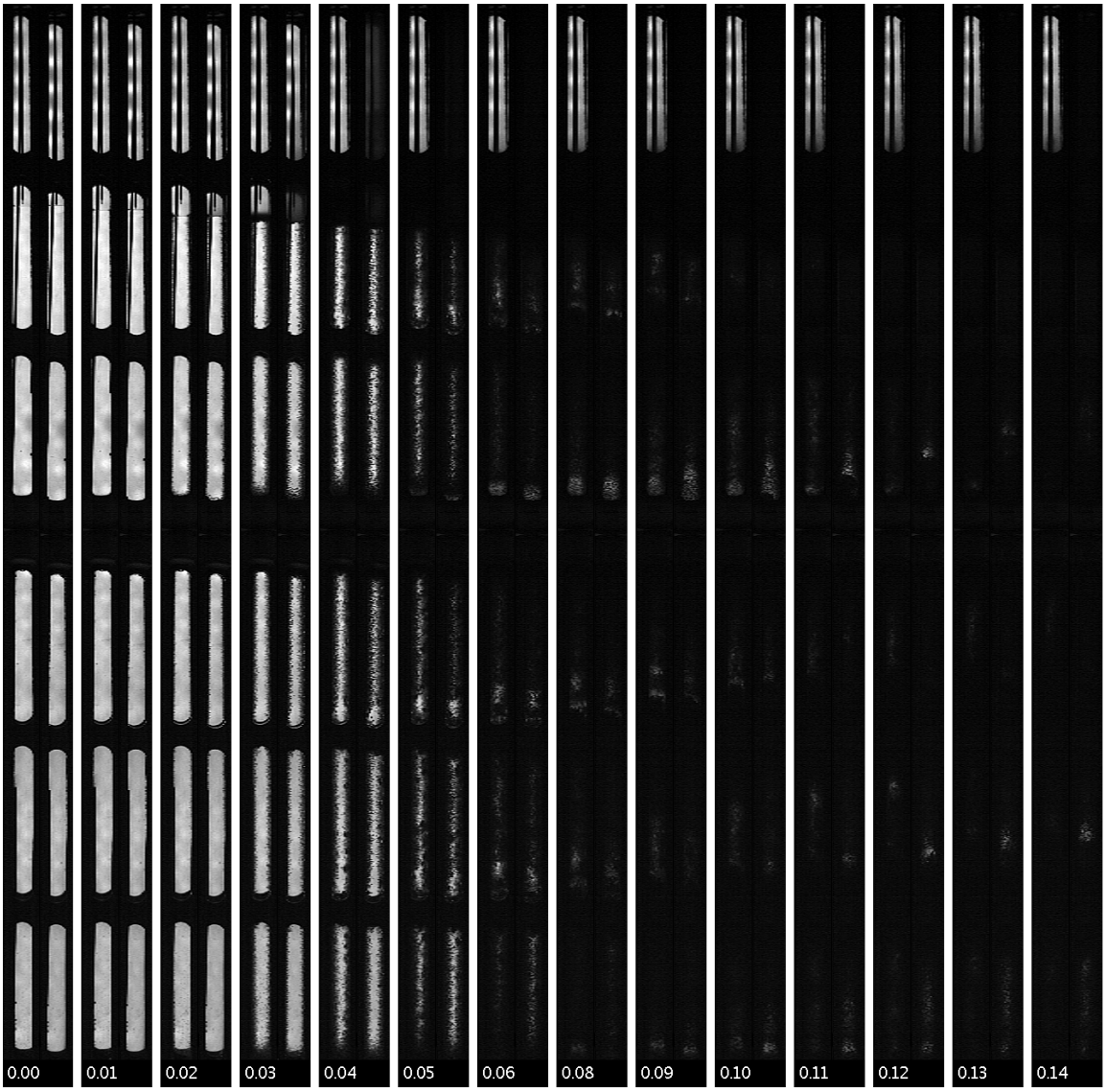

Figure 4.107: Image sequence comparison for early times from the CO_2 (left) and N_2O (right) tests. Each pair of frames are taken from the two tests at the same normalized time, indicated by the number below.

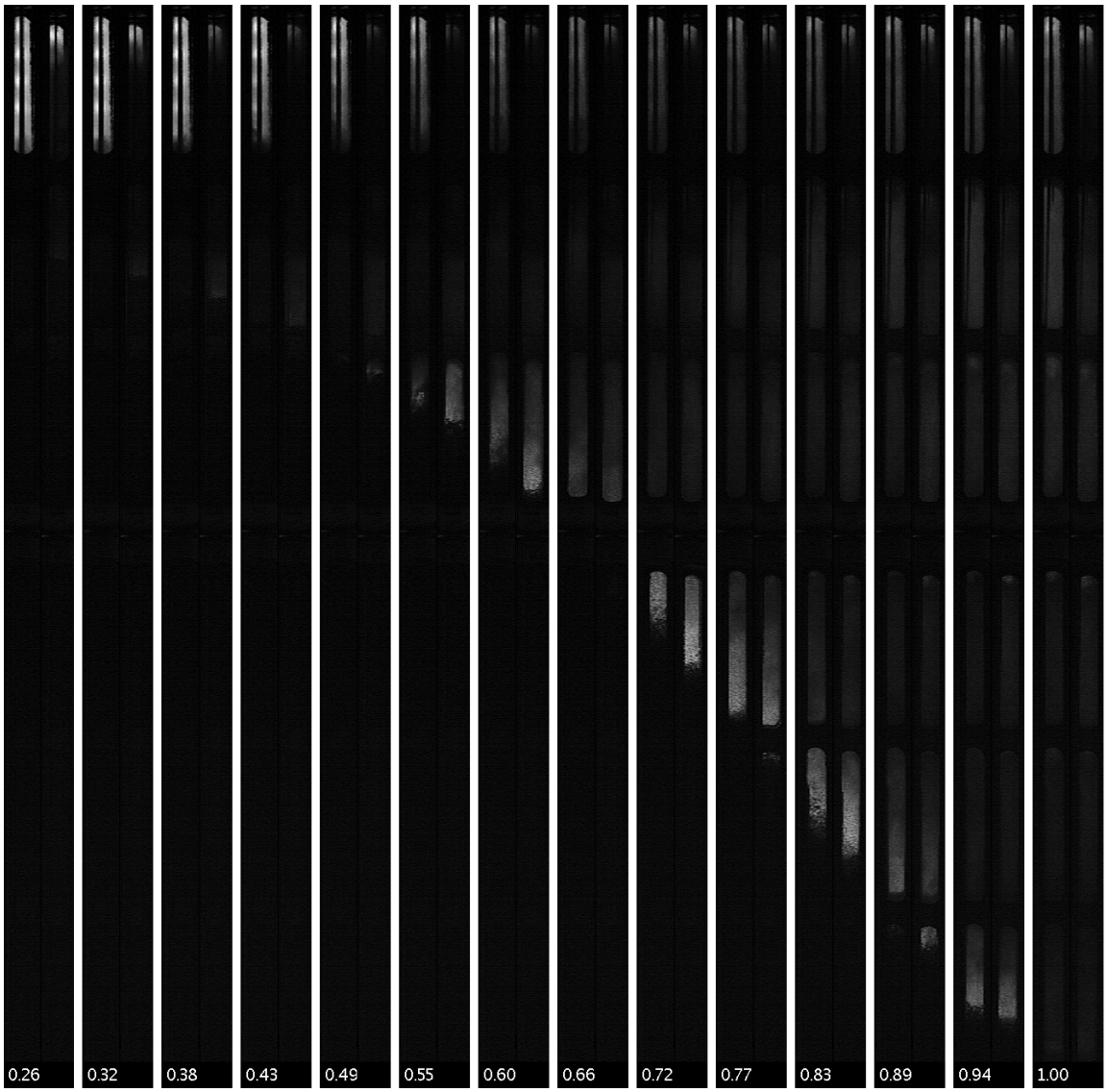

Figure 4.108: Image sequence comparison for later times from the CO_2 (left) and N_2O (right) tests. Each pair of frames are taken from the two tests at the same normalized time, indicated by the number below.

was indeed possible with both fluids. This system demonstrated that the two fluids do behave similarly and differences observed earlier were likely caused by variations in the initial temperature field within the test vessel. Additionally, results with N_2O at elevated temperature were shown that exhibited the functional temperature dependence as that of carbon dioxide. Lastly, the flat glass gauge was used to show a comparison of the two fluids at larger size scales. No significant differences between the two fluids was detectable in this system.

We can therefore conclude that carbon dioxide can be used as an accurate simulant fluid for nitrous oxide in this type of research. The only significant caveat to this is that the largest size scales examined here are quite small compared to many practical propulsion systems. Therefore any engineers or scientists studying larger vessels should demonstrate that CO_2 still functions similarly to N_2O before using CO_2 as a simulant fluid in those systems.

4.4 Multicomponent Mixtures

Mixtures of nitrous oxide with other fluids have been proposed [80, 81] as a way to mitigate the decomposition hazards associated with pure nitrous oxide, establish another degree of freedom that can be used to control the propellant's P, ρ, T relationship, or increase the propulsion system's performance. A more exotic application is in the in-situ production of oxidizers on Mars (such as carbon dioxide, carbon monoxide, or oxygen) and possibly mixing it with N_2O or other oxidizers brought from Earth [82]. Others have even suggested mixtures of nitrous oxide with hydrocarbon fuels as a "pre-mixed" monopropellant [83] however this greatly increases the likelihood of a decomposition reaction occurring within the tank and is therefore presents significant explosion hazards [51].

Depending on how the second component is introduced, there are many new possible operating conditions but here we will consider just two. First, if the fluids are well mixed then the entire tank becomes a multicomponent system with different concentrations of the two components in the liquid and vapor. The second case is if the second fluid is added to the ullage volume shortly before the motor firing begins and hence it has little time to mix with the liquid in the tank. In this case the liquid remains pure nitrous oxide while the ullage is a two component mixture and in this case we refer to the second fluid as an external pressurant. If this external pressurant is continuously added to the ullage throughout the firing and the pressure is maintained above the saturation pressure of the liquid propellant there will be no boiling and the resultant tank dynamics are relatively simple. This may be desirable as a way to prevent two-phase flow in the lines between the tank and injector or as a way to help establish critical flow and thereby mitigate a feed-coupled instability [84, 85].

To study the behavior of each of these cases, a variety of experiments have been performed with CO_2 as a simulant for N_2O and N_2 as the second component. We begin with cases where the N_2 has been added to the ullage alone and is not thoroughly mixed with the liquid. This case is sometimes referred to as "supercharging" although that term has also been used by some to refer any situation in which the N_2O is pressurized above the saturation point (also termed subcooling). Subsequently, the

case in which N_2 has been mixed with both the liquid and ullage vapor will be presented.

4.4.1 Nitrogen Added to Ullage

In this section we begin by discussing two different tests in which N_2 has been added to the ullage prior to the start of a test, but not during the test. No N_2 flows into the tank while the test is underway. The procedure for these two tests was slightly different however. In the first case the N_2 was simply added to the ullage and then the test was begun after a delay of 10 minutes. In the second test, after the N_2 was added the top end cap was chilled down to roughly $0°C$. As CO_2 vapor encountered the top end cap either via diffusion or convection from the liquid level it condensed on the cold surface. Droplets formed and fell back into the liquid CO_2 and created a layer at the top of the liquid with some amount of N_2 dissolved into it. These tests will be referred to simply as "pure" and "dissolved" for brevity.

Although the liquid temperatures were relatively similar (18.0, 15.5 $°C$), the ullage of the second test was of course much colder than in the first test. The fill levels were also somewhat different (72, 82%) but they did use the same orifice diameter (0.559 mm) and the test times were similar ($t_{LRO} = 13.0, 14.5\ s$). The two tests were also pressurized to slightly different levels (6.53, 7.00 MPa) as a result of some variability in the performance of the the regulator used on the N_2 tank.

The data from these two tests are shown in figures 4.109 to 4.112. Figure 4.109 shows both pressure traces and the normalized pressure traces, while figure 4.110 shows the initial temperature profiles. Figures 4.111 and 4.112 show a comparison of the still image sequences from these two tests.

The pressure time histories shown in figure 4.109 are quite different than those shown in other tests. The transient pressure drop is quite large while the recovery is very small in magnitude. In the dissolved test there is no actual recovery, instead the pressure merely stabilizes rather than increasing.

The image sequence from the early times shown in figure 4.111 is quite interesting. In the pure test, there is some CO_2 condensation in the ullage but only in

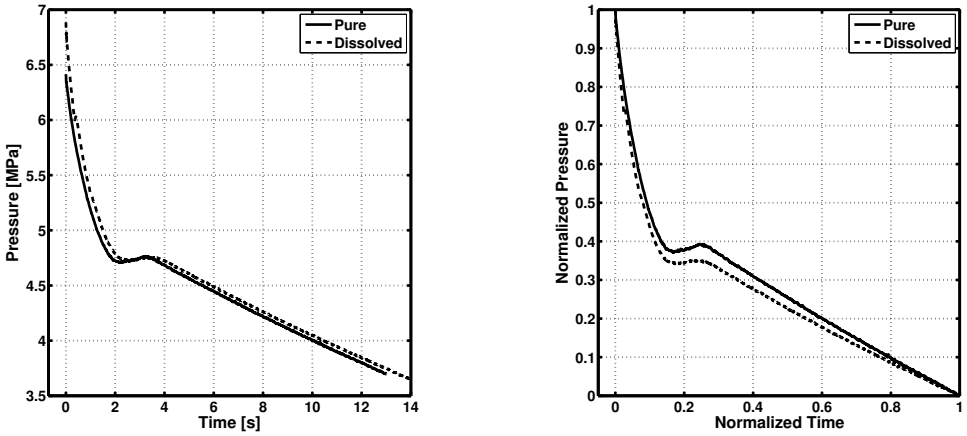

Figure 4.109: Pressure and normalized pressure time histories for the pure and dissolved tests. Tests performed with CO_2.

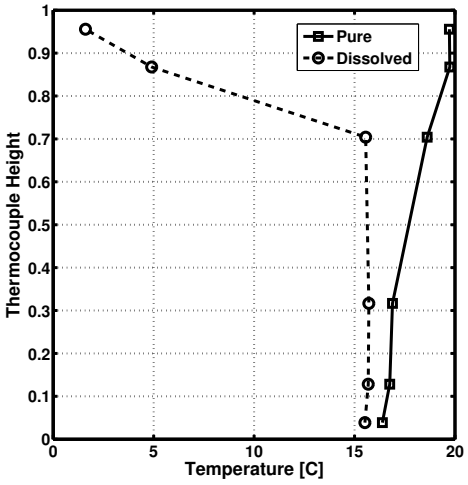

Figure 4.110: Initial temperature profiles for the pure and dissolved tests. Tests performed with CO_2.

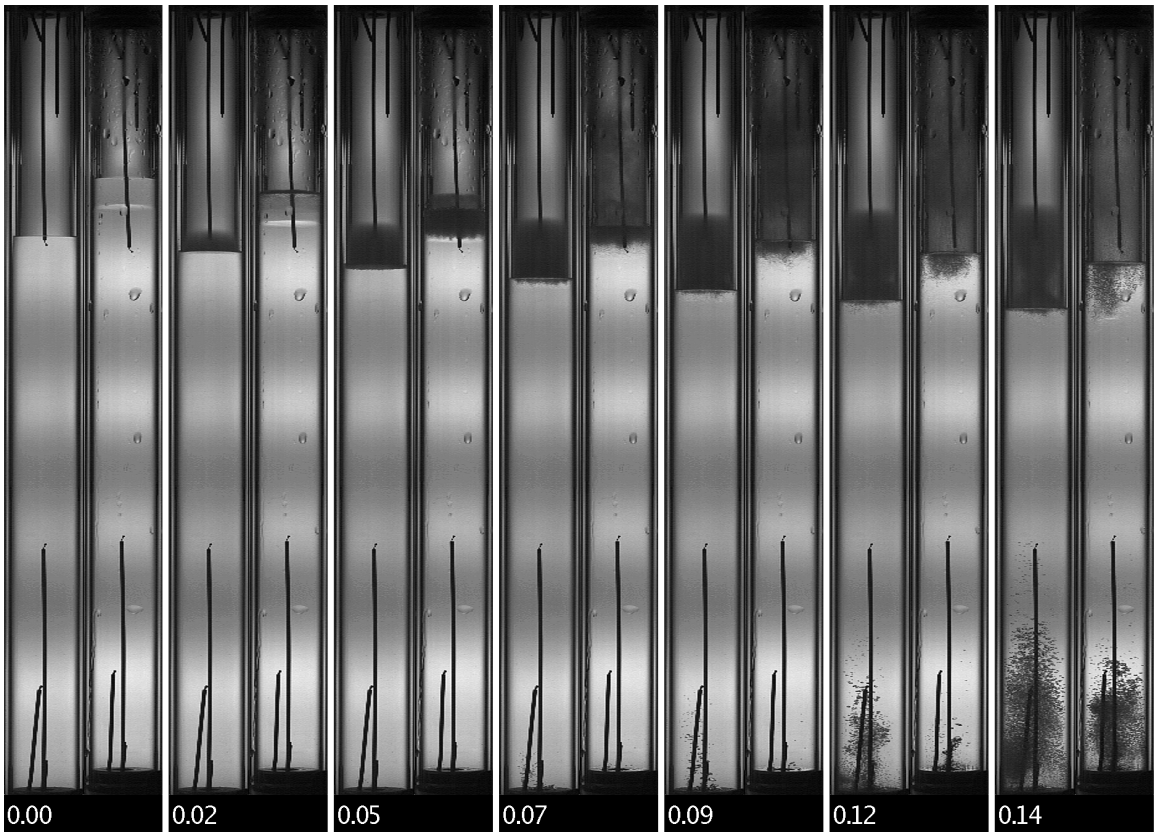

Figure 4.111: Image sequence comparison for early times from the pure (left) and dissolved (right) tests. Each pair of frames are taken from the two tests at the same normalized time, indicated by the number below. In the dissolved test, some water droplets are visible on the outside of the tube. Tests performed with CO_2.

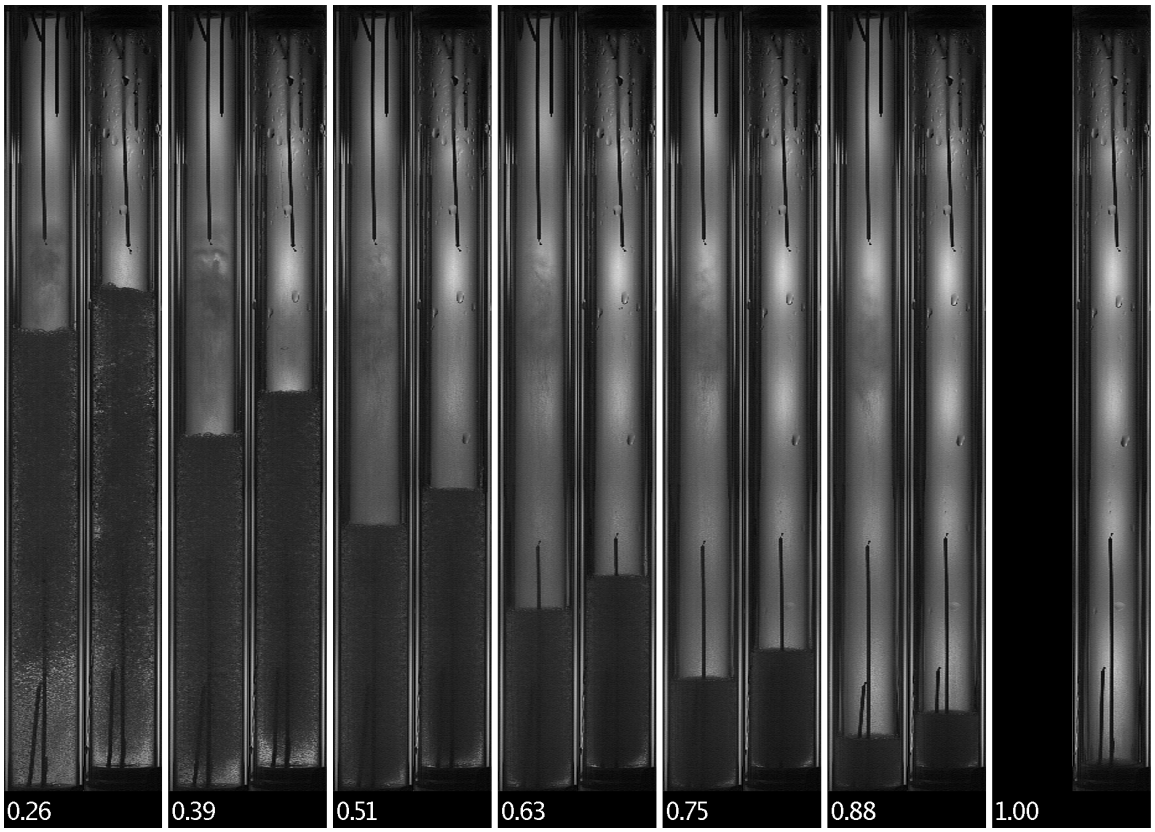

Figure 4.112: Image sequence comparison for later times from the pure (left) and dissolved (right) tests. Each pair of frames are taken from the two tests at the same normalized time, indicated by the number below. In the dissolved test, some water droplets are visible on the outside of the tube. Tests performed with CO_2.

the lower half. This lower region is likely the area in which CO_2 vapor has diffused into the ullage, while the upper part has a lower concentration of CO_2 and hence no condensation occurs there as the pressure drops.

In the dissolved test we see the region of liquid CO_2 with N_2 dissolved into it nucleate numerous bubbles at $t_n = 0.05$ and the ullage condenses uniformly shortly after at $t_n = 0.07$. These are both expected behaviors, as the bubble point in the liquid CO_2 and N_2 mixture is above the saturation pressure of the pure CO_2 . The ullage has also been well mixed by chilling the upper end cap, as natural convection cells would no doubt be established within the ullage. In the later times shown in figure 4.112 the two tests are much more similar, and a steady state regime has been established in the pure liquid carbon dioxide.

The nucleation within the upper part of the liquid in the dissolved test is reminiscent of the "top hot" test shown earlier in subsection 4.2.3, specifically figure 4.33. In that case, transient and steady state regimes were established in just this top region and so we may expect similar behavior here. In figure 4.113, the pressure history from the very early times is shown. Visible is a short drop and recovery of pressure around $t = 0.4\ s$ in the dissolved test, showing that we do indeed have a transient regime established in this small portion of liquid.

Another phenomenon that can be investigated here is the rate at which N_2 will diffuse into the liquid CO_2 without any external mixing mechanisms such as the chilled end cap used for the dissolved test. To test this experimentally, a test series was conducted in which the time delay between the addition of N_2 to the ullage and the commencement of the test was varied from less than a minute to one hour. The specific times were: $30\ s, 120\ s, 8\ min$, and $60\ min$. In other senses the tests were similar and all were pressurized to about 6.9 MPa. The results are shown in figure 4.114, which compares the appearance of the liquid adjacent to the ullage during the early times. It is in these times that we would expect to see some boiling if indeed any N_2 has diffused into the liquid.

If the four tests are compared at any one time, there is a clearly increasing amount of boiling from the top test to the bottom. The amount of dissolved N_2 is still relatively low, even for the test with a 60 min delay. No drop and recovery like that

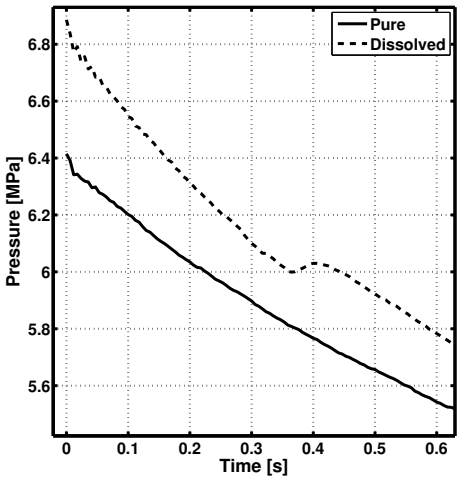

Figure 4.113: Pressure time histories for the pure and dissolved tests in the very early times. Tests performed with CO_2.

seen in the dissolved test in 4.113 was observed for these.

4.4.2 Nitrogen Added to Liquid and Ullage

We now examine tests in which N_2 has been mixed into the liquid as well as the ullage. Specifically, two variations will be presented: one in which the the N_2 concentration within the liquid is fairly uniform, and a second in which it is not. The uniform concentration field was constructed by pressurizing the test vessel with N_2 before pumping in the CO_2. The non-uniform concentration was formed by performing this process incrementally, with alternating additions of N_2 and CO_2 and resulted in three distinct sections or layers with different N_2 concentrations within the liquid. In both cases the top end cap was chilled once again to established a well-mixed ullage volume. These two tests will be referred to "uniform" and "layered" respectively.

All other parameters of the two tests were reasonably matched, including the fill levels (93, 95%), mean initial temperatures (14.3, 14.7 $°C$), the initial temperature profiles, starting pressures (8.85, 8.68 MPa), orifice diameters (0.559 mm), and test times $t_{LRO} = 11.3, 13.1\ s$ for the uniform and layered tests respectively. The data from these two tests are shown in figures 4.115 to 4.118. Figure 4.115 shows both

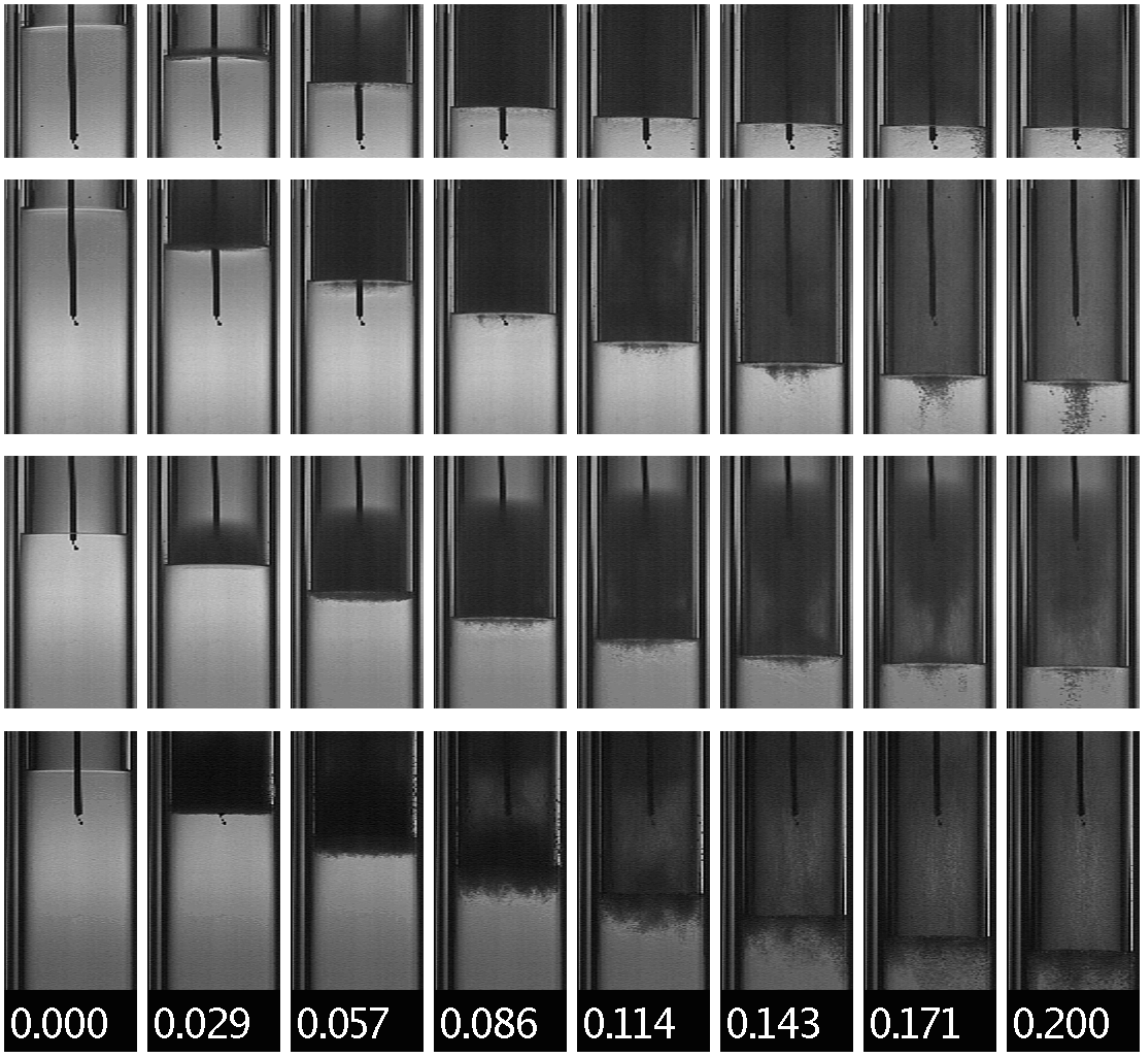

Figure 4.114: Image sequence comparison between four different tests. Only shown is the region around the liquid level for early times. Each vertical set of four images is taken at the same normalized time, indicated by the number below. In the top test, N_2 was added to the ullage immediately prior to the start of the test. The second test was started precisely two minutes after N_2 was added to the ullage. For the third test there was a delay of eight minutes, and for the bottom test the delay was increased to one hour. Tests performed with CO_2.

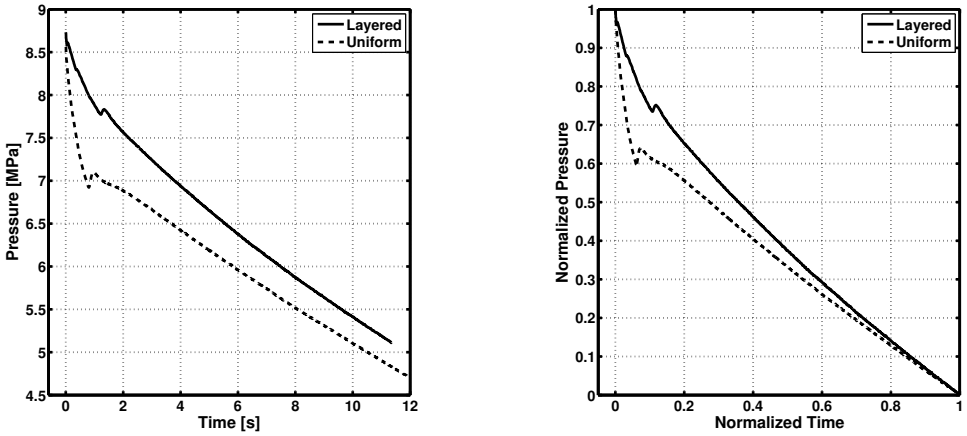

Figure 4.115: Pressure and normalized pressure time histories for the layered and uniform tests. Tests performed with CO_2.

pressure traces and the normalized pressure traces, while figure 4.116 shows the initial temperature profiles. Figures 4.117 and 4.118 show a comparison of the still image sequences from these two tests.

The pressure traces in figure 4.115 show the same basic features of most CO_2 or N_2O tests, with a transient regime with a drop and recovery followed by a linear steady state. However the transient regimes here have much larger pressure drops, the recoveries are quite small, and the layered test's steady state regime is less uniform with distinct positive curvature.

The image sequence for the early times is fascinating. In the uniform test, the first relevant feature is seen in the very top region of the liquid where nucleation begins at $t_n = 0.02$ simultaneously with condensation of the ullage. This is a thin layer of high N_2 concentration formed by the chilled top end cap, similar to the dissolved test of the previous subsection. Later at $t_n = 0.05$ uniform heterogeneous bubble nucleation begins in the liquid although in the next frame at $t_n = 0.07$ it appears that there is a somewhat higher nucleation rate in the upper half of the tube. By $t_n = 0.14$ the mixture quality of the liquid does appear uniform throughout the entire tube.

For the layered test the process is quite different. The ullage does not condense until $t_n = 0.09$, and the three separate layers of different N_2 concentration can be

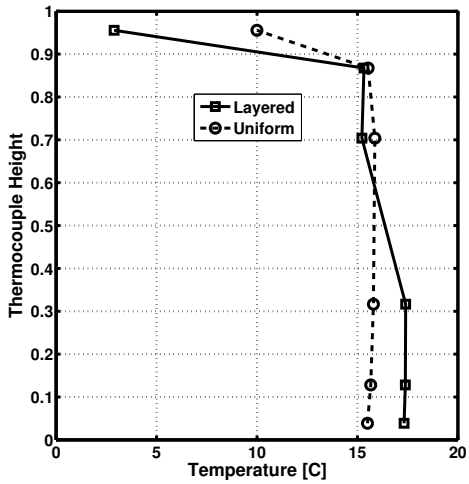

Figure 4.116: Initial temperature profiles for the layered and uniform tests. Tests performed with CO_2.

seen with bubble nucleation starting at different times. The first is at $t_n = 0.02$, the second at $t_n = 0.05$, and the third at $t_n = 0.12$. At each of these the bubble nucleation process is uniform within the layer. After the third layer has nucleated, the mixture appears to be spatially homogeneous and similar to the uniform test. The image sequence from the later times as well as the pressure time histories prove this, with the two tests showing little or no differences after $t_n \sim 0.2$.

To examine the interesting behavior of the layered test, another image sequence is given in figure 4.119 and the pressure time history for the very early times is shown in figure 4.120. The combination of these two figures shows that each of these layers functions the same as the dissolved test of the last section or the top hot test from section 4.2. In each case there is a small pressure drop and recovery, followed by a steady state until the next layer has been activated.

4.4.3 Summary and Conclusions

In this section tests have been presented that used mixtures of N_2 and CO_2. Two general cases were considered: one in which the N_2 was added primarily to the ullage gas and in the second the N_2 was mixed into the liquid as well.

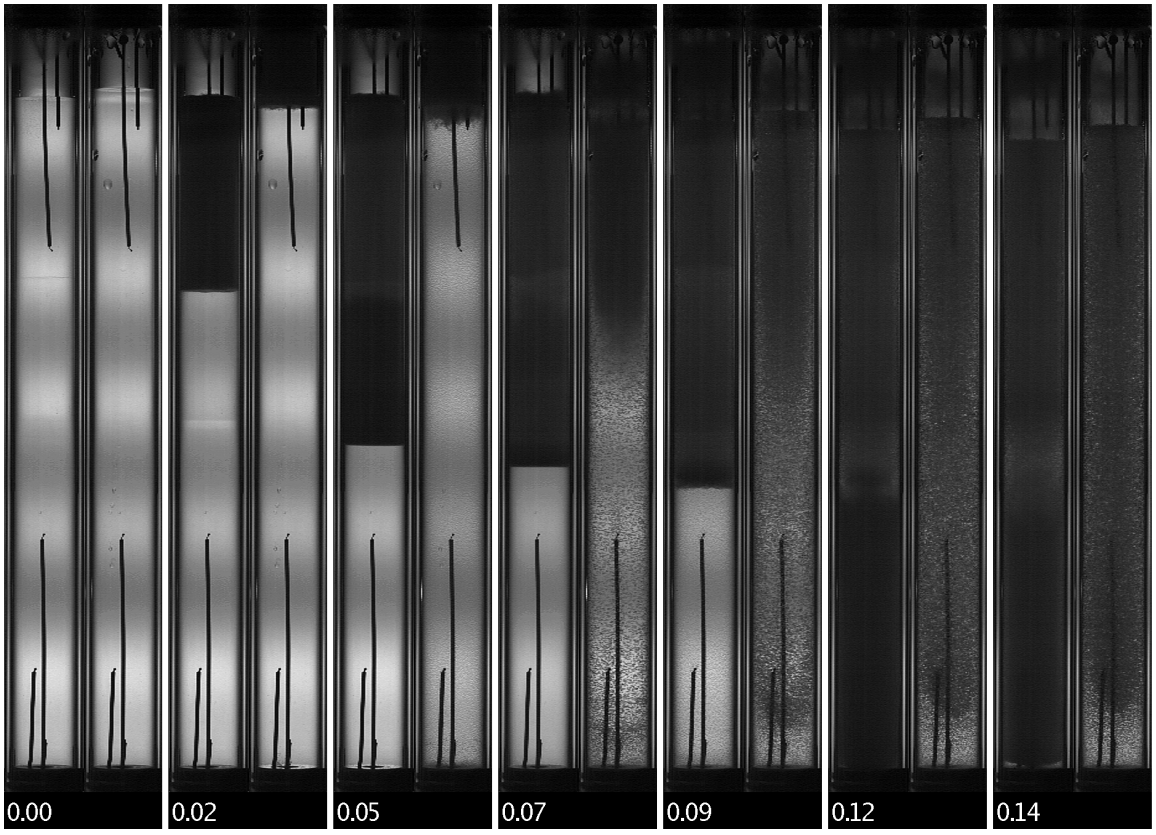

Figure 4.117: Image sequence comparison for early times from the layered (left) and uniform (right) tests. Each pair of frames are taken from the two tests at the same normalized time, indicated by the number below. In the uniform test, some water droplets are visible on the outside of the tube. Tests performed with CO_2.

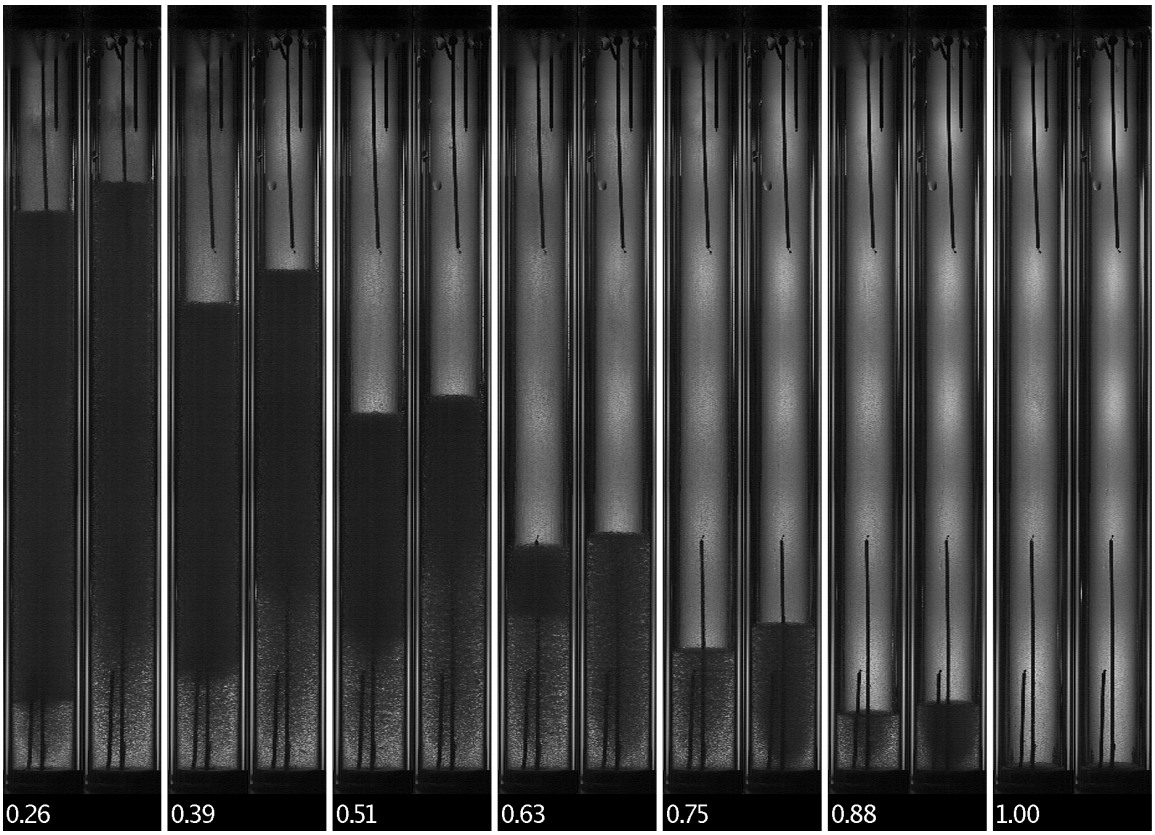

Figure 4.118: Image sequence comparison for later times from the layered (left) and uniform (right) tests. Each pair of frames are taken from the two tests at the same normalized time, indicated by the number below. In the uniform test, some water droplets are visible on the outside of the tube. Tests performed with CO_2.

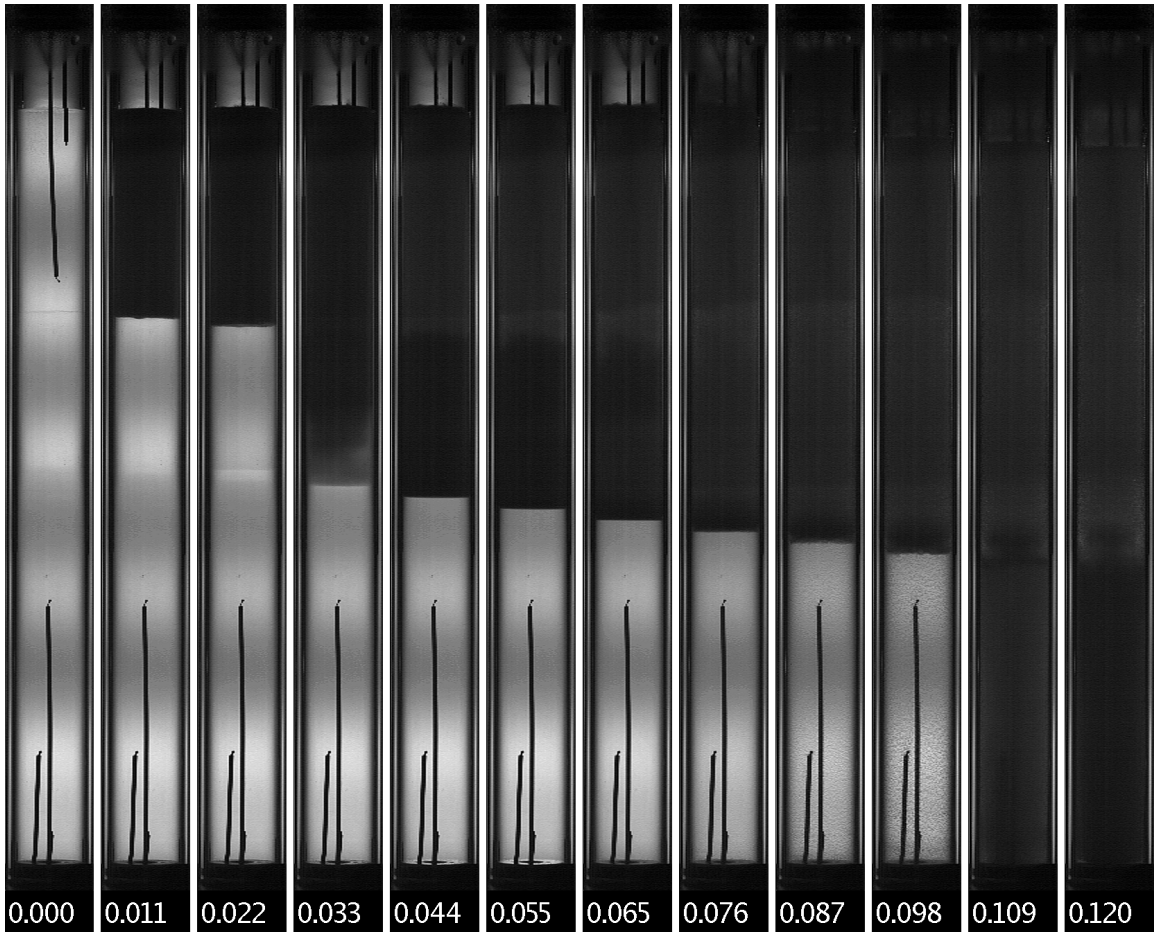

Figure 4.119: Image sequence for the layered test highlighting the bubble nucleation process. Numbers below each frame indicate the normalized time. Test performed with CO_2.

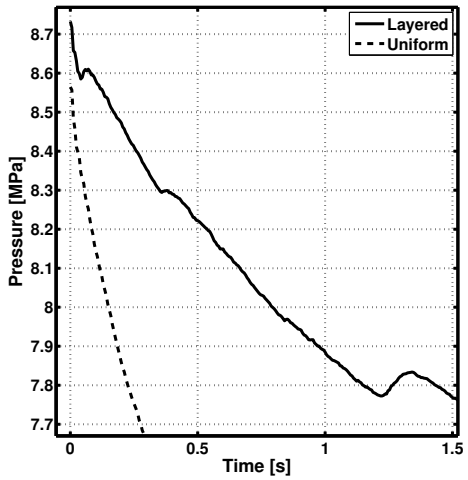

Figure 4.120: Initial temperature profiles for the layered and uniform tests. Tests performed with CO_2.

When the N_2 was present in the ullage alone, the transient pressure drop began at a much higher pressure, but once it dropped to the vapor pressure of the liquid the system quite similarly to tests with CO_2 alone, with a subsequent pressure rise followed by a steady state regime. Additionally, having a small layer of liquid CO_2 with N_2 dissolved into it made it behave similar to the "top hot" test shown in figure 4.33, where a transient and steady state regime were established with only this small volume active.

Tests were also presented with N_2 mixed into the liquid either in a uniform or non-uniform fashion. In the uniform case, the system behaved similarly to the basic pure CO_2 test, with a transient and steady state regime still present although distorted. In the non-uniform case three distinct regions of different N_2 concentration were present in the liquid. Each of these behaved like the "top-hot" case presented earlier, with the pressure time history showing three different transient/steady-state regime sections.

Chapter 5

Proposed Model

In this section, a new model for self-pressurizing propellant tank dynamics will be described, based on the experimental results shown in chapter 4. First, a the key conclusions from the experiments are summarized along with their implications for modeling. Then the basic governing equations for the model are derived, followed by a description of several submodels needed and the numerical methods used. Results of the model are shown next including results showing the effect of various model parameters.

5.1 Conclusions from Experiments

The single most important discovery from the experiments has been the importance of boiling. Boiling is the dominant heat and mass transfer mechanism between the liquid and ullage and is responsible for the transient pressure drop and recovery. For a model to accurately describe this system, a focus must be made on describing the complete bubble dynamics including heterogeneous nucleation, departure, growth, coalescence, and transfer of the vapor within the bubbles to the ullage when they reach the free surface.

The ullage was observed to be an equilibrium two-phase mixture for much of the test in most experiments. The quality of the ullage had strong spatial gradients and also appeared to vary with time as well. Previous models assumed the ullage to be

a saturated vapor, with a constant $x = 1$, an assumption that now appears to be inaccurate. Nevertheless, the ullage can likely still be modeled accurately with a single node, with $0 \leq x \leq 1$.

This is because the pressure is decreasing for the majority of the test, meaning that the ullage is generally expanding. If external heat transfer is not too large, this means that any fluid element within the ullage that is superheated will eventually reach the saturation line, undergo condensation, and become a mixture. Since all mass that is transferred to the ullage enters as saturated vapor (from within a bubble), the entire ullage will be composed of a two-phase mixture. Then, because a two-phase mixture exists throughout the ullage at the same pressure, the temperature must also be uniform and equal $T_{sat}(P)$.

The liquid was observed to have superheats of up to $\sim 5°C$ and due to the sensitivity of fluid properties to temperature and pressure it must be modeled as a metastable fluid. In many tests the liquid appeared spatially non-uniform during the transient regime with bubbles initially present in only some parts of the tube, but uniform in the steady state regime. In others the liquid was relatively uniform, such as the tests in the flat glass gauge and those at elevated temperature. Therefore a spatially uniform liquid will be assumed because it greatly simplifies the model development and will allow it be compared against these selected experimental data. If the model is shown to be accurate in these cases it could be extended to have a non-uniform liquid in order to be usable in more situations.

5.2 Overview

A set of overview diagrams is given in figure 5.1 to outline the model. The model begins with a similar foundation to those of previous researchers, presented earlier in chapter 2, where the liquid and vapor are each modeled with a single node and conservation equations for mass and energy are used to derive a set of differential equations. However' add a third node is now added to represent the bubbles within the liquid.

The heat and mass transfer processes that are captured within this model are

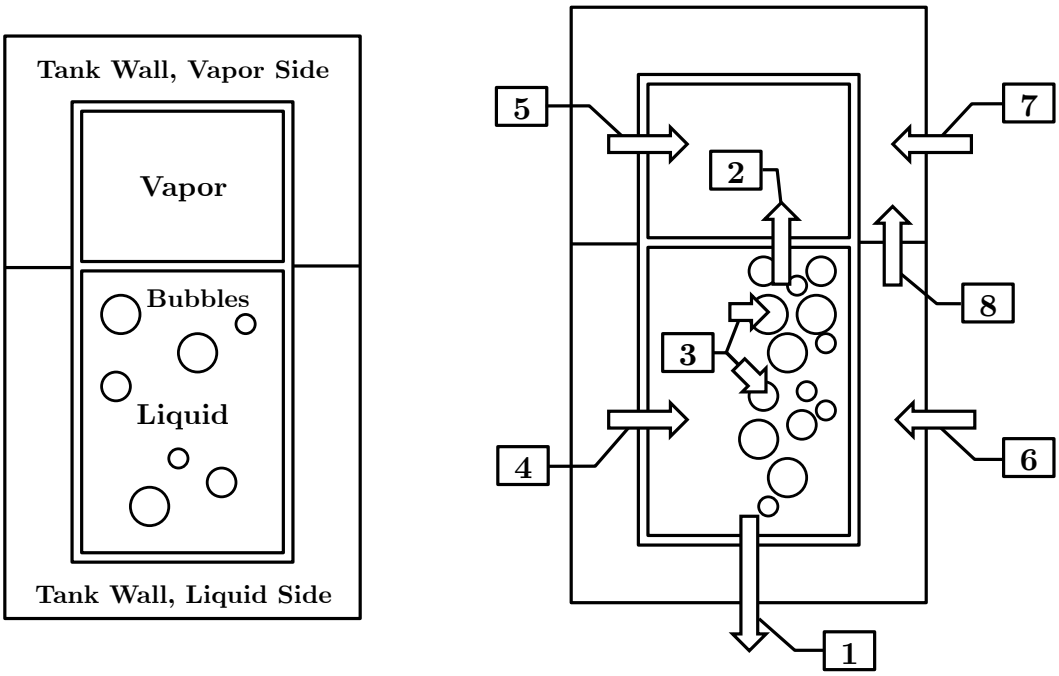

(a) Nodes (b) Heat and Mass Transfer

Figure 5.1: Diagrams showing the nodes and the heat and mass transfer processes between them for the proposed model.

numbered in figure 5.1 and described here:

1. Mass flow of liquid and bubbles out of the tank
2. Heat and mass transfer from the bubbles to the vapor
3. Heat and mass transfer from the liquid to the bubbles
4. Heat transfer from the liquid side of the tank wall to the liquid
5. Heat transfer from the vapor side of the tank wall to the vapor
6. Heat transfer from the atmosphere to the liquid side of the tank wall
7. Heat transfer from the atmosphere to the vapor side of the tank wall
8. Heat and mass transfer from the liquid side of the tank wall to the vapor side via conduction and motion of the boundary

The liquid and ullage will be described using conservation equations for their mass and energy, again similar to the previous researchers' models, and yielding a set of ordinary differential equations. The bubbles will not be described in this way. Instead, the liquid will be discretized in the vertical direction and a new set of partial differential conservation equations will be added for the bubbles alone.

The tank walls will also be modeled differently than in the past. Previously they were modeled using a simple 0D conservation of energy approach. Here, the transient heat conduction equation is solved in the radial direction for the ullage and liquid walls separately.

Overall, this model is a mix of 0-D elements and 1-D elements and therefore it is classified as a hybrid 0-D/1-D.

5.3 Governing Conservation Equations

In this section the governing 0-D and 1-D conservation equations are developed. First the 0-D equations that describe the mass and energy of the liquid and ullage will be

discussed. Then, the 1-D equations used to track the bubble population in the vertical direction are derived. The equations used for heat conduction within the tank wall will be discussed in the next section.

5.3.1 Mass and Energy

This model begins with a foundation similar to those described earlier, with the liquid and ullage each represented by a single node. The ullage is assumed to be saturated, but with a vapor mass fraction (also known as the quality, x) that is allowed to vary with time. The liquid is not assumed to be saturated and hence is allowed to become superheated. The basic conservation equations that must be solved are similar to those of the ZK model but without any mass transfer from the ullage into the liquid via condensation:

$$\frac{dm_{ull}}{dt} = \dot{m}_{boiling} \tag{5.1}$$

$$\frac{dm_{liq}}{dt} = -\dot{m}_{boiling} - \dot{m}_{outlet} \tag{5.2}$$

$$\frac{dU_{ull}}{dt} = \dot{m}_{boiling} h_{boiling} - P\frac{dV_{ull}}{dt} + \dot{Q}_{in,ull} \tag{5.3}$$

$$\frac{dU_{liq}}{dt} = -\dot{m}_{outlet} h_{outlet} - \dot{m}_{boiling} h_{boiling} - P\frac{dV_{liq}}{dt} + \dot{Q}_{in,liq} \tag{5.4}$$

These are the result of applying conservation of mass and energy to the liquid and vapor. The boiling terms refer to the interactions with the bubbles within the tank described in figure 5.1. Similar to how the ZK model was presented, equation (5.4) is rearranged in order to use T_{liq} instead of U_{liq} as a variable of integration.

$$\begin{aligned}
\frac{dU}{dt} &= u\frac{dm}{dt} + m\frac{du}{dt} \\
&= u\frac{dm}{dt} + m\left[\left(\frac{\partial u}{\partial T}\right)_{\rho}\frac{dT}{dt} + \left(\frac{\partial u}{\partial \rho}\right)_{T}\frac{d\rho}{dt}\right] \\
\frac{dT}{dt} &= \frac{1}{c_V}\left[\frac{1}{m}\left(\frac{dU}{dt} - u\frac{dm}{dt}\right) - \left(\frac{\partial u}{\partial \rho}\right)_{T}\frac{d\rho}{dt}\right]
\end{aligned} \tag{5.5}$$

The pressure constraint is used to find dV/dt, but now since the ullage is saturated

the temperature derivative is quite different.

$$P_{ull} = P_{liq} \tag{5.6}$$

$$\frac{dP_{ull}}{dt} = \frac{dP_{liq}}{dt} \tag{5.7}$$

$$\left.\frac{dP}{dT}\right|_{sat} \frac{dT_{ull}}{dt} = \left[\left(\frac{\partial P}{\partial T}\right)_{\rho} \frac{dT}{dt} + \left(\frac{\partial P}{\partial \rho}\right)_{T} \frac{d\rho}{dt}\right]_{liq} \tag{5.8}$$

Now, recall that the goal here is to obtain an expression for dP_{ull}/dt as a function of dV_{ull}/dt, such that equation (5.8) can be solved to find an expression for dV_{ull}/dt. Therefore an expression for dT_{ull}/dt must now be obtained using the known values of dU_{ull}/dt and dm_{ull}/dt. This begins with the specific internal energy of the ullage:

$$\begin{aligned} u &= u_v x + (1-x)u_l \\ \frac{du}{dt} &= x\frac{du_v}{dt} + (1-x)\frac{du_l}{dt} + (u_v - u_l)\frac{dx}{dt} \\ &= \left[(1-x)\left.\frac{du_l}{dT}\right|_{sat} + x\left.\frac{du_v}{dT}\right|_{sat}\right]\frac{dT}{dt} + (u_v - u_l)\frac{dx}{dt} \\ &= \frac{\dfrac{dU_{ull}}{dt} - \dfrac{dm_{ull}}{dt}u}{m} \end{aligned} \tag{5.9}$$

If an expression for dx/dt were available, this equation could be solved for dT/dt and plugged into equation (5.8). To find such an expression, the known value of dm_{ull}/dt is used:

$$\frac{dm_{ull}}{dt} = V\frac{d\rho}{dt} + \frac{m}{V}\frac{dV}{dt} \tag{5.10}$$

$$= V\left[\left.\frac{\partial \rho}{\partial P}\right|_{x,sat}\frac{dP}{dt} + \left.\frac{\partial \rho}{\partial x}\right|_{P,sat}\frac{dx}{dt}\right] + \frac{m}{V}\frac{dV}{dt} \tag{5.11}$$

$$\frac{dx}{dt} = \left[\left(\frac{dm_{ull}}{dt} - \frac{m}{V}\frac{dV}{dt}\right)\frac{1}{V} - \left.\frac{\partial \rho}{\partial P}\right|_{x,sat}\frac{dP}{dt}\right]\left(\left.\frac{\partial \rho}{\partial x}\right|_{P,sat}\right)^{-1} \tag{5.12}$$

$$= \left[\left(\frac{dm_{ull}}{dt} - \frac{m}{V}\frac{dV}{dt}\right)\frac{1}{V} - \left.\frac{\partial \rho}{\partial P}\right|_{x,sat}\left.\frac{dP}{dT}\right|_{sat}\frac{dT}{dt}\right]\left(\left.\frac{\partial \rho}{\partial x}\right|_{P,sat}\right)^{-1} \tag{5.13}$$

This has almost yielded the desired result, but unfortunately now dx/dt is a function of dT/dt as well. Therefore equation (5.13) is substituted into equation (5.9) and then solved for dT/dt. The result is:

$$\frac{dT}{dt} = \frac{-(u_v - u_l)\left(\left.\frac{\partial \rho}{\partial x}\right|_{P,sat}\right)^{-1}\left(\frac{dm}{dt} - \frac{m}{V}\frac{dV}{dt}\right)\frac{1}{V} + \frac{du}{dt}}{x\left.\frac{du_v}{dT}\right|_{sat} + (1-x)\left.\frac{du_L}{dT}\right|_{sat} - (u_v - u_l)\left(\left.\frac{\partial \rho}{\partial x}\right|_{P,sat}\right)^{-1}\left.\frac{\partial \rho}{\partial P}\right|_{x,sat}\left.\frac{dP}{dT}\right|_{sat}} \tag{5.14}$$

The thermodynamic derivatives needed for this expression are

$$\left.\frac{\partial \rho}{\partial x}\right|_{P,sat} = -\rho^2\left(\frac{1}{\rho_v} - \frac{1}{\rho_l}\right) \tag{5.15}$$

$$\left.\frac{\partial \rho}{\partial P}\right|_{x,sat} = \left.\frac{dT}{dP}\right|_{sat}\rho^2\left(\frac{x}{\rho_v^2}\left.\frac{d\rho_v}{dT}\right|_{sat} + \frac{1-x}{\rho_l^2}\left.\frac{d\rho_l}{dT}\right|_{sat}\right) \tag{5.16}$$

These are both most easily derived by starting with the specific volume of the mixture, $v = xv_v + (1-x)v_l$, and then converting back to density after taking the appropriate derivatives and simplifying the resulting expressions. With these, the required relations have been obtained and equation (5.8) can be solved for dV/dt. Unfortunately the result is quite lengthy and little insight would be gained from giving it here. The full equation is given in appendix B.

5.3.2 Direct Quadrature Method of Moments

Now that a basic formulation has been given for solving the governing equations, attention must be given to the various terms in equations (5.1) to (5.4). To begin, the most prominent physical feature is addressed: boiling.

The main goal is to find a way to capture the complete bubble dynamics, including nucleation along the bottom and sides of the tank, departure and rise up through the liquid, and the transfer of mass to the ullage once the liquid level was reached. In other words, a model was needed that could capture a bubble population that was changing with both space and time. A technique known as population balances was

selected for this. This technique has never been used directly in rocket propulsion to this author's knowledge, and hence a substantial discussion of the method is given in appendix C. Here, a short summary is given.

The term population balances refers to a technique used to describe fluid flows that contain discrete particles. Instead of tracking individual particles, which is impractical with large numbers of particles, equations are derived to describe the evolution of the population. In other words, partial differential equations (PDEs) are generated that describe how the particle number distribution changes with both space and time. This adds one or more dimensions to the problem.

While some solution methods solve for a discretized number distribution directly, this is often an inefficient or inaccurate. Instead, a variety of methods have been developed that solve for the statistical moments of the distribution, in recognition that most quantities of engineering interest (eg the number density or void fraction) are in fact computed as moments of a size distribution. The PDEs that describe the particle distribution can be converted to PDEs for these moments, and usually the number of equations decreases because only a small number of moments are needed.

The limitation of these moment methods is that they are restricted to cases where a closed set of equations can be derived. This requires that for a given set of moments, the PDEs describing them cannot be a function of other higher order moments. Often this requirement cannot be satisfied and a different technique is required. One such technique that solves this problem is the direct quadrature method of moments (DQMOM), developed by Marchisio and Fox [86].

In DQMOM, Gauss quadrature is used to derive a set of abscissas and weights that reproduce the moments exactly:

$$\begin{aligned} \mu_k &= \int x^k f_1 dx \\ &= \sum_{i=1}^{N} w_i x_i^k \end{aligned} \tag{5.17}$$

where μ_k is the k^{th} moment.

These abscissas and weights are then treated simply as scalar properties of the flow,

and transport equations for them are derived. These new PDEs for the abscissas and weights are solved to find their evolution in time and space. A secondary advantage of DQMOM is that the abscissas and weights can be used to approximate any quantity that is integrated over the distribution, a convenient property when evaluating various terms arising from particle dynamics and interactions.

The DQMOM PDEs for the abscissas and weights are simply transient advection-diffusion equations with a source term:

$$\begin{aligned} a_i &= \frac{\partial w_i}{\partial t} + \frac{\partial u_i w_i}{\partial y} - \frac{\partial}{\partial y}\left(D_i \frac{\partial w_i}{\partial y}\right) \\ b_i &= \frac{\partial g_i}{\partial t} + \frac{\partial u_i g_i}{\partial y} - \frac{\partial}{\partial y}\left(D_i \frac{\partial g_i}{\partial y}\right) \end{aligned} \tag{5.18}$$

where a_i and b_i are the source terms, w_i is the i^{th} weight, u_i is the velocity of w_i, and y is the vertical direction. r_i is the i^{th} abscissa, and g is a weighted abscissa ($g_i = r_i w_i$) and is used in place of the abscissa in order to enable the derivation of a simpler PDE. D_i is the diffusion coefficient for w_i. The source terms a_i and b_i are calculated from:

$$\mathbf{A}\begin{bmatrix} a_i \\ b_{s,i} \end{bmatrix} = \left[\mathbf{A_3}\bar{C}_{s,k} + \bar{S}_{s,k}\right] \tag{5.19}$$

where $b_{s,i}$ is a normalized version of b_i that reduces some numerical problems found in solving this equation, $\bar{C}_{s,k}$ is a source term from bubble diffusion, and $\bar{S}_{s,k}$ is a source term that includes bubble growth, birth, and death. $\mathbf{A}$ and $\mathbf{A_3}$ are matrices constructed from the abscissas (r_i). $\mathbf{A}$ is calculated from $\mathbf{A} = [\mathbf{A_1}\ \mathbf{A_2}]$, and $\mathbf{A_1}$ and

$\mathbf{A_2}$ are:

$$\mathbf{A_1} = \begin{bmatrix} 1 & \dots & 1 \\ 0 & \dots & 0 \\ -r_{s,1}^2 & \dots & -r_{s,N}^2 \\ \vdots & \vdots & \vdots \\ 2(1-N)r_{s,1}^{2N-1} & \dots & 2(1-N)r_{s,N}^{2N-1} \end{bmatrix}$$
$$\mathbf{A_2} = \begin{bmatrix} 0 & \dots & 0 \\ 1 & \dots & 1 \\ 2r_{s,1} & \dots & 2r_{s,N} \\ \vdots & \vdots & \vdots \\ (2N-1)r_{s,1}^{2N-2} & \dots & (2N-1)r_{s,N}^{2N-2} \end{bmatrix} \tag{5.20}$$

While $\mathbf{A_3}$ is:

$$\mathbf{A_3} = \begin{bmatrix} 0 & \dots & 0 \\ 0 & \dots & 0 \\ 2 & \dots & 2 \\ 6r_{s,1} & \dots & 6r_{s,N} \\ \vdots & \vdots & \vdots \\ 2(2N-1)r_{s,1}^{2N-3} & \dots & 2(2N-1)r_{s,N}^{2N-3} \end{bmatrix} \tag{5.21}$$

Finally, $\bar{S}_{s,k}$ is calculated as:

$$\bar{S}_{s,k} = \sum_{i=1}^{N} \frac{k}{r_m} w_i r_{s,i}^{k-1} \left.\frac{dr}{dt}\right|_{r=r_i} + \int r_s^k (h_{birth} - h_{death})\, dr_s \tag{5.22}$$

The fundamental governing equations for this system have now been established. Conservation of mass and energy for the ullage and liquid (equations (5.1), (5.2), (5.3), (5.5)), and the bubble transport equations (equations (5.18), (5.22), and (5.19)). To implement DQMOM in the system studied here however, expressions for dr/dt, h, and u_i, or bubble growth, nucleation, death, and velocity in physical space are all needed. These expressions will be discussed in subsequent sections.

5.4 Submodels

Numerous submodels are required to complete this model in order to find expressions for the various terms in the governing equations:

Translational motion of bubbles within the liquid Bubbles will rise due to buoyancy as well in addition to being convected by the bulk flow and diffusing upwards and downwards. A model here will provide u_i and D_i that can be used in equation (5.18).

Heat and mass transport from the liquid into the bubbles Models are needed for bubble nucleation and growth dynamics, in which liquid mass is vaporized at the liquid-vapor interface and heat is conducted from the liquid towards the bubble surface. This will give $\bar{S}_{s,k}$ that is needed for equation (5.19), as well as several terms in equations (5.4) and (5.1).

Heat and mass transport from the bubbles into the ullage Some mathematical treatment is needed to describe the process whereby when bubbles reach the free surface, they burst and their contents are added to the ullage. This provides the boiling terms in equations (5.1) and (5.3).

Heat transport from the tank wall into the liquid and ullage the heterogeneous boiling process absorbs significant amounts of heat from the tank wall, which is transformed into newly formed bubbles. This will give the $\dot{Q}$ terms in equations (5.3) and (5.4).

Mass transport out of the tank propellant flows out the base of the tank and through an orifice. A model is needed to calculate this flow rate as a function of the pressure, temperature, and quality of the fluid. This will give the $\dot{m}_{outlet}$ term needed for equations (5.2) and (5.4).

An unfortunate theme is that in all of these submodels there are no models in the literature specifically for CO_2 or N_2O or even models that have been compared with experimental data with these fluids. Therefore two approaches have been used. In

some cases models were selected that have been shown to be accurate with a wide range of fluids or conditions in the hope that they will also be accurate with CO_2 or N_2O. In the second case, experimental data have been found with one of these fluids and these data are taken and used directly in the model via interpolation.

5.4.1 Bubble Dynamics

Here, the various models needed to describe the bubble dynamics are discussed in chronological order. The discussion begins with nucleation of bubbles on the tank walls, followed by their growth rate and eventual departure into the liquid where they continue to grow as they diffuse and rise towards the free surface. Then the discussion will cover their possible coalescence after encountering other bubbles, and eventually the condition by which they exit the liquid at the free surface whereupon their contents are transferred to the ullage.

Nucleation

Heterogeneous bubble nucleation in a superheated liquid has been previously studied by many researchers, however the case of a uniformly superheated liquid (as opposed to a subcooled liquid in contact with a heated wall) is less common. In close proximity to the wall the dynamics of the two are similar as the liquid close to a heated wall will generally be superheated as a result of conduction and convection. Therefore much of the literature on the conventional heated wall case can be leveraged.

There are three quantities related to bubble nucleation that must be obtained: the size at which bubbles nucleate, the rate at which new bubbles are produced from a single nucleation site, and the number of nucleation sites on a given surface.

In the case of a spherical bubble, the Young-Laplace equation defines the pressure difference across the bubble interface:

$$P_{bub} - P_\infty = \frac{2\sigma}{r} \tag{5.23}$$

where P_{bub} is the pressure inside the bubble and P_∞ is the static pressure far from the bubble. This equation is derived from a simple force balance. In the case of

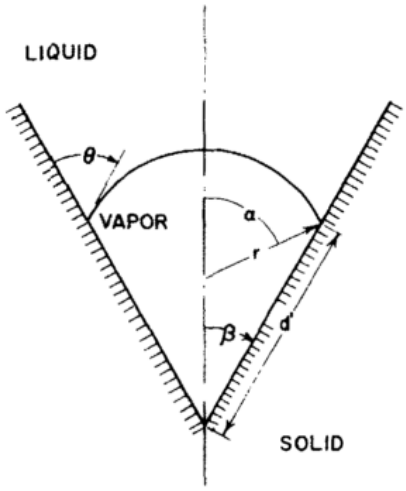

Figure 5.2: Diagram of bubble nucleation in a conical cavity, from Cole [87]. Reprinted with permission.

boiling, the pressure difference can be related to the level of superheat because the internal pressure is the saturation pressure based on the temperature. This is because relatively high surface-area-to-volume ratio of a small bubble allows for significant interfacial heat and mass transport.

On a surface however the contact angle influences the force balance, and the relation changes to $\Delta P = 2\sigma \sin\theta / r$ where θ is the contact angle. The situation is more complex when the surface is not flat, such as in a conical cavity like the one shown in figure 5.2. In this case ΔP is reduced and a bubble can exist even when $\Delta P < 0$ if $\theta > \alpha + \pi/2$ because surface tension is opposing the pressure from the liquid. For a bubble to emerge from a cavity however it must reach the mouth and surpass it. Therefore at some point it will make an ice-cream cone shape, where the bubble's radius will be equal to the cavity mouth radius. At this point the Young-Laplace equation can be used without contact angle modifications to determine the required level of superheat. All real surfaces have cavities of various sizes and shapes microscopically or macroscopically.

This also dictates that cavities smaller than this value will not allow a bubble to grow to the edge of the cavity but larger cavities will. Therefore, at a given level

of superheat the cavities that are active will have a mouth radius greater than or equal to $r_{min,active} = 2\sigma/\Delta P$. Therefore, the number of active nucleation sites can be written as

$$N_{active} = \int_{r_{min,active}}^{\infty} n_{sites}(r)dr \tag{5.24}$$

Where N_{active} is the number density of active sites and n_{sites} is the number density of sites at a given size, per size. Note that for boiling on a heated wall there is an upper limit to this integral because if a bubble is too large, it will extend from the heated surface past the layer of superheated liquid and into the subcooled liquid and will begin to shrink. For the present situation however there is no upper limit.

To relate the ΔP term within $r_{min,active}$ to the superheat (a more useful quantity) the Clausius-Clapeyron equation is linearized:

$$\left.\frac{dP}{dT}\right|_{sat} = \frac{\Delta h_{LV}}{T(v_{vap} - v_{liq})} \tag{5.25}$$

$$\frac{\Delta P}{\Delta T} \simeq \frac{\Delta h_{LV}}{T(v_{vap} - v_{liq})} \tag{5.26}$$

$$r_{active} = 2\sigma/\Delta P \tag{5.27}$$

$$= \frac{2\sigma T(v_{vap} - v_{liq})}{\Delta h_{LV}\Delta T} \tag{5.28}$$

Equation (5.28) is usually written as $2\sigma T/(\rho_{vap}\Delta h_{LV}\Delta T)$ by assuming that $\rho_{liq} \gg \rho_{vap}$, an incorrect assumption when dealing with N_2O or CO_2 at saturation conditions near the critical point. Using equation (5.28) the size of bubbles that are nucleating can now be determined with the understanding that it ranges from this minimum value up to ∞. Then, with equation (5.24) the number of active nucleation sites can be found if the function $n(r)$ is known.

Experimental data has shown that the number of active nucleation sites increases rapidly as the cavity size decreases, generally as $n_{active} \sim r_{active}^{-m}$ where m ranges from 2 to 3 [72, 88]. For this reason, it is sufficient to only consider the smallest active cavity size when computing nucleation rates because the number of larger sites is

comparatively small. Therefore:

$$\begin{aligned} N_{active} &= \int_{r_{min,active}}^{\infty} n_{sites}(r)dr \\ &\simeq n_{sites}(r = r_{min,active}) \end{aligned} \tag{5.29}$$

At this point a nucleation size, $r_{min,active}$ and part of a relation for the number of active nucleation sites have been established. To proceed further, a semi-empirical relation developed by Hibiki & Ishii [89], who compiled data from a wide range of sources on bubble nucleation site density in boiling. These data were from a wide range of fluids, temperatures, pressures, and heat fluxes and while they did not include dat with CO_2 or N_2O it is hoped that their results will still be accurate.

Their expression is:

$$N_{ns} = \bar{N_n}\left(1 - \exp\left[-\frac{\theta_{cont}^2}{8\mu_{HI}}\right]\right)\left(\exp\left[\frac{f(\rho^+)\lambda'}{r_{nuc}}\right] - 1\right) \tag{5.30}$$

where N_{ns} is the nucleation site surface density. $\bar{N_n}, \mu_{HI}$, and λ' are all constants and equal to $4.72 \cdot 10^5$ $sites/m^2$, 0.722 rad, and $2.56 \cdot 10^{-6}$ m respectively. r_{nuc} is the radius of nucleation, and $f(\rho^+)$ is an empirical function of a non-dimensional $\Delta\rho$:

$$\begin{aligned} \rho^+ &= \log_{10}\left(\frac{\Delta\rho}{\rho_{vap}}\right) \\ f(\rho^+) &= -0.01064 + 0.48246\rho^+ - 0.22712(\rho^+)^2 + 0.05468(\rho^+)^3 \end{aligned} \tag{5.31}$$

Lastly, θ_{cont} is the contact angle. The only source identified for contact angle measurements between the fluids and wall materials of interest is that of Pei et al [90], who measured the contact angle between carbon dioxide and stainless steel using the pendant drop method. In this method, a liquid droplet forms on the underside of a flat horizontal surface and measurements of its shape are used to determine the contact angle. Data from this source were used by this author to develop the following

curve fits:

$$\begin{aligned}\theta_{adv} &= -0.003417T^2 - 0.2873T + 29.83 \\ \theta_{rec} &= -0.004171T^2 - 0.3386T + 16.38\end{aligned} \tag{5.32}$$

where θ_{adv} is the advancing contact angle and θ_{rec} is the receding contact angle (in degrees) and T is the temperature in $°C$. A single value is needed for the nucleation site density expression and therefore the mean of the advancing and receding contact angles was used.

In addition to the nucleating site density, the nucleation frequency is also needed. For this quantity, a semi-empirical relation developed by Shin, Jones, Blinkov, and Nigmatulin [91, 73], who studied bubble nucleation in cavitating nozzles, is used. Cavitation typically involves superheating a liquid uniformly (in space) as the fluid flows through a restriction, it is more similar to the situation within a propellant tank than a system in which the liquid is in contact with a heated wall. Therefore the results of this work may be more applicable to propellant tanks than relations developed for heated walls. These researchers developed a detailed model for the nucleation kinetics and then used empirical data to fit unknown constants. The results are:

$$f_{max,dep} = [10^4 Hz\ K^{-3}]\Delta T_s^3 \tag{5.33}$$

Where f_{dep} is the departure frequency. The departure radius will be discussed in a later section. With equation (5.33), all quantities needed to describe bubble nucleation on the walls of a propellant tank have been obtained.

Since it has been established that all bubbles nucleate at a single size, one term of the integral in equation (5.22) can be simplified:

$$\begin{aligned}\int r_s^k h_{birth,nuc}\, dr_s &= \int r_s^k \delta(r - r_{min,active}) f_{max,dep} N_{ns} \frac{A}{V}\, dr_s \\ &= \left(\frac{r_{min,active}}{r_m}\right)^k f_{max,dep} N_{ns} \frac{A}{V}\end{aligned} \tag{5.34}$$

The term $N_{ns}A/V$ converts the nucleation site density to the specific nucleation rate, or the number of bubbles nucleated per volume. This term is evaluated in each cell within the liquid, where A is the area of the cell that is in contact with the solid wall, and V is the cell volume. Given the current fluid state and value of ΔT, $r_{min,active}$, r_{dep}, N_{ns} and $f_{max,dep}$ can all be calculated.

The assumption that bubbles nucleate only at $r_{min,active}$ was studied numerically in the proposed model by incorporating various distributions of nucleation sizes. Distributions studied include uniform, Gaussian, and curves with $N \sim r^{-m}$. No measurable difference was found. The likely cause is that bubble growth strongly favors bubbles of small radius, and so a group of bubbles with various radii will rapidly converge on the same radius.

At elevated temperatures close to the critical point, homogeneous nucleation is possible. This can be included using the model described in chapter 4.

$$f_{hom} = N_v \frac{v_v}{v_l} \sqrt{\frac{2\sigma}{\pi m_M}} \exp\left[-4\pi\sigma \frac{r^{*2}}{3k_B T_v}\right] \tag{5.35}$$

Now, r^* is the radius of a bubble rather than a droplet, $r^* \simeq r_{active}$. The nucleation rate predicted by equation (5.35) can hence be simply added to that predicted by equation (5.33) because the size of nucleated bubbles is the same. Equation (5.34) now becomes:

$$\int r_s^k h_{birth,nuc}\, dr_s = \left(\frac{r_{min,active}}{r_m}\right)^k (f_{max,dep} + f_{hom}) N_{ns} \frac{A}{V} \tag{5.36}$$

Conveniently, the homogeneous nucleation rate falls precipitously with temperature (see figure 4.6) and so this expression does not need to be altered for cases where homogeneous nucleation is not expected to occur.

The last aspect of bubble nucleation that must be considered is a hysteresis effect. It was postulated earlier that gas cavities are concave, that is the gas protrudes out from the cavity. But researchers have shown that these cavities may be convex in some circumstances [92]. In that case, the pressure difference across the interface is now $P_{bub} - P_\infty = -\frac{2\sigma}{r}$, with the internal pressure lower than the external. This

enables the gas cavity to exist even when the external pressure is higher than the saturation pressure.

In particular, Qi & Klausner [93] showed in depressurization experiments that cavities are initially convex, but become concave once they are activated when the superheat becomes large enough. This effect was included in the proposed model by comparing the current level of superheat to the maximum level reached (up to this point) during the test. If the current superheat is the maximum encountered, then the cavities are assumed to be convex and r_{nuc} is twice the value in equation (5.28). Otherwise, if a previous value of superheat is larger than the current value, the cavities are concave and equation (5.28) is accurate.

Growth

Bubble growth rates may be controlled by a variety of factors depending on the situation. Here the scope is narrowed to the specific case of thermally-controlled growth, in which the rate at which heat is transported from the liquid to the bubble interface is the controlling parameter. This heat is required to supply Δh_{LV} needed to vaporize the liquid. It may not be obvious that this is the correct assumption and in fact during the earliest stages of bubble growth the inertia of the liquid that must be displaced for the bubble to grow is the limiting factor. Brennen [74] suggests the following time scale as the delineation between the two regimes:

$$\begin{aligned} t_{c,1} &= \frac{P_{sat} - P_\infty}{\rho_{liq}\Sigma^2} \\ \Sigma &= \frac{\Delta h_{LV}^2 \rho_{vap}^2}{\rho_{liq}^2 c_{p,liq} T_\infty \sqrt{\alpha_{liq}}} \end{aligned} \tag{5.37}$$

Where P_∞ is the pressure far from the bubble. This relation is derived by comparing the growth rates for thermally-controlled and inertially-controlled growth and finding the time at which they are equal. For the system here, $\Sigma \sim 10^{-9}$ and $t_{c,1} \leq 10^{-14}$ s, confirming that inertial effects are unimportant.

Nearly all models for thermally controlled bubble growth begin by assuming that

the liquid-vapor interface is maintained at the saturation temperature. This assumption is somewhat questionable theoretically because of the high evaporation rates that are possible within the bubble, but it has been verified by numerous experiments [74]. These experiments showed that by assuming the interface to be at the saturation temperature, the resulting predictions for bubble growth closely match experimental data. With the interface at saturation, this defines a boundary condition for heat conduction within the liquid. From there researchers have made various assumptions to arrive at solutions with differing accuracy and domains of applicability.

One complication in this system is that the pressure in the tank is varying as function of time, which produces two effects that must be accounted for: the growth or shrinkage of the bubble caused by the change in gas density as the pressure changes, and the fluctuating thermal boundary layer around the bubble caused by the varying saturation point and hence interfacial temperature. Jones and Zuber [94] developed a solution in this situation however it requires complete knowledge of a bubble's history in order to compute its growth rate. Therefore the differential equations that must be solved in this model become integro-differential equations, a difficulty that should be avoided if possible.

To this end, it will be shown later that the density changes by a relatively small amount and the relevant time scales for bubble growth are much smaller than those associated with the fluctuating saturation temperature. Therefore a model that uses a constant pressure is pursued. This is not the only complication with this system however.

Another common assumption in bubble growth models is that $\rho_{vap} \ll \rho_{liq}$ however in this system $0.1 \leq \rho_{vap}/\rho_{liq} \leq 0.3$ which makes this assumption invalid. Therefore a relatively complex growth model, that of Scriven [95], is used. Scriven derived bubble growth rates in terms of a growth constant, β: $r = 2\beta\sqrt{\alpha_{liq}t}$, where β is found by solving the equation:

$$\frac{\tau}{\xi + \omega\nu\tau} = \phi \tag{5.38}$$

$$= 2\beta^3 \exp[\beta^2 + 2\epsilon\beta^2] \int_\beta^\infty x^{-2} \exp[x^{-2} - 2\epsilon\beta^3 x^{-1}]dx \tag{5.39}$$

Where $\xi = \rho_v \Delta h_{LV}/(\rho_l c_{p,l} T_\infty)$ is similar to an inverse of the Jakob number. Also, $\tau = (T_\infty - T_{sat})/T_\infty$ and is a non-dimensional superheat while $\omega = \rho_v/\rho_l$ and $\nu = (c_{p,l} - c_{p,g})/c_{p,l}$. Given values of these parameters, this equation must be solved for β. Note that there is an error in Scriven's original work and an additional $\exp(\beta^2$ appears in his equation (not shown here), with no closing parenthesis. His plots were replicated when that term was left out and equation (5.39) was used.

Unfortunately equation (5.39) is difficult to use directly in a tank model because of its highly non-linear dependence on β. Fortunately, Scriven also developed approximate relations that allow for direct calculation of β when it is large or small:

$$\beta_{small} = \sqrt{\frac{\frac{1}{2}Ja}{(1+\nu\omega Ja)}} \tag{5.40}$$

$$\beta_{large} = \sqrt{\frac{12}{\pi}}\beta_{small}^2 \tag{5.41}$$

These have been rewritten from Scriven's form to be in terms of the Jakob number ($Ja = \rho_l c_{p,l} \Delta T_s/(\rho_v \Delta h_{LV})$). A general approximation for both large and small values of β was found by this author as simply

$$\begin{aligned}
\beta &= 0.85(\beta_{small} + \beta_{large}) \\
&= 0.85\sqrt{\frac{\frac{1}{2}Ja}{(1+\nu\omega Ja)}} + 0.85\sqrt{\frac{12}{\pi}}\frac{\frac{1}{2}Ja}{(1+\nu\omega Ja)} \\
&= 0.85\sqrt{\frac{\frac{1}{2}Ja}{\left(1+\frac{\rho_v(c_{p,l}-c_{p,g})}{\rho_l c_{p,l}}Ja\right)}} + 0.85\sqrt{\frac{12}{\pi}}\frac{\frac{1}{2}Ja}{\left(1+\frac{\rho_v(c_{p,l}-c_{p,g})}{\rho_l c_{p,l}}Ja\right)}
\end{aligned} \tag{5.42}$$

These two are compared in figure 5.3. The horizontal axis was limited here to values that are relevant to this system ($c_{p,L}/\Delta h_{LV} \sim 0.01$).

While the results of Scriven will provide the thermally-controlled growth rate of a bubble at rest, once it begins to translate convection will provide additional heat to the liquid-vapor interface and increase the growth rate. This problem was modeled by Ruckenstein [96] by examining the heat transfer rate to a spherical bubble with

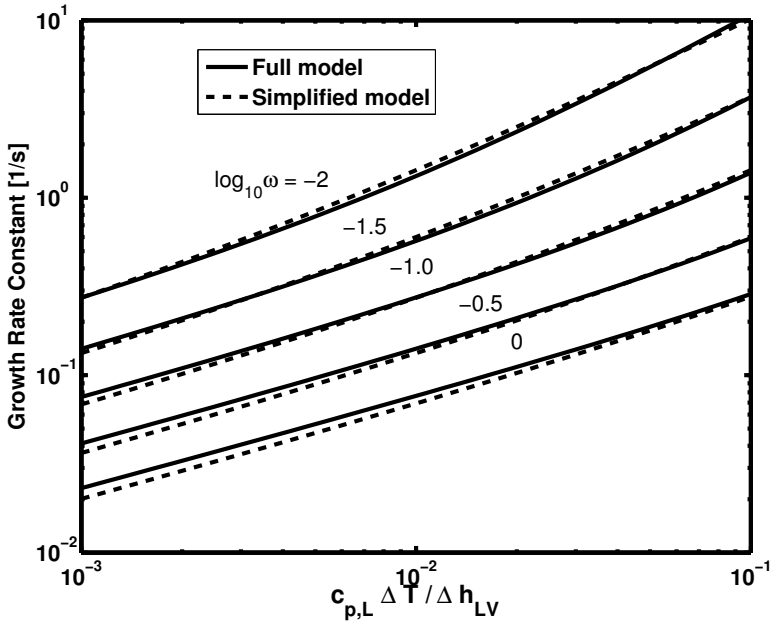

Figure 5.3: Bubble growth rate constant from the Scriven's full model (equation (5.39)) and the simplified version (equation (5.42)). No variation for different values of ν is visible in this range of $c_{p,L}\Delta T/\Delta h_{LV}$.

constant radius in a potential flow. His result was:

$$\frac{dr}{dt} = Ja\sqrt{\frac{2\alpha u}{\pi(r - r_i)}} \tag{5.43}$$

Where u is the free stream velocity. Legendre et al [97] performed CFD simulations of bubbles rising and growing in superheated liquids and demonstrated this relation's accuracy at a wide range of Ja and Re.

To capture the effects of buoyant convection as well as conduction, the two growth rates will be simply added together. This is possible because at low velocities and small radii the Scriven solution dominates and at high velocities and large radii the Ruckenstein solution takes over. To combine these, Scriven's $r = 2\beta\sqrt{\alpha_{liq}t}$ must be converted into a differential equation. To do so, it is differentiated and a substitute used for t. The result is

$$\frac{dr}{dt} = \frac{2\beta^2\alpha_{liq}}{r - r_i} \tag{5.44}$$

And now the combined growth rate is:

$$\frac{dr}{dt} = Ja\sqrt{\frac{2\alpha_{liq}u}{\pi(r - r_i)}} + \frac{2[0.85(\beta_{small} + \beta_{large})]^2\alpha_{liq}}{r - r_i} \tag{5.45}$$

To demonstrate that this bubble growth model will be accurate for self-pressurizing propellant tank dynamics, experimental data captured in the visualization experiments can be used. Several tests were performed with the high-speed camera placed close to the quartz tube so that $r(t)$ could be measured from the video. The quartz tube itself is a poor surface for bubble nucleation while the stainless steel thermocouple sheaths are much better due to the difference in surface roughness. This presents a situation where bubbles can be visualized for a decent length of time. Images showing this are given in figure 5.4.

In contrast, in the flat glass gauge the nucleation on the walls of the tank occurs at roughly the same rate as on the thermocouple probe sheaths and the view is quickly obstructed. These types of tests were attempted in the flat glass gauge but the bubbles were only visible for very short time periods and hence the $r(t)$ data were less useful. Therefore only data from the quartz tube system will be presented here.

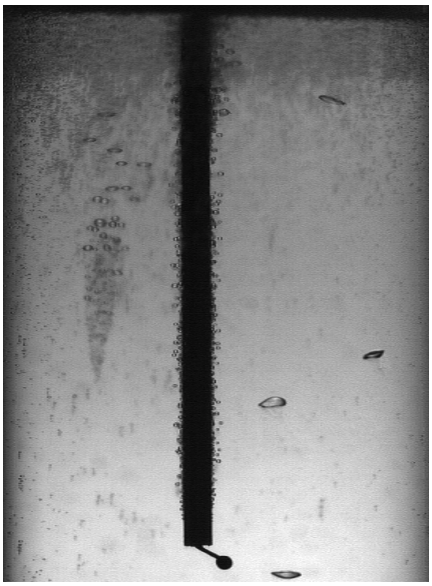

(a) Full view of camera.

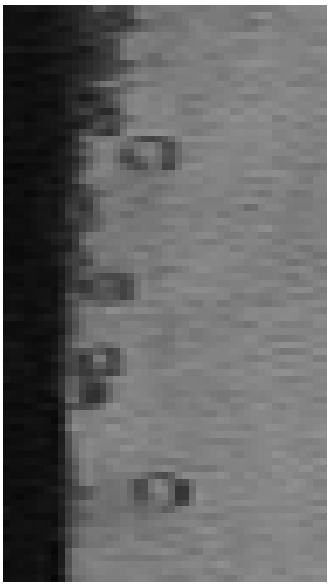

(b) Individual bubbles. Dark surface on the left is the probe sheath.

Figure 5.4: Images showing how bubbles nucleating on the thermocouple probe sheath can be tracked in the high speed camera data.

To determine the $r(t)$ from the videos, an ellipse was fitted to the bubble profile by hand in each frame. Then, the width and height of this ellipse (a and b) were used to calculate an equivalent radius, assuming that the bubble is symmetric about its longitudinal axis: $r_{eq} = (\frac{1}{8}ab^2)^{1/3}$. The centroid of the ellipse was used to determine the bubble's position and velocity with time as well. The physical resolution of the camera in terms of mm per pixel was determined using the diameter of the thermocouple probe sheath as a reference. Since the bubbles were nucleating on this surface, it is likely to be an accurate estimate.

Results from these measurements are shown in figures 5.5 and 5.6, which show both the radius and velocity as a function of time. It is difficult to measure the radius at any earlier times because the resolution of the camera is about 44 μm per pixel. This highlights the relatively low accuracy of this measurement system. At later times the bubble is obscured by others, moves out of the focal plane, or coalesces with another bubble. The data shown here span 105 ms, which is the longest any single bubble could be imaged.

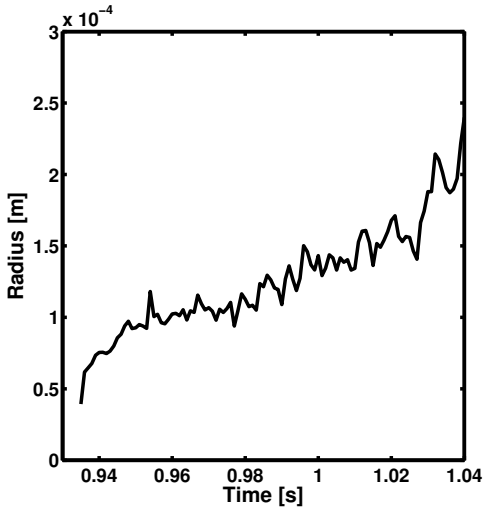

Figure 5.5: Experimentally measured bubble radius versus time.

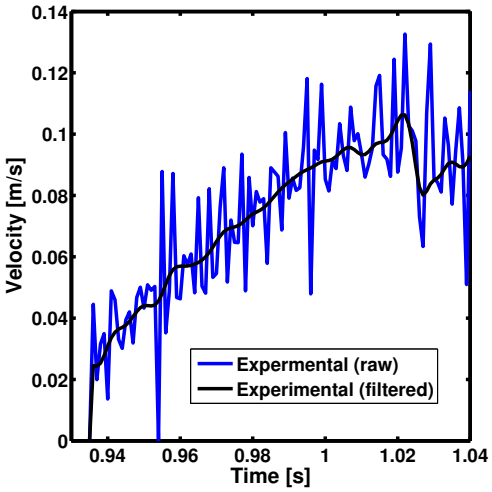

Figure 5.6: Experimentally measured bubble rise velocity. Both the raw data and the filtered result are shown.

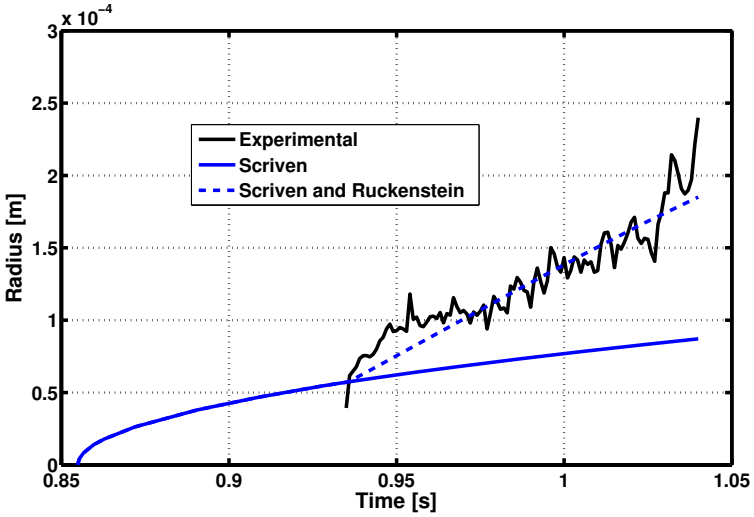

Figure 5.7: Comparison of model predictions and experimental measurements of bubble growth rates. Shown are the experimental data, the prediction of Scriven for a bubble at rest, and the combined prediction (equation (5.45)) using the measured rise rate.

The experimentally measured bubble radius data is compared with the growth model (equation (5.45)) in figure 5.7. The velocity was taken to be 0 before the bubble was imaged and then the filtered experimental value was used subsequently. Figure 5.6 suggests that the velocity is quite small before this time and so this assumption appears to be reasonably accurate.

A significant complication when trying to compare the model to the data is encountered when choosing the start time and initial radius, quantities that are impossible to measure without much higher optical resolution, a practical impossibility in this system. The initial radius was shown earlier in chapter 4 to be on the order of 10^{-9} m and thus it can be taken as 0 in these equations without loss of accuracy.

The start time is more problematic, and the results shown here were generated by varying it to give a result that agrees well with the data. Therefore it cannot be concluded from this analysis that this growth model is necessarily the correct choice, however the weaker statement that it is not *inconsistent* with the experimental data can be made.

In the 105 ms duration of the data, the bubble radius increases from 39 µm to 240 µm, an increase of 6.2 times and a volume that increases by 233 times. In this time the pressure changes by only 0.28% (from 5.366 $MPa$to 5.351 MPa) and the vapor density by 0.45% (174.44 to 173.66 kg/m^3). This justifies the earlier assumption of a constant pressure and vapor density used in Scriven's bubble growth model.

With an expression for the bubble growth rate, this can be input into the growth term of equation (5.22):

$$\sum_{i=1}^{N} \frac{k}{r_m} w_i r_{s,i}^{k-1} \left.\frac{dr}{dt}\right|_{r=r_i} = \sum_{i=1}^{N} \frac{k}{r_m} w_i r_{s,i}^{k-1} Ja \sqrt{\frac{2\alpha_{liq} u_i}{\pi r_i}} + \frac{2[0.85(\beta_{small} + \beta_{large})]^2 \alpha_{liq}}{r_i} \tag{5.46}$$

Where $U_{i,\infty}$ is the rise velocity of bubbles with size r_i, and will be discussed in a later section.

Bubble growth has been discussed here, but bubble shrinkage or collapse should also be mentioned. During the later portion of the transient regime the superheat is decreasing with time while the pressure increases, and it is therefore possible for

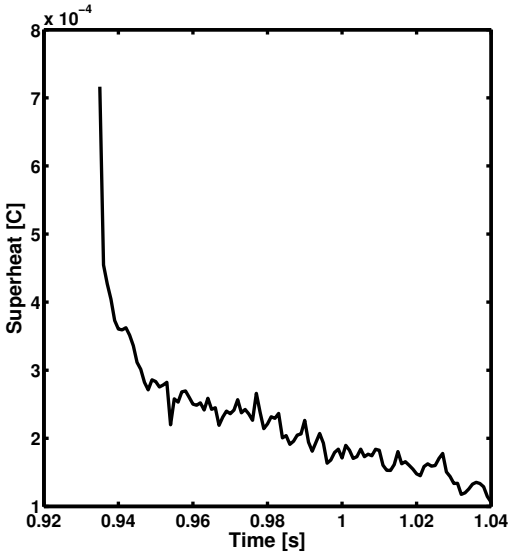

Figure 5.8: Minimum superheat to prevent bubble from shrinking. Calculated based on the experimental data in figure 5.5.

the external pressure to exceed the internal bubble pressure, causing the bubble to shrink. However, the time scales associated with bubble growth are much smaller than those associated with the rate of change of superheat, making bubble shrinkage and collapse impossible.

To demonstrate, the data shown in figure 5.5 can be examined once again. From the bubble radius, the minimum superheat necessary to prevent the bubble from shrinking can be computed using equation (5.28). This value is plotted in figure 5.8, and shows not only that the required superheat is quite small ($< 10^{-3}\ ^{\circ}C$) but also that it decreases quite rapidly. In the time before the bubble has grown to the size measured here the required superheat will be larger, but figure 5.7 shows how this time period is only approximately 10 ms, much shorter than the time scale associated with the pressure increase at the end of the transient regime.

Departure

For the bubble departure data, again no data were available for CO_2 or N_2O and therefore a general correlation was used. The correlation selected was that developed

by Jensen and Memmel [98], who collected a great amount of data from the literature, including 504 data points, 15 different fluids, and pressures ranging from 4.7 kPa to 14.5 MPa. The resulting correlation is:

$$Eo_{dep} = \left[0.19(1.8 + 10^5 K_1)^{2/3}\right]^2 \tag{5.47}$$

$$K_1 = \left(\frac{Ja}{Pr_{liq}}\right)^2 \left[\frac{g\rho_{liq}\Delta\rho}{\mu_{liq}^2}\left(\frac{\sigma}{g\Delta\rho}\right)^{1.5}\right]^{-1} \tag{5.48}$$

where K_1 is an empirical parameter, Eo is the Eotvos number ($Eo = (\rho_l - \rho_v)gD^2/\sigma$), $\Delta\rho = \rho_{liq} - \rho_{vap}$, g is the acceleration due to gravity and σ is the surface tension. The departure radius can then be found from the Eotvos number as:

$$r_{dep} = \frac{1}{2}\sqrt{\frac{Eo_{dep}\sigma}{g\Delta\rho}} \tag{5.49}$$

Confusingly, various authors that have used this correlation have used differing expressions for K_1. The most common difference is that the first term (Ja/Pr) is not squared however other differences also occur in some sources. The expression that Jensen and Memmel use is derived from the work of Kutateladze and Gogonin [99], who did have this term squared and so that is the form used in this work.

Determining bubble departure diameter is a difficult problem and there is a wide variation between different experimenters' results. In fact, departure size correlations are generally only accurate to roughly an order of magnitude. To demonstrate, figure 5.9 shows a comparison of this fit with the data from which it was derived. Examining this plot, it is expected that this fit may have to be adjusted in order to be accurate in this system, however the functional form is likely to be correct.

One reason for favoring this correlation above others such as the Kutateladze and Gogonin correlation also shown in figure 5.9 is that it has improved accuracy near the critical point. With conditions inside a CO_2 or N_2O tank relatively close to this point, it is important to accurately capture the dynamics in that region.

The departure radius is not directly used in the governing equations, but instead is one of the terms in the bubble nucleation equations, specifically within equation

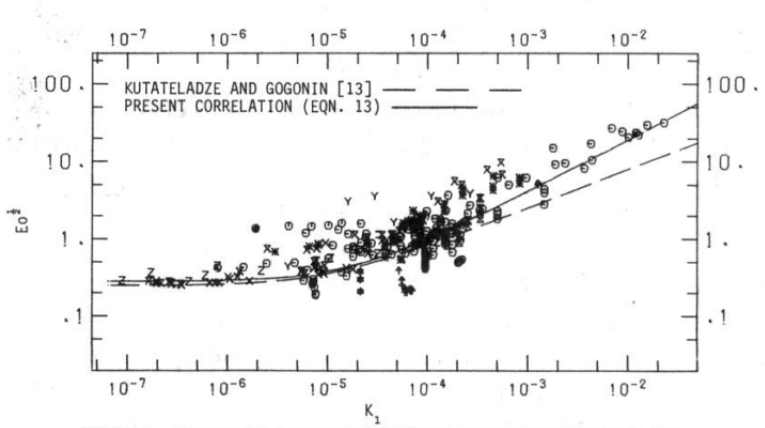

FIGURE 8. COMPARISON BETWEEN EXPERIMENTAL BUBBLE DIAMETER DATA AND KUTATELADZE AND GOGONIN [13] AND PRESENT CORRELATION.

Figure 5.9: Comparison of Jensen and Memmel's correlation with data. The "present correlation" line is equation (5.48).

(5.33).

Rise Due to Buoyancy

In general, there are four forces acting on a particle submerged in a fluid: drag, buoyancy, virtual mass, and Basset. The drag and buoyancy forces are familiar to most engineers, however the virtual mass and Basset forces are less common and are only generated when the particle's velocity (relative to the fluid) is changing with time. The virtual mass force arises due to the accelerating flow around the particle, and is an inviscid effect. The Basset force is generated by the changing boundary layer thickness as the relative velocity changes and is related to the diffusion of vorticity out from the particle, a viscous effect. From this point onward, only the case of a particle accelerating in a stationary fluid will be considered for simplicity as that is the situation found in a self-pressurizing propellant tank.

The virtual mass force can be written as

$$F_{VM} = C_{VM} \frac{4}{3} \pi r^3 \rho_l \frac{du}{dt} \tag{5.50}$$

where C_{VM} is a constant of order 1 and depends on the shape of the particle. For a sphere $C_{VM} = 0.5$. The Basset force can be written as

$$F_{Basset} = C_{Ba} 6r^2 \sqrt{\pi \rho_l \mu_l} \int_0^t \frac{\left.\frac{du}{dt}\right|_{t=s}}{\sqrt{t-s}} ds \tag{5.51}$$

where C_{Ba} is a constant of order 1 and u is the particle velocity. C_{Ba} is included usually so that other effects may be approximately incorporated such as non-spherical particles. The drag and buoyancy forces are simply:

$$\begin{aligned} F_B &= \frac{4}{3} r^3 (\rho_l - \rho_v) g \\ F_D &= \frac{1}{2} \rho_l u^2 C_D \pi r^2 \end{aligned} \tag{5.52}$$

The bubble rise velocity will be determined by the sum of these four forces, and can be calculated by deriving an differential equation of motion:

$$\begin{aligned} \sum F &= ma \\ ma &= \text{buoyancy} + \text{drag} + \text{virtual mass} + \text{Basset} \\ \frac{4}{3}\pi r^3 \frac{du}{dt} \rho_v &= \frac{4}{3}\pi r^3 (\rho_l - \rho_v) g - \frac{1}{2}\rho_l u^2 C_D \pi r^2 - C_{VM} \frac{4}{3}\pi r^3 \rho_l \frac{du}{dt} \\ &\quad - C_{Ba} 6r^2 \sqrt{\pi \rho_l \mu_l} \int_0^t \frac{\left.\frac{du}{dt}\right|_{t=s}}{\sqrt{t-s}} ds \end{aligned} \tag{5.53}$$

This can be simplified somewhat to obtain an integro-differential equation for u:

$$\begin{aligned} \frac{4}{3}\pi r^3 \frac{du}{dt} (\rho_v + C_{VM} \rho_l) &= \frac{4}{3}\pi r^3 (\rho_l - \rho_v) g - \frac{1}{2}\rho_l u^2 C_D \pi r^2 \\ &\quad - C_{Ba} 6r^2 \sqrt{\pi \rho_l \mu_l} \int_0^t \frac{\left.\frac{du}{dt}\right|_{t=s}}{\sqrt{t-s}} ds \end{aligned} \tag{5.54}$$

$$\frac{du}{dt} = \frac{g(\rho_l - \rho_v)}{\rho_v + C_{VM}\rho_l} - \frac{3}{8} \frac{\rho_l u^2 C_D}{r(\rho_v + C_{VM}\rho_l)} - \frac{9}{2} \frac{C_{Ba} \sqrt{\frac{\rho_l \mu_l}{\pi}}}{r(\rho_v + C_{VM}\rho_l)} \int_0^t \frac{\left.\frac{du}{dt}\right|_{t=s}}{\sqrt{t-s}} ds$$

Equation (5.54) is complex, and involves an integral term that must be evaluated

numerically. It would be inconvenient to include this equation in the complete self-pressurized propellant tank model, and therefore simplifications will now be made. Ideally, a quasi-steady assumption could be applied such that $du/dt \to 0$, eliminating the ma, virtual mass force, and Basset force terms and reducing the equation of motion to a simple balance between drag and buoyancy.

To determine if such an assumption is accurate here, two different approaches will be used. First, the experimental data in figure 5.5 and 5.6 will be used to calculate the magnitude of each of these terms. The drawback of this approach is that the data are available only for a brief time period, spanning a relatively small range of bubble size and velocity. Therefore, a simulation will be subsequently be performed by integrating the full equation of motion (equation (5.54)) for a test case and comparing the results with and without various terms. If both of these methods suggest that the quasi-steady assumption is accurate, a simplified relation for the bubble rise velocity can be used with confidence.

Taking the experimental data and converting the various terms given in equations (5.50), (5.51), (5.52), a new problem is encountered: values are needed for C_{Ba}, C_{VM}, and C_D. The first two are chosen relatively easily for this bubble since it is close to spherical ($C_{Ba} = 1$, $C_{VM} = 0.5$) however C_D is more difficult to specify. While a model from the literature will be introduced later to evaluate C_D, here instead a normalized drag force will be presented (F_D/C_D) in order to limit the results to those obtainable solely from the experimental data. Recall that the purpose of the present analysis is simply to determine if the quasi-steady assumption is accurate. In the Reynolds number range encountered here, approximately 10-500, the C_D will likely be of order 1 and therefore if the drag force is off by say a factor of 3, it will not alter the result.

Figure 5.10 shows the results. The buoyancy and normalized drag forces clearly dominate by the later times, however at early times it is less evident. To aid in distinguishing these early times, figure 5.11 shows the same forces, normalized by the sum of their absolute values. From this figure it is clear that throughout the entire time period the acceleration-dependent terms never exceed 10% of the total and therefore the quasi-steady assumption is justified.

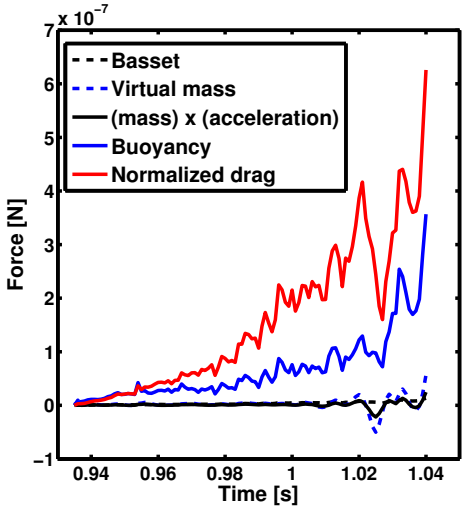

Figure 5.10: Comparison of forces on bubble, using data from figures 5.5 and 5.6.

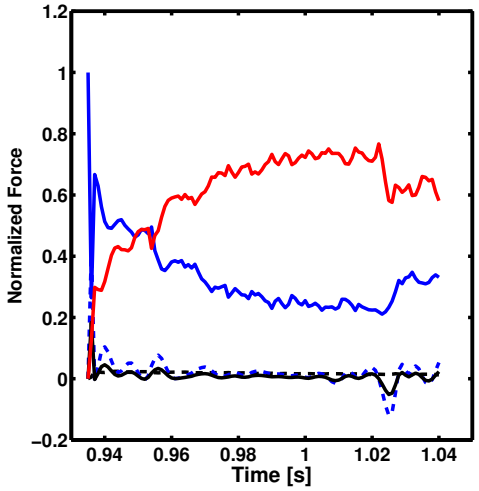

Figure 5.11: Comparison of forces on bubble, using data from figures 5.5 and 5.6. Legend is identical to that shown in figure 5.10.

Now, a simulation will be performed to see if this conclusion can be extended to smaller and larger bubble sizes. To integrate equation (5.54) numerically, two additional terms are needed: the bubble radius and the drag coefficient. The bubble growth rate is directly related to its velocity as convection is one of the main methods by which heat is transported to the bubble, vaporizing fluid at the interface and causing it to grow. Therefore a second differential equation describing the rate of change of the bubble size is also needed. This is taken from the section that discussed the bubble growth rate, equation (5.45), reproduced here for convenience:

$$\frac{dr}{dt} = Ja\sqrt{\frac{2\alpha_{liq}u}{\pi(r-r_i)}} + \frac{2[0.85(\beta_{small}+\beta_{large})]^2\alpha_{liq}}{r-r_i} \tag{5.55}$$

Unlike the previous analysis, a large range of Reynolds numbers are expected here and one cannot assume that C_D is of order 1. Additionally, there are two effects that cause the drag on a bubble to deviate from the familiar C_D vs Re behavior of a sphere. First, when the drag is high enough the surface pressure distribution will cause the bubble to distort and flatten out, increasing the drag coefficient. Second, as

a bubble moves through a liquid with other bubbles present it induces some motion of these other bubbles. Since the bubbles are generally more resistant to deformation than the liquid (due to the surface tension) the drag felt by the moving bubble is increased. While the simple test case that is of present interest would only require inclusion of the first effect, a more complex model that includes the mixture effects as well will be used so that this drag model can be used later in a complete tank model.

Ishii and Zuber [100] developed a set of semi-empirical relations for the drag coefficient of bubbles, drops, and particles that include both of these effects, and are widely used in the multiphase flow modeling community. They identified three regimes. At the smallest sizes is the viscous regime, where the drag coefficient essentially follows the traditional relation $C_D \sim 24/Re$, with a mixture viscosity used in the Reynolds number calculation. At larger sizes the bubble begins to flatten and enters the distorted regime. At even larger sizes the bubble becomes a hemishperical cap, and the drag coefficient becomes dependent solely on the void fraction of the liquid. These large cap bubbles dominate the flow field at large void fractions, with the drag of all other bubbles strongly controlled by the wakes of these large caps. This regime is termed the churn-turbulent regime.

The correlations are:

$$
\begin{aligned}
C_D &= \begin{cases} C_{D,viscous} = \frac{24}{Re_{bm}}(1 + 0.1Re_{bm}^{0.75}), & \text{if } Mo^{1/4} \leq 0.11\dfrac{1+\psi}{\psi^{8/3}} \\ C_{D,distorted} = \frac{2}{3}\sqrt{Eo}\left[\frac{1+17.67(1-\phi)^{6/7}}{18.67(1-\phi)}\right]^2, & \text{if } Mo^{1/4} > 0.11\dfrac{1+\psi}{\psi^{8/3}} \\ C_{D,churn-turb.} = \frac{8}{3}(1-\phi)^2, & \text{if } \phi > 0.3 \end{cases} \\
\psi &= 0.55\left[\left(1 + 0.08(r_d^*)^3\right)^{4/7} - 1\right]^{3/4} \\
r_d^* &= r\left[\frac{\rho_l g(\rho_l - \rho_v)}{\mu_l^2}\right]^{1/3}
\end{aligned}
\tag{5.56}
$$

where ϕ is the void fraction, Eo the Eotvos number ($Eo = (\rho_l - \rho_v)gD^2/\sigma$), Mo the Morton number ($Mo = \mu_l^4 g(\rho_l - \rho_v)/\rho_l\sigma^3$), and Re_{bm} is the Reynolds number of the bubble in the mixture ($Re_{bm} = \rho_{liq}uD/\mu_m$). ψ is a function of the normalized radius (r_d^*) found via fitting experimental data. The normalized radius that Ishii and Zuber

used can be rearranged to be an expression of classic nondimensional numbers:

$$r_d^* = r\left[\frac{\rho_l g(\rho_l - \rho_v)}{\mu_l^2}\right]^{1/3} = \frac{1}{2}\left[Eo\ La\right]^{1/3} = \frac{1}{2}\left[Eo\ \frac{Re^2}{We}\right]^{1/3} \tag{5.57}$$

where La is the Laplace number ($La = \sigma D\rho_l/\mu_l^2$) and We is the Weber number ($We = \rho_l u^2 D/\sigma$). Returning to equation (5.56), μ_m is the mixture viscosity, calculated as:

$$\mu_m = \mu_{liq}\left(1 - \frac{\phi}{\phi_{dm}}\right)^{-2.5\phi_{dm}\frac{\mu_{vap}+0.4\mu_{liq}}{\mu_{vap}+\mu_{liq}}} \tag{5.58}$$

and ϕ_{dm} ranges from 0.5 to 1 depending on the system, however a value of 1 is recommended for bubbly flows. Note that in Ishii and Zuber's original work a parameter N_μ was used in place of the Morton number however $N_\mu = Mo^{1/4}$ and so the Morton number was used here. Also, in their Table 2, which summarizes their expressions for the drag coefficient, an error is present and the condition for switching from the viscous regime to the distorted particle regime is written as $0.11 + \frac{1+\psi}{\psi^{8/3}}$, while elsewhere in the text it is written in the form shown here in equation (5.56).

For this simple test case, constant fluid properties and superheat can be assumed in order to focus on determining the magnitude of the effect of the acceleration-dependent terms. The results are shown in figures 5.12 and 5.13 for CO_2 at 20°C and a constant $\Delta T_s = 4°C$. Five cases are presented. First, the quasi-steady results are shown, including only the drag and buoyancy terms and no ma, virtual mass force, or Basset force. The next curve includes ma as well as the drag and buoyancy forces. The third curve includes ma, drag, buoyancy, and the virtual mass force. The fourth shows ma, drag, buoyancy, and the Basset force. The final curve shows the complete system shown in equation (5.54).

The results are shown in figure 5.12 and 5.13, and only show minor differences between the various cases. While the radius increases continually, the velocity becomes constant upon reaching about 0.083 m/s. This point is when the bubble enters the distorted regime, when the expression for C_D becomes proportional to $\sqrt{Eo}$, which also means $C_D \sim r$. To explain how this causes the velocity to become constant, it

is useful to examine the simple quasi-steady case where the drag and buoyancy are matched:

$$\begin{aligned} F_B &= F_D \\ \frac{4}{3}\pi r^3(\rho_l - \rho_v)g &= \frac{1}{2}\rho_l u^2 C_D \pi r^2 \\ \frac{8}{3}r(\rho_l - \rho_v)g &= \rho_l u^2 C_D \\ u &= \sqrt{\frac{8}{3}\frac{r(\rho_l - \rho_v)g}{\rho_l C_D}} \end{aligned} \tag{5.59}$$

If $C_D \sim r$, then the rise velocity becomes a function of the fluid properties alone.

Due to the proximity of the various curves it is difficult to distinguish the importance of the various terms. Therefore figures 5.14 and 5.15 show the normalized difference in the first four cases, referenced to the complete model. From these plots, it is clear that the Basset force has a much greater effect when compared with ma and the virtual mass force. The rise velocity shows larger differences than the bubble radius, reaching 100% at the earliest times however as time increases the curves rapidly converge on the complete model's result. At these early times the bubble velocity is also quite low, less than 1 cm/s and therefore the error in position generated by using the quasi-steady assumption is expected to be negligible. The bubble size shows maximum differences of less than 10%, again peaking at relatively early times and hence low values of r. Similar results are observed at different fluid temperatures and superheats.

The results of this simulation, in combination with the experimental data presented in figures 5.10 and 5.11, prove that the quasi-steady assumption is justified in this system.

Now that it has been shown that the virtual mass and Basset forces are insignificant, the Ishii and Zuber drag model can be compared with experimental data by assuming that buoyancy is exactly balanced by drag, and using the experimentally measured values of r and u to determine C_D. This is done by equating the two terms in equation (5.52) and solving for C_D.

In order to use Ishii and Zuber's model, a value of ϕ must be chosen and a value

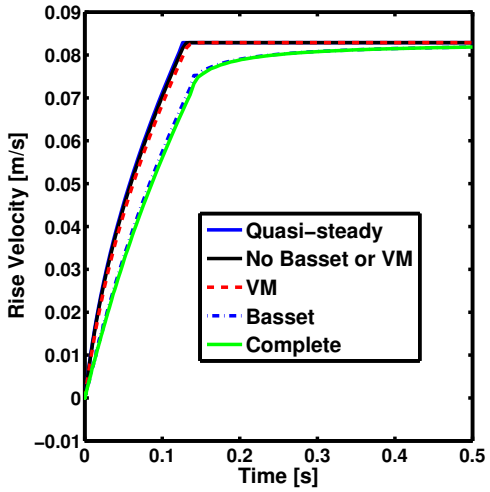

Figure 5.12: Bubble rise velocity versus time as predicted by simulation. Five cases are shown: (1) quasi-steady, (2) *ma* included, (3) virtual mass and *ma* included (4) Basset and *ma* included (5) virtual mass, Basset, and *ma* included (the complete form of equation (5.54)).

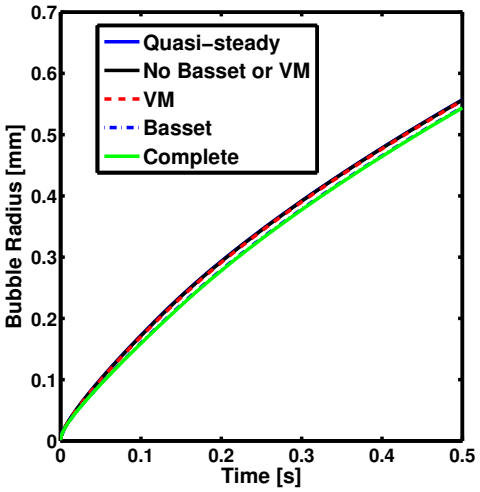

Figure 5.13: Bubble radius versus time as predicted by simulation. Five cases are shown: (1) quasi-steady, (2) *ma* included, (3) virtual mass and *ma* included (4) Basset and *ma* included (5) virtual mass, Basset, and *ma* included (the complete form of equation (5.54)).

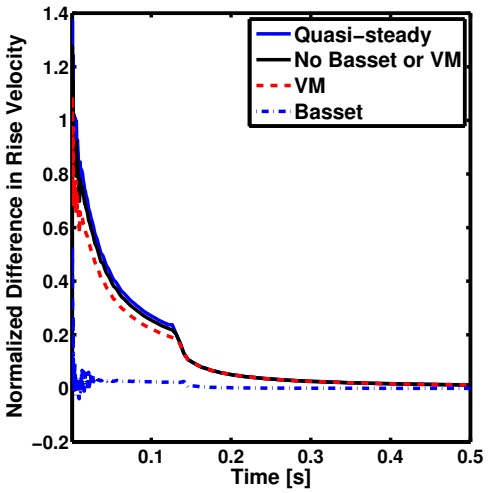

Figure 5.14: Normalized difference in bubble rise velocity. Data are taken from figure 5.12, and the normalized difference is computed as $(u - u_{complete})/u_{complete}$.

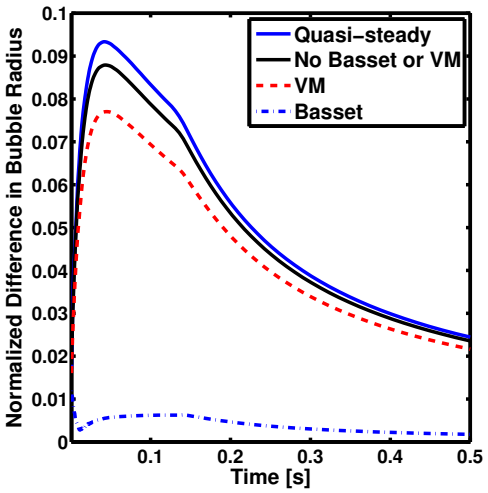

Figure 5.15: Normalized difference in bubble radius. Data are taken from figure 5.12, and the normalized difference is computed as $(r - r_{complete})/r_{complete}$.

of 0 is selected here because of the relatively small bubble population at these early times. The results are shown in figure 5.16. In the times before $t = 0.95$ s and after 1.00 s, the model performs quite well and the difference between its predictions and the experimental data are in the neighborhood of 10% or less. However in between, the model predicts a drag coefficient that is almost twice as large as the measured value.

One possible cause for this temporarily low C_D is that the bubble was entrained within the wake of another bubble. In addition, The model used here is not necessarily intended to apply to a specific bubble, but is an average drag coefficient that can be used in computations and models when considering large populations. Overall the Ishii and Zuber model appears to be reasonably accurate in this system.

By assuming that buoyancy is matched by drag, equation (5.56) can be solved for the rise velocity given a bubble size, fluid properties, and the local void fraction. This term is then used in a variety of locations. It is the velocity needed for computing the spatial derivative terms in equation (5.18), the velocity needed for the bubble

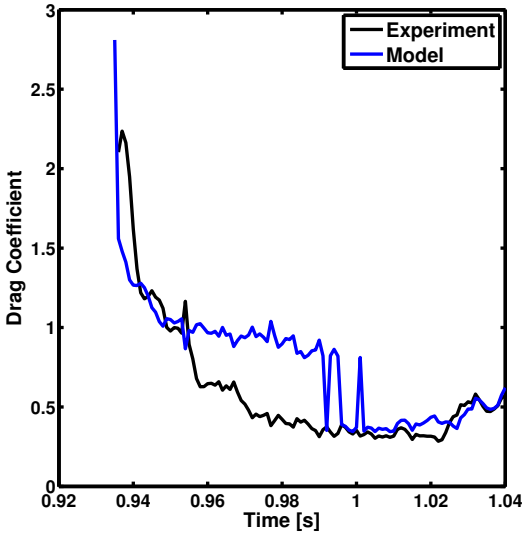

Figure 5.16: Comparison of measured drag coefficient and that predicted by Ishii and Zuber [100].

growth rate in equation (5.45), and it is also the velocity used to calculate the flux of bubbles traveling across the liquid level and hence the mass flow rate into the ullage (equation (5.74)).

Diffusion

Bubbles, like any particle in a fluid, will diffuse from areas of higher concentration to those of lower concentration. This is also known as dispersion, and in many fluid systems is dominated by the effects of turbulence. Therefore, the rate of diffusion is controlled by many system parameters and not just the liquid and bubble fluid properties. The rate is defined by the diffusion coefficient, D_i and has been characterized experimentally by multiple researchers studying bubble columns. Here, an empirical correlation developed by Hikita and Kikukawa is used [101]:

$$D = \left(0.15 + 0.69 u_G^{0.77}\right) D_{tank}^{1}.25 \mu_{liq}^{-0.12} \tag{5.60}$$

where D_{tank} is the tank internal diameter (in m), μ_{liq} is the liquid viscosity (in $Pa\ s$), u_G is the gas superficial velocity (in m/s), and D is the diffusion coefficient (in m^2/s). The superficial velocity is a concept used heavily in the study of multiphase flows and is defined as the volume flux of a given phase. In a bubble column this is an easily-defined quantity because a gas is usually being injected at the base of the column at a controlled rate.

Instead, in this system the volume flux of bubbles at any given point must be calculated. This flux of bubble volume is related to the third moment of the distribution:

$$\begin{aligned} u_{vap,\ superficial} &= \int_0^\infty \frac{4}{3}\pi r^3 f_1(r) u(r) dr \\ &= \sum_i \frac{4}{3}\pi w_i r_i^3 u(r_i) \end{aligned} \tag{5.61}$$

Where $u(r_i)$ is the velocity of bubbles with size r_i passing through the surface.

Coalescence

When bubbles encounter one another, they may coalesce to form a single larger bubble. Physically the process by which bubbles coalesce can be broken into three steps [102]: first, some external factor causes two bubbles to collide such as buoyancy, mean shear within the flow field, or turbulent fluctuations. Then, some liquid is trapped between the bubbles and the bubbles must remain in contact long enough for this liquid film to drain. Finally, the film ruptures and surface tension forces pull the two bubbles into one larger bubble.

The model used here for bubble coalescence is that of Prince and Blanch [103], developed for turbulent dispersed two-phase flows in bubble columns. The model calculates the bubble collision frequency due to a variety of factors and then assesses the likelihood that a give bubble collision will result in coalescence, or the collision efficiency. This model is in turn developed from a number of submodels that were developed by previous researchers and are cited in Prince and Blanch.

The first factor that causes bubbles to collide is from turbulent velocity fluctuations. In short, two bubbles will collide when a turbulent eddy propels one bubble into another. The eddies responsible are of the same size as the bubble, for eddies that are smaller will not be strong enough to move the bubble and larger eddies will simply move a large group of bubbles at the same rate. It is also assumed that the turbulence is isotropic at these scales and the eddies are within the inertial subrange. The collision rate is:

$$\begin{aligned} \theta^T_{i,j} &= n_i n_j S_{i,j} \sqrt{\bar{u}^2_{t,i} + \bar{u}^2_{t,j}} \\ S_{i,j} &= \frac{\pi}{4}(r_i + r_j)^2 \\ u_t &= 1.4(\epsilon 2r)^{1/3} \\ \epsilon &= \frac{Qg}{\pi R_T^2}\left(\frac{P_2 \ln {}^{P_1}/_{P_2}}{P_1 - P_2}\right) \end{aligned} \tag{5.62}$$

where n_i and n_j are the concentrations of bubbles with radius r_i and r_j, $\bar{u}_t$ is the average turbulent fluctuation velocity of the bubble and S_{ij} is the collision cross sectional area of the two bubbles, ϵ is the turbulent energy dissipation rate per unit mass, P_1 and P_2 are the pressure at the bottom and top of the liquid column, R_T is the radius of the column.

The second factor causing bubble collisions is buoyancy, with bubbles of different sizes rising at different rates.

$$\begin{aligned} \theta^B_{i,j} &= n_i n_j S_{i,j}(u_i - u_j) \\ u_i &= \sqrt{\frac{1.07\sigma}{\rho_l r_i} + 1.01 g r_i} \end{aligned} \tag{5.63}$$

where u_i is the rise velocity of a bubble with radius r_i. Although a different expression will be used for calculating the bubble rise velocity in the DQMOM equations, the relation in equation (5.63) is used here because the overall coalescence model has been shown to be accurate.

The third factor is the laminar shear in the liquid phase. This shear develops because bubbles will generally congregate in the center of the column, causing an upwards velocity in the center of the column and a downwards velocity near the wall.

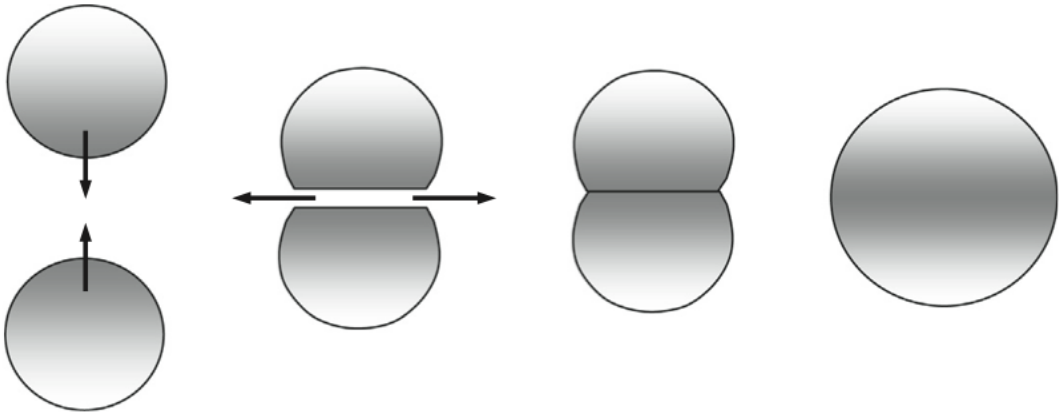

Figure 5.17: Diagram showing the steps of bubble coalescence. Diagram from Yeoh et al, [102]. Reprinted with permission.

This velocity gradient results in collisions as bubbles are convected at different rates. Using an empirical velocity profile and an average value of the shear rate the collision rate can be defined:

$$\begin{aligned} \theta_{i,j}^{LS} &= n_i n_j \frac{4}{3}(r_i + r_j)^3 \frac{\overline{dU_l}}{dR} \\ \frac{\overline{dU_l}}{dR} &= 5.3 \frac{U_{l,max}}{R_T} \\ U_{l,max} &= \left(\frac{1 - 0.75\phi}{1 - \phi} \right) \frac{\phi g R_T^2}{12 \nu_t} \\ \nu_t &= 0.0536 \frac{(2R_T)^{1.77}}{\rho_l} \end{aligned} \tag{5.64}$$

where $\frac{\overline{dU_l}}{dR}$ is the local mean shear rate, $U_{l,max}$ is the maximum liquid velocity, ϕ is the gas holdup, and ν_t is the turbulent kinetic viscosity.

To determine the collision efficiency, the time in which bubbles are in contact as the result of a collision with the time required for them to coalesce are compared. The fact that a finite time is required has been measured experimentally and modeled as a film drainage problem. When two bubbles move towards each other, the liquid film separating them must have time to drain away and decrease in size, shown in figure 5.17. If it has time to reach some critical size, it will rupture and the two bubbles

will coalesce.

Using this model, the collision efficiency is:

$$\begin{aligned} \lambda_{i,j} &= \exp -t_{i,j}/\tau_{i,j} \\ t_{i,j} &= \sqrt{\frac{r_{i,j}^3 \rho_l}{16\sigma}} \ln \frac{h_o}{h_f} \\ r_{i,j} &= \frac{1}{2}\left(\frac{1}{r_i} + \frac{1}{r_j}\right)^{-1} \\ \tau_{i,j} &= \frac{r_{i,j}^{2/3}}{\epsilon^{1/3}} \end{aligned} \tag{5.65}$$

where $t_{i,j}$ is the time required for coalescence, $\tau_{i,j}$ is the time in which the two bubbles are in contact, $r_{i,j}$ is the equivalent radius. h_o and h_f are the starting and ending film thicknesses, with the film rupturing when the film reaches h_f. Chesters [104] suggests the following for h_f:

$$h_f \simeq \left(\frac{A r_{i,j}}{8\pi\sigma}\right)^{1/3} \tag{5.66}$$

where A is the Hammaker constant, a measure of the attraction force between the molecules on the surface of one bubble to those on the other. It is estimated as $10^{-20} J$. The initial film thickness is estimated simply as 10 μm.

The final coalescence rate for bubbles of size r_i and r_j is

$$\Gamma_{i,j} = (\theta_{i,j}^T + \theta_{i,j}^B + \theta_{i,j}^{LS}) \exp -t_{i,j}/\tau_{i,j} \tag{5.67}$$

and the overall coalescence rate for all bubbles is

$$\Gamma = \frac{1}{2} \sum_i \sum_j (\theta_{i,j}^T + \theta_{i,j}^B + \theta_{i,j}^{LS}) \exp -t_{i,j}/\tau_{i,j} \tag{5.68}$$

where the 1/2 factor is needed because every collision rate involves two bubbles. It is important to note that several aspects of the derivation are only accurate to an order of magnitude, and so it is expected that the actual coalescence rate should include an adjustable factor.

The coalescence rate is used to compute two terms in equation (5.22): the birth

and death rates due to coalescence. To do so, equation (5.67) is first converted into what is termed the coalescence "kernel" within the field of population balance modeling, usually written as $\beta(r,\gamma)$. The kernel is the rate at which bubbles of size r and γ will coalesce, normalized by their concentrations. This can be derived simply as $\beta = \Gamma_{i,j}/(n_i n_j)$.

The total rate at which bubbles of size r will die via coalescence is then

$$h_{death}(r) = \int_0^\infty \beta(r,\gamma) f_1(r) f_1(\gamma) d\gamma \tag{5.69}$$

Recall that for equation (5.22), $\int r_s^k (h_{birth} - h_{death})\, dr_s$ must be calculated so for the death term now

$$\int r_s^k (-h_{death})\, dr_s = -\int r_s^k \left[\int_0^\infty \beta(r,\gamma) f_1(r) f_1(\gamma) d\gamma\right] dr_s \tag{5.70}$$

$$= -\sum_i w_i r_{s,i}^k \sum_j w_j \beta(r_i, r_j) \tag{5.71}$$

For the birth term it is first recognized that when two bubbles coalesce, there is conservation of mass and hence volume at that instance. Therefore it is simpler to write the kernel in terms of r^3 and leverage this fact:

$$h_{birth}(r) = \frac{r^2}{2} \int_0^r \frac{\beta((\lambda^3 - \gamma^3)^{1/3}, \gamma)}{(\lambda^3 - \gamma^3)^{2/3}} f_1((\lambda^3 - \gamma^3)^{1/3}) f_1(\gamma) d\gamma \tag{5.72}$$

and the actual term needed in equation (5.22) is now

$$\begin{aligned} \int_0^\infty r_s^k (h_{birth})\, dr_s &= \frac{1}{2} \int_0^\infty f_1(\gamma) \left[\int_0^\infty \beta(\lambda,\gamma)(\lambda^3 + \gamma^3)^{k/3} f_1(\lambda) d\lambda\right] d\gamma \\ &= \frac{1}{2} \sum_i^N w_i \sum_j^N w_j (r_{s,i}^3 + r_{s,j}^3)^{k/3} \beta(r_i, r_j) \end{aligned} \tag{5.73}$$

Free Surface

At the free surface, the rate at which mass is transferred to the ullage by bubbles bursting there must be calculated. This is calculated similarly to the superficial velocity described earlier in the context of the diffusion rate, but now it is multiplied

by the density and cross sectional area of the tank:

$$\begin{aligned}\frac{dm}{dt} &= A\int_0^\infty \rho_{vap}\frac{4}{3}\pi r^3 f_1(r)u(r)dr \\ &= A\sum_i \rho_{vap}\frac{4}{3}\pi w_i r_i^3 u(r_i)\end{aligned} \tag{5.74}$$

Where $u(r_i)$ is the velocity of bubbles with size r_i passing through the surface. Using the expression earlier for u_{rise}, the velocity of the surface must also be taken into account: $u = u_{rise} - u_{surface}$. This second term can be calculated based on the overall rate of change of V_{liq} and $V_{bubbles}$:

$$u_{surface} = \frac{d(V_{liq} + V_{bubbles})}{dt}\frac{1}{A} \tag{5.75}$$

Equation (5.74) is used to calculate $\dot{m}_{boiling}$, needed for equations (5.1) to (5.4). The $h_{boiling}$ term in the liquid conservation of energy equation (equation (5.4)) is taken as the saturation value of the current pressure.

5.4.2 Wall Heat Transfer

There are four different heat transfer processes that involve the walls of the tank. Inside the tank, there is boiling on the liquid portion of the tank wall while in the ullage there is some mix of forced and natural convection. On the outside of the tank there is some convection between the wall and the ambient air and finally within the tank wall itself there is conduction. These four processes will be discussed separately.

The heat transfer from the tank wall into the liquid is generally via boiling on the surface. This heat is assumed to be added directly to the liquid, rather than the bubbles since there is no obvious way of incorporating an external heat addition into the equations for the bubble dynamics. The heat then passes from the liquid into the bubbles via the bubble nucleation and growth processes.

Predicting the heat flux due to boiling is a notoriously difficult problem, and here experimental data rather than a model are used. Studies were conducted by Gorenflo and Kotthoff [105] where an electrically heated horizontal copper tube was placed in

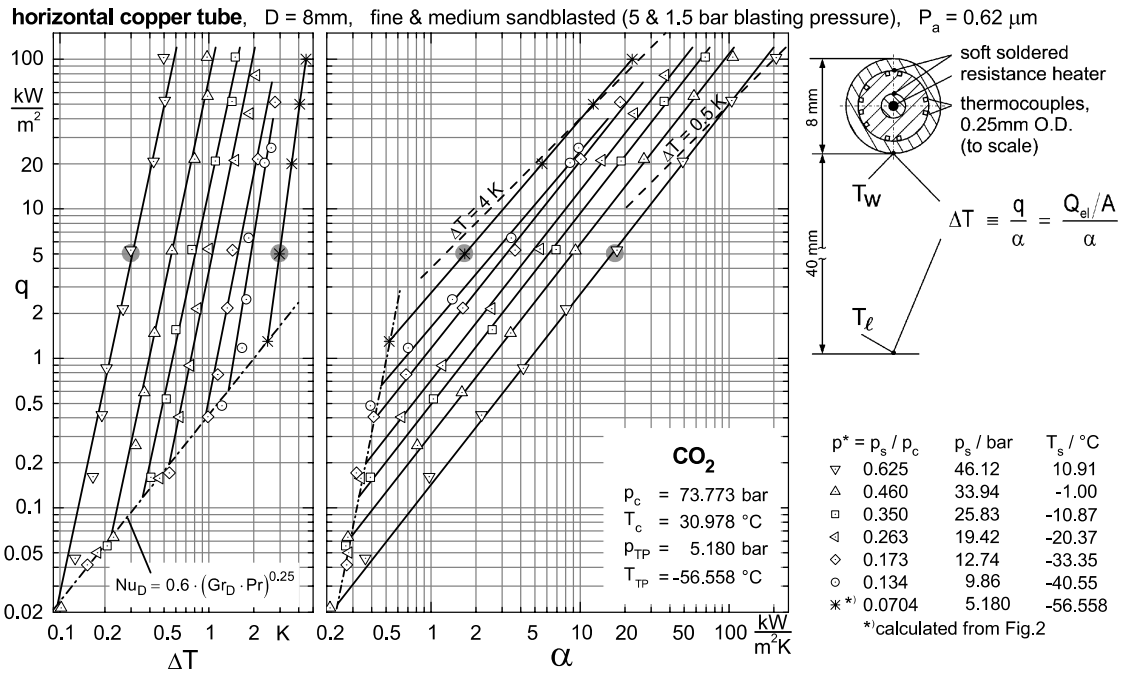

Figure 5.18: Boiling heat transfer data for carbon dioxide, from Gorenflo and Kotthoff [105]. q is the heat flux, α the heat transfer coefficient, and ΔT the superheat. Reprinted with permission.

a vessel of liquid CO_2 and the heat flux was measured at a range of conditions. The results are shown in figure 5.18.

Gorenflo and Kotthoff note that the heat flux appears to be linear with respect to the heat transfer coefficient on a double logarithmic scale, $h \sim q^n$, and suggest the value $n = 1 - 0.3P_r^{0.3}$. Given this slope, only a single point is needed to fix the relationship between h and q. This was performed by this author by fitting a curve to data from another of their plots. The result is:

$$\ln h_{20} = 0.3092(\ln P_r)^3 + 1.649(\ln P_r)^2 + 3.641 \ln P_r + 5.272 \qquad (5.76)$$

where h_{20} is the heat transfer coefficient when the heat flux is 20 kW/m^2, with units of $kW/(m^2K)$. The root mean squared error for this fit was 0.0191. Therefore, given

the wall superheat ($\Delta T_w = T_{wall} - T_{sat}(P)$) the actual heat flux can be calculated as

$$q = \left[\frac{[\Delta T_w \ h_{20}(P_r)]^{\frac{1}{n}}}{q_{20}} \right]^{\frac{n}{1-n}} \tag{5.77}$$

where q_{20} is the heat flux associated with h_{20}, which is simply 20 kW/m^2.

It is important to note that the data presented here were gathered in conditions that are quite different from those found within a self-pressurizing propellant tank. Additionally, the maximum P_r tested was only 0.625 ($T_{sat} = 10.91\ ^\circ C$) so tests at higher temperatures will require significant extrapolation. The conclusion is that some adjustment of this relation may be needed however the general functional form should be correct.

For heat transfer from the tank walls to the ullage as well as from the tank wall to the air, simple correlations for natural convection were used. These are identical to those presented in chapter 2, follow the form $Nu = cRa^n$ where c and n are constants. More detail on the values and implementation are given in chapter 2.

The heat transfer relations described earlier are now used as boundary conditions for the transient heat conduction within the wall itself. Given that N_2O propellant tanks usually have a high length-to-diameter ratio, the problem can be simplified to consider the radial variation alone. The transient heat conduction equation in cylindrical coordinates is then:

$$\frac{\partial T}{\partial t} = \alpha \left[\frac{1}{r} \frac{\partial T}{\partial r} + \frac{\partial^2 T}{\partial r^2} \right] \tag{5.78}$$

The known boundary conditions are the fluxes at the inside and outside ($q = k\partial T/\partial r$) walls.

Conduction in the vertical direction is taken into account approximately using the relation developed by Corpening [39] and presented earlier in chapter 2.

5.4.3 Outflow

Another difficulty found in modeling self-pressurized propellant tanks is capturing the downstream boundary condition, typically a combustion chamber. Fortunately since the flow out of the tank is near saturation, if the pressure drop across the injector is sufficiently large the flow will be choked. This choking phenomenon is often referred to as critical flow in the multiphase flow literature. The importance is that it means that the conditions downstream of the injector are unimportant and the mass flow rate is only dependent on the upstream conditions such as pressure, temperature, and quality.

For this work, numerous critical flow models were evaluated. However, none could be found that were proven against experimental data to accurately predict the flow of CO_2 or N_2O at saturation, with a quality greater than or equal to 0. Indeed, even experimental data with these fluids is difficult to find. Waxman [84] studied this problem experimentally in the case of systems with subcooled liquid but his measurement system would not function with saturated liquid and so his data is not useful here. One good source for the flow of saturated CO_2 was identified however: the work done by James Hesson for his PhD thesis in the late 1950s [35].

Hesson studied the critical flow of subcooled and saturated CO_2 at a wide variety of conditions through orifices. His system began with a run tank fed by a large storage vessel. From this run tank he would flow CO_2 through an orifice, and then through a long heat exchanger with a large internal diameter. This would bring the flow to room temperature without introducing a large back pressure. After the heat exchanger the now gaseous CO_2 would flow through a venturi and the flow rate was accurately measured. From there it was exhausted to the atmosphere.

These experimental data, tabulated in Hesson's thesis, were entered into a database that could be interpolated to find the flow rate as a function of the flow conditions. In short, given a saturation temperature and quality, the mass flux is found from Hesson's tables.

This equation is used to calculate $\dot{m}_{outlet}$, needed for equations (5.2) and (5.4). Based on the current state at the base of the tank (P, T, x) the corresponding mass flux is calculated using Hesson's data. Then it is converted to a mass flow rate using an

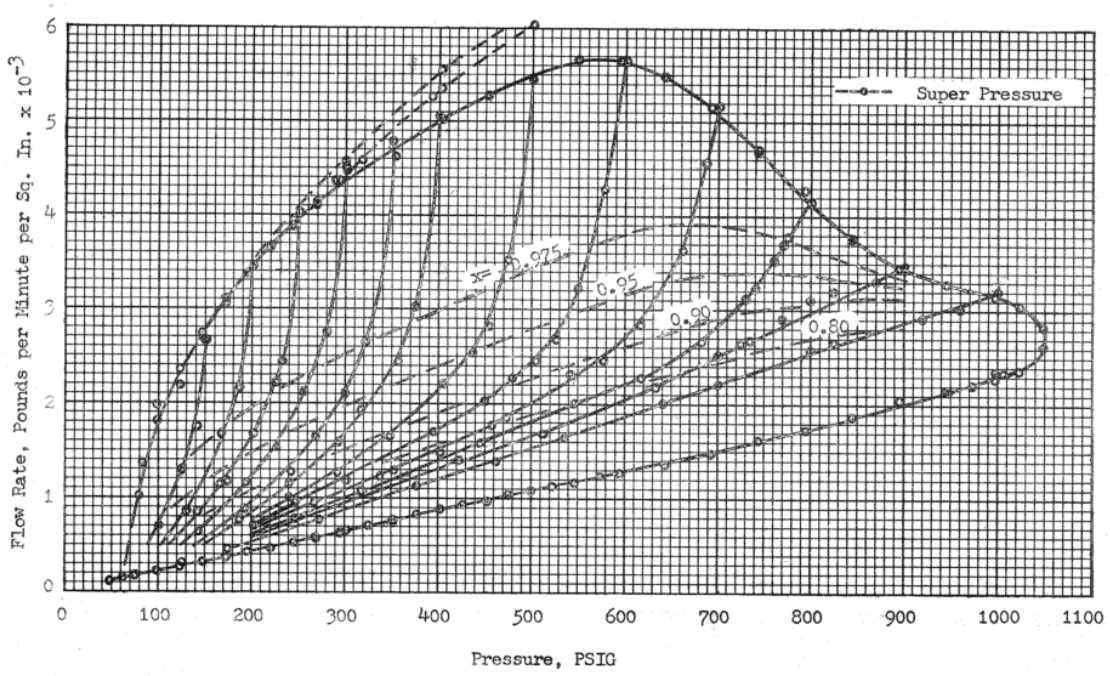

Figure 5.19: Mass flux of carbon dioxide through an orifice as a function of pressure and quality. This is figure 18 from Hesson [35].

assumed injector area. The h_{outlet} term is taken as a mixture value, $h_{vap}x + h_{liq}(1-x)$, where h_{vap} is taken as the saturation value based on the current pressure.

The major downside to this approach is that these data are of course for CO_2 alone, and not for N_2O. Recent experimental work by Waxman [106, 84] with both fluids has shown that they behave similarly in choked orifices. Therefore the data of Hesson will be used for both N_2O and CO_2.

A slight complication is that there are no data on the C_d of the orifices used in this work. Therefore, it is expected that the C_d will be an adjustable parameter in the overall model.

5.4.4 Adjustable Constants

In the descriptions of several of these submodels, it was mentioned that they were only expected to have the correct functional form and not necessarily give exact values. Therefore a set of adjustable constants are introduced. These are:

1. $C_{nucleation\ rate}$. This will multiply the calculated nucleation rate, but accounts for variability in the departure radius, nucleation site density, and nucleation rate. This is possible because all three quantities are multiplied together in the model.

2. $C_{laminar\ shear}$. This multiplies the coalescence rate due to laminar shear.

3. $C_{collision\ efficiency}$. This multiplies the collision efficiency term within the coalescence submodel.

4. $C_{turbulence}$. This multiplies the coalescence rate due to turbulence.

5. $C_{\dot{Q}_{lw}}$. This multiplies the heat flux from the wall into the liquid as a result of heterogeneous boiling.

6. C_d. This multiplies the mass flow rate out of the tank calculated via the data of Hesson.

The effect of variations in these parameters will be discussed later.

5.5 Numerical Methods

In this section the general discretization and integration methods used to solve the relevant ordinary and partial differential equations are given. First, the DQMOM and wall conduction PDEs are discussed, followed by the umbrella time integration method.

5.5.1 DQMOM

In the direct quadrature method of moments two partial differential equations must be solved for each set of weights and abscissas, equation (5.18). To do so, these equations were converted to large sets of ordinary differential equations and then the scheme described in the previous subsection was used to integrate them in time. The spatial terms that must be discretized are those related to advection and diffusion:

$$\frac{\partial u_{i,j} w_{i,j}}{\partial y}, \quad \frac{\partial u_{i,j} g_{i,j}}{\partial y}, \quad \frac{\partial}{\partial y}\left(D_{i,j}\frac{\partial w_{i,j}}{\partial y}\right), \quad \text{and} \quad \frac{\partial}{\partial y}\left(D_{i,j}\frac{\partial w_{i,j}}{\partial y}\right)$$

here i refers to the index of the weights and abscissas, while j is the index of the vertical node.

The first two terms are the advection terms and were calculated using a MUSCL (monotonic upstream-centered scheme for conservation laws) which blends second order and first order upwind-biased schemes. The second order scheme is favored when gradients are small in order to increase the solution accuracy while first order scheme is favored when the gradients become large to preserve the stability of the numerical solution.

The terms can be recast using traditional notation used for computational fluid dynamics:

$$U = \begin{bmatrix} w \\ g \end{bmatrix}, \quad F = F(U) = \begin{bmatrix} uw \\ ug \end{bmatrix} \tag{5.79}$$

where F is the flux, and U is the property vector. The spatial flux gradient is the

quantity of interest: $\partial F/\partial y$.

$$\begin{aligned}
\frac{\partial F}{\partial y} &= \frac{1}{\Delta y}[F^*_{i+1/2} - F^*_{i-1/2}] \\
F^*_{i+1/2} &= \frac{1}{2}[(F(U^R_{i+1/2}) + F(U^L_{i+1/2})) - a_{i+1/2}(U^R_{i+1/2} - U^L_{i+1/2})] \\
U^R_{i+1/2} &= U_{i+1} - 0.5\phi(r_{i+1})(U_{i+2} - U_{i+1}) \\
U^L_{i+1/2} &= U_i + 0.5\phi(r_i)(U_{i+1} - U_i) \\
r_i &= \frac{U_i - U_{i-1}}{U_{i+1} - U_i} \\
\phi(r) &= \max[0, \min(1, r)] \\
a_{i+1/2} &= \max(|u^R_{i+1/2}|, |u^L_{i+1/2}|) \\
u^R_{i+1/2} &= u_{i+1} - 0.5\phi(r_{i+1})(u_{i+2} - u_{i+1}) \\
u^L_{i+1/2} &= u_i + 0.5\phi(r_i)(u_{i+1} - u_i)
\end{aligned} \tag{5.80}$$

Quantities evaluated at $i + 1/2$ and $i - 1/2$ represent those quantities at the boundaries of the cell, while i is the center point. The superscripts L and R refer to the two sides of the cell boundary. For example $U^R_{i+1/2}$ is the property vector at the upper side of the boundary between cell i and cell $i+1$. ϕ is the limiter function and controls the relative weighting of the first and second order schemes. Many possible expressions can be used but the one selected here is known as the "minmod" limiter function. The expression for $F^*_{i+1/2}$ used here is the Kurganov and Tadmor central scheme. At the top and bottom boundaries, a simple first order backwards or forwards differencing scheme is used instead.

The diffusion terms were calculated by first finding the value of the gradient at the cell boundary using a central difference with the neighboring cell value. Then the values at the opposite boundaries of the cell were centrally differenced to calculate the second derivative:

$$\frac{\partial}{\partial y}\left(D_{i,j}\frac{\partial w_{i,j}}{\partial y}\right) = \frac{D_{i,j+1/2}(w_{i,j+1} - w_{i,j}) - D_{i,j-1/2}(w_{i,j} - w_{i,j-1})}{\Delta y^2} \tag{5.81}$$

In the vertical direction, the tank is discretized into a number of cells. These cells

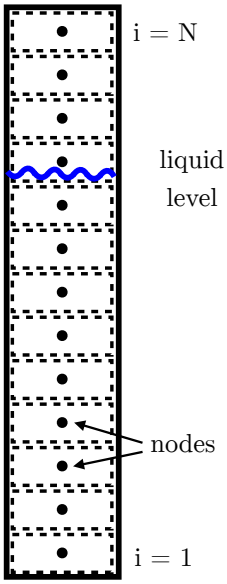

Figure 5.20: Diagram showing the grid geometry for the DQMOM terms.

represent a fixed grid within the tank, with nodes at their centers and at which the weights and abscissas are evaluated. A diagram showing the grid is given in figure 5.20.

The liquid level varies with time and therefore the liquid occupies a varying number of cells. Each time the time derivative terms must be calculated, the current position of the liquid level is determined based on the current bubble volume fraction in every node and the overall liquid volume. To determine where the liquid level lies, the fill level of each cell is defined as γ, which varies from 0 to 1. The basic constraint is:

$$\begin{aligned} V_{liq,pure} + V_{bubbles} &= \sum_i \gamma_i V_{i,cell} \\ &= V_{liq,pure} + \sum_i \gamma_i V_{i,cell} \phi_i \\ \sum_i \gamma_i V_{i,cell} &= V_{liq,pure} + \sum_i \gamma_i V_{i,cell} \phi_i \end{aligned} \tag{5.82}$$

To solve this, γ_i is calculated for each cell, if that cell is assumed to be the cell in which the liquid level lies. This assumption will only be true for one cell, and in that

case the value will satisfy $0 < \gamma_i < 1$. For all other cells, the result will be $\gamma_i > 1$ or $\gamma_i < 0$.

$$\gamma_i = \frac{V_{liq,pure} + \sum_{j=1}^{i-1} \phi_j V_{j,cell} - \sum_{j=1}^{i-1} V_{j,cell}}{V_{i,cell}\,(1-\phi_i)} \tag{5.83}$$

Where N_{full} is the number of nodes that are full (ie $\gamma_i = 1$). So, this equation is evaluated for each i from 1 to N, and the one that gives a value of γ_i between 0 and 1 is the correct value.

An additional complication with the DQMOM equations is that the **A** matrix can be ill conditioned. To solve equation (5.19), a technique from [107] is used:

If the equation $Ax = b$ is solved with some error $x_{wrong} = x_{right} + \delta x$, this incorrect solution satisfies the equation $A(x + \delta x) = b + \delta b$. If the true equation is subtracted from this, the result is $A\delta x = \delta b$. This equation can be solved for δx, and an updated solution computed. This process is repeated until $\delta x \to 0$.

5.5.2 Wall Conduction

The heat conduction within the wall is described by equation (5.78). To solve this, this partial differential equation is converted to a set of ordinary differential equations by semi-discretization, also known as the method of lines. Then, the same time integration scheme used for other ODEs in this system will be applied, as described in the next section. To accomplish this transformation the wall is discretized in radial space and second order central difference approximations for the spatial derivatives are used:

$$\frac{\partial T_i}{\partial r} = \frac{T_{i+1} - T_{i-1}}{2\Delta r} \tag{5.84}$$

$$\frac{\partial^2 T_i}{\partial r^2} = \frac{T_{i+1} - 2T_i + T_{i-1}}{\Delta r^2} \tag{5.85}$$

Here i is the index of the radial node. When this is inserted into the transient heat conduction equation (equation (5.78)) the result is a system of ordinary differential

equations:

$$\frac{\partial \vec{T}}{\partial t} = \frac{\alpha}{2\Delta r}\begin{bmatrix} 0 & r_1^{-1} & & & & \\ -r_2^{-1} & 0 & r_2^{-1} & & & \\ & -r_3^{-1} & 0 & r_3^{-1} & & \\ & & & \ddots & & \\ & & & & -r_N^{-1} & 0 \end{bmatrix}\vec{T} + \frac{\alpha}{\Delta r^2}\begin{bmatrix} -2 & 1 & & & & \\ 1 & -2 & 1 & & & \\ & 1 & -2 & 1 & & \\ & & & \ddots & & \\ & & & & 1 & -2 \end{bmatrix}\vec{T} \tag{5.86}$$

The boundary conditions are implemented by adding ghost points ($i = 0, N+1$) and defining the temperature at those points such that the flux across the boundary (at $i = 1, N$) matches the correct value. 32 points was found to be sufficient in the radial discretization.

5.5.3 Time Integration

There is now a large set of ordinary differential equations (ODEs) that must be integrated in time. This includes the ODEs describing the mass and energy of the liquid and ullage as well as several sets of ODEs resulting from the semi-discretization of various partial differential equations, including the transient heat conduction relation for the wall and the transport equations for the weights and abscissas derived from the direct quadrature method of moments. To simplify the overall process, all ODEs will be integrated together using a single scheme.

Initially, various explicit Runge-Kutta type schemes were applied including Runge-Kutta-Fehlberg [47], Dormand-Prince [103], Cash-Karp [108], and Bogacki-Shampine [109]. These schemes are adaptive and the step size was varied in order to maintain the truncation error below a threshold. Unfortunately though, very small step sizes on the order of 10^{-7} s were required for even very loose error tolerances (eg 10^{-2}), indicating a relatively stiff problem that could not be solved efficiently be explicit solvers.

While implicit schemes are a popular choice for stiff problems because their stability allows for very large time steps, they typically require repeated calculation of

the Jacobian which in turn requires numerous calculations of the time derivatives. In this problem that entails many calls to REFPROP, the fluid properties software package, which is computationally expensive and therefore much of the benefit gained by using an implicit solver is lost. Therefore, a stabilized explicit solver was implemented (second order orthogonal Runge-Kutta-Chebyshev, ROCK2 [110, 111]) that was developed to allow for extremely high stability. While there were some gains in computation time, it was not significant. Next a linearly implicit Runge-Kutta type solver, the third order Rosenbrock scheme ROS3P [112], was implemented. These types of schemes require only one calculation of the Jacobian per time step and therefore minimize the computational penalty associated with an implicit solver. Again unfortunately significant gains were not realized.

The scheme that was found to have the best performance was the trapezoidal rule with a second order backwards difference formula (TRBDF2, [113]), combined with Broyden's "good" update method [114]. TRBDF2 is a popular implicit scheme and unlike Runge-Kutta type solvers only requires one intermediate step. It operates by taking this intermediate step using the trapezoidal rule, and then completing the step with the second order backwards difference formula. An attractive feature of this scheme is that the Jacobian of the set of nonlinear equations that must be solved is identical for the two parts of the step, allowing it to be reused without recomputing the various time derivatives. This greatly minimizes the calls to REFPROP required.

Broyden's "good" update method is a technique used to solve sets of nonlinear equations iteratively without computing the Jacobian. Information from each iteration is used to update an estimate of the Jacobian. The true Jacobian must still be computed from time to time, however this is limited to situations when the step size has changed substantially, the solver is not converging, or the estimated truncation error isn't dropping as expected as the step size is reduced. Effectively, the true Jacobian is only computed every 10-100 time steps. By using TRBDF2 and Broyden's method, an implicit solver was found that yielded large time steps and low computational costs.

The details of this scheme will now be outlined. It begins with a trapezoidal rule step, from t_n to $t_n + \gamma\Delta t$. Then, the backwards difference formula step will complete

the step from $t_n + \gamma\Delta t$ to $t_n + \Delta t$. The value of γ defines what fraction of the total step the two methods will take. The trapezoidal rule step can be written as:

$$u^{n+\gamma} - \frac{\gamma h}{2} f(u^{n+\gamma}) = u^n + \frac{\gamma h}{2} f(u^n) \tag{5.87}$$

or

$$\begin{aligned} \left(u^{n+\gamma} - u^n\right) - \frac{\gamma h}{2}\left(f(u^{n+\gamma}) - f(u^n)\right) &= 0 \\ F(u^{n+\gamma}) &= 0 \end{aligned} \tag{5.88}$$

and this equation must be solved for $u^{n+\gamma}$. Note that here u^n is a constant as it is a result of the previous time step. The Jacobian is:

$$\frac{\partial F}{\partial u^{n+\gamma}} = J = 1 - \frac{\gamma h}{2}\frac{\partial f}{\partial u} \tag{5.89}$$

For the second order backwards difference formula, the step is

$$\begin{aligned} u^{n+1} - \frac{1-\gamma}{2-\gamma} h f(u^{n+1}) &= \frac{1}{\gamma(2-\gamma)} u^{n+\gamma} - \frac{(1-\gamma)^2}{\gamma(2-\gamma)} u^n \\ u^{n+1} - \frac{1-\gamma}{2-\gamma} h f(u^{n+1}) - \frac{1}{\gamma(2-\gamma)} u^{n+\gamma} + \frac{(1-\gamma)^2}{\gamma(2-\gamma)} u^n &= 0 \\ F(u^{n+1}) &= 0 \end{aligned} \tag{5.90}$$

which is solved for u^{n+1}. The Jacobian here is

$$\frac{\partial F}{\partial u^{n+1}} = 1 - \frac{1-\gamma}{2-\gamma} h \frac{\partial f}{\partial u} \tag{5.91}$$

which is identical to that of the trapezoidal rule step if $\gamma = 2 - \sqrt{2}$. This enables the same Jacobian to be used for both the trapezoidal rule step and the backwards difference formula step. Additionally, this value of γ can be shown to minimize the Frobenius norm of truncation error of the total step and so it will be used here. An

estimate of the local truncation error is calculated by comparing the two steps:

$$\varepsilon_{truncation} = 2\left(\frac{-3\gamma^2+4\gamma-2}{12(2-\gamma)}\right)\left[\frac{1}{\gamma}f(u^n) - \frac{1}{\gamma(1-\gamma)}f(u^{n+\gamma}) + \frac{1}{1-\gamma}f(u^{n+1})\right] \tag{5.92}$$

Broyden's method is now employed twice: once to solve equation (5.88) and then again to solve equation (5.90). In each case, it operates iteratively to solve the basic $F(u) = 0$ nonlinear relation. For equation (5.88), the iteration can be written as:

$$J_k^{-1} = J_{k-1}^{-1}\left[1 + \frac{(u_k^{n+\gamma} - u_{k-1}^{n+\gamma}) - J_{k-1}^{-1}[F(u_k^{n+\gamma}) - F(u_{k-1}^{n+\gamma})]}{(u_k^{n+\gamma} - u_{k-1}^{n+\gamma})^T J_{k-1}^{-1}[F(u_k^{n+\gamma}) - F(u_{k-1}^{n+\gamma})]}(u_k^{n+\gamma} - u_{k-1}^{n+\gamma})^T\right] \tag{5.93}$$

With the estimate of the inverse of the Jacobian provided by equation (5.93), a new step is taken as

$$u_{k+1}^{n+\gamma} = u_k^{n+\gamma} + J_k^{-1}F(u_k^{n+\gamma}) \tag{5.94}$$

This process is performed repeatedly until a converged value of $u_k^{n+\gamma}$ is found, but typically only requires 3-5 iterations. Convergence is assessed by first calculating

$$r = \frac{||J_k^{-1}F(u_k^{n+\gamma})||}{||J_{k-1}^{-1}F(u_{k-1}^{n+\gamma})||} \tag{5.95}$$

and determining if

$$\frac{r}{1-r}\left\|\frac{J_k^{-1}F(u_k^{n+\gamma})}{u_k^{n+\gamma}}\right\| \leq \varepsilon_{tolerance} \tag{5.96}$$

The time step is varied according to the algorithm of Abdulle [110], which is outlined here in pseudocode:

Take a time step with the current value of h and calculate ε_{trunc}
$sh_n \leftarrow \sqrt{\frac{\varepsilon_{tol}}{\varepsilon_{trunc}}}$
if last step was acceptable **then**
  $sh_n \leftarrow \min(sh_n, sh_{n-1})$

end if

$sh_n \leftarrow \min(sh_{max}, \max(0.1, 0.8 * sh_n))$

if $\varepsilon_{trunc} \leq \varepsilon_{tol}$ **then**

accept step

$sh_{max} \leftarrow 2$

else

reject step

$sh_{max} \leftarrow 1$

$sh_n \leftarrow 0.8 * sh_n$

end if

$h_{new} \leftarrow sh_n * h_n$

5.5.4 Fluid Properties

All fluid properties are calculated via the REFPROP software package [2]. This includes the various thermodynamic derivatives needed for equations such as (5.14). Some of these are not given explicitly by REFPROP, but can be calculated via basic thermodynamic relations and the outputs that REFPROP does possess.

Two more difficult calculations must be made. The first is simply finding the density of a metastable state. REFPROP in general will give any thermodynamic property as a function of any other two (with some restrictions). However, for metastable calculations it only takes temperature and density as inputs. So, to calculate the density of superheated liquid given the temperature and pressure the equation $P - P_{REFPROP}(T, \rho) = 0$ must be solved using a non-linear equation solver (eg Matlab's `fzero`).

It is worth noting that all equations of state, including those used within REFPROP, have been developed to give accurate results in the thermodynamically stable regions. Therefore there is not necessarily any expectation that values in the metastable region should be accurate. This problem was discussed earlier in chapter 2. Unfortunately, there is nothing that can be done here to assess the accuracy of

REFPROP in the metastable region for either N_2O or CO_2. It will be used nevertheless because results have shown that the fluid never travels far into the metastable region, with superheats usually less than 5 $°C$.

A more difficult situation arises when the fluid pressure must be calculated from the thermodynamic variables at hand: $T_{liq}, m_{liq}, m_{ull}, U_{ull}$. This is done by using the constraint that the tank volume is constant:

$$\begin{aligned} V_{tank} &= V_{ullage} + V_{liquid} + V_{bubbles} \\ &= \frac{m_{liq}}{\rho_{iq}} + \frac{m_{ull}}{\rho_{ull}} + \sum_i \phi_i V_{i,cell} \end{aligned} \tag{5.97}$$

Where ρ_{ull} is calculated from:

$$\begin{aligned} \rho_{ull} &= \phi_{ull}\rho_{ull,vap} + (1-\phi_{ull})\rho_{ull,liq} \\ \phi_{ull} &= \left[1 + \frac{\rho_{ull,vap}}{\rho_{ull,liq}}\frac{1-x_{ull}}{x_{ull}}\right]^{-1} \\ x_{ull} &= \frac{u_{ull} - u_{ull,liq}}{u_{ull,vap} - u_{ull,liq}} \\ u_{ull} &= \frac{U_{ull}}{m_{ull}} \end{aligned} \tag{5.98}$$

Where $\rho_{ull,liq}$ and $\rho_{ull,vap}$ are the saturated liquid and vapor densities calculated at the ullage pressure. The terms $u_{ull,ilq}$ and $u_{ull,vap}$ are calculated similarly. Note that the calculation of x_{ull} is a simple way of verifying the assumption of a saturated, two-phase mixture within the ullage: if $x_{ull} < 0$ or $x_{ull} > 1$, then the vapor has either become a subcooled liquid or a superheated vapor, respectively.

It was mentioned in the previous section that REFPROP is relatively computationally expensive. An alternative was attempted by generating a large lookup table and then interpolating (linearly or via splines) between values to calculate the needed fluid properties. Unfortunately this yielded substantially different model results unless the table was extremely dense, and at that point the storage and computation required to use the lookup table made it more computationally expensive than simply using REFPROP.

Table 5.1: Parameters used in model results.

Parameter	Value
T_i	17.6 $°C$
Fill level	83%
C_d	0.8
Orifice diameter	2.261 mm
Number of spatial nodes for DQMOM	32
Number of radial nodes in tank wall	32
Number of moments	4
$C_{nucleation\ rate}$	10^{-8}
$C_{\dot{Q}_l w}$	$2 \cdot 10^{-5}$
$C_{collision\ efficiency}$	0.1
$C_{turbulence}$	1
$C_{laminar\ shear}$	1
Relative error tolerance in time	10^{-3}

5.6 Model Results

In this section, some results of the model will be presented and discussed. A test case of experimental data is used as validation. Specifically, a test with CO_2 in the flat glass gauge with the following test parameters is used: $t_{LRO} = 5.94\ s$, $\overline{T_i} = 17.6\ °C$, fill level = 83%, orifice diameter = 2.261 mm. The initial temperature profile from this test is give in figure 5.21 and a full list of parameters used in the model are given in table 5.1. The tank dimensions used were those of the flat glass gauge, and C_d was found via trial and error in order to match t_{LRO}. A test in the flat glass gauge is used because the submodel for wall heat transfer was developed using a metal surface and it is hypothesized that it will be more accurate with a stainless steel tank than with quartz.

5.6.1 Results

Some basic results from the model are given in figures 5.22 through 5.32. The pressure time history is first given in figure 5.22, along with the experimental data. The

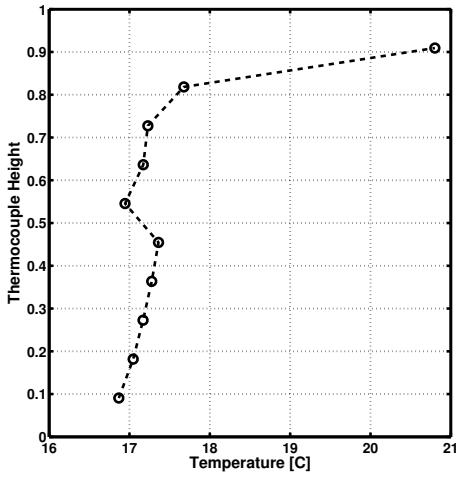

Figure 5.21: Initial temperature profile for experimental data used as model test case.

only other experimental data that can be used for comparison are the video data. Specifically, the location of the liquid level can be measured from the images, however often there is too much condensation in the ullage and boiling within the liquid to clearly identify it (see figures 4.107 and 4.108 as an example). As a result, there are some gaps in the experimental data. The predicted and measured data are shown in figure 5.23.

In both of these figures the proposed model gives results that are similar to the experimental data but there is some deviation. In the pressure time history the model predicts a lower minimum and higher maximum, followed by a steady state regime value that is about 0.2 MPa lower than the experimental data. The liquid level data are unavailable from the experiment after $t = 0.30\ s$ until $t = 2.95\ s$. In the early times the model agrees quite closely with the experimental data, but in the later part of the test the model predicts a fill level that is too low.

The liquid and ullage temperatures are given in figure 5.24, and the superheat is shown in figure 5.25. The liquid temperature drops steadily until around $t = 3\ s$, at which point the rate of decrease slows, and finally increases briefly before oscillating and rising at the end of the test. The ullage temperature is essentially a scaled version of the pressure time history because the ullage follows the saturation line.

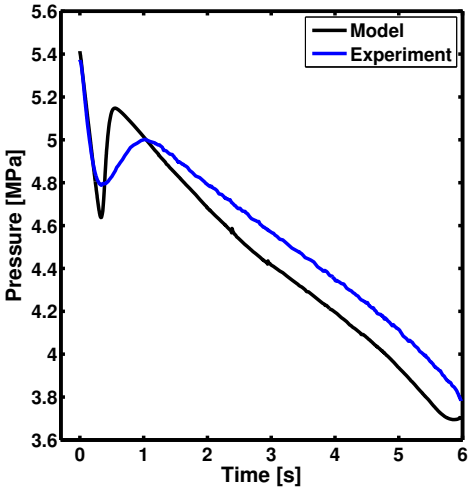

Figure 5.22: Pressure time history comparison of model results and experiment.

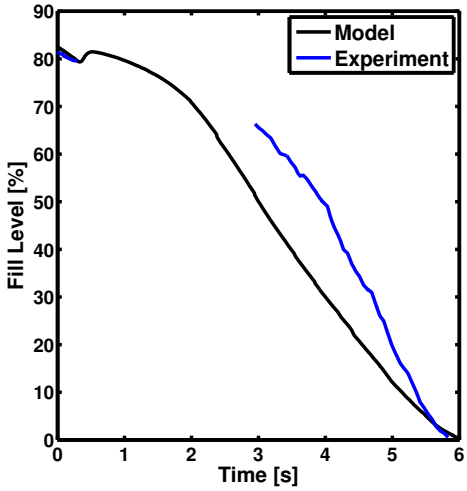

Figure 5.23: Fill level time history comparison of model results and experiment. Gaps in experimental data occur because the fill level is sometimes not distinguishable.

The level of superheat in the liquid is simply the difference between these two curves, but for convenience it is plotted as well. In the transient regime the superheat reaches a peak of 5.3 $°C$ before dropping back to 0.4 $°C$. It stays near that level until about $t = 3\ s$ when it begins to increase rapidly, reaching a peak of 5.8 $°C$ before decreasing momentarily and then increasing until the end of the test. The final value is 7.5 $°C$.

The mass flow rate predicted by the model is shown in figure 5.26 and is relatively constant, varying only between 0.11 and 0.15 kg/s for most of the test and then dropping rapidly near the end. This is despite the large pressure variations seen in figure 5.22. Also shown in figure 5.26 is the vapor mass fraction at the base of the tank. It begins close to zero, but once a significant amount of bubbles are generated when the pressure reaches its minimum in the transient regime, it increases to 0.02 and stays constant until about $t = 3\ s$, at which point it begins to rise. Near the end of the test it becomes very large, peaking at 0.66.

The quality of the ullage (ie the vapor mass fraction) is shown in figure 5.27. The

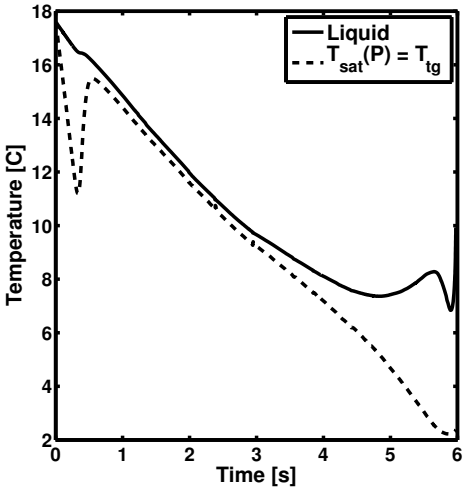

Figure 5.24: Temperature time history for the liquid and ullage. Since the ullage is saturated, its temperature is simply $T_{sat}(P)$.

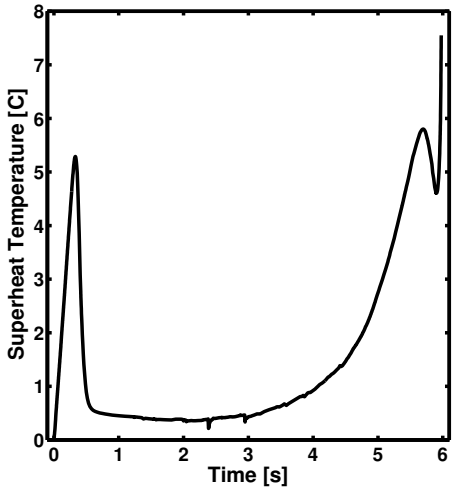

Figure 5.25: Level of superheat within the liquid as a function of time.

ullage quality begins as one might expect from the expansion and contraction of the ullage volume: in the transient regime, the quality rapidly drops and then increases. In the steady state regime the quality drops slowly over time but in a non-monotonic fashion.

Now, several quantities related to the bubble distribution are examined. These quantities are functions of both space and time and therefore will be plotted versus the vertical location with curves at several equally-spaced time points: $t = 0$, 0.66, 1.33, 1.99, 2.66, 3.32, 3.98, 4.65, 5.31, and 5.98 s. Due to the fixed grid and the decreasing liquid volume, the length of these curves decreases with time. Figures 5.28 and 5.29 show the raw weights and abscissas predicted by DQMOM.

The weights are generally decreasing with time. Note that at the earliest time point the weights are near zero and therefore are not visible. This is also true for the second abscissa. At the early times, the weights show a plateau and are constant over much of the tank. In later times however they transition to a constant gradient from the base to the liquid surface and steadily decrease. Note the order of magnitude of these weights.

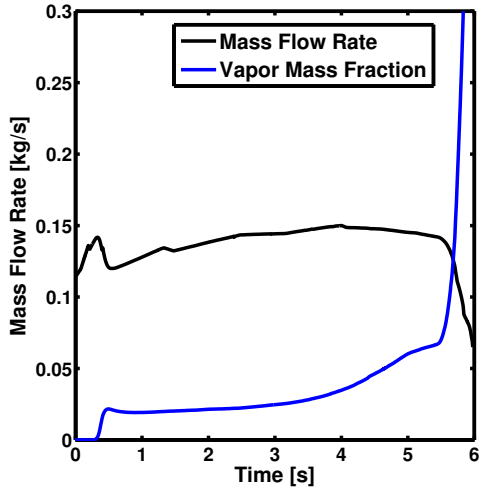

Figure 5.26: Mass flow rate out of the tank as a function of time. Also shown is the vapor mass fraction of the liquid at the base of the tank.

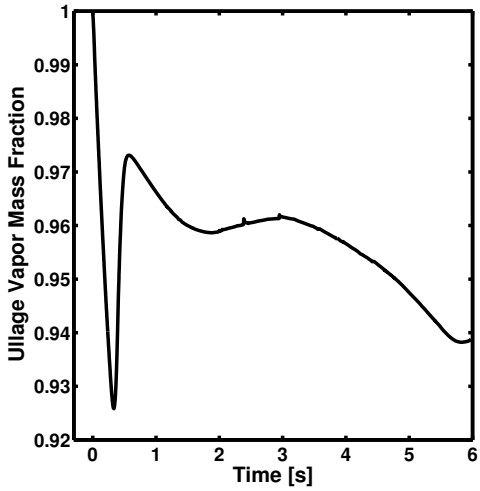

Figure 5.27: Time history of the ullage vapor mass fraction.

The abscissas show very little variation across the tank's length except at the latest time points, when a slight gradient can be seen. Also, while they generally increase with time at the last time point the first abscissa decreases substantially while the second continues to increase.

Using these values of weights and abscissas, several quantities of engineering interest are then calculated: 5.30 and 5.31 show the void fraction and bubble number density. Another important quantity is the average bubble size, however it is not clear what type of averaging should be used.

Commonly in flows with particles the Sauter mean diameter (d_{32}) is used for this purpose [102]. It gives the size of a particle that has the same volume-to-surface area

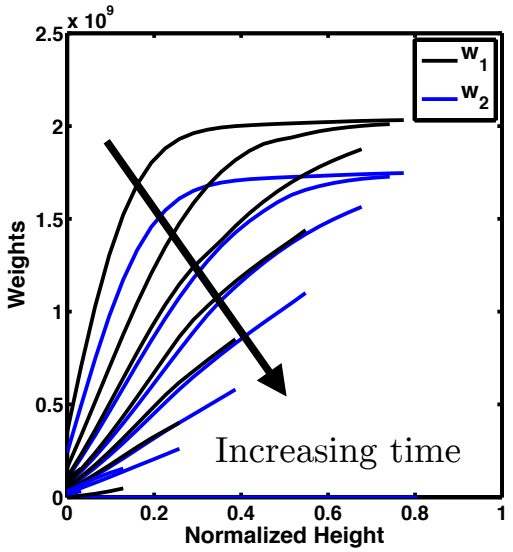

Figure 5.28: DQMOM weights versus height, at 8 time points: $t = 0.66$, 1.33, 1.99, 2.66, 3.32, 3.98, 4.65, 5.31 s. The length of the curve corresponds to its time, with longer curves occurring earlier.

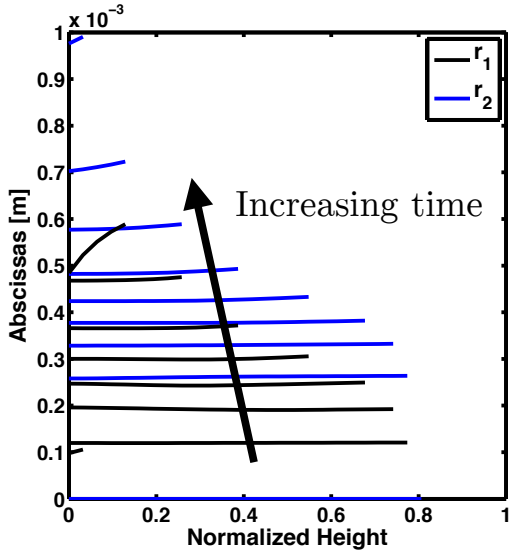

Figure 5.29: DQMOM abscissas versus height, at 8 time points: $t = 0.66$, 1.33, 1.99, 2.66, 3.32, 3.98, 4.65, 5.31 s. The length of the curve corresponds to its time, with longer curves occurring earlier.

ratio as that of the whole population. Here it can be calculated as

$$\begin{aligned} d_{32} &= 6\frac{V_{bubbles}}{A_{bubbles}} \\ &= 6\frac{\int_0^\infty \frac{4\pi}{3} r^3 f_1(r) dr}{\int_0^\infty 4\pi r^2 f_1(r) dr} \\ &= 2\frac{\sum_i w_i r_i^3}{\sum_i w_i r_i^2} \end{aligned} \tag{5.99}$$

This quantity is shown in figure 5.32.

The void fraction and bubble number density both show some similar features to those seen in the weights. In the early times the population is relatively uniform along the length of the tank, while in later times a strong gradient develops with

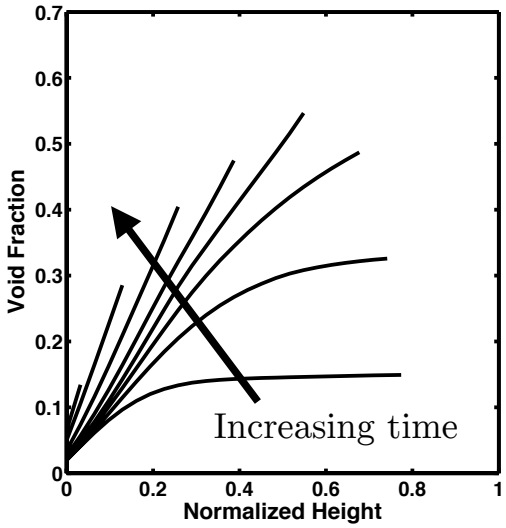

Figure 5.30: Void fraction within the liquid versus height, at 8 time points: $t = 0.66$, 1.33, 1.99, 2.66, 3.32, 3.98, 4.65, 5.31 s. The length of the curve corresponds to its time, with longer curves occurring earlier.

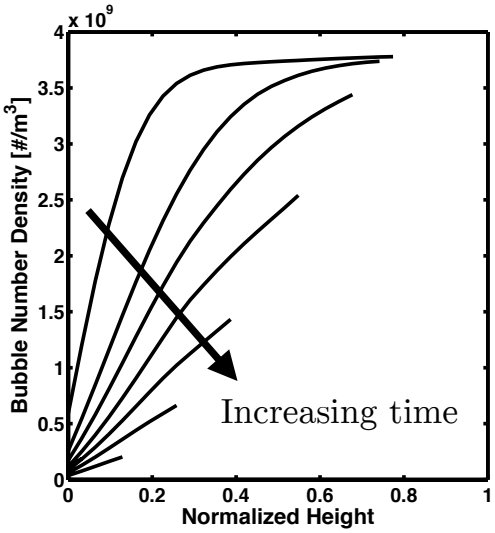

Figure 5.31: Bubble number density within the liquid versus height, at 8 time points: $t = 0.66$, 1.33, 1.99, 2.66, 3.32, 3.98, 4.65, 5.31 s. The length of the curve corresponds to its time, with longer curves occurring earlier.

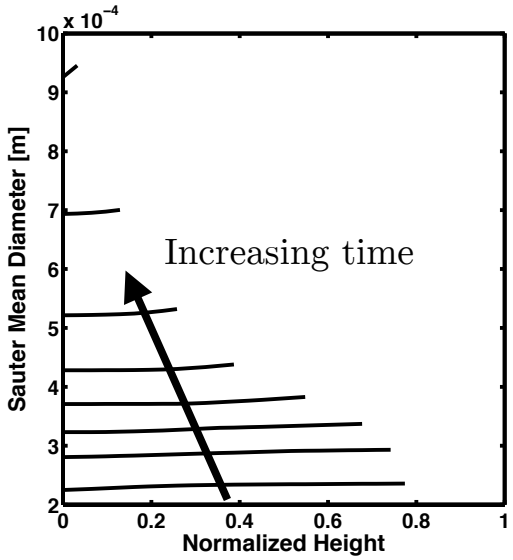

Figure 5.32: Bubble Sauter mean diameter versus height, at 8 time points: $t = 0.66$, 1.33, 1.99, 2.66, 3.32, 3.98, 4.65, 5.31 s. The length of the curve corresponds to its time, with longer curves occurring earlier.

fewer bubbles and a lower void fraction at the bottom while near the top there are more bubbles and also a larger void fraction.

The bubble size data shown in figure 5.32 show that the average bubble diameter is steadily increasing during the test, reaching almost 1 mm by the end and behaving similarly to the abscissas. This connects the void fraction that is generally increasing with time with the number density that is decreasing. In later times the tank contains fewer, larger bubbles.

A benefit of using the full transient conduction equation within the wall is that the temperature profiles can be examined. These are shown in figures 5.33 and 5.34, where the temperature profiles are plotted at several time points. These are the same time points used earlier in figure 5.30. In both figures the wall temperatures decrease as the liquid and ullage temperatures both drop, although the portion of the wall in contact with the liquid shows much larger temperature changes. Also visible are oscillations in the profile at the later time points. These oscillations are the result of numerical instability and will be discussed later.

Finally, the history of the time step is plotted in 5.35. The value is generally around 10^{-2}, but is much lower during the transient regime when the sudden increase in nucleation rate causes rapid changes in the weights and abscissas. Also, the value periodically drops rapidly whenever errors are thrown somewhere within the code which can happen when the inputs of REFPROP exceed its boundaries, or the implicit routine fails to converge, or any one of a number of other scenarios. This automatically causes a decrease in the time step by a factor of 10 and accounts for the sharp drops in the time step.

5.6.2 Discussion

A common feature to several of the plots presented is that some change seems to occur around $t = 2.5$ or 3 s. This was first seen in the fill level in figure 5.23 where there is a relatively sudden increase in its rate of change and then in the liquid temperature in figure 5.24 where it begins to level off, then oscillate and increase. The vapor mass fraction at the base of the tank in figure 5.26 begins to increase at this time as well.

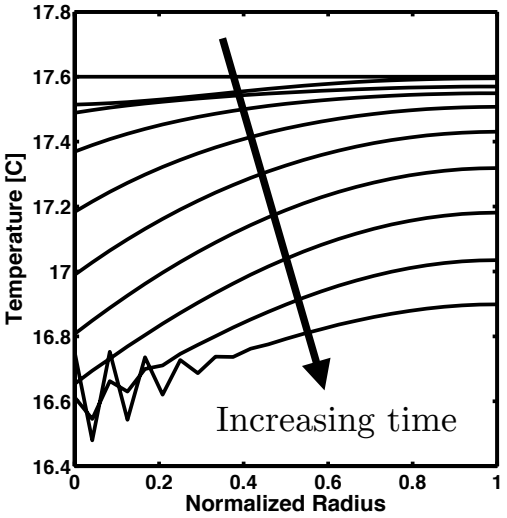

Figure 5.33: Temperature profile within the wall on the lower part of the tank, in contact with the liquid. This is plotted at 8 time equally spaced time points: $t = 0.66, 1.33, 1.99, 2.66, 3.32, 3.98, 4.65, 5.31\ s$.

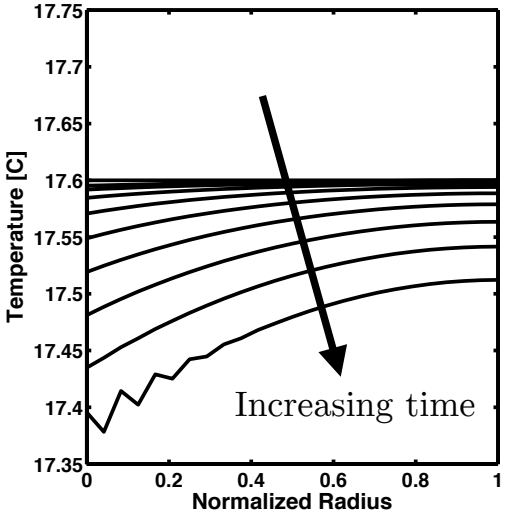

Figure 5.34: Temperature profile within the wall on the upper part of the tank, in contact with the ullage. This is plotted at 8 time equally spaced time points: $t = 0.66, 1.33, 1.99, 2.66, 3.32, 3.98, 4.65, 5.31\ s$.

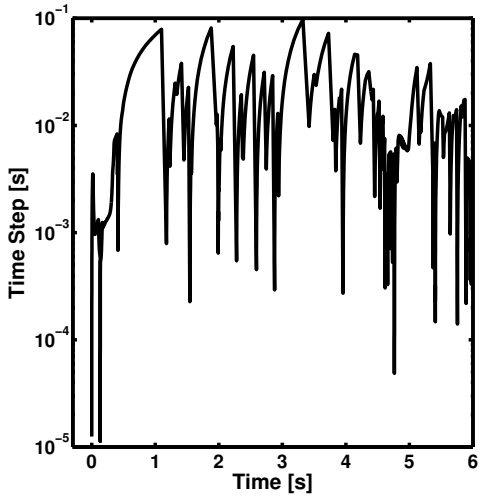

Figure 5.35: Time step used by integration scheme versus time.

The profiles of void fraction and bubble number density in figures 5.31 and 5.32 also show a change here, with a transition from having a flat portion of the profiles to a more constant gradient across the tank.

These profiles describing the bubble population are the key to understanding the physical process here. In the transient regime the superheat reaches fairly high levels, nucleating a large population of bubbles uniformly throughout the tank. Subsequently however the superheat decreases to a much smaller amount and the nucleation rate drops accordingly.

Recall in chapter 4 it was shown that the nucleation rate is a very strong function of temperature and so at these early times the entire bubble population within the tank is composed of a single generation that was formed at a single instance in time, when the superheat reached a maximum.

Now, as time goes on the liquid is still superheated so this generation will grow in diameter and the overall void fraction will increase. However as they grow buoyancy causes the rise velocity to increase, and this population then moves somewhat uniformly towards the ullage. This explains why the flat part of the curves in figures 5.30 through 5.32 is becomes shorter and more curved - the population is dying off as it rises and reaches the liquid surface.

After this point, the bubble population shows a strong vertical gradient, meaning that bubbles are being continuously nucleated throughout the tank and there is no single dominant generation.

Several other features are worth highlighting. One is the rapid increase in liquid temperature near the end of the test. This temperature increase is likely caused by the heat flux into the liquid from the walls. As the liquid volume drops its surface-area-to-volume ratio increases at a rate that is also increasing. Therefore, the heat flux from the wall is going to have a relatively larger and larger impact on the liquid temperature. Put more simply, the ratio $\dot{Q}/m_{liq}$ is increasing.

A region where the model deviates far from the experimental data is seen in the pressure time history for the transient regime (figure 5.22), where the model predicts a much higher and earlier pressure maximum. This is most likely caused by the 0-D aspect of the model, wherein the liquid temperature is uniform throughout, causing

the superheat and hence nucleation rate to be constant throughout the tank. In reality of course there will be variations in the temperature of the liquid and any regions with a higher temperature would have higher nucleation rates, producing large quantities of bubbles before other areas reach the same level of superheat. The net result is that the pressure minimum and maximum would both be spread out in time. This effect is not captured in the model and therefore the model predicts a sharper pressure minimum and maximum, and also misses their timing and magnitude.

The mass flow rate data are also of interest. These data shown in figure 5.26 may be counter-intuitive, with a flow rate that decreases as the pressure increases, but this same behavior was shown earlier in figure 5.19 when the orifice flow rate submodel was discussed. As the pressure decreases the density increases because the fluid is relatively close to saturation. This increase in density is larger than the decrease in the driving pressure. This trend does not continue forever, and in figure 5.19 it is also clear that if the pressure is too low then the flow rate should drop as well. At the very end of the test the flow rate begins to drop rapidly. This is caused by the large vapor mass fraction of the fluid at the base of the tank. Hesson's data in 5.19 also shows this effect, with relatively small decreases in x causing large changes in $\dot{m}$.

The wall temperature data in figures 5.33 and 5.34 show how the wall in contact with the liquid loses much more energy to the fluid than the wall in contact with the ullage. This is due to the high heat flux caused by boiling occurring directly on the tank wall. The curves are taken from equally spaced time points and so the variability of the heat flux out of the wall into the liquid is also visible. The difference between the first time point and the initial condition is much larger than that of the first and second. This indicates a higher wall heat flux in the transient regime, which is expected because of the high superheat during that time causing significant boiling induced heat transfer. A reduced heat flux near the end of the test is also visible as the liquid temperature climbs. In the ullage the wall heat flux is increasing in time as a result of the steadily decreasing ullage temperature.

The oscillations that are visible in both the liquid and ullage wall temperature profiles is a well-known numerical instability that is present in some transient conduction problems that use central differencing [115]. A grid Fourier number can be

defined as:

$$Fo = \frac{\alpha \Delta t}{\Delta x^2} \tag{5.100}$$

where α is the thermal diffusivity of the wall, Δt is the time step, and Δx is the wall grid spacing. The Fourier number is a ratio of the characteristic diffusion time scale ($\Delta x^2/\alpha$) to the numerical time step.

For $Fo > 0.25$ stable oscillations may occur and if $Fo > 0.5$ unstable oscillations may occur. In this model the time step may vary by more than four orders of magnitude during the course of the test and therefore picking Δx such that Fo is always less than 0.5 is not practical. However, experience has shown that these oscillations will decay on their own once the time step increases and the effect of these oscillations on the overall model predictions (eg pressure or fill level) is negligible. Therefore they can generally be safely ignored. It will also be shown in the next section that increasing the number of nodes in the wall grid has very little effect on the model, again suggesting that these oscillations are not important.

5.7 Effect of Model Parameter Variation

In this section the effect of the various parameters within the model are examined, beginning with the numerical parameters and then discussing the adjustable constants needed for the submodels.

5.7.1 Numerical Parameters

The numerical parameters in this model include the spatial grid resolution both in the liquid and in the wall, the number of abscissas and weights, and the time integration error tolerance. Each of these will be individually varied and the resultant solutions compared to a reference case. The model output used for this study will be the pressure time history. While the entire histories can be compared, it is also useful to have a single scalar quantity with which to assess convergence. For this an integrated

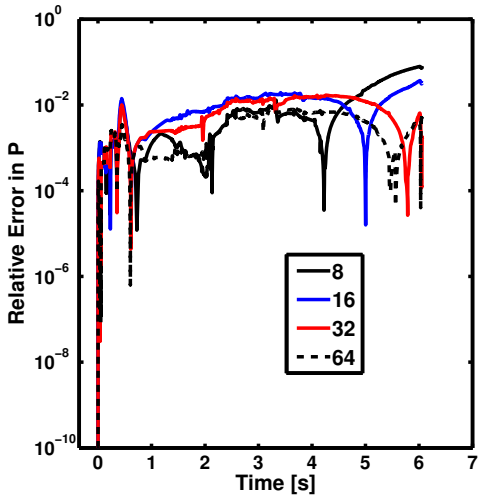

Figure 5.36: Relative error in pressure versus time. The different curves correspond to different spatial grid resolution. Errors are calculated relative to the solution with 128 nodes.

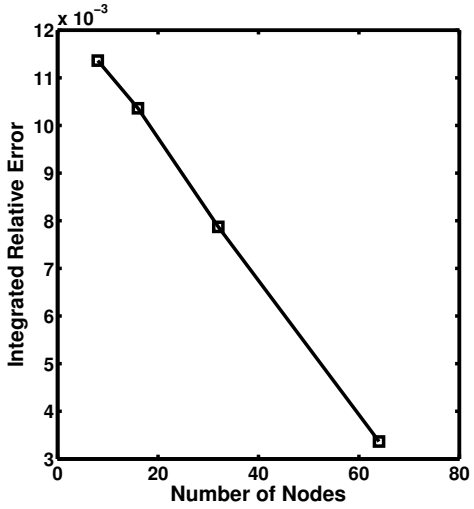

Figure 5.37: Integrated relative error versus the number of nodes in the spatial grid. Errors are calculated relative to the solution with 128 nodes.

error term is used, similar to that used in chapter 2:

$$\varepsilon_{integrated} = \frac{\int_0^{t_{LRO}} (P(t) - P_{ref}(t))dt}{\int_0^{t_{LRO}} P_{ref}(t)dt} \tag{5.101}$$

This will be referred to as the integrated relative error. Due to the adaptive time integration method data are not available at identical time points. Therefore in each case the $P(t)$ data will be interpolated onto the t_{ref} vector using cubic splines.

The results of this analysis for varying the number of nodes in the spatial grid are shown in figure 5.36 and 5.37. The number of nodes was varied by powers of 2: 8, 16, 32, 64, 128. These plots show how values of $\varepsilon_{integrated} < 0.01$ can be achieved with a relatively small number of nodes, and a value of 32 is sufficient for most purposes. At lower numbers of nodes, large differences are visible at the end of the test, with relative pressure errors of almost 10%.

The results for varying the number of moments are shown in figure 5.38 and 5.39.

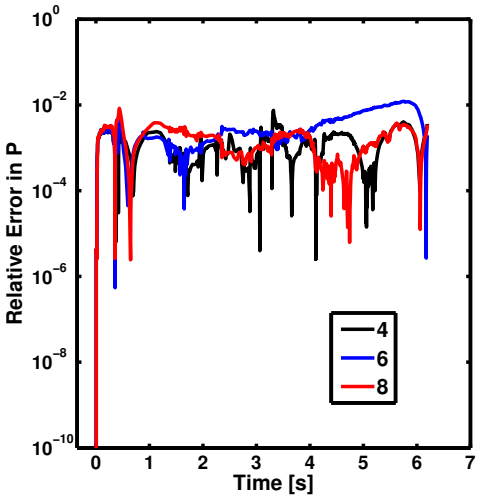

Figure 5.38: Relative error in pressure versus time. The different curves correspond to different solutions with different numbers of moments (and hence weights and abscissas). Errors are calculated relative to the solution with 10 moments.

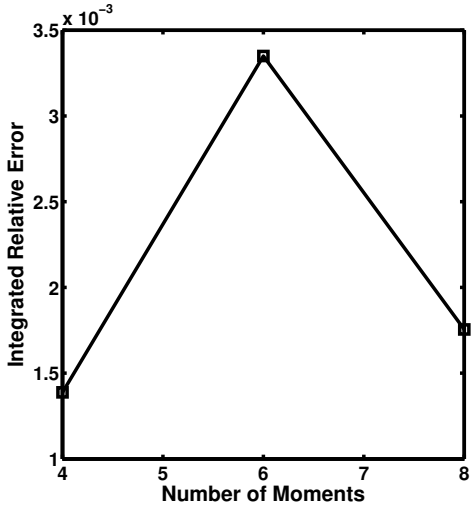

Figure 5.39: Integrated relative error versus the number of moments used in the model. Errors are calculated relative to the solution with 10 moments.

Recall that there must be an even number of moments to satisfy the basic Gauss quadrature relations (equation (5.17)). Additionally, at least 4 moments are needed so that μ_3, the bubble volume fraction, can be tracked. Therefore here the number of moments is varied from 4 to 10. A higher number of moments was attempted but caused the $\mathbf{A}$ matrix in equation (5.19) to become too ill-conditioned for a stable solution. The results show that 4 moments is sufficient to resolve the 10 moment solution such that $\varepsilon_{integrated} \simeq 10^{-3}$, which is adequate for most applications. Typically in the literature DQMOM is used with 6 or fewer moments.

The results for varying the time integration tolerance are shown in figure 5.40 and 5.41. The time integration tolerance can be viewed as a proxy for the time step size. Previously a value of 10^{-3} was used and these plots demonstrate that this produces a pressure time history that is accurate (when compared to the 10^{-6} solution) enough to reduce $\varepsilon_{integrated}$ to 10^{-2}. Of the factors studied here, this is

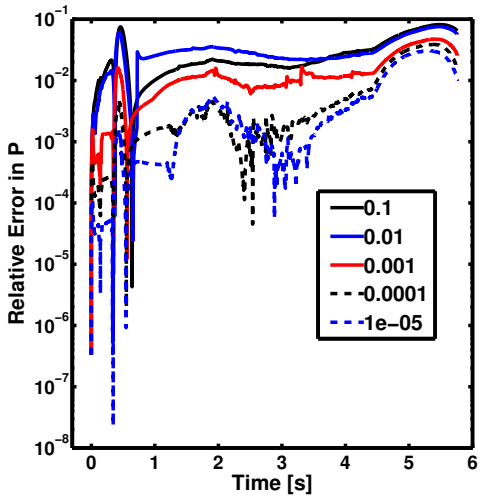

Figure 5.40: Relative error in pressure versus time. The different curves correspond to different relative error tolerances used in the time integration scheme. Errors are calculated relative to the solution with a tolerance of 10^{-6}.

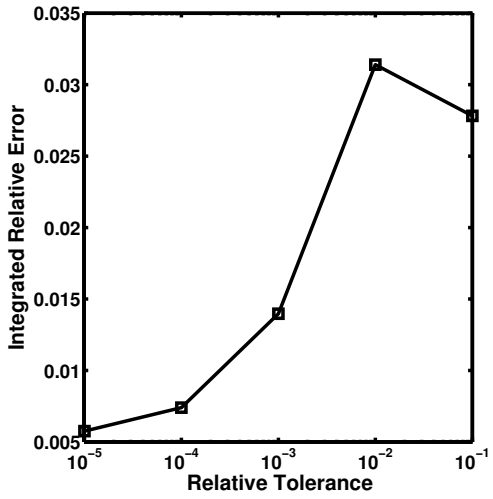

Figure 5.41: Integrated relative error versus the relative error tolerance for the time integration scheme. Errors are calculated relative to the solution with a tolerance of 10^{-6}.

the largest source of error however it is still much less than the error of the model relative to the experimental data. Decreasing the integration tolerance to finer values greatly increases the computational cost of the model. Therefore, the relatively loose tolerance of 10^{-3} should still be sufficient for practical applications.

The results for varying the number of nodes in the wall are shown in figure 5.42 and 5.43. Previously, a value of 32 was used, and these plots demonstrate that this produces a pressure time history that is accurate (when compared to the 128 node solution) enough to reduce $\varepsilon_{integrated}$ to $3 \cdot 10^{-3}$. The value of 32 makes the error resulting from this discretization lower than that of other sources and therefore there is no benefit to reducing it further. Also note that increasing the number of nodes in the wall will help suppress the oscillations shown in figures 5.33 and 5.34 but this clearly does not significantly affect the overall results of the model, at least in terms of the pressure.

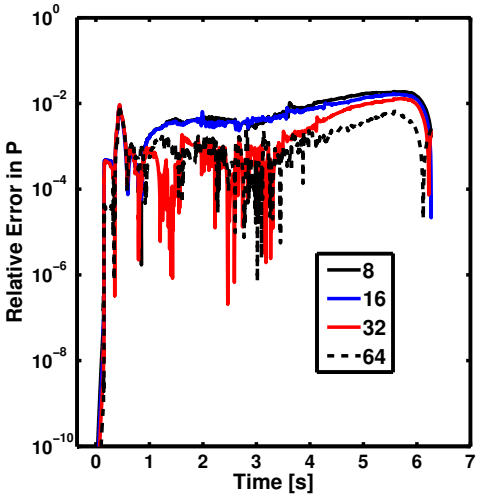

Figure 5.42: Relative error in pressure versus time. The different curves correspond to different solutions with different numbers of nodes in the wall. Errors are calculated relative to the solution with 128 nodes.

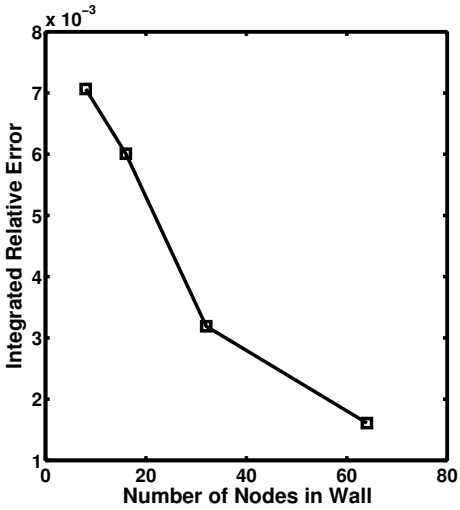

Figure 5.43: Integrated relative error versus the number of nodes in the wall. Errors are calculated relative to the solution with 128 nodes.

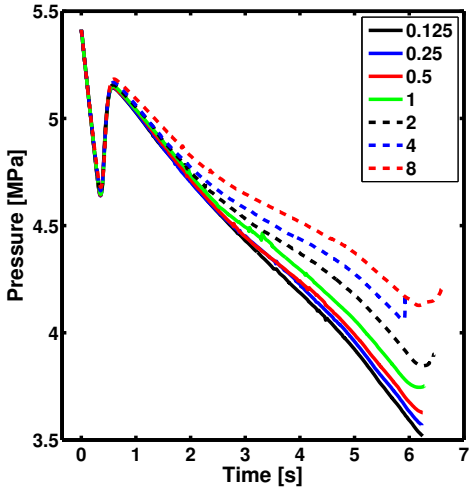

Figure 5.44: Pressure time histories for various values of $C_{\dot{Q}_{lw}}$. Value in the legend notes the scaling factor applied to the nominal value of $2 \cdot 10^{-5}$.

5.7.2 Adjustable Constants

The effect of variations in the adjustable parameters mentioned in the discussion of the submodels is now studied. Each of these will be varied by factors of 1/8, 1/4, 1/2, 2, 4, and 8, relative to the nominal values shown in table 2.4.

The heat transfer rate from the wall into the liquid, controlled by $C_{\dot{Q}_{lw}}$, is varied first. The value used in the model results presented earlier was $2 \cdot 10^{-5}$, and so here it is varied as: $2.5 \cdot 10^{-6}$, $5 \cdot 10^{-6}$, 10^{-5}, $2 \cdot 10^{-5}$, $4 \cdot 10^{-5}$, $8 \cdot 10^{-5}$, and $1.6 \cdot 10^{-4}$. The resulting pressure time histories are shown in figure 5.44. As $C_{\dot{Q}_{lw}}$ is increased, the pressure time history also increases.

The explanation here is relatively simple: CO_2 has a vapor pressure that is quite sensitive to temperature, and as additional heat is added the pressure is driven up rapidly. The fact that $C_{\dot{Q}_{lw}} \ll 1$ makes physical sense once the experimental setup that was used to generate the expression used in this model is recalled. That was a small diameter ($8mm$) heated horizontal tube in a large pool of liquid. Natural convection cells would help to establish a large heat transfer rate in that system, and would continuously supply the tube with a high flow rate of subcooled liquid.

Next, the constant controlling coalescence is varied. In actuality there are three

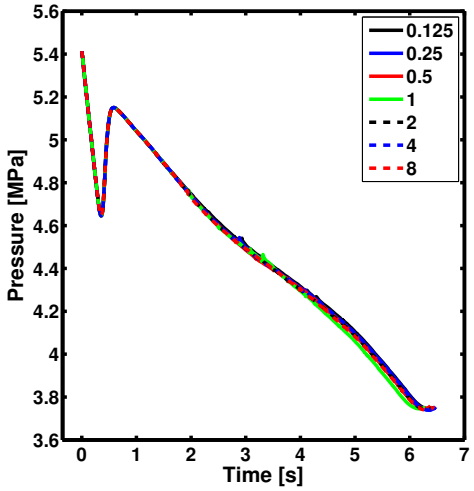

Figure 5.45: Pressure time histories for various values of $C_{collision\ efficiency}$. Value in the legend notes the scaling factor applied to the nominal value of 0.1.

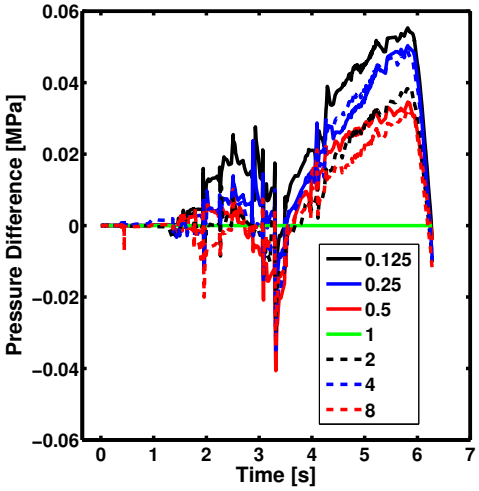

Figure 5.46: Difference in pressure versus time. Each curve is for the difference in the pressure time history, relative to that with $C_{collision\ efficiency} = 0.1$. Value in the legend notes the scaling factor applied to the nominal value of 0.1.

parameters but here only $C_{collision\ efficiency}$ is varied because it has the most significant effect and it also directly multiplies all three contributors to coalescence. The nominal value was 0.1, and so here the values 0.0125, 0.025, 0.05, 0.1 0.2 0.4, 0.8 are used. The results are shown in figures 5.45 and 5.46. The first shows the different pressure time histories obtained and the second plot simply shows the difference in pressure relative to the curve produced with $C = 0.1$ to help visualize the differences since they are relatively small.

Now the nucleation rate is varied via $C_{nucleation\ rate}$. In the previous plots its value was $1 \cdot 10^{-8}$, now it is varied as $1.25 \cdot 10^{-9}$, $2.5 \cdot 10^{-9}$, $5 \cdot 10^{-9}$, 10^{-8}, $2 \cdot 10^{-8}$, $4 \cdot 10^{-8}$, and $8 \cdot 10^{-8}$. The results are shown in figures 5.47 and 5.48. $C_{nucleation\ rate}$ has the most effect in the transient regime where it controls the magnitude and length of the initial pressure drop and recovery. It does not affect the rate at which pressure drops or increases, but merely the starting and ending points.

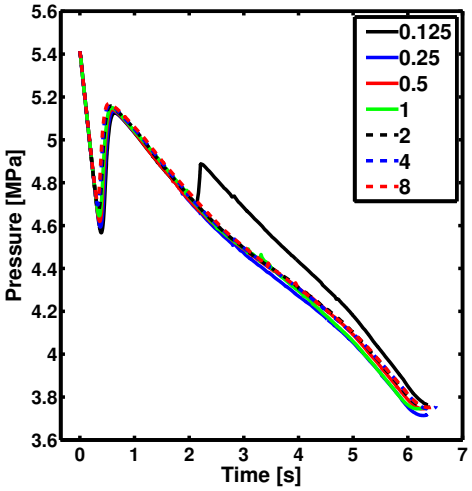

Figure 5.47: Pressure time histories for various values of $C_{nucleation\ rate}$. Value in the legend notes the scaling factor applied to the nominal value of 10^{-8}.

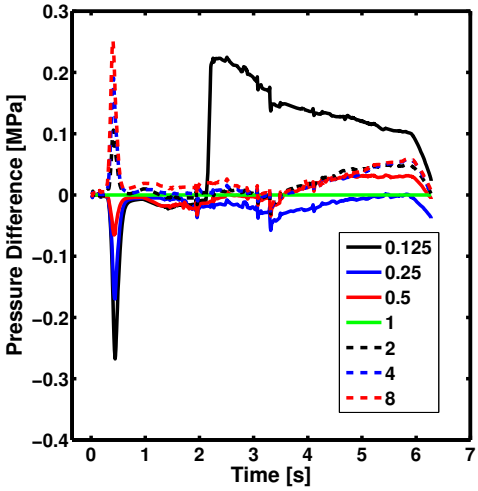

Figure 5.48: Difference in pressure versus time. Each curve is for the difference in the pressure time history, relative to that with $C_{nucleation\ rate} = 10^{-8}$. Value in the legend notes the scaling factor applied to the nominal value of 10^{-8}.

An interesting phenomenon is visible in the solution for $1.25 \cdot 10^{-9}$ with a large sudden jump in pressure at $t = 2\ s$. This is a numerical phenomenon and has no physical cause. At each time step a nonlinear equation is solved in order to calculate the pressure from the mass and energy contained in the liquid and ullage, equation (2.38). From time to time, the nonlinear equation solver converges on an incorrect root and a sudden change in pressure results. This behavior can usually be prevented by using a tighter time integration tolerance however it is rare enough that the computational cost induced by tighter tolerances is not offset by the benefit.

5.8 Summary and Conclusions

In this chapter, a new model for self-pressurizing propellant tank dynamics has been proposed. Insight gained from the experiments in the previous chapter led to the

development of a hybrid 0-D/1-D model that uses a lumped approach for the fluid properties and a 1-D grid for bubble properties.

The 0-D method is similar to that of previous researchers except that the ullage was assumed to be a two phase mixture, rather than simply saturated vapor. Conservation of mass and energy were then used to derive a set of 4 ordinary differential equations that could be used to find the mass and energy (or temperature) of each node with time.

The 1-D method employs population balance modeling techniques to describe the bubble population as a function of time as well as vertical location within the tank. This is done by developing a set of partial differential equations for the parameters that approximate the bubble size distribution, a technique known as the direct quadrature method of moments (DQMOM).

Numerous submodels were needed to determine physical quantities related to bubble dynamics, heat transfer rates, and critical flow through the orifice. This resulted in a set of adjustable constants within the model that must be fit using experimental data.

The model was then compared with experimental data and produced accurate results, although there are areas of deviation. Studies showing the effect of various model parameters have also been presented to justify the values used.

Chapter 6

Summary, Conclusions, and Suggestions for Future Work

6.1 Summary and Conclusions

In the field of hybrid rockets, self-pressurized N_2O is a popular choice for an oxidizer. However, there is no robust and accurate model for thy dynamics of a self-pressurized tank and therefore motor performance predictions are difficult. Fundamentally, there is a lack of knowledge about the physical phenomena that occur within such a tank.

This was demonstrated in chapter 2, where the three existing models in the literature were examined in detail. This includes the equilibrium model, the model of Zilliac & Karabeyoglu, and the model of Casalino & Pastrone. Each of these models the tank using a 0-D or lumped approach whereby the liquid and ullage are each represented by a single node with averaged properties. Conservation of mass and energy are then used to derive a set of ordinary differential equations that can be integrated with time to give the system evolution.

Pressure time histories were used to compare these models with one another as well as to several sets of experimental data. The Zilliac & Karabeyoglu model performed the best in 5 of the 6 test cases but is limited by its complexity and its requirement of an empirical factor that is system-dependent. The equilibrium model did not capture the initial transient behavior and often over-predicted the pressure but is the simplest

model and requires properties at saturation only. The Casalino & Pastrone model is a compromise between the two but did not perform well here, possibly due to differences in sources for thermodynamic properties.

Overall, the models have insufficient accuracy for many design purposes. Additionally, there is a wide variation in the accuracy of a given model from one system to another. Each of these models made very different assumptions about the basic heat and mass transfer phenomena within a tank, and their performance suggests that the correct foundation for a tank model remains elusive. Therefore a series of visualization experiments were conducted.

To identify the physical phenomena within a self-pressurized propellant tank, several experimental systems were developed that included optical access to the interior of the tank. This allowed for visualization of the fluid and identification of boiling, condensation, and the liquid level. An array of temperature sensors were also included within the tank although tests determined that invasive temperature probes are unreliable in a fluid that may be condensing or boiling.

Initially as the liquid begins to drain out of the tank the ullage rapidly expands, briefly becoming subcooled before condensing and establishing phase equilibrium and continuing its expansion. The liquid becomes significantly superheated and eventually begins to boil, generating a large population of bubbles in the liquid. As the bubble population grows in size and number the volume recompresses the tank, causing an increase in pressure.

In later times the liquid and vapor remain largely unchanged in general character and composition. At this point the bubble population has reached an approximately constant value, with a balance between new bubbles being nucleated in the liquid and older bubbles reaching the free surface. This implies an approximately constant level of superheat and drives the transfer of heat and mass to the ullage, in turn establishing a region of pure vapor near the liquid level while the vapor throughout the ullage continues to condense. As energy is absorbed from the liquid to produce the phase change, the temperature of the liquid and the system pressure steadily drop.

Further testing was conducted in order to examine the effect of parameter variations on this overall picture. This includes variations in fill level, flow rate, temperature, feed system configuration, and initial bubble population. Tests were also conducted in vessels of differing sizes to assess scaling effects. The fundamental features were unchanged by many these parameter variations. Temperature had perhaps the largest effect, dramatically altering the transient regime if the mean temperature or the temperature field were altered.

A thorough experimental comparison was done between CO_2 and N_2O. The purpose was to prove that CO_2 can be used as an accurate simulant for N_2O whenever cold flow testing is required. CO_2 does not possess N_2O's decomposition risk, meaning it is much safer for personnel to work with. In addition, N_2O is a strong greenhouse gas and cold flow testing typically involves venting large volumes to the environment. Testing with the two fluids showed that no real differences in behavior were evident over a range of system parameters. Tests were also compared in vessels of different size.

These experimental results were used to develop a new model that focused on capturing the bubble population within the liquid. To this end, a hybrid 0-D/1-D model was proposed that described the traditional fluid properties such as temperature or density using lumped nodes, but discretized the liquid in the vertical direction in order to describe the spatial variation in the bubble population.

This was accomplished using the direct quadrature method of moments, whereby the bubble size distribution is approximated by a discrete set of weights and abscissas. Then a set of partial differential conservation equations for these weights and abscissas is used to determine their evolution with time. This method was coupled with the 0-D nodes describing the fluid properties as well as a transient heat conduction routine to determine the temperature profile within the tank wall.

In order to complete the model, numerous submodels were needed for bubble nucleation, growth, coalescence, translation, wall heat transfer, and exit flow through an orifice. These models were either taken from the literature or published experimental data were used to develop fits. A handful of adjustable constants were needed to apply these models and fits.

Results of this model were compared to data from the visualization experiments and showed good agreement, although some deviations were noted. A set of studies evaluating the effect of various model parameters were presented in order to justify choices of the adjustable submodel constants. The various numerical parameters needed to discretize the system in time, space, and bubble size were evaluated to determine relative errors from each.

6.2 Recommendations

Recommendations are made in this section for current operations, as well as future research efforts in experiments or modeling.

6.2.1 Current Operations

Experiments in this work have shown how the system dynamics can change significantly due to small variations in initial condition. For this reason, any vehicles using self-pressurized N_2O should use temperature instrumentation to determine the temperature field inside their tank prior to starting a cold flow, hot fire test, or flight. Changes to the feed system or propellant loading procedure can also affect the dynamics even if the temperature field within the tank is the same, as evidenced by the tests presented with different initial bubble populations or feed line lengths. If this instrumentation is not practical due to cost, weight, size, or other reasons then extreme care must be used in creating a repeatable initial condition.

If modeling the system is to be attempted, there is a clear trade off between complexity and accuracy. While the proposed model is more accurate than previous works, it is significantly more complex and has much higher computational cost. If this model is not used, the model of Zilliac & Karabeyoglu is recommended if the factor E is known. Otherwise the equilibrium model should be used. If the time scale of the system is very large, the equilibrium model becomes more accurate and thus propulsion systems with long burn times may find it the best choice.

Any systems using helium, oxygen, or another fluid in addition to N_2O should

carefully select a method for adding the second component. This includes systems that only seek to pressurize the N_2O and those that wish to turn the liquid into a two-component mixture. Given that there is no easy way to measure the concentration field of the second component, significant testing must be performed to develop an indirect measure of it.

Cold flow tests can be done with CO_2 as a means to reduce costs and environmental, fire, and explosion hazards. Tank and injector tests with CO_2 and N_2O show very similar dynamics and accurate equations of state can be used to correct for the difference in fluid properties.

6.2.2 Future Experiments

If a new experimental setup were designed without any visualization capability, several other measurements would be possible. First, in such a case the tank wall would likely be much thinner and surface temperature measurements would be possible. This was attempted with the flat glass gauge, but the heavy wall (14 mm) and relatively small size combined to make the outside surface temperature change little during the test. If the surface temperature could be measured and it showed more variation during the test it could be used to check the various wall heat transfer submodels within a tank model. For example, this could be used to fix $C_{\dot{Q}_{lw}}$ within this model.

A second benefit of thinner walls is a lighter tank. This would enable a simple weight measurement by supporting the tank on load cells or suspending it from one. These options were not possible with the visualization setups described here because their static weight far exceeded the change in weight as the tank emptied, making any weight measurements impossible. For example, in the quartz tube system the mass changed by about 140 g during a test but the relevant part of the system had a mass of 30 kg.

Without visualization, the fill level is not easily measurable. If an array of temperature sensors is included, this could be used in combination with the weight measurement to determine the fill level by using the measured temperature and pressure to calculate the density field.

Scaling effects were examined in this work, but both of the vessels used were relatively small compared to practical systems. Therefore a larger vessel that included some visualization capability would be useful to see if the results from this work extend to larger sizes or if there are any new physical phenomena that occur.

A discussion was given in chapter 3 about the difficulties in measuring the time-varying temperature field within the test vessel. Therefore the actual temperature field within the tank is still unknown and this presents another opportunity for future work. Optical methods, such as absorption spectroscopy, are likely the best method as they are non-invasive and therefore wouldn't suffer from the same problems as immersed temperature probes.

For any rocket propulsion system, an obvious area of concern is the effect of acceleration. To date, only one comparison has been made between ground test data and flight data, using data of Prince et al [49] and shown in chapter 2. These data show very similar pressure time histories for the two cases, however the data were sampled at a low rate and few system parameters were accurately measured, such as the initial fill level or temperature. Therefore, the effect that accelerations other than 9.81 m/s^2 is an unknown. Obviously this is also a difficult effect to measure, and a number of flight tests would most likely be needed, preferably with a heavily-instrumented tank.

In chapter 4, some data were presented with CO_2 and N_2 showing the possible dynamics when a second component is added. There is much room for additional tests of these types at different temperatures, pressures, concentrations of the second component, and concentration profiles. This is of course in addition to the other test parameters such as flow rate, fill level, and others. The components should also be varied, including helium, oxygen, carbon monoxide, and other fluids. A comparison of N_2O and CO_2 in this respect may also be interesting as the Henry's Law constants and diffusion constants for the two fluids may be quite different.

Another effect that was not studied in this system is the effect of impurities in the propellant. This could take two forms: particulates could be added to the tank as an analog for dust or debris that may enter a real propellant tank during manufacturing, transportation, or use. These particulates could act as nucleation sites and alter the

dynamics of the heterogeneous nucleation observed in the transient regime. Secondly, if the fluid itself was not pure but contained non-negligible traces of other fluids it may begin to behave as a multicomponent mixture. These additional components would likely be different than the components studied in practical applications such as helium or oxygen.

6.2.3 Future Modeling Efforts

The proposed model is a hybrid 0-D/1-D where the fluid properties use a lumped node or 0-D grid, while the bubble distribution uses a 1-D grid within the liquid. Experimental evidence has shown the impact of a non-uniform initial temperature profile, yet this model is incapable of capturing it. If the model were extended to be truly 1-D, with fluid properties also changing in the axial direction, it would be capable of capturing more physical phenomena.

It was mentioned earlier in chapter 2 that different sources of data on N_2O properties often conflict and sometimes by quite large amounts. Therefore, a useful modeling exercise would be to compare model results with several different equations of state or empirical correlations used to calculate the numerous fluid properties needed for the tank model.

Multicomponent experiments were performed but there was no attempt made to model this situation. Adding a second component to the model would be complex but it is a tractable problem that would be applicable for the many systems that propose using N_2O mixed with other fluids.

The proposed model of this work assumes a purely cylindrical tank, while practical tanks typically have hemispherical ends. This would be a relatively minor change to the model, only modifying the volume and surface area of the grid cells within the hemispherical end.

A wide variety of submodels have been taken from the literature and implemented within the proposed model. In some cases a large number of models exist in the literature (eg bubble nucleation) and a variety of these could be compared to see if a better overall model can be obtained.

An explicit time integration method was used in this model. It is well known that implicit methods are much more stable although they are often computationally more complex, requiring many iterations at each time step to converge on a solution. This model could be implemented with an implicit scheme, possibly achieving lower overall computational cost by allowing for larger time steps without introducing instabilities.

Bubbles were assumed to translate only due to buoyancy forces. However bubbles are also known to diffuse within a liquid. Diffusion can be incorporated into DQMOM at the cost of increasing complexity.

Appendix A

Test Parameters

Various parameters from each test presented in this thesis are given in table A.1. While the test number is provided in table A.1, these values were not used in this thesis and are merely a reference for the author.

Table A.1: Test parameters table.

Test Number	Section	Title	System	Fluid	Orifice Diameter [mm]	Fill Level [%]	$\overline{T_i}$ [$^{\circ}C$]	t_{LRO} [s]	P_i [MPa]	P_{LRO} [MPa]	P_{min} [MPa]	$P_{n,min}$	t_{min} [s]	$t_{n,min}$	P_{max} [MPa]	$P_{n,max}$	t_{max} [s]	$t_{n,max}$
13	Basic Behavior		Quartz	CO_2	0.8128	90.9	18.52	7.153	5.545	3.742	4.906	0.6454	0.4235	0.0539	5.226	0.8229	0.877	0.1116
94	Flow	Slow	Quartz	CO_2	0.2794	85.3	10.06	73.459	4.466	3.530	4.313	0.8358	0.7588	0.0103	4.342	0.8673	1.918	0.0260
99	Rate	Fast	Quartz	CO_2	1.3208	84.6	10.11	3.041	4.461	2.880	3.835	0.6041	0.1471	0.0425	4.023	0.7226	0.482	0.1392
13	Fill	91%	Quartz	CO_2	0.8128	90.9	18.52	7.153	5.545	3.742	4.906	0.6454	0.4235	0.0539	5.226	0.8229	0.877	0.1116
15	Level	70%	Quartz	CO_2	0.8128	72.0	19.16	5.812	5.554	3.916	4.982	0.6507	0.5941	0.0870	5.146	0.7509	1.071	0.1568
133	Elevated	Ambient	Quartz	CO_2	0.8128	81.5	18.27	6.600	5.518	3.769	4.908	0.6513	0.8647	0.1242	5.063	0.7400	1.824	0.2619
128	Temperature	Hot	Quartz	CO_2	0.8128	81.3	24.15	6.200	6.215	4.269	5.773	0.7728	0.3471	0.0532	5.799	0.7862	0.671	0.1027
48	Reduced	Ambient	Quartz	CO_2	0.5588	83.0	16.20	14.147	5.205	3.685	4.820	0.7469	0.8941	0.0605	4.896	0.7968	2.071	0.1401
229	Temperature	Cold	Quartz	CO_2	0.5588	83.4	-8.15	19.488	2.821	2.160	2.610	0.6804	0.9294	0.0470	2.683	0.7915	2.282	0.1154
197	Temperature	Uniform	Quartz	CO_2	0.5588	87.5	19.83	14.635	5.711	4.008	5.304	0.7610	0.8647	0.0579	5.469	0.8579	2.006	0.1343
46	Stratification	Top Hot	Quartz	CO_2	0.5588	86.5	19.38	14.218	5.947	3.819	4.850	0.4843	2.6180	0.1762	4.970	0.5411	3.453	0.2324
199		Bottom Cold	Quartz	CO_2	0.5588	89.7	19.87	14.441	5.812	3.986	5.314	0.7276	0.7941	0.0538	5.526	0.8433	1.382	0.0936
47	Initial Bubble	Flat	Quartz	CO_2	0.5588	71.0	17.42	11.865	5.142	3.734	4.820	0.7713	0.6118	0.0486	4.852	0.7937	1.241	0.0985
204	Population	Bubbly	Quartz	CO_2	0.5588	70.6	19.40	11.918	5.571	3.997	5.035	0.6597	1.4290	0.1166	5.144	0.7286	2.659	0.2169
273	Feed System	0 cm	Quartz	CO_2	0.5588	83.2	20.59	14.165	5.707	4.004	5.202	0.7035	1.3940	0.0959	5.305	0.7639	2.635	0.1812
270	Length	24 cm	Quartz	CO_2	0.5588	83.7	20.01	14.347	5.594	3.923	5.152	0.7355	1.2410	0.0837	5.244	0.7903	2.424	0.1636
272		52 cm	Quartz	CO_2	0.5588	83.0	20.65	14.565	5.693	3.977	5.066	0.6347	0.4353	0.0291	5.398	0.8280	1.088	0.0727
262	Orifice	Flat	Quartz	CO_2	1.0922	80.9	18.47	3.753	5.484	3.602	4.756	0.6134	0.4765	0.1181	4.995	0.7402	0.841	0.2085
264	Geometry	Round	Quartz	CO_2	1.0008	83.0	18.84	4.241	5.465	3.626	4.749	0.6105	0.5000	0.1123	5.023	0.7600	0.847	0.1902
135	Valve	Fast	Quartz	CO_2	0.8128	79.2	17.18	6.435	5.323	3.613	4.624	0.5909	0.8235	0.1220	4.778	0.6812	1.924	0.2849
139	Opening Time	Slow	Quartz	CO_2	0.8128	82.0	19.25	6.635	5.561	3.755	4.867	0.6159	1.2820	0.1822	5.015	0.6975	1.941	0.2759
124	Vessel	Quartz	Quartz	CO_2	0.8128	80.0	18.75	6.553	5.428	3.696	4.763	0.6157	0.5824	0.0838	4.979	0.7410	1.253	0.1804
257	Size	Glass Gauge	Glass Gauge	CO_2	2.2606	82.5	17.56	5.944	5.402	3.829	4.813	0.6256	0.7111	0.1123	5.022	0.7586	1.378	0.2176
101	Exotic	High Flow Rate	Quartz	CO_2	6.35	84.0	11.99	0.618	4.577	1.278	3.128	0.5606	N/A	0.1049	3.324	0.6200	0.194	0.2037
40	Conditions	Near-Critical	Quartz	CO_2	0.8128	83.6	29.52	5.382	7.058	4.936	7.058	N/A	N/A	N/A	7.058	N/A	N/A	N/A
29		Supercritical	Quartz	CO_2	0.8128	N/A	34.29	4.782	7.851	5.212	7.851	N/A	N/A	N/A	7.851	N/A	N/A	N/A
273	N_2O	CO_2	Quartz	CO_2	0.5588	83.2	20.59	14.165	5.707	4.004	5.202	0.7035	1.3940	0.0959	5.305	0.7639	2.635	0.1812
275	vs CO_2	N_2O	Quartz	N_2O	0.5588	83.3	20.39	14.600	5.004	3.584	4.616	0.7271	0.9824	0.0655	4.713	0.7951	2.271	0.1513
281	N_2O Elevated	Ambient	Quartz	N_2O	0.8128	82.8	19.54	7.171	4.937	3.385	4.331	0.6095	0.8588	0.1150	4.468	0.6978	2.071	0.2772
287	Temperature	hot	Quartz	N_2O	0.8128	82.7	28.45	6.388	6.103	4.131	5.533	0.7106	N/A	N/A	5.554	0.7216	N/A	N/A
171	Geysering	CO_2	Quartz	CO_2	1.0922	83.2	9.07	4.347	4.546	2.930	3.619	0.4264	0.8235	0.1724	3.810	0.5446	1.841	0.3855
279		N_2O	Quartz	N_2O	1.3208	83.4	10.75	3.247	4.251	2.657	3.247	0.3703	0.9294	0.2620	3.365	0.4445	1.588	0.4477
257	N_2O	CO_2	Glass Gauge	CO_2	2.2606	82.5	17.56	5.944	5.402	3.829	4.813	0.6256	0.7111	0.1123	5.022	0.7586	1.378	0.2176
289	vs CO_2	N_2O	Glass Gauge	N_2O	2.2606	82.7	19.12	5.922	5.045	3.609	4.409	0.5575	0.8000	0.1259	4.646	0.7220	1.511	0.2377
212	Multicomponent	Pure	Quartz	CO_2	0.5588	72.1	18.02	13.006	6.526	3.811	4.829	0.3751	2.5590	0.1913	4.873	0.3913	3.612	0.2700
215		Dissolved	Quartz	CO_2	0.5588	82.4	11.50	14.459	7.004	3.721	4.850	0.3438	2.7530	0.1870	4.867	0.3490	3.729	0.2533
218		Uniform	Quartz	CO_2	0.5588	93.4	14.26	11.347	8.853	5.227	7.886	0.7334	1.4880	0.1281	7.941	0.7487	1.600	0.1377
219		Layered	Quartz	CO_2	0.5588	94.9	14.73	13.129	8.686	4.598	7.043	0.5980	1.1240	0.0836	7.217	0.6406	1.271	0.0945

Appendix B

dV/dt Expression

This is the relation described in chapter 5, specifically equation (5.8). It was derived using symbolic mathematical manipulation software (Mathematica). We begin by defining two values for convenience:

$$C_5 = \frac{u_{vap} - u_{liq}}{\left.\frac{\partial \rho}{\partial x}\right|_P} \tag{B.1}$$

$$C_4 = \left(x \left.\frac{du_{vap}}{dT}\right|_{sat} + (1-x) \left.\frac{du_{liq}}{dT}\right|_{sat} - \frac{C_5}{\left.\frac{\partial \rho}{\partial P}\right|_x \left.\frac{dP}{dT}\right|_{sat}} \right) \tag{B.2}$$

and now two larger ones:

$$\begin{aligned} C_6 = V_{liq} \Bigg(\Bigg(& c_{v,liq} \left.\frac{dP}{dT}\right|_{sat} m_{liq} \left(\frac{dU^*_{tg}}{dt} - \frac{dm_{tg}}{dt} u_{tg} + P \frac{dV_{bub}}{dt} \right) V_{liq} + \\ C_4 m_{tg} \Bigg(& -c_{v,liq} \frac{dm_{liq}}{dt} \left.\frac{\partial P}{\partial rho}\right|_{liq} m_{liq} + \frac{dm_{liq}}{dt} \left.\frac{\partial P}{\partial T}\right|_{liq} \left.\frac{\partial u}{\partial \rho}\right|_{liq} m_{liq} - \\ & \left.\frac{\partial P}{\partial T}\right|_{liq} \frac{dU^*_{liq}}{dt} V_{liq} + \frac{dm_{liq}}{dt} \left.\frac{\partial P}{\partial T}\right|_{liq} u_{liq} V_{liq} \Bigg) \Bigg) V_{tg}^2 - \\ & C_5 c_{v,liq} \left.\frac{dP}{dT}\right|_{sat} m_{liq} m_{tg} V_{liq} \left(m_{tg} \frac{dV_{bub}}{dt} + \frac{dm_{tg}}{dt} V_{tg} \right) \Bigg) \end{aligned} \tag{B.3}$$

and

$$C_7 = C_5 c_{v,liq} \left.\frac{dP}{dT}\right|_{sat} m_{liq} m_{tg}^2 V_{liq}^2 - \left(C_4 \left(c_{v,liq} \left.\frac{\partial P}{\partial \rho}\right|_{liq} - \left.\frac{\partial P}{\partial T}\right|_{liq} \left.\frac{\partial u}{\partial \rho}\right|_{liq} \right) m_{liq}^2 m_{tg} + \left(c_{v,liq} \left.\frac{dP}{dT}\right|_{sat} m_{liq} + C_4 \left.\frac{\partial P}{\partial T}\right|_{liq} m_{tg} \right) P V_{liq}^2 \right) V_{tg}^2 \tag{B.4}$$

Where we have defined for convenience:

$$\begin{aligned} \frac{dU_{liq}^*}{dt} &= \frac{dU_{liq}}{dt} + P\frac{dV_{liq}}{dt} \\ \frac{dU_{tg}^*}{dt} &= \frac{dU_{tg}}{dt} + P\frac{dV_{tg}}{dt} \end{aligned} \tag{B.5}$$

These terms are useful because they do not include the $\frac{dV}{dt}$ terms. (Recall that $\frac{dU_{liq}}{dt}$ and $\frac{dU_{vap}}{dt}$ each contain a $-P\frac{dV}{dt}$ term). Now, the final result is simply

$$\frac{dV_{liq}}{dt} = \frac{C_6}{C_7} \tag{B.6}$$

Appendix C

Overview of the Direct Quadrature Method of Moments

In this appendix, a brief overview of population balance equations and in particular the direct quadrature method of moments (DQMOM) is given. The fundamental derivation of population balance equations is taken from Ramkrishna [116], and much of the derivation of DQMOM is taken from Marchisio and Fox [86].

The basic concept of population balances is to introduce a population of particles (solid, liquid, or gas) into a fluid flow. These particles may be described by a coordinate space with dimensions such as size, age, mass, composition, or any other parameter that differentiates one particle from another. This is referred to as the internal coordinate space, and particle's position in the environment is described using external coordinates (eg x, y, z). The external and internal coordinates can be written as vectors as $\vec{x}$ and $\vec{r}$, respectively.

If the number density of particles with internal coordinates $\vec{x}$ and location $\vec{r}$ is now introduced as $f_1(\vec{x}, \vec{r})$, the number of particles in the physical volume dV_r and with internal coordinates that lie in the internal volume dV_x is $f_1(\vec{x}, \vec{r})dV_r dV_x$. In another sense, f_1 can be thought of as the particle distribution function. The total number of particles in a unit volume of physical space can be written as

$$N(\vec{r}) = \int f_1(\vec{x}, \vec{r})dV_x \tag{C.1}$$

One can also consider the flux of particles in both physical space and internal space:

$$\begin{aligned} G_r &= f_1(\vec{x},\vec{r})\dot{\vec{R}}(\vec{x},\vec{r},\vec{Y}) \\ G_x &= f_1(\vec{x},\vec{r})\dot{\vec{X}}(\vec{x},\vec{r},\vec{Y}) \end{aligned} \tag{C.2}$$

Where $\vec{Y}$, the continuous phase vector, that contains the traditional fluid variables such as velocity, temperature, or pressure has been introduced. $\dot{\vec{R}}$ is the particle velocity in physical space while $\dot{\vec{X}}$ is the velocity in internal space, for example the growth rate.

A useful conservation equation can be derived by beginning with Leibniz's rule in three dimensions:

$$\frac{D}{Dt}\int_{V_r(t)} f_1(\vec{x},\vec{r},t)dV_r = \int_{V_r(t)} \frac{\partial f_1(\vec{x},\vec{r},t)}{\partial t}dV_r + \int_{A_r(t)} f_1(\vec{x},\vec{r},t)\dot{\vec{R}}\cdot\hat{n}_r dA_r \tag{C.3}$$

Note that a time dependence of f_1 has been included. Now, Leibniz's rule is extended into the internal space as well:

$$\begin{aligned} \frac{D}{Dt}\int_{V_r(t)}\int_{V_x(t)} f_1(\vec{x},\vec{r},t)dV_x dV_r = &\int_{V_r(t)}\int_{V_x(t)} \frac{\partial f_1(\vec{x},\vec{r},t)}{\partial t}dV_x dV_r \\ &+ \int_{A_r(t)}\int_{A_x(t)} f_1(\vec{x},\vec{r},t)\dot{\vec{X}}\cdot\hat{n}_x dA_x \dot{\vec{R}}\cdot\hat{n}_r dA_r \end{aligned} \tag{C.4}$$

Note that a Lagrangian control volume has been assumed. In other words, the particles can be considered to be embedded in continuum of internal and external coordinates that deforms at a rate of $(\dot{\vec{X}},\dot{\vec{R}})$. Now, Gauss' divergence theorem allows the surface integral on the right hand side to be converted into a volume integral that can be combined with the first term:

$$\frac{D}{Dt}\int_{V_r(t)}\int_{V_x(t)} f_1 dV_x dV_r = \int_{V_r(t)}\int_{V_x(t)} \left[\frac{\partial f_1}{\partial t} + \vec{\nabla}_x\cdot\dot{\vec{X}}f_1 + \vec{\nabla}_r\cdot\dot{\vec{R}}f_1\right] dV_x dV_r \tag{C.5}$$

With the Lagrangian control volume, there are no particle fluxes through the surfaces and only sources and sinks of bubbles within the control volume can affect the

total number of particles. In the field of population balance modeling, the terms birth and death are generally used to describe the generation or destruction of particles and this convention is followed here. A general birth/death term h is now defined:

$$\frac{D}{Dt}\int_{V_r(t)}\int_{V_x(t)} f_1 dV_x dV_r = \int_{V_r(t)}\int_{V_x(t)} h dV_x dV_r \tag{C.6}$$

Which can be used in the previous equation to write

$$\int_{V_r(t)}\int_{V_x(t)}\left[\frac{\partial f_1}{\partial t} + \vec{\nabla}_x \cdot \dot{\vec{X}} f_1 + \vec{\nabla}_r \cdot \dot{\vec{R}} f_1 - h\right] dV_x dV_r = 0 \tag{C.7}$$

The specific geometry of the control volume is arbitrary and so the kernel of this integral must be zero:

$$\frac{\partial}{\partial t} f_1 + \vec{\nabla}_x \cdot \dot{\vec{X}} f_1 + \vec{\nabla}_r \cdot \dot{\vec{R}} f_1 = h \tag{C.8}$$

To proceed further, there are a variety of options. The most straightforward option involves solving equation (C.8) numerically to find f_1, along with the mass, momentum, and energy equations needed to describe the fluid flow.

Another set of solution methods can be developed by recognizing that the quantities of interest to most researchers and engineers are not found in f_1 itself, but instead in various integral quantities. For example, in a gas reacting with solid particles one may wish to know the total particle surface area in a unit volume of fluid. Therefore f_1 describes the number density of particles of a certain size in the gas, and now suppose that $\vec{x}$ has only one component and that component is the particle radius. The surface area is:

$$A(\vec{r}, t) = \int_0^\infty 4\pi x^2 f_1(x, \vec{r}, t) dx \tag{C.9}$$

Where the particles have been assumed to be spherical. Note that for some internal coordinates the limits of integration may extend to $-\infty$. Other integral quantities of interest include the total number density or volume density of particles. These all

are proportional to statistical moments of the distribution f_1:

$$\mu_k(\vec{r},t) = \int_0^\infty x^k f_1(x,\vec{r},t)dx \tag{C.10}$$

Given this, it would be advantageous to derive a transport equation for these quantities, rather than the more basic f_1. This is the basis of a technique known as the method of moments. If equation (C.8) is reduced to a single internal coordinate for simplicity and then multiplied by x^k and integrated, the result is:

$$\frac{\partial}{\partial t}f_1 + \frac{\partial}{\partial x}\dot{X}f_1 + \vec{\nabla}_r \cdot \dot{\vec{R}}f_1 = h \tag{C.11}$$

$$\int x^k \frac{\partial}{\partial t}f_1 dx + \int x^k \frac{\partial}{\partial x}\dot{X}f_1 dx + \int x^k \vec{\nabla}_r \cdot \dot{\vec{R}}f_1 dx = \int x^k h dx \tag{C.12}$$

$$\frac{\partial \mu_k}{\partial t} - \int k x^{k-1}\dot{X}f_1 dx + \int x^k \vec{\nabla}_r \cdot \dot{\vec{R}}f_1 dx = \int x^k h dx \tag{C.13}$$

The second term has been integrated by parts and the quantity $f_1 x^k \dot{X}$ has been assumed to vanish at the limits of integration. This constraint is generally easily enforced because one of the three components (f_1, x, $\dot{X}$) typically vanishes as x becomes very large or very small. Equation (C.13) can be simplified further if the fluid velocity is assumed to be independent of the particle size: $\dot{\vec{R}}(x,\vec{r},t) = \dot{\vec{R}}(\vec{r},t)$:

$$\frac{\partial \mu_k}{\partial t} - \int k x^{k-1}\dot{X}f_1 dx + \vec{\nabla}_r \cdot \dot{\vec{R}}\mu_k = \int x^k h dx \tag{C.14}$$

From here, if relatively simple expressions for $\dot{X}$ and h can be found, a transport equation for the statistical moments of the distribution μ_k can be derived. These moments are then solved for in addition to the fluid dynamic variables as a function of space and time. An additional constraint is that the set of equations be closed, so that an infinite number of moments is not needed to solve the system of equations. Many systems have been found to obey these constraints and reasonable results have been obtained.

For systems that do not obey these constraints, a modification known as the quadrature method of moments can be introduced, developed by McGraw [117]. This method uses Gauss quadrature to approximate the integral quantities in equation

(C.14) and allow any expression for $\dot{X}$ to be used, and many expressions for h. The process begins with the known values of the moments μ_k at a time step and then using them to calculate the necessary weights and abscissas (w_i and x_i):

$$\begin{aligned} \mu_k &= \int x^k f_1 dx \\ &= \sum_{i=1}^{N} w_i x_i^k \end{aligned} \tag{C.15}$$

The values w_i and x_i are selected to make equation (C.15) exact. For a set of N weights and abscissas, a total of $2N$ moments can be represented $(0, 1, \ldots, 2N-1)$. Note that this requires an even number of moments to be used. Now that w_i and x_i are known, they can be used to approximate an integral quantity involving f_1, including the $\dot{X}$ term:

$$\int g(x) f_1 dx \simeq \sum_{i=1}^{N} w_i g(x_i) \tag{C.16}$$

$$\int k x^{k-1} \dot{X} f_1 dx \simeq \sum_{i=1}^{N} k x_i^{k-1} \dot{X}(x_i) \tag{C.17}$$

Where $g(x)$ is any function of x. In this way if h can be represented as $g(x)f_1$, then it too can be approximated using the weights and abscissas. This method becomes more accurate as more moments are included and the number of moments can be thought of as a grid resolution in the moment dimension.

The quadrature method has been used extensively to model systems with particulate populations, including aerosol sprays [117], gas-liquid reactors [118], and systems with crystallization and precipitation [119]. However, three significant limitations exist with this method. First, process by which the weights and abscissas are calculated from the moments, known as the product-difference method, can become inaccurate and/or computationally expensive in cases where the moments vary over many orders of magnitude [120]. Second, it is difficult to model systems where the particle velocity is strongly dependent on the internal variables [120]. Finally, QMOM cannot handle systems with multiple internal variables [86].

To solve these problems, the direct quadrature method of moments (DQMOM) was developed by Marchisio and Fox [86]. The fundamental principle of DQMOM is to use the weights and abscissas introduced by QMOM (w_i, x_i) as the transported variables instead of the moments μ_k.

To develop the DQMOM equations, one must first revisit equation (C.15) and recognize that the same result can be obtained by taking the Gauss quadrature representation of the moments and instead using it as a direct approximation of the particle distribution f_1:

$$\begin{aligned} f_1 &\simeq \sum_{i=1}^{N} w_i \delta(x - x_i) \\ \mu_k &= \int x^k f_1 dx \\ \mu_k &= \int x^k \sum_{i=1}^{N} w_i \delta(x - x_i) dx \\ &= \sum_{i=1}^{N} w_i x_i^k \end{aligned} \tag{C.18}$$

Where δ is the dirac delta function. Note that since the weights and abscissas are selected to calculate the moments exactly and bear no direct relation to f_1, there is no guarantee that the first line of equation (C.18) will produce a plot of $f_1(x)$ that in any way resembles its true value. This approximation for f_1 can then be substituted into the fundamental particle transport equation, equation (C.8). In doing so, Marchisio and Fox's notation is followed and the $\dot{X}$ term is folded into the source term h and now called S:

$$\frac{\partial}{\partial t} \sum_{i=1}^{N} w_x \delta(x - x_i) + \dot{\vec{\nabla}} \cdot \dot{\vec{R}} \sum_{i=1}^{N} w_i \delta(x - x_i) = S \tag{C.19}$$

To proceed further, index notation is introduced: $\dot{\vec{\nabla}} \cdot \dot{\vec{R}} \rightarrow \frac{\partial}{\partial r_j} \dot{R}_j$. The result is

$$\frac{\partial}{\partial t} \sum_{i=1}^{N} w_x \delta(x - x_i) + \frac{\partial}{\partial r_j} \sum_{i=1}^{N} u_{j,i} w_i \delta(x - x_i) = S \tag{C.20}$$

The derivative of $\delta(x-x_i)$ will be notated as $\delta'(x-x_i)$. The first term (time derivative) can therefore be written as:

$$\frac{\partial}{\partial t}\sum_{i=1}^{N} w_x\delta(x-x_i) = \sum_{i=1}^{N}\left(\delta(x-x_i)\frac{\partial w_i}{\partial t} + w_i\frac{\partial}{\partial t}\delta(x-x_i)\right) \tag{C.21}$$

$$= \sum_{i=1}^{N}\left(\delta(x-x_i)\frac{\partial w_i}{\partial t} - w_i\delta'(x-x_i)\frac{\partial x_i}{\partial t}\right) \tag{C.22}$$

and the second term (spatial derivative):

$$\frac{\partial}{\partial r_j}\sum_{i=1}^{N}\dot{R}_j w_i\delta(x-x_i) =$$

$$\sum_{i=1}^{N}\left[\frac{\partial \dot{R}_j}{\partial r_j}w_i\delta(x-x_i) + \dot{R}_j\left(\delta(x-x_i)\frac{\partial w_i}{\partial r_j} - w_i\delta'(x-x_i)\frac{\partial x_i}{\partial r_j}\right)\right] \tag{C.23}$$

$$= \sum_{i=1}^{N}\left[\delta(x-x_i)\left(\dot{R}_j\frac{\partial w_i}{\partial r_j} + w_i\frac{\partial \dot{R}_j}{\partial r_j}\right) - \delta'(x-x_i)w_i\dot{R}_j\frac{\partial x_i}{\partial r_j}\right] \tag{C.24}$$

$$= \sum_{i=1}^{N}\left[\delta(x-x_i)\frac{\partial w_i\dot{R}_j}{\partial r_j} - \delta'(x-x_i)w_i\dot{R}_j\frac{\partial x_i}{\partial r_j}\right] \tag{C.25}$$

Combining these:

$$\sum_{i=1}^{N}\left(\delta(x-x_i)\frac{\partial w_i}{\partial t} - w_i\delta'(x-x_i)\frac{\partial x_i}{\partial t}\right)$$

$$+\sum_{i=1}^{N}\left[\delta(x-x_i)\frac{\partial w_i\dot{R}_j}{\partial r_j} - \delta'(x-x_i)w_i\frac{\partial x_i}{\partial r_j}\right] = S \tag{C.26}$$

$$\sum_{i=1}^{N}\delta(x-x_i)\left(\frac{\partial w_i}{\partial t} + \frac{\partial w_i\dot{R}_j}{\partial r_j}\right) - \sum_{i=1}^{N}\delta'(x-x_i)\left(w_i\frac{\partial x_i}{\partial t} + w_i\dot{R}_j\frac{\partial x_i}{\partial r_j}\right) = S \tag{C.27}$$

To facilitate simplifications later on, the following term is added and subtracted:

$$x_i\delta'(x-x_i)\left(\frac{\partial w_i}{\partial t} + \frac{\partial w_i\dot{R}_j}{\partial r_j}\right) \tag{C.28}$$

Note that there appears to be an error in Marchisio and Fox's original work because this term is missing from the intermediate relations, his equations (4) and (5) but

appears in the final equation (8).

$$\begin{aligned}
&\sum_{i=1}^{N}\left[\delta(x-x_i)+x_i\delta'(x-x_i)\right]\left(\frac{\partial w_i}{\partial t}+\frac{\partial w_i\dot{R}_j}{\partial r_j}\right)\\
-\sum_{i=1}^{N}\delta'(x-x_i)&\left(w_i\frac{\partial x_i}{\partial t}+w_i\dot{R}_j\frac{\partial x_i}{\partial r_j}+x_i\frac{\partial w_i}{\partial t}+x_i\frac{\partial w_i\dot{R}_j}{\partial r_j}\right)=S\\
&\sum_{i=1}^{N}\left[\delta(x-x_i)+x_i\delta'(x-x_i)\right]\left(\frac{\partial w_i}{\partial t}+\frac{\partial w_i\dot{R}_j}{\partial r_j}\right)\\
&-\sum_{i=1}^{N}\delta'(x-x_i)\left(\frac{\partial w_ix_i}{\partial t}+\frac{\partial w_ix_i\dot{R}_j}{\partial r_j}\right)=S
\end{aligned}$$

The weighted abscissas $g_i = w_i x_i$ are now introduced and used to replace the abscissas so that this can be simplified further:

$$\begin{aligned}
&\sum_{i=1}^{N}\left[\delta(x-x_i)+x_i\delta'(x-x_i)\right]\left(\frac{\partial w_i}{\partial t}+\frac{\partial w_i\dot{R}_j}{\partial r_j}\right)\\
&-\sum_{i=1}^{N}\delta'(x-x_i)\left(\frac{\partial g_i}{\partial t}+\frac{\partial g_i\dot{R}_j}{\partial r_j}\right)=S
\end{aligned}\tag{C.29}$$

Next a_i and b_i are defined such that they become source terms in transport equations for w_i and g_i:

$$\begin{aligned}
a_i &= \frac{\partial w_i}{\partial t}+\frac{\partial \dot{R}_j w_i}{\partial r_j}\\
b_i &= \frac{\partial g_i}{\partial t}+\frac{\partial \dot{R}_j g_i}{\partial r_j}
\end{aligned}\tag{C.30}$$

In this way equation (C.29) can be simplified:

$$\sum_{i=1}^{N}\left[\left(\delta(x-x_i)+x_i\delta'(x-x_i)\right)a_i-\delta'(x-x_i)b_i\right]=S \tag{C.31}$$

This equation is now integrated across the internal coordinate to remove the δ

terms and obtain the source term S in terms of the moments:

$$\begin{aligned}\int_{-\infty}^{\infty} x^k \delta(x - x_i) dx &= x_i^k \\ \int_{-\infty}^{\infty} x^k \delta'(x - x_i) dx &= -k x_i^{k-1}\end{aligned} \tag{C.32}$$

If equation (C.31) is multiplied by x^k and integrated over x, the result is then

$$\sum_{i=1}^{N} \left[\left(x_i^k - k x_i^k \right) a_i + k x_i^{k-1} b_i \right] = \int_{-\infty}^{\infty} x^k S dx \tag{C.33}$$

$$\sum_{i=1}^{N} \left[(1-k) x_i^k a_i + k x_i^{k-1} b_i \right] = \int_{-\infty}^{\infty} x^k S dx \tag{C.34}$$

In many problems the x_i are small quantities such as particle sizes and they can also span several orders of magnitude. Then, when computing x_i^k and summing terms, round-off error can be significant. To alleviate this problem the x_i terms are scaled by $x_m = \max(x_i)$ and equation (C.34) is divided by x_m^k:

$$\sum_{i=1}^{N} \left[(1-k) \left(\frac{x_i}{x_m} \right)^k a_i + k \left(\frac{x_i}{x_m} \right)^{k-1} \frac{b_i}{x_m} \right] = \int_{-\infty}^{\infty} \left(\frac{x}{x_m} \right)^k S dx \tag{C.35}$$

$$\sum_{i=1}^{N} \left[(1-k) x_{s,i}^k a_i + k x_{s,i}^{k-1} b_{s,i} \right] = \int_{-\infty}^{\infty} x_s^k S dx_s \tag{C.36}$$

The s subscript will denote a scaled variable. Note that an extraneous x_m has been dealt with by introducing a scaled version of b_i. These modifications were developed by Fox [121]. Introducing the notation $\bar{S}_{s,k}$ as the scaled moment transform of S, the result is now

$$\sum_{i=1}^{N} \left[(1-k) x_{s,i}^k a_i + k x_{s,i}^{k-1} b_{s,i} \right] = \bar{S}_{s,k} \tag{C.37}$$

Recall that S was the summation of the flux term in the internal coordinate ($\frac{\partial}{\partial x} \dot{X} f_1$)

and the source term (h). So,

$$\begin{aligned}\bar{S}_k &= \int x^k(-\frac{\partial}{\partial x}\dot{X}f_1 + h)dx \\ &= \int x^k \left(-\frac{\partial}{\partial x}\dot{X}\sum_{i=1}^{N} w_i\delta(x-x_i) + h\right)dx\end{aligned} \tag{C.38}$$

The first part of this integral can be simplified using integration by parts just as was done with equation (C.13) to become

$$\begin{aligned}\bar{S}_k &= \int kx^{k-1}\dot{X}\sum_{i=1}^{N} w_i\delta(x-x_i) + x^k h\ dx \\ &= \sum_{i=1}^{N} kw_i x_i^{k-1}\dot{X}(x=x_i) + \int x^k h\ dx\end{aligned} \tag{C.39}$$

and with the scaling it becomes

$$\bar{S}_{s,k} = \sum_{i=1}^{N} \frac{k}{x_m} w_i x_{s,i}^{k-1}\dot{X}(x=x_i) + \int x_s^k h\ dx_s \tag{C.40}$$

Further simplification of the h term is not possible without knowledge of its functional form. If h is a function of f_1 then the integral is trivial using the Gauss quadrature approximation, equation (C.18). Otherwise one must calculate the integral of h analytically or numerically. Either way, a value of $\bar{S}_{s,k}$ can now be calculated. With this, equation (C.37) is solved in the following way for a_i and $b_{s,i}$:

$$\mathbf{A}\begin{bmatrix} a_i \\ b_{s,i} \end{bmatrix} = \begin{bmatrix} \bar{S}_{s,k} \end{bmatrix} \tag{C.41}$$

Where each matrix $\mathbf{A} = [\mathbf{A_1}\ \mathbf{A_2}]$ is built from the bracketed term in equation (C.37)

and can be written as:

$$\mathbf{A_1} = \begin{bmatrix} 1 & \dots & 1 \\ 0 & \dots & 0 \\ -x_{s,1}^2 & \dots & -x_{s,N}^2 \\ \vdots & \vdots & \vdots \\ 2(1-N)x_{s,1}^{2N-1} & \dots & 2(1-N)x_{s,N}^{2N-1} \end{bmatrix}$$
$$\mathbf{A_2} = \begin{bmatrix} 0 & \dots & 0 \\ 1 & \dots & 1 \\ 2x_{s,1} & \dots & 2x_{s,N} \\ \vdots & \vdots & \vdots \\ (2N-1)x_{s,1}^{2N-2} & \dots & (2N-1)x_{s,N}^{2N-2} \end{bmatrix} \tag{C.42}$$

The solution process begins with calculating $\bar{S}_{s,k}$ and the terms of $\mathbf{A}$ based on w_i and x_i. Then, equation (C.41) is solved for a_i and $b_{s,i}$, which are used in equation (C.30) to solve the system of PDEs for w_i and x_i. Note that the conversion $b_i = x_m b_{s,i}$ must be performed before usage in (C.30).

To this point, the DQMOM equations have been presented in a general form. Now, they are applied more specifically to the system under consideration here. This will involve two components: simplifying the spatial variation to a single dimension and renaming variables.

Within a propellant tank we only variations in the vertical direction will be considered, so r_j is replaced with y. Additionally, to describe the velocity of bubbles in physical space the traditional u_i is used, where the subscript refers to the velocity of the i^{th} abscissa and weight. Unfortunately, given that bubbles are being discussed it is convenient to discuss the radius with the variable r despite its previous use as a spatial variable.

Implementing these changes (C.30) now becomes:

$$\begin{aligned} a_i &= \frac{\partial w_i}{\partial t} + \frac{\partial u_i w_i}{\partial y} \\ b_i &= \frac{\partial g_i}{\partial t} + \frac{\partial u_i g_i}{\partial y} \end{aligned} \tag{C.43}$$

and equation (C.40) is now

$$\bar{S}_{s,k} = \sum_{i=1}^{N} \frac{k}{r_m} w_i r_{s,i}^{k-1} \left.\frac{dr}{dt}\right|_{r=r_i} + \int r_s^k (h_{birth} - h_{death})\, dr_s \tag{C.44}$$

The fundamental governing equations for this system have now been established. Conservation of mass and energy for the ullage and liquid (equations (5.1), (5.2), (5.3), (5.5)), and the bubble transport equations (equations (C.43), (C.44), and (C.41)). To implement DQMOM in the system studied here however, expressions for dr/dt, h, and u_i, or bubble growth, nucleation, death, and velocity in physical space are all needed. These expressions will be discussed in subsequent sections.

While DQMOM, QMOM, and MOM are methods that that have enabled the solutions to many problems, they do share one important drawback: they give very limited information about the particle (here, bubble) distribution itself. Each of these methods allows for accurate or exact calculation of the moments of this distribution however reconstructing the actual distribution from these moments is mathematically impossible, and a wide range of distributions can produce the same set of moments [122]. This is generally not a problem for the purpose of modeling propellant tank dynamics as the quantities of interest (such as the void fraction or vapor mass fraction) can be calculated from the moments however it limits the physical insight that can be gained from the model.

DQMOM in particular can be frustrating in this regard as the abscissas and weights appear to yield a discretized distribution. Some researchers have even used these to compare with an experimentally measured size distribution (for example Cheung et al [123]). However, it is important to remember that there is no guarantee that the abscissas and weights resemble the actual distribution whatsoever. Only the

moments are guaranteed to be accurate.

Appendix D

Model Equations

In this appendix, the equations needed for each model will be given with the goal of making it easier for others to implement these in a consistent manner.

Bibliography

[1] Lohner, K., Dyer, J., Doran, E., and Dunn, Z., "Design and Development of a Sub-Scale Nitrous Oxide Monopropellant Gas Generator," *43rd AIAA/ASME/SAE/ASEE Joint Propulsion Conference & Exhibit*, No. July, 2007, pp. 1–10.

[2] Lemmon, E., Huber, M., and McLinden, M., "NIST Standard Reference Database 23: Reference Fluid Thermodynamic and Transport Properties (REFPROP), Version 9.0," 2010.

[3] Pelt, D. V., Hopkins, J., Skinner, M., Buchanan, A., Gulman, R., Chan, H., Karabeyoglu, M. A., and Cantwell, B. J., "Overview of a 4-inch OD Paraffin-Based Hybrid Sounding Rocket Program," *40th AIAA/ASME/SAE/ASEE Joint Propulsion Conference and Exhibit*, No. July, Fort Lauderdale, FL, 2004, pp. 1–27.

[4] Moran, M. J. and Howard N Shapiro, *Fundamentals Of Engineering Thermodynamics*, Wiley, Hoboken, NJ, 5th ed., 2004.

[5] Reiss, H., *Methods of Thermodynamics*, Blaisdell Publishing Compan, New York, NY, 1st ed., 1965.

[6] Zakirov, V. A. and Li, L., "1-D , Homogeneous Liquefied Gas Self-Pressurization Model," *European Conference for Aerospace Sciences (EUCASS)*, AAAF/RAs/ASBC, Moscow, Russia, 2005, pp. 1–7.

[7] Zilliac, G. G. and Karabeyoglu, M. A., "Modeling of Propellant Tank Pressurization," *41st AIAA/ASME/SAE/ASEE Joint Propulsion Conference & Exhibit*, Tucson, Arizona, 2005, pp. 1–25.

[8] Morey, T. F. and Traxler, J. J., "Pressurizing Gas Thermodynamics," *Rocket Propellant and Pressurization Systems*, edited by E. Ring, chap. 18, Prentice-Hall, Inc., Englewood Cliffs, New Jersey, 1964, pp. 211–245.

[9] Casalino, L. and Pastrone, D., "Optimal Design of Hybrid Rockets with Self-Pressurizing Oxidizer," *42nd AIAA/ASME/SAE/ASEE Joint Propulsion Conference & Exhibit*, Sacramento, California, 2006, pp. 1–10.

[10] Whitmore, S. A. and Chandler, S. N., "Engineering Model for Self-Pressurizing Saturated-N2O-Propellant Feed Systems," *Journal of Propulsion and Power*, Vol. 26, No. 4, jul 2010, pp. 706–714.

[11] Campbell, H. M. J., "Fluid Quality in a Self-Pressurized Container Discharge Line," Tech. rep., George C. Marshall Space Flight Center, Huntsville, Alabama, 1965.

[12] Ewig, R., McKinney, B., and Hudson, G., "Performance Modeling of Launch Vehicles utilizing Vapor Pressurization (VaPak) based Propulsion Systems," , No. September, 2006, pp. 1–11.

[13] Ewig, R., McKinney, B., and Hudson, G., "Pressurization (VaPak) based Propulsion Systems," *JANNAF 2007*, 2007, pp. 1–12.

[14] Lepore, D. F. and Ewig, "SSC08-IX-5 Results of QuickReach âĎć Small Launch Vehicle Propulsion Testing and Next Steps to Demonstration Flights SSC08-IX-5," *22nd Annual AIAA/USU Conference on Small Satellites*, 2008.

[15] Ewig, R., "Active Control of Vapor Pressurization (VaPak) Systems," Tech. rep., Holder Consulting Group, 2009.

[16] Ewig, R., "Vapor Pressurization (VaPak) Systems History, Concepts, and Applications," Tech. rep., Holder Consulting Group, 2009.

[17] Dunn, B. P., "Self-Pressurized Bipropellant Liquid Rockets," 2000.

[18] Herdy, R., "Nitrous Oxide/Hydrocarbon Fuel Advanced Chemical Propulsion: DARPA Contract Overview," *16th Thermal & Fluids Analysis Workshop*, 2006.

[19] Bentz, M. and Wilkinson, C. L., "Experimental Study of Flash Boiling in Liquid Nitrogen," *19th AIAA/SAE/ASME Joint Propulsion Conference*, AIAA, Seattle, WA, 1983, pp. 1–4.

[20] Akyuzlu, K. M., Patel, M., Coote, D., and Jones, S., "A Numerical Study of Heat and Mass Transfer at the Liquid-Vapor Interface of a Cryogenic Fluid Under Sudden Depressurization," *Heat and Mass Transfer: An Era of Change*, edited by T. N. Veziroglu, Nova Science Publications, Inc., 1993, pp. 1183–1197.

[21] Coote, D., *Numerical Simulation of Blowdown from a Cryogenic Tank*, Msc, University of New Orleans, 1998.

[22] Hutcherson, M. N., *Contribution to the theory of the two phase blowdown phenomenon*, Ph.D. thesis, University of Missouri, 1975.

[23] Hutcherson, M. N., Henry, R. E., and Wollersheim, D. E., "Two-Phase Vessel Blowdown of an Initially Saturated Liquid-Part 1: Experimental," *Journal of Heat Transfer*, Vol. 105, No. 4, 1983, pp. 687.

[24] Hutcherson, M. N., Henry, R. E., and Wollersheim, D. E., "Two-Phase Vessel Blow down of an Initially Saturated Liquid - Part 2 : Analytical," *Journal of Heat Transfer*, Vol. 105, No. November, 1983, pp. 694–699.

[25] Pinhasi, G. A., *Source Term Modeling of Gas and Liquid Releases from a Breached Pressure Vessel*, Ph.D. thesis, Tel Aviv University, 2000.

[26] Pinhasi, G. A., Ullmann, A., and Dayan, A., "Modeling of Flashing Two-Phase Flow," *Reviews in Chemical Engineering*, Vol. 21, No. 3-4, 2005, pp. 133–264.

[27] Elliott, D. G., Garrison, P. W., Klein, G. a., Moran, K. M., and Zydowicz, M. P., "Flow of nitrogen-pressurized Halon 1301 in fire extinguishing systems," Tech. rep., Jet Propulsion Laboratory, Pasadena, CA, 1984.

[28] Yang, J. C., Cleary, T. G., Huber, M. L., and Grosshandler, W. L., "Vapour nucleation in a cryogenic-fluid-dissolved-nitrogen mixture during rapid depressurization," *Proceedings of the Royal Society A: Mathematical, Physical and Engineering Sciences*, Vol. 455, No. 1985, 1999, pp. 1717–1738.

[29] Haque, M., Richardson, S., and Saville, G., "Blowdown of pressure vessels-II. Experimental validation of computer model and case studies," *Process Safety and*, 1992.

[30] Haque, M. and Richardson, S., "Blowdown of pressure vessels-I. Computer Model," *Process Safety and*, 1992.

[31] Mahgerefteh, H. and Wong, S., "A numerical blowdown simulation incorporating cubic equations of state," *Computers & Chemical Engineering*, Vol. 23, No. 9, 1999, pp. 1309–1317.

[32] Casalino, L. and Pastrone, D., "Optimal Design of Hybrid Rocket Motors for Microgravity Platform," *Journal of Propulsion and Power*, Vol. 24, No. 3, may 2008, pp. 491–498.

[33] Dyer, J., Doran, E., Dunn, Z., and Lohner, K., "Modeling Feed System Flow Physics for Self-Pressurizing Propellants," *43rd AIAA/ASME/SAE/ASEE Joint Propulsion Conference & Exhibit*, No. July, Cincinnati, Ohio, 2007, pp. 1–13.

[34] Solomon, B. J., *Engineering Model to Calculate Mass Flow Rate of a Two-Phase Saturated Fluid Through an Injector Orifice*, Ph.D. thesis, Utah State University, 2011.

[35] Hesson, J. C., *Flow of Two-Phase Carbon Dioxide Through Orifices*, Phd, Illinois Institute of Technology, 1957.

[36] Hesson, J. C. and Peck, R. E., "Flow of Two-phase Carbon Dioxide Through Orifices," *AIChE Journal*, Vol. 4, No. 2, 1958, pp. 207–210.

[37] Waxman, B. S., Zimmerman, J. E., Cantwell, B. J., and Zilliac, G. G., "Effects of Injector Design on Combustion Stability in Hybrid Rockets Using Self-Pressurizing Oxidizers," *50th AIAA/ASME/SAE/ASEE Joint Propulsion Conference*, AIAA, Cleveland, OH, 2014, pp. 1–29.

[38] Bergman, T., Incropera, F., Lavine, A., and DeWitt, D., *Fundamentals of Heat and Mass Transfer*, John Wiley & Sons, seventh ed., 2011.

[39] Corpening, J. H., "Analytic Modeling of Pressurization and Cryogenic Propellant Conditions for Lunar Landing Vehicle," *57th JPM / 7th Modeling and Simulation / 5th Liquid Propulsion / 4th Spacecraft Propulsion Joint Subcommittee Meeting, Colorado Springs, CO*, 2010.

[40] Span, R. and Wagner, W., "Equations of state for technical applications. I. Simultaneously optimized functional forms for nonpolar and polar fluids," *International journal of thermophysics*, Vol. 24, No. 1, 2003, pp. 1–39.

[41] Span, R. and Wagner, W., "Equations of State for Technical Applications . III . Results for Polar Fluids," *International Journal*, Vol. 24, No. 1, 2003.

[42] Lemmon, E. W. and Span, R., "Correlations Short Fundamental Equations of State for 20 Industrial Fluids," *Journal of Chemical and Engineering Data*, Vol. 51, No. 3, 2006, pp. 785–850.

[43] Shamsundar, N. and Lienhard, J., "Equations of state and spinodal lines âĂŤ a review," *Nuclear Engineering and Design*, Vol. 141, No. 1-2, jun 1993, pp. 269–287.

[44] Peng, D.-Y. and Robinson, D. B., "A New Two-Constant Equation of State," *Industrial & Engineering Chemistry Fundamentals*, Vol. 15, No. 1, feb 1976, pp. 59–64.

[45] Walter, G. H., "Thermophysical properties of nitrous oxide," Tech. Rep. September, IHS ESDU, 1991.

[46] Lee, C. S., Yoo, K.-P., Kim, W. Y., and Lee, H., "Korea Thermophysical Properties Data Bank: Properties of Pure Nitrous Oxide," Tech. rep., Chemical Engineering Research Information Center.

[47] Fehlberg, E., "Low-order classical Runge-Kutta formulas with stepsize control and their application to some heat transfer problems," Tech. Rep. July, NASA (TR R-315), Washington, D.C., 1969.

[48] Fernandez, M., *Propellant tank pressurization modeling for a hybrid rocket*, Ph.D. thesis, 2009.

[49] Prince, E. R., Krishnamoorthy, S., Ravlich, I., Kotine, A., Fickes, A. C., Fidalgo, A. I., Freeman, K., Anderson, K., and Gerson, D., "Design, Analysis, Fabrication, Ground-Test, and Flight of a Two-Stage Hybrid and Solid Rocket," *49th AIAA/ASME/SAE/ASEE Joint Propulsion Conference and Exhibit*, AIAA, San Jose, CA, 2013, pp. 1–25.

[50] Simurda, L. and Zilliac, G., "Continued Testing of a High Performance Hybrid Propulsion System for Small Satellites," *51st AIAA/ASME/SAE/ASEE Joint Propulsion Conference*, AIAA, Orlando, FL, 2015, pp. 1–23.

[51] Karabeyoglu, M. A., Dyer, J., Stevens, J., and Cantwell, B. J., "Modeling of N2O Decomposition Events," *44th AIAA/ASME/SAE/ASEE Joint Propulsion Conference & Exhibit*, Hartford, Connecticut, 2008, pp. 1–29.

[52] Munke, K., "Nitrous Oxide Trailer Rupture," *CGA Seminar: Safety and Reliability of Industrial Gases, Equipment, and Facilities*, Linde Gas AG, St. Louis, Missouri, 2001.

[53] Merrill, C., "Nitrous Oxide Explosive Hazards (Preprint)," *Defense Explosives Safety Seminar*, Palm Springs, CA, 2008.

[54] "Scaled Composites Safety Guidelines for N2O," Tech. rep., Scaled Composites, LLC, 2009.

[55] Cawthra, J. K. and Eisenstadt, M., "Summary of nitrous oxide investigations," *AFWL-TR-75-231*, 1976.

[56] Rhodes, G., "Investigation of Decomposition Characteristics of Gaseous and Liquid Nitrous Oxide," Tech. Rep. July, DTIC Document, 1974.

[57] Forster, P. and Ramaswamy, V., "Changes in Atmospheric Constituents and in Radiative Forcing," *Climate Change 2007: The Physical Science Basis*, Cambridge University Press, 2007.

[58] Wark, K. J., *Advanced Thermodynamics for Engineers*, McGraw-Hill, New York, sixth ed., 1995.

[59] Ashraf-Khorassani, M., Taylor, L. T., and Zimmerman, P., "Nitrous oxide versus carbon dioxide for supercritical-fluid extraction and chromatography of amines," *Analytical Chemistry*, Vol. 62, No. 11, jun 1990, pp. 1177–1180.

[60] Lundanes, E., Iversen, B., and Greibrokk, T., "Group Separation of Petroleum Using Supercritical Fluids: A Comparison of Supercritical Nitrous Oxide and Carbon Dioxide as Mobile Phases," *Journal of Chromatography*, Vol. 366, 1986, pp. 391–395.

[61] "Nitrous Oxide Compatibility Test," Tech. Rep. October, Advanced Pressure Technology, 2010.

[62] "DuPont Chemical Resistance Guide," .

[63] "Parker O-ring handbook," Tech. rep., Parker Hannifin Corporation, O-Ring Division, Lexington, KY, 2007.

[64] Swagelok, "Valve Sizing Technical Bulletin," Tech. rep., Swagelok.

[65] Harris, D. C., *Materials for Infrared Windows and Domes: Properties and Performance*, SPIE Optical Engineering Press, 1999.

[66] Yoder, Paul, J. and Vukobratovich, D., *Opto-Mechanical Systems Design*, CRC Press, Boca Raton, FL, 4th ed., 2015.

[67] Salamin, E., "The Weibull Distribution in the Strength of Glass," Tech. rep., University of Arizona, 2003.

[68] Klein, C. a., "High-energy laser windows: case of fused silica," *Optical Engineering*, Vol. 49, No. 9, sep 2010, pp. 091006.

[69] Barron, R. F. and Barron, B., *Design for Thermal Stresses*, John Wiley & Sons, Hoboken, NJ, 2012.

[70] Pettersen, J., "Experimental study on boiling liquid expansion in a CO2 vessel," *The Fifth IIR-Gustav Lorentzen Conference on Natural Working Fluids. Guangzhou, China*, 2002, pp. 106–113.

[71] Ghiaasiaan, S. M., *Two-Phase Flow, Boiling and Condensation: in conventional and miniature systems*, Cambridge University Press, 2008.

[72] Griffith, P. and Wallis, J. D., "The Role of Surface Conditions in Nucleate Boiling," , No. 14, 1958, pp. 1–32.

[73] Shin, T. S. and Jones, O. C., "Nucleation and Flashing in Nozzles - 1," *International Journal of Multiphase Flow*, Vol. 19, No. 6, 1993, pp. 943–964.

[74] Brennen, C. E., *Cavitation and Bubble Dynamics*, 1995.

[75] Henry, R. E. and Fauske, H. K., "The Two-Phase Critical Flow of One-Component Mixtures in Nozzles, Orifices, and Short Tubes," *Journal of Heat Transfer*, , No. May, 1971, pp. 179–187.

[76] Blander, M. and Katz, J. L., "Bubble nucleation in liquids," *AIChE Journal*, Vol. 21, No. 5, sep 1975, pp. 833–848.

[77] Alamgir, M. and Lienhard, J. H., "Correlation of Pressure Undershoot During Hot-Water Depressurization," *Journal of Heat Transfer*, Vol. 103, 1981, pp. 1979–1982.

[78] Morgan, S. K. and Brady, H. F., "Elimination of the Geysering Effect in Missiles," *Rocket Propellant and Pressurization Systems*, edited by E. Ring, chap. 11, Prentice-Hall, Inc., Englewood Cliffs, New Jersey, 1964, pp. 89–101.

[79] Murphy, D., "An experimental investigation of geysering in vertical tubes," *Advances in Cryogenic Engineering*, 1965, pp. 353–359.

[80] Karabeyoglu, M. A., "Nitrous Oxide and Oxygen Mixtures (Nytrox) as Oxidizers for Rocket Propulsion Applications," *Journal of Propulsion and Power*, Vol. 30, No. 3, may 2014, pp. 696–706.

[81] Karabeyoglu, M. A., "Mixtures of Nitrous Oxide and Oxygen (Nytrox) as Oxidizers for Rocket Propulsion Applications," *45th AIAA/ASME/SAE/ASEE Joint Propulsion Conference & Exhibit*, No. August, Denver, Colorado, 2009.

[82] Karabeyoglu, M. A., "Mixtures of Nitrous Oxide, Carbon Dioxide and Oxygen as Oxidizers for Mars Applications," *46th AIAA/ASME/SAE/ASEE Joint Propulsion Conference & Exhibit*, No. July, 2010.

[83] Vozoff, M. and Mungas, G., "NOFBX: A Non-Toxic, "Green" Propulsion Technology with High Performance and Low Cost," *AIAA SPACE 2012 Conference & Exposition*, No. September 2012, AIAA, Pasadena, CA, 2012, pp. 1–15.

[84] Waxman, B. S., *An Investigation of Injectors for Use with High Vapor Pressure Propellants with Applications to Hybrid Rockets*, Ph.D. thesis, Stanford University, 2014.

[85] Zilliac, G., Waxman, B. S., Evans, B., Karabeyoglu, M. A., and Cantwell, B., "Peregrine Hybrid Rocket Motor Development," *50th AIAA/ASME/SAE/ASEE Joint Propulsion Conference*, 2014, pp. 1–17.

[86] Marchisio, D. L. and Fox, R. O., "Solution of population balance equations using the direct quadrature method of moments," *Journal of Aerosol Science*, Vol. 36, No. 1, jan 2005, pp. 43–73.

[87] Cole, R., "Boiling Nucleation," *Advances in Heat Transfer*, Vol. 10, 1974, pp. 85–166.

[88] Shoukri, M., *Nucleation Site Activation in Saturated Boiling*, Master of engineering, McMaster University, 1974.

[89] Hibiki, T. and Ishii, M., "Active nucleation site density in boiling systems," *International Journal of Heat and Mass Transfer*, Vol. 46, No. 14, 2003, pp. 2587–2601.

[90] Pei, N., Guo, K., Liu, J., and Li, T., "Measurement of contact angle between stainless steel surface and carbon dioxide by pendant drop method," *Chinese Science Bulletin*, Vol. 53, No. 16, 2008, pp. 2560–2564.

[91] Blinkov, V. N., Jones, O. C., and Nigmatulin, B. I., "Nucleation and flashing in nozzles-2: comparison with experiments using a five-equation model for vapor void development," *International Journal of Multiphase Flow*, Vol. 19, No. 6, 1993, pp. 965–986.

[92] Cornwell, K., "On boiling incipience due to contact angle hysteresis," *International Journal of Heat and Mass Transfer*, Vol. 25, No. 2, 1982, pp. 205–211.

[93] Qi, Y. and Klausner, J. F., "Heterogeneous Nucleation With Artificial Cavities," *Journal of Heat Transfer*, Vol. 127, No. 11, 2005, pp. 1189.

[94] Jones, O. C. and Zuber, N., "Bubble Growth in Variable Pressure Fields," *Journal of Heat Transfer*, Vol. 100, No. August 1978, 1978, pp. 453–459.

[95] Scriven, L., "On the dynamics of phase growth," *Chemical Engineering Science*, Vol. 10, No. 1-2, 1959, pp. 1–13.

[96] Ruckenstein, E., "On heat transfer between vapour bubbles in motion and the boiling liquid from which they are generated," *Chemical Engineering Science*, Vol. 10, No. 1-2, 1959, pp. 22–30.

[97] Legendre, D., Boree, J., and Magnaudet, J., "Thermal and dynamic evolution of a spherical bubble moving steadily in a superheated or subcooled liquid," *Physics of Fluids*, Vol. 10, No. 6, 1998, pp. 1256.

[98] Jensen, M. K. and Memmel, G. J., "Evaluation of Bubble Departure Diameter Correlations," *Proceedings of the Eighth International Heat Transfer Conference*, San Francisco, CA, 1986, pp. 1907–1912.

[99] Kutateladze, S. and Gogonin, I., "Growth rate and detachment diameter of a vapor bubble in free convection boiling of a saturated liquid," *High Temperature Science*, Vol. 17, No. 4, 1980, pp. 667–671.

[100] Ishii, M. and Zuber, N., "Drag coefficient and relative velocity in bubbly, droplet or particulate flows," *AIChE Journal*, Vol. 25, No. 5, 1979, pp. 843–855.

[101] Hikita, H. and Kikukawa, H., "Liquid-phase mixing in bubble columns: Effect of liquid properties," *The Chemical Engineering Journal*, Vol. 8, No. 3, 1974, pp. 191–197.

[102] Yeoh, G. H., Cheung, C. P., and Tu, J., *Multiphase Flow Analysis Using Population Balance Modeling*, Elsevier, Waltham, MA, 2014.

[103] Prince, M. J. and Blanch, H. W., "Bubble coalescence and break-up in air-sparged bubble columns," *AIChE Journal*, Vol. 36, No. 10, oct 1990, pp. 1485–1499.

[104] Chesters, A., "The Modelling of Coalescence Processes in Fluid-Liquid Dispersions: A review of Current Understanding," *Chemical engineering research & design*, Vol. 69a, No. A, 1991, pp. 259–270.

[105] Gorenflo, D. and Kotthoff, S., "Review on pool boiling heat transfer of carbon dioxide," *International Journal of Refrigeration*, Vol. 28, No. 8, 2005, pp. 1169–1185.

[106] Waxman, B. S., Zimmerman, J. E., Cantwell, B. J., and Zilliac, G. G., "Mass Flow Rate Characterization of Injectors for Use with Self-Pressurizing Oxidizers in Hybrid Rockets," *60th JANNAF Propulsion Meeting*, 2013.

[107] Press, W. H., Teukolsky, S. A., Vetterling, W. T., and Flannery, B. P., *Numerical Recipes in Fortran 77: The Art of Scientific Computing*, Cambridge University Press, Cambridge, UK, 2nd ed., 1992.

[108] Cash, J. R. and Karp, A. H., "A variable order Runge-Kutta method for initial value problems with rapidly varying right-hand sides," *ACM Transactions on Mathematical Software*, Vol. 16, No. 3, 1990, pp. 201–222.

[109] Bogacki, P. and Shampine, L., "A 3(2) Pair of Runge-Kutta Formulas," *Appl Math Lett*, Vol. 2, No. 4, 1989, pp. 321–325.

[110] Abdulle, A. and Medovikov, A. A., "Second order Chebyshev methods based on orthogonal polynomials," *Numerische Mathematik*, Vol. 90, 2001, pp. 1–18.

[111] Abdulle, A., "Fourth Order Chebyshev Methods with Recurrence Relation," *SIAM Journal on Scientific Computing*, Vol. 23, No. 6, 2002, pp. 2041–2054.

[112] Lang, J. and Verwer, J. G., "ROS3P : An accurate third-order Rosenbrock solver designed for parabolic problems," *Report - Modelling, analysis and simulation*, Vol. 41, No. 13, 2000, pp. 1–7.

[113] Bank, R., Coughran, W., Fichtner, W., Grosse, E., Rose, D., and Smith, R., "Transient simulation of silicon devices and circuits," *IEEE Transactions on Electron Devices*, Vol. 32, No. 4, 1985, pp. 1992–2007.

[114] Broyden, C. G., "A class of methods for solving nonlinear simultaneous equations," *Mathematics of Computation*, Vol. 19, No. 92, 1965, pp. 577–593.

[115] Hensen, J. L. M. and Nakhi, A. E., "Fourier and Biot Nmubers and the Accuracy of Conduction Modeling," *Building Environmental Performance*, 1994.

[116] Ramkrishna, D., *Population Balances: Theory and Applications to Particulate Systems Engineering*, Academic Press, 1st ed., 2000.

[117] McGraw, R., "Description of Aerosol Dynamics by the Quadrature Method of Moments," *Aerosol Science and Technology*, Vol. 27, No. 2, jan 1997, pp. 255–265.

[118] Petitti, M., Nasuti, A., Marchisio, D. L., Vanni, M., Baldi, G., Chimica, I., and Torino, P., "Bubble Size Distribution Modeling in Stirred Gas-Liquid Reactors with QMOM Augmented by a New Correction Algorithm," *AIChE Journal*, Vol. 56, No. 1, 2010, pp. 3–5.

[119] Marchisio, D. L., Vigil, R., and Fox, R. O., "Quadrature method of moments for aggregation-breakage processes," *Journal of Colloid and Interface Science*, Vol. 258, No. 2, feb 2003, pp. 322–334.

[120] Su, J., Gu, Z., Li, Y., Feng, S., and Yun Xu, X., "Solution of population balance equation using quadrature method of moments with an adjustable factor," *Chemical Engineering Science*, Vol. 62, No. 21, 2007, pp. 5897–5911.

[121] Fox, R., "Bivariate direct quadrature method of moments for coagulation and sintering of particle populations," *Journal of Aerosol Science*, Vol. 37, No. 11, nov 2006, pp. 1562–1580.

[122] John, V., Angelov, I., a.a. Öncül, and Thévenin, D., "Techniques for the reconstruction of a distribution from a finite number of its moments," *Chemical Engineering Science*, Vol. 62, No. 11, jun 2007, pp. 2890–2904.

[123] Cheung, S. C. P., Deju, L., Yeoh, G. H., and Tu, J. Y., "Modeling of bubble size distribution in isothermal gas-liquid flows: Numerical assessment of population balance approaches," *Nuclear Engineering and Design*, Vol. 265, 2013, pp. 120–136.